

# Photo-physical Properties of Perovskites on Curved Surfaces

Thèse N° 7518

Présentée le 1<sup>er</sup> novembre 2019

à la Faculté des sciences de base

Laboratoire de physique de la matière complexe

Programme doctoral en physique

pour l'obtention du grade de Docteur ès Sciences

par

**Konstantins MANTULNIKOVS**

Acceptée sur proposition du jury

Prof. F. Mila, président du jury

Prof. L. Forró, Dr A. Sienkiewicz, directeurs de thèse

Prof. T. Garma, rapporteur

Prof. K. Kamarás, rapporteuse

Prof. F. Nüesch, rapporteur

2019





# Abstract

Organic-inorganic metal halide perovskites (MHPs) have recently attracted increasing attention as highly-efficient light-harvesting materials for photovoltaic applications. The technical ease of solution processing of these materials is one of their major advantages on the route towards fabrication of low-cost solar cells and optoelectronic devices. However, the precise control of crystallization and morphology of MHPs deposited from solutions, considered crucial for enhancing the final photovoltaic performance, still remains challenging.

In this context, the present work deals with morphology and photo-physical properties of thin polycrystalline films of two archetypal MHPs, i.e. methylammonium lead triiodide,  $\text{CH}_3\text{NH}_3\text{PbI}_3$  (MAPbI<sub>3</sub>) and methylammonium lead tribromide,  $\text{CH}_3\text{NH}_3\text{PbBr}_3$  (MAPbBr<sub>3</sub>), deposited by solution processing on non-conducting substrates with different curvatures.

Firstly, the PhD thesis focuses on novel and thus far unexplored issues of crystallization mechanisms and photo-physical characterization of polycrystalline MAPbI<sub>3</sub> and MAPbBr<sub>3</sub> coated via one-step solution processing onto the surface of elongated, cylinder-shaped, quartz substrates with unprecedentedly high curvatures (diameters in the range of 80 to 1800  $\mu\text{m}$ ). The obtained results are then compared with the ones gathered for deposits of polycrystalline MAPbI<sub>3</sub> and MAPbBr<sub>3</sub> on planar substrates.

Secondly, the deposits of polycrystalline MAPbI<sub>3</sub> and MAPbBr<sub>3</sub> on cylindrical substrates are used to track the changes in photoluminescence (PL) and photocurrent (PC) of these materials in the presence of various gaseous media. In particular, the advantages offered by small cross-sectional dimensions and the cylindrical geometry of thus obtained deposits of MAPbI<sub>3</sub> and MAPbBr<sub>3</sub> made it possible to easily combine them with simple gas-flow observation chambers having both optical and electrical accesses. This approach enabled to perform simultaneous measurements of PL and PC for polycrystalline deposits of MAPbI<sub>3</sub> and MAPbBr<sub>3</sub> exposed to the precisely controlled flow of different gaseous media, including technologically important oxygen ( $\text{O}_2$ ) and nitrogen ( $\text{N}_2$ ). Thus, an insight could be gained into the role and importance of surface defects for the general optoelectronic properties, such as photo-brightening and photo-bleaching, as well as long-term stability of these materials.

Thirdly, a study of selective photo-bleaching of MAPbI<sub>3</sub> under illumination with specific wavelengths is performed. In particular, we show that exposures of polycrystalline deposits of this material to the blue light (470 nm) resulted in a rapid partial photo-bleaching, whereas exposures to the green light (546 nm) lead to a partial photo-recovery of the PL intensity. Moreover, by performing for the first time this type of experiments under precisely controlled atmosphere of either  $\text{O}_2$  or  $\text{N}_2$ , additional insight could be gained on the influence of these

## Abstract

---

gaseous media on the mechanism of selective, wavelength-dependent photo-bleaching in MAPbI<sub>3</sub>.

Lastly, a study of the photo-induced charge transfer in a model system of the interface between MAPbI<sub>3</sub> and TiO<sub>2</sub> is carried out. Specifically, a contactless technique based on a combination of low-temperature electron spin resonance (ESR) with *in situ* illumination (Photo-ESR) is used to directly track the photo-carriers at the MAPbI<sub>3</sub>/TiO<sub>2</sub> interface. In particular, this approach shows that the ESR signal intensity of paramagnetic defects in TiO<sub>2</sub> (Ti<sup>3+</sup>-related centers) markedly changes upon illumination of the MAPbI<sub>3</sub>/TiO<sub>2</sub> interface. It is then inferred that the presented novel methodology can be used to monitor the flow of light-excited electrons from MAPbI<sub>3</sub> to TiO<sub>2</sub>.

Altogether, in addition to exploring morphological and photo-physical aspects of thin polycrystalline films of two archetypal MHPs, that is MAPbI<sub>3</sub> and MAPbBr<sub>3</sub>, coated onto strongly curved substrates, this PhD dissertation also provides a novel approach for designing MHPs-based devices. In particular, it paves the way for designing sensitive differential gas sensors, which are expected to function under various environmental conditions.

**Key words:** Organometallic perovskites, MAPbI<sub>3</sub>, MAPbBr<sub>3</sub>, curved substrates, morphology, photoluminescence, photocurrent, gaseous media, differential gas sensing

# Résumé

Les pérovskites organo-métalliques (POMs) attirent de plus en plus l'attention grâce à leur haute efficacité de la récolte de lumière pour des applications photovoltaïques. La facilité technique du traitement en solution de ces matériaux est l'un des principaux avantages menant à une fabrication de cellules solaires et de dispositifs optoélectroniques à faible coût. Cependant, le contrôle précis de la cristallisation ainsi que la morphologie des POMs déposées à partir de solutions, considérées comme essentielles pour améliorer les performances photovoltaïques finales, reste difficile.

Dans ce contexte, ce travail traite la morphologie et les propriétés photo-physiques des couches minces polycristallines de deux matériaux pérovskites archétypiques, à savoir le méthylammonium iodure de plomb,  $\text{CH}_3\text{NH}_3\text{PbI}_3$  ( $\text{MAPbI}_3$ ) et méthylammonium bromure de plomb,  $\text{CH}_3\text{NH}_3\text{PbBr}_3$  ( $\text{MAPbBr}_3$ ) qui sont déposés par traitement en solution sur des substrats isolants à courbes variées.

Premièrement, la thèse porte tout d'abord sur des problèmes nouveaux, et jusqu'ici inexplorés, liés aux mécanismes de cristallisation et à la caractérisation photo-physique de  $\text{MAPbI}_3$  et  $\text{MAPbBr}_3$  polycristallins, déposés via une "procédure en une étape" sur la surface de substrats de quartz allongées en forme de cylindre avec des faibles diamètres sans précédents (de 80 à 1800  $\mu\text{m}$ ). Les résultats obtenus sont ensuite comparés à ceux rassemblés pour les dépôts de  $\text{MAPbI}_3$  et  $\text{MAPbBr}_3$  polycristallins sur des substrats plats.

Deuxièmement, les dépôts de  $\text{MAPbI}_3$  et  $\text{MAPbBr}_3$  polycristallins sur des substrats cylindriques sont utilisés pour suivre les changements de photoluminescence (PL) et de photocourant (PC) de ces matériaux en présence de divers milieux gazeux. En particulier, les avantages offerts par les petites sections efficaces et la géométrie cylindrique des dépôts de  $\text{MAPbI}_3$  et  $\text{MAPbBr}_3$  obtenus ont permis de les combiner facilement avec de simples chambres d'observation du flux de gaz ayant à la fois des accès optiques et électriques. Cette approche a permis d'effectuer simultanément des mesures de PL et de PC pour les dépôts polycristallins de  $\text{MAPbI}_3$  et de  $\text{MAPbBr}_3$  exposés au flux contrôlé avec précision des différents milieux gazeux, y compris de deux gaz technologiquement importants, l'oxygène ( $\text{O}_2$ ) et azote ( $\text{N}_2$ ). Ceci permettrait de mieux comprendre le rôle et l'importance des défauts de surface pour les propriétés optoélectroniques générales, telles que le photo-éclaircissement et le photo-blanchiment, ainsi que la stabilité à long terme de ces matériaux.

Troisièmement, une étude du photo-blanchiment sélectif de  $\text{MAPbI}_3$  sous illumination avec des longueurs d'onde spécifiques est réalisée. Nous montrons en particulier que les dépôts polycristallins de ce matériau exposés à la lumière bleue (470 nm) ont entraîné un photo-

blanchiment rapide et partiel, alors que les expositions à la lumière verte (546 nm) ont entraîné une récupération partielle de l'intensité PL. De plus, en effectuant, pour la première fois, ce type d'expériences sous atmosphère précisément contrôlé (soit de O<sub>2</sub>, soit de N<sub>2</sub>), il serait possible de mieux comprendre l'influence de ces milieux gazeux sur le mécanisme de photo-blanchiment sélectif, suivant la longueur d'onde, dans le MAPbI<sub>3</sub>.

Enfin, une étude du transfert de charge photo-induit dans un système modèle de l'interface entre MAPbI<sub>3</sub> et TiO<sub>2</sub> est réalisée. Plus précisément, une technique sans contact, basée sur une combinaison de résonance paramagnétique électronique (RPE) à basse température et d'éclairage *in situ* (Photo-RPE), est utilisée pour suivre directement les photo-porteurs au niveau de l'interface MAPbI<sub>3</sub>/TiO<sub>2</sub>. En particulier, cette approche montre que l'intensité du signal RPE des centres paramagnétiques des défauts de Ti<sup>3+</sup> dans TiO<sub>2</sub> est considérablement altérée lors de l'éclairage de l'interface MAPbI<sub>3</sub>/TiO<sub>2</sub>. On en déduit que cette nouvelle méthodologie peut être utilisée pour surveiller le flux d'électrons excités par la lumière depuis MAPbI<sub>3</sub> vers TiO<sub>2</sub>.

Au total, en plus d'explorer les aspects morphologiques et photophysiques de couches minces polycristallines de deux POMs archétypes (MAPbI<sub>3</sub> et MAPbBr<sub>3</sub>, appliqués sur des substrats fortement courbés, cette thèse fournit également une nouvelle approche pour la conception de dispositifs basés sur les POMs. En particulier, il ouvre la voie à la conception de détecteurs de gaz différentiels sensibles, qui devraient fonctionner dans diverses conditions environnementales.

Mots clefs : Pérovskites organometalliques, MAPbI<sub>3</sub>, MAPbBr<sub>3</sub>, substrats courbés, morphologie, photoluminescence, photocourant, milieux gazeux, détection de gaz différentielle

## Thesis overview

The investigation of photo-physical properties of thin deposits of archetypal MHPs, such as MAPbI<sub>3</sub> and MAPbBr<sub>3</sub>, is of crucial importance for the emerging MHPs-based photovoltaic technology. In this light, Chapter 1 introduces the reader to the field of renewable energy sources and the most important properties of the MHPs relevant for further discussion in this PhD thesis.

A detailed insight into the technical aspects of all the experiments and techniques used can be found in Chapter 2.

Currently, the most frequently reported studies have been focused on morphology and photo-physical properties of thin MHPs polycrystalline films coated onto planar substrates. In this regard, this PhD thesis explores a different approach, which is based on growing micro-crystalline deposits of MAPbI<sub>3</sub> and MAPbBr<sub>3</sub> on curved surfaces of cylinder-shaped quartz rods with diameters in the range of 80 to 1800  $\mu\text{m}$  – this part of the work is covered in Chapter 3. A comprehensive characterization by optical and fluorescence microscopy techniques, as well as by scanning electron microscopy and X-ray diffraction, has shown that the substrate curvature has a strong influence on the morphology of polycrystalline deposits of these MHPs. Notably, the obtained results indicated that with increasing substrate curvatures a marked size-reduction of micro-crystallites, concomitant with an increased crystal packing density, occurred for both MAPbI<sub>3</sub> and MAPbBr<sub>3</sub>. Furthermore, this study has highlighted the major morphological difference between the polycrystalline deposits of both MHPs, by indicating that their crystallites grow as micro-wires for MAPbI<sub>3</sub> and as micro-cubes for MAPbBr<sub>3</sub>.

Although the crystallite sizes of both MHPs markedly decrease for substrates with higher curvatures, the present study also shows that the corresponding luminescence emission spectra, including PL spectral peak positions and spectral line shapes, do not significantly evolve for deposits on substrates with different diameters.

The decrease in crystallite sizes and a denser coverage of micro-crystalline MHPs coated onto cylinder-shaped substrates with higher curvatures were attributed to two major factors, both related to the annealing step of the deposits. In particular, the substrate diameter-dependent variability of the heat capacities and the substrate curvature-enhanced solvent evaporation rate seemed to contribute the most to the crystallization process and the resulting morphology changes of MAPbI<sub>3</sub> and MAPbBr<sub>3</sub> deposits on cylinder-shaped quartz substrates with various diameters.

Despite extensive research efforts concerning physicochemical properties of both archetypal MHPs, MAPbI<sub>3</sub> and MAPbBr<sub>3</sub>, the impact of gaseous media on their photo-electric properties

still remain poorly understood. Therefore, another major contribution of this thesis, described in great detail in Chapter 4, is the study on the effects of gaseous media on the photo-physical properties of these two MHPs. In particular, an elongated cylinder-shaped geometry and high surface-to-volume ratios of thin film deposits of MHPs coated onto the curved surfaces of quartz substrates (rods) revealed advantageous for designing miniature gas-flow chambers. Due to transparency to light and facile implementation of electrical contacts, this approach made it possible to simultaneously investigate the PL and PC responses of both MHPs exposed to the precisely controlled recurrent flow of various gaseous media, with particular attention to the flow of O<sub>2</sub> and N<sub>2</sub>.

Specifically, for collecting the PL spectra and PC responses of two MHPs, two different excitation wavelengths ( $\lambda_{exc}$ ) were used, that is  $\lambda_{exc} = 546$  nm for MAPbI<sub>3</sub> and  $\lambda_{exc} = 470$  nm for MAPbBr<sub>3</sub>. We found that under exposure to O<sub>2</sub>, the PL responses of MAPbI<sub>3</sub> and MAPbBr<sub>3</sub> were markedly opposite, i.e. the PL decreased for MAPbI<sub>3</sub>, whereas it increased for MAPbBr<sub>3</sub>. In contrast, under the exposure to N<sub>2</sub>, the PL of MAPbI<sub>3</sub> increased, while it decreased for MAPbBr<sub>3</sub>. A considerably differential behavior was also found for the PC responses. In particular, under intermittent exposures to N<sub>2</sub> or O<sub>2</sub>, the PL and PC responses of MAPbBr<sub>3</sub> correlated, whereas for MAPbI<sub>3</sub> they anti-correlated.

In addition, the simultaneous exposure to  $\lambda_{exc} = 470$  nm of two different MHPs, positioned *side-by-side* in the miniature gas-flow chamber and therefore exposed to the exactly identical environmental conditions, clearly confirmed the differential responses of MAPbI<sub>3</sub> and MAPbBr<sub>3</sub> deposits to the recurrent flow of either of N<sub>2</sub> or O<sub>2</sub>.

The work described in Chapter 5 helps to further uncover the photo-physical properties of thin polycrystalline films of MAPbI<sub>3</sub>, additional experiments were carried out to pinpoint the impact of O<sub>2</sub> molecules on the selective photo-bleaching of this material exposed to illumination with either the blue light ( $\lambda_{exc} = 470$  nm) or to co-excitation with two wavelengths, i.e. at  $\lambda_{exc} = 546$  nm and  $\lambda_{exc} = 470$  nm. To this end, recurrent photo-bleaching and photo-recovery PL cycles in polycrystalline films and single crystals of MAPbI<sub>3</sub> were monitored under intermittent illumination with strong fluxes of one of the chosen excitation wavelengths ( $\lambda_{exc} = 546$  nm or  $\lambda_{exc} = 470$  nm).

Specifically, the same spot of the deposit was exposed for several times to multiple cycles of “light ( $\lambda_{exc} = 470$  nm) – dark – light ( $\lambda_{exc} = 546$  nm)”. During the subsequent illumination cycles, the exposure times were of ~2 min and ~10 min, for the excitation wavelengths of 470 nm and 546 nm, respectively. Each short exposure to the wavelength of 470 nm repeatedly resulted in a rapid diminishment of the PL intensity (by ~50%). This marked PL decrease could also be followed as a function of time under the continuous excitation at 470 nm. Interestingly, after switching the excitation wavelength to 546 nm, the PL intensity could be partially recovered on a time scale of ~10 min.

In addition, we could also demonstrate that under simultaneous illumination with two wavelengths (co-excitation with  $\lambda_{exc} = 546$  nm and  $\lambda_{exc} = 470$  nm) the characteristic PL peak of MAPbI<sub>3</sub> at ~780 nm rapidly decreased (by ~20 – 30%). This observation points to a possibility of modulation of the PL intensity of MAPbI<sub>3</sub> with using two incident illumination wavelengths. Overall, the recurrent exposures to 470 nm light resulted in a relatively rapid photo-bleaching,

whereas exposures to 546 nm light lead to a somewhat slower recovery of the PL intensity. Moreover, since the photo-recovery of the PL intensity was not entirely complete, after the recurrent photo-bleaching events, a net decrease in the PL intensities was also observed as a function of illumination time.

It is widely accepted that the performance of MHPs-based photovoltaic devices critically depends on the design and material properties of the interface between the light-harvesting MHP layer and the electron transport layer (ETL). Therefore, the detailed insight into the transfer mechanisms of photo-generated carriers at the ETL/MHP interface is of paramount importance.

Therefore, Chapter 6 of this dissertation was also focused on elaboration of a contactless method to directly track the photo-carriers at the ETL/MHP interface. To this end, the technique of low-temperature electron spin resonance (ESR) in combination with in situ illumination (Photo-ESR) was implemented. Specifically, we paid attention to a model nanohybrid material consisting of  $\text{TiO}_2$ -based nanowires ( $\text{TiO}_2\text{NWs}$ ) dispersed in the polycrystalline  $\text{MAPbI}_3$  matrix. Our approach was based on observation of the light-induced decrease in intensity of the ESR signal of paramagnetic defects of trivalent titanium ( $\text{Ti}^{3+}$ ,  $S = 1/2$ ) in thermally reduced  $\text{TiO}_2\text{NWs}$ . The diminishment of the ESR signal intensity was associated with the photo-excited electrons that cross the ETL/MHP interface and contribute to the conversion of paramagnetic  $\text{Ti}^{3+}$  states to ESR-silent  $\text{Ti}^{2+}$  states.

Finally, chapter 7 brings the conclusion giving a broad overview and synthesis of the work performed during this thesis as well as gives outlook to further investigations.





# Acknowledgements

On my journey to obtain a Ph.D. degree I have been surrounded by many people who have made this journey a lot of fun, helped me out and in general made it possible.

**Prof. László Forró** – thank you very much for letting me have an amazing opportunity to join a great research group and to contribute to the field of organic-inorganic perovskites. Moreover, I am extremely grateful for your guidance and the freedom you gave me to explore and find an interesting and somewhat non-conventional direction of research inside this broad field.

**Dr. Andrzej Sienkiewicz** – I greatly enjoyed our scientific work. Thank you very much for constantly supporting me and sharing your immense experience with me. I have learned a ton and have explored many exciting scientific and engineering concepts thanks to your amazing pool of ideas.

**Prof. Frank Nüesch, Prof. Katalin Kamarás, Prof. Tonko Garma and Prof. Frédéric Mila** – I would like to thank the jury committee for accepting to participate in my thesis examination, their service and valuable remarks.

**Dr. Endre Horváth** – thank very much for helping out with all the chemistry related things. Without that there'd be none of the perovskite-related work made. Also it was great to work with you and to tap into all your ideas and seemingly limitless positive attitude.

**Dr. Péter Matus** – thank you for your friendly support, especially during the earlier stages of my Ph.D. A special thanks for letting me work hand-in-hand with you on the NMR project and all the great trips to KFKI.

**Dr. Péter Szirmai** – it was a great run with our EPR study. Thanks for all the help and support you have provided during the four years.

**Anastasiia Glushkova** – thank you very much for all the artwork and amazing SEMs you made for our research.

**Dr. Márton Kollár** – great thanks for taking over Endre's craft and providing us with the much needed precursor solutions as well as XRD measurements.

**Lidia Rossi** – thank you very much for all the support. It was very nice to discuss various science and not-so-scientific topics. Not to forget the great job you did with EDX for our joint projects.

**Dr. Gaétan Giriat** – it was interesting, albeit hard to try and learn your craft of high pressures. I enjoyed working with you and your thoroughness. Also it was a lot of fun to be office mates for the whole duration of my Ph.D. and throughout all the offices we changed.

**Pavao Andričević** – thanks for your help with the measurements and nice discussions.

**Dr. Bálint Náfrádi** – thank you for helping me to start learning the ESR techniques and your

## Acknowledgements

---

overall support.

**Dr. Andrea Pisoni** – great thanks for being my first mentor in the transport lab. I enjoyed the short time we have been working together.

**Dr. Xavier Mettan** – thank you for teaching me about all the different things in the transport lab. I appreciated your tidiness and systematic approach. Also a big thanks for our discussions – it helped me a lot.

**Edoardo Martino** – thank you for being always interested in my work even though it was very different from yours. I enjoyed being excited to tell you about the new cool thing we have done.

**András Bojtor** – thanks for continuing the project. Hope you will get it out soon.

**Prof. Karoly Holczer** – I am grateful that I could meet with you and discuss the various topics of my research as well as more political and everyday life-related topics.

**LPMC** – lastly, a big thanks to all the other LPMC group members who have been around and helped in various ways. It was a great pleasure to work with you.

*Lausanne, 25 September 2019*

K. M.

# Contents

<b>Abstract</b>	<b>i</b>
<b>Thesis overview</b>	<b>v</b>
<b>Acknowledgements</b>	<b>ix</b>
<b>List of figures</b>	<b>xv</b>
<b>List of tables</b>	<b>xix</b>
<b>List of abbreviations</b>	<b>xxi</b>
<b>1 Introduction</b>	<b>1</b>
1.1 Renewable energy sources . . . . .	1
1.2 Organic-inorganic perovskites . . . . .	5
1.3 General concepts of crystallization . . . . .	8
1.4 Fabrication methods of metal-halide perovskites . . . . .	9
1.4.1 One-step methods: nucleation and growth . . . . .	10
1.4.2 Two-step methods: nucleation and growth . . . . .	10
1.5 Point defects in semiconducting materials . . . . .	11
1.6 Charge transfer materials . . . . .	12
1.7 Challenges of implementing perovskite materials . . . . .	14
<b>2 Methodology and experimental techniques</b>	<b>17</b>
2.1 Organic-inorganic perovskite material and sample preparation . . . . .	17
2.1.1 Single-step solution-casting of MAPbI <sub>3</sub> /MAPbBr <sub>3</sub> on cylinder-shaped substrates: preparation of MAPbI <sub>3</sub> /MAPbBr <sub>3</sub> precursors in DMF solution	17
2.1.2 Single-step solution-casting of MAPbI/Br <sub>3</sub> on cylinder-shaped substrates: thin-film deposition . . . . .	18
2.1.3 Preparation of single crystals of MAPbI <sub>3</sub> . . . . .	18
2.2 MAPbI <sub>3</sub> /blue-TiO <sub>2</sub> NWs nanohybrid sample preparation . . . . .	19
2.2.1 Preparation of MAPbI <sub>3</sub> /TiO <sub>2</sub> nanohybrid material . . . . .	19
2.2.2 MAPbI <sub>3</sub> /blue-TiO <sub>2</sub> NWs nanohybrid sample preparation for SEM and EDX	20
2.2.3 Synthesis of reduced TiO <sub>2</sub> single crystals . . . . .	20
2.3 Metal-halide perovskite material characterization techniques . . . . .	21
	xi

## Contents

---

2.3.1	Scanning electron microscopy imaging . . . . .	21
2.3.2	X-ray diffraction . . . . .	22
2.3.3	Atomic force microscopy . . . . .	24
2.3.4	Photoluminescence . . . . .	25
2.3.5	Optical microscopy imaging and steady-state photoluminescence measurements . . . . .	28
2.3.6	Measurements of the photocurrent for the deposits of MAPbI <sub>3</sub> and MAPbBr <sub>3</sub> intermittently exposed to the flow of either O <sub>2</sub> or N <sub>2</sub> . . . . .	31
2.4	Modified version of the experimental setup for performing PL measurements under photo-bleaching of MAPbI <sub>3</sub> with selective wavelengths . . . . .	33
2.5	Gas flow . . . . .	34
2.5.1	Characterization of the type of flow of gaseous media in custom-made gas-flow chambers . . . . .	34
2.5.2	Control of gas flow . . . . .	35
2.6	Electron spin resonance . . . . .	36
2.6.1	Underlying principles of ESR . . . . .	36
2.6.2	Instrumentation . . . . .	38
2.7	3D printing . . . . .	39
2.8	Experiment control software . . . . .	40
<b>3</b>	<b>Morphology and photoluminescence of thin film polycrystalline deposits of MAPbI<sub>3</sub> and MAPbBr<sub>3</sub> on non-planar, strongly curved substrates</b>	<b>43</b>
3.1	Introduction . . . . .	43
3.2	Results and discussion . . . . .	45
3.2.1	Morphology of MAPbI <sub>3</sub> deposits . . . . .	45
3.2.2	Morphology of MAPbBr <sub>3</sub> deposits . . . . .	53
3.2.3	Mechanisms behind the morphological changes in crystallinity of MHPs . . . . .	58
3.3	Conclusion . . . . .	63
<b>4</b>	<b>Impact of gaseous media on photoluminescence and photocurrent of polycrystalline MAPbI<sub>3</sub> and MAPbBr<sub>3</sub>.</b>	<b>65</b>
4.1	Introduction . . . . .	66
4.2	Results and discussion . . . . .	67
4.2.1	Influence of the gas flow on photoluminescence of polycrystalline deposits of MAPbI <sub>3</sub> . . . . .	67
4.2.2	Photoluminescence response of polycrystalline deposits of MAPbI <sub>3</sub> and MAPbBr <sub>3</sub> under recurrent exposures to the flow of either O <sub>2</sub> or N <sub>2</sub> . . . . .	71
4.2.3	Correlations between the photoluminescence and the photocurrent for polycrystalline deposits of MAPbI <sub>3</sub> and MAPbBr <sub>3</sub> during intermittent exposures to either O <sub>2</sub> or N <sub>2</sub> . . . . .	76
4.2.4	Stability of photoluminescence of MAPbI <sub>3</sub> and MAPbBr <sub>3</sub> under under exposure to a constant gas pressure: towards gas sensing . . . . .	79
4.3	Conclusion . . . . .	81

<b>5 Wavelength-dependent selective photo-bleaching in MAPbI<sub>3</sub> – impact of the variable oxygen/nitrogen atmosphere</b>	<b>83</b>
5.1 Introduction . . . . .	83
5.2 Results and discussion . . . . .	85
5.2.1 Co-excitation experiments on the polycrystalline deposits of MAPbI <sub>3</sub> under controlled atmosphere . . . . .	85
5.2.2 Co-excitation experiments on single crystals of MAPbI <sub>3</sub> under controlled atmosphere . . . . .	88
5.3 Conclusion . . . . .	89
<b>6 Light-induced charge transfer at the MAPbI<sub>3</sub>/TiO<sub>2</sub> interface – a low-temperature Photo-ESR assay</b>	<b>91</b>
6.1 Introduction . . . . .	91
6.2 Results and discussion . . . . .	92
6.2.1 Morphological and elemental characterization of the MAPbI <sub>3</sub> /blue-TiO <sub>2</sub> NWs nanohybrid material . . . . .	93
6.2.2 Spin state configurations of Ti defect centers in blue-TiO <sub>2</sub> NWs . . . . .	95
6.2.3 Photo-ESR study of the commercial nanocrystalline TiO <sub>2</sub> anatase – a control experiment . . . . .	96
6.2.4 Low-temperature photo-ESR measurements of a strongly reduced (self-doped) crystalline TiO <sub>2</sub> anatase . . . . .	98
6.2.5 ESR characterization of blue-TiO <sub>2</sub> NWs . . . . .	100
6.2.6 Photo-ESR study of the MAPbI <sub>3</sub> /blue-TiO <sub>2</sub> NWs nanohybrid interface . .	100
6.3 Conclusion . . . . .	104
<b>7 Conclusion and outlook</b>	<b>105</b>
7.1 Conclusion . . . . .	105
7.2 Outlook . . . . .	108
<b>A Technical drawings of parts used in the experiments</b>	<b>111</b>
A.1 Cylindrical geometry gas-flow chamber setup . . . . .	111
A.2 Flat-cell geometry gas-flow chamber setup . . . . .	114
<b>B Experiment control code</b>	<b>119</b>
B.1 Data management class . . . . .	119
B.2 Photocurrent measurement script . . . . .	120
B.3 Photoluminescence measurement script . . . . .	122
<b>Bibliography</b>	<b>142</b>
<b>Curriculum Vitae</b>	<b>143</b>



# List of Figures

1.1	Total renewable energy consumption by energy source . . . . .	3
1.2	NREL Research Solar Cell Efficiency chart . . . . .	5
1.3	Crystalline structure of perovskites . . . . .	6
1.4	Band structures of different materials . . . . .	7
1.5	Types of intrinsic point defects . . . . .	12
1.6	Typical material stack of a perovskite-based device . . . . .	13
2.1	Scheme of sample annealing setup . . . . .	19
2.2	Schematic representation of a scanning electron microscope (SEM) . . . . .	22
2.3	Schematic representation of the XRD principle (Bragg's law) . . . . .	23
2.4	Schematic representation of an atomic force microscope (AFM) . . . . .	25
2.5	Energy transitions and their relation to the absorption and emission spectra of semiconducting materials . . . . .	27
2.6	Scheme of the photo-physical characterization setup . . . . .	29
2.7	Spectral compositions and powers of the two main excitation lights . . . . .	30
2.8	Setup for PL and PC measurements with a sample mounted in the miniature gas-flow chamber . . . . .	31
2.9	Setup for PL measurements with a sample mounted in the flat miniature gas-flow chamber . . . . .	32
2.10	2- and 4-point resistance measurement methods . . . . .	33
2.11	Scheme of the photo-physical characterization setup for co-excitation experiments	34
2.12	Setup for photo-ESR measurements and an image of the sample coated onto the sample holder . . . . .	38
2.13	Representations and images of the 3D-printed parts for gas-flow chambers . . . . .	40
3.1	Optical microscopy images of deposits of MAPbI <sub>3</sub> on planar substrates . . . . .	45
3.2	Comparison of the optical microscopy images of MAPbI <sub>3</sub> deposits on cylinder- shaped quartz substrates having diameters of 330 $\mu\text{m}$ and 1800 $\mu\text{m}$ . . . . .	46
3.3	Typical MAPbI <sub>3</sub> photoluminescence spectrum . . . . .	47
3.4	Comparison of optical images of deposits of MAPbI <sub>3</sub> on curved and flat substrates	48
3.5	Comparison of morphology of MAPbI <sub>3</sub> deposits on cylinder-shaped quartz rods with diameters of 700 $\mu\text{m}$ and 400 $\mu\text{m}$ . . . . .	49
3.6	SEM images of microcrystalline MAPbI <sub>3</sub> deposits on curved substrates . . . . .	50

## List of Figures

3.7	The histograms of distributions of the crystallite widths of MAPbI <sub>3</sub> microwires	51
3.8	The histograms of distributions of the crystallite lengths of MAPbI <sub>3</sub> microwires	52
3.9	Optical microscopy images of deposits of MAPbBr <sub>3</sub> on planar substrates . . . .	53
3.10	Typical MAPbBr <sub>3</sub> photoluminescence spectrum . . . . .	54
3.11	Comparison of the optical microscopy images of MAPbBr <sub>3</sub> deposits on cylinder-shaped quartz substrates having diameters of 330 $\mu$ m and 1100 $\mu$ m . . . . .	54
3.12	Comparison of optical images of deposits of MAPbBr <sub>3</sub> on curved and flat substrates	55
3.13	SEM images of microcrystalline MAPbBr <sub>3</sub> deposits on curved substrates . . . .	56
3.14	The histograms of distributions of the crystallite lengths of MAPbBr <sub>3</sub> microcubes	57
3.15	SEM images of quartz substrates . . . . .	58
3.16	AFM images of quartz substrates and their roughness profiles . . . . .	59
3.17	Crystallization frame sequence for non-preheated substrates . . . . .	60
3.18	Crystallization frame sequence for preheated substrates . . . . .	61
3.19	Characteristic sizes of MAPbI <sub>3</sub> microwires and MAPbBr <sub>3</sub> microcubes as a function of the substrate curvature . . . . .	63
4.1	Initial observation of photoluminescence evolution of MAPbI <sub>3</sub> microwire deposits exposed to either O <sub>2</sub> or N <sub>2</sub> . . . . .	68
4.2	Photoluminescence kinetics of MAPbI <sub>3</sub> microwire deposits under intermittent exposures to either O <sub>2</sub> or N <sub>2</sub> . . . . .	69
4.3	Optical and fluorescence microscopy images of the deposits of MAPbI <sub>3</sub> and MAPbBr <sub>3</sub> in a <i>side-by-side</i> configuration . . . . .	72
4.4	PL responses of the polycrystalline deposits of MAPbI <sub>3</sub> and MAPbBr <sub>3</sub> during intermittent exposures to either O <sub>2</sub> or N <sub>2</sub> . . . . .	73
4.5	Overlapped plots of the increasing/decreasing portions of the PL responses of MAPbBr <sub>3</sub> under exposure to O <sub>2</sub> and N <sub>2</sub> . . . . .	74
4.6	MAPbBr <sub>3</sub> photo-brightening under exposure to air . . . . .	75
4.7	XRD patterns of deposits of MAPbI <sub>3</sub> and MAPbBr <sub>3</sub> before and after exposures to either O <sub>2</sub> or N <sub>2</sub> . . . . .	76
4.8	Correlations between the PL and the PC collected for MAPbI <sub>3</sub> and MAPbBr <sub>3</sub> during intermittent exposures to either O <sub>2</sub> or N <sub>2</sub> . . . . .	77
4.9	Schematic representation of the energy levels of shallow and deep quenching centers governing the processes of radiative and non-radiative recombinations in MAPbI <sub>3</sub> and MAPbBr <sub>3</sub> under the combined exposure to above the band gap energy photons and O <sub>2</sub> . . . . .	79
4.10	Long-term stability of the PL responses of polycrystalline deposits of MHPs . .	80
5.1	PL kinetics under controlled atmospheres of O <sub>2</sub> or N <sub>2</sub> . . . . .	86
5.2	PL kinetics under controlled atmospheres of O <sub>2</sub> or N <sub>2</sub> with co-excitation . . . .	87
5.3	Optical and fluorescence microscopy images of the single crystal of MAPbI <sub>3</sub> . .	88
5.4	PL kinetics of the MAPbI <sub>3</sub> single crystal under co-excitation and in controlled atmospheres of O <sub>2</sub> or N <sub>2</sub> with co-excitation . . . . .	88



5.5	Schematic representation of the energy levels under single wavelength and co-excitation in the presence of $O_2$ . . . . .	89
6.1	Morphology of blue- $TiO_2$ NWs and nanohybrid deposits of $MAPbI_3$ /blue- $TiO_2$ NWs	93
6.2	SEM/EDX elemental analysis maps of $MAPbI_3$ /blue- $TiO_2$ NWs nanohybrid deposit	94
6.3	Photo-ESR spectra of commercial AMT600 anatase under illumination with red light (650 nm) . . . . .	96
6.4	Photo-ESR spectra of commercial AMT600 anatase under illumination with UVA (365 nm) . . . . .	97
6.5	Comparison of the ESR spectra obtained for strongly reduced single crystal $TiO_2$ anatase (blue-SC- $TiO_2$ ), microcrystalline composite ( $MAPbI_3$ /MC-blue- $TiO_2$ ) under exposure to visible light and UVA . . . . .	99
6.6	The temperature dependence plots of inverse susceptibility and linewidth for blue- $TiO_2$ NWs . . . . .	100
6.7	Comparison of ESR spectra collected for the interface between $MAPbI_3$ and blue- $TiO_2$ NWs under various illumination conditions . . . . .	101
6.8	Energy band alignment diagram at the $MAPbI_3$ /blue- $TiO_2$ NWs interface . . . .	103
A.1	Representations and images of the 3D-printed parts for cylindrical geometry gas-flow chambers . . . . .	111
A.2	Drawing of the microscope slide for gas-flow chambers of cylindrical geometry	112
A.3	for gas-flow chambers of cylindrical geometry . . . . .	113
A.4	Representations and images of the 3D-printed parts for flat-cell geometry gas-flow chambers . . . . .	114
A.5	Drawing of the microscope slide for gas-flow chambers of flat-cell geometry . .	115
A.6	Drawing of the holder clip for gas-flow chambers of flat-cell geometry . . . . .	116
A.7	Drawing of the connector for gas-flow chambers of flat-cell geometry . . . . .	117
A.8	Drawing of the blank connector for gas-flow chambers of flat-cell geometry . .	118



## List of Tables

2.1	Reynolds numbers for different gas-flow chambers . . . . .	35
4.1	Summary of correlations between PL and PC acquired for polycrystalline deposits of $\text{MAPbI}_3$ and $\text{MAPbBr}_3$ during intermittent exposures to either $\text{O}_2$ or $\text{N}_2$ . . . . .	77



# List of abbreviations

## Abbreviations

AFM	Atomic Force Microscopy
CAD	Computer Aided Design
CB	Conduction Band
CCD	Charge-coupled Device
CMi	Center of MicroNano Technology
CTL	Charge Transfer Layer
CTM	Charge Transfer Material
DIA	Diameter
DMF	Dimethylformamide
DSC	Dye-sensitized solar cell
EDX	Energy-dispersive X-Ray Spectroscopy
EPFL	École Polytechnique Fédérale de Lausanne
ESR	Electron Spin Resonance
ETL	Electron Transfer Layer
ETM	Electron Transfer Material
FWHM	Full Width Half Maximum
HTL	Hole Transfer Layer
HTM	Hole Transfer Material
ID	Inner Diameter
ITO	Indium tin oxide
LED	Light Emitting Diode
MA	Methylammonium
MAPbBr <sub>3</sub>	Methylammonium lead bromide (CH <sub>3</sub> NH <sub>3</sub> PbBr <sub>3</sub> )
MAPbI <sub>3</sub>	Methylammonium lead iodide (CH <sub>3</sub> NH <sub>3</sub> PbI <sub>3</sub> )
MPH	Metal-Halide Perovskite
NMR	Nuclear Magnetic Resonance
NREL	National Renewable Energy Laboratory
NW	Nanowire
OD	Outer Diameter
PC	Photocurrent
PCBM	[6,6]-phenyl-C61-butyric acid methyl ester
PCE	Power Conversion Efficiency

## List of abbreviations

---

PEO	Polyethylene oxide
PL	Photoluminescence
PSC	Perovskite solar cell
PV	Photovoltaic
SEM	Scanning Electron Microscopy
Spiro-OMeTAD	2,2',7,7'-Tetrakis-(N,N-di-4-methoxyphenylamino)-9,9'-spirobifluorene
TA	Transient absorption
TRMC	Time-resolved microwave photoconductivity
TRPL	Transient photoluminescence
TRTS	Transient terahertz absorption
UV	Ultraviolet
VB	Valence Band
XRD	X-Ray Diffraction

## Mathematical symbols

$B_0$	External magnetic field
$B_x$	linearly polarized alternating magnetic field along the $x$ -axis
$E_f$	Fermi energy
$g_J$	Lande factor
$g_L$	orbital Lande factor
$g_S$	electron Lande factor
$\hat{H}_{ext}$	Zeeman hamiltonian in external magnetic field
$J_z$	quantized projection of the total angular momentum on the $z$ -axis
$k_B$	Boltzmann constant
$\lambda_{exc}$	Excitation wavelength
$\lambda_{co-exc}$	Co-excitation wavelength
$M_0$	equilibrium magnetization through the $z$ -axis
$M_{x,y,z}$	projection of the magnetization on the $x$ , $y$ and $z$ axis, respectively
$\mu_B$	Bohr magneton
$\omega_L$	Larmor frequency
$P_0$	escaping tendency from a surface with radius $r_0$
$r_0$	radius corresponding to a curvature close to a flat surface
$R_l$	Lead resistance
$R_n$	Reynolds number
$T_1$	spin lattice or longitudinal relaxation time
$T_2$	spin-spin or transversal relaxation time

# 1 Introduction

## 1.1 Renewable energy sources

For over many centuries humanity has been using fossil fuels to provide itself with energy. The precursors of these fuels formed from the fossilized sediments of the remains of plants and animals, which made them carbon-rich and thus suitable for releasing energy upon burning. Even today, although being country-specific, the largest part of the global energy generation is still fossil fuel-based.

The use of fossil fuels as the main source of energy causes several negative environmental impacts, ranging from the obvious air and water pollution, as well as global warming, to more indirect, such as pollution by plastics and the inability to efficiently and cheaply degrade them. This, in turn, causes harm to both flora and fauna of the eco-systems [1]. Such consequences forced people to turn their gaze towards more environmentally friendly forms of energy, including renewable energy sources. Although numerous scientific advances have already been made in an attempt to bridle renewable energy resources, such as sunlight, wind or tides, yet there were and still are many challenges to overcome.

In this context, already in 1975, Pyotr Leonidovich Kapitsa, a renowned Soviet physicist and Nobel Prize laureate, made an address to the Soviet Academy of Sciences highlighting the problems of the eventual energy crisis. His thoughts were based on the fundamental laws of physics, such as energy conservation and the second law of thermodynamics, as well as calculations, which included the energy flux densities corresponding to the actual energy output ratios for a given surface area [2].

In particular, Kapitsa argued that the production of energy for the human consumption simply boils down to the energy conversion from one type into another. A simple example of that is coal, whose energy is stored in chemical bonds and is released upon burning in the form of heat, which can further be transformed into kinetic energy to propel a steam turbine and produce electrical energy as the final output.

One way to get clean energy is obviously to use the incoming sunlight. According to the above mentioned reasoning and calculations, Kapitsa arrived to a conclusion that a  $1 \text{ m}^2$  solar panel would produce a maximum of 100 W of energy. Based on this estimation, he puts into doubt the feasibility of scaling up the solar power for generation of large quantities of energy.

Since this PhD thesis deals with solar power materials, we will definitely not delve further into details on the whole criticism of other renewable energy sources made by Kapitsa. Yet, it is worth mentioning that there are only two energy sources that stand such a harsh trial by numbers, *i.e.* the nuclear fission and thermonuclear fusion.

As of today, the most efficient and the cleanest way to generate electricity is nuclear fission, *i.e.* nuclear power plants. Yet, they are still considered to be potentially extremely dangerous and require the highest grade safety procedures as well as a place to store the depleted nuclear fuel. Both problems have been foreseen by Kapitsa in the above-mentioned address of 1975. While he argued that, with time, the humanity will find a solution to those problems, especially when it will face the energy crisis, he also mentioned a solution to the problem of dangers related to operation of nuclear power plants. For example, he suggested localizing them on most remote uninhabited islands – to minimize the damage in case of a meltdown.

Currently, nuclear fusion, which can be performed in thermonuclear reactors, is considered to be the most efficient known energy source. So far, however, the research-grade thermonuclear reactors can barely generate a bit more energy than is used to run them. In case of ITER (“The Way” in Latin) [3] it is envisioned that upon start of normal operation in 2025 it should produce tenfold of the energy ( $\sim 500 \text{ MW}$ ) required to sustain the plasma burn. Nothing to speak about actually generating electricity and having an engineering power output – as it is envisioned for the next iteration reactor – DEMO [4].

Over the last 50 years, we have witnessed a significant progress in the field of sustainable energy sources. In addition to the early concepts from the 1940’s and 1960’s of using nuclear and thermonuclear power and, later on, more environmentally-friendly wind and hydro-generated power sources, a great improvement has been achieved in technology and efficiency of solar cells, which directly generate electricity from the sunlight.

Hydro-generated electricity is relatively widespread but requires a suitable landscape. For example, both Switzerland and Norway utilize this type of renewable energy generation, thus providing “green energy batteries” for Europe [5]. Power generated by wind is also quite widespread. However, it has a big disadvantage of being very unstable in generation, *i.e.* it requires to store energy during windless periods, as well as to meet periods of increased demand of energy. Clearly, paired with hydroplants, the energy provided by wind can be efficiently stored and used via the hydroplants’ capabilities – whenever the excess of that energy is needed.

The last big player to mention is the solar energy. In the recent years, the potential of solar energy gained increasing attention. This renewable energy sector has also seen a drastic



technological progress, as well as numerous innovations. Although solar energy bears similar limitations as wind energy, like the necessity of using it in pair with efficient energy storage, it can be utilized in the majority of locations around the globe.

In 2016, approximately 16894 TWh of renewable energy has been consumed. Out of those, 35% was accounted for such renewable energy sources as hydro- and solar-power, wind and geothermal. The rest of renewable energy was produced by traditional biofuels, which encompass fuelwood, forestry products, animal and agricultural wastes. In fact, solar energy accounted for only 2% of the whole renewable energy consumed, thus coming in last, after all the other renewable energy sources. These numbers, put into perspective over the last half century (from 1965 to 2016), can be seen in Figure 1.1, which depicts the total consumed renewable energy produced by various kinds or renewable energy sources [6].

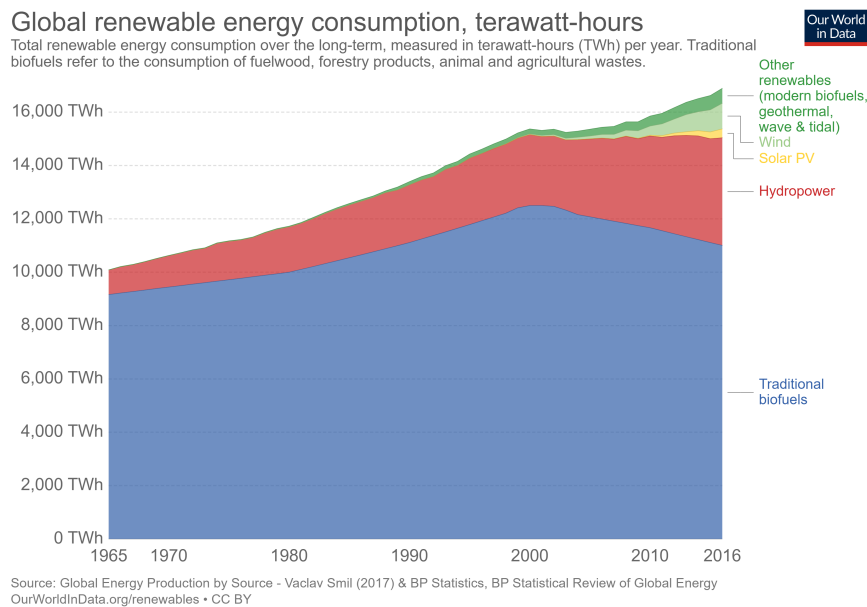


Figure 1.1 – Total renewable energy consumption over the long-term, measured in terawatt-hours (TWh) per year. Blue represents the traditional biofuels such as fuelwood, forestry products, animal and agricultural wastes. Red depicts hydropower consumption, yellow – solar power, light-green stands for wind and green for other renewable energy sources such as modern biofuels, geothermal, wave and tidal power generation. Figure adapted from [6].

As this thesis deals with novel materials used in the field of solar energy generation, in the following, the main focus will be on this type of renewable energy.

Nowadays, the leaders in solar energy production are China (78.07 GWh), Germany (42.28 GWh) and the USA (40.36 GWh) [6]. China is also the biggest producer of the solar cells of all types.

In the historical perspective, a first *proof-of-principle* solar cell device was based on selenium and was created way back in 1876, after the discovery of generation of electrical current in selenium upon illumination [7]. These selenium cells were far from being efficient, but

## Chapter 1. Introduction

---

they proved a very important point – light can be transformed into electrical energy without intermediate media such as, for example, heat.

Commercially available solar cells would appear in the 1950's after a prototype of a silicon p-n junction solar cell has been created at Bell Telephone Laboratories [8]. Even though such cells were available, their prices were quite high (at the level of ~300 \$ per 1 Watt), thus not easily accessible to the general public – apart from being integrated into electronic toys and portable radios.

The next big application where solar cells found their use was the space program [9, 10]. Already in the late 1950's and early 1960's, being relatively easily available to install and capable of harvesting the energy from the sun, the solar panels became the primary power source of satellites launched into the Earth orbit both the USA and the Soviet Union.

In 1970's, the research lead by Exxon paved the way for much cheaper solar cells, which reduced their prices to the level of 20 \$ per 1 Watt. At that time, Exxon used the solar panels to power the warning lights on top of their oil rigs. Fast forward to 1990's and solar cells are used at railroad crossings, traffic lights, to power homes in remote locations, to improve Australia's communication capabilities and even in deserts – to provide water, where line electricity is not an option.

In 2016, 93% of all solar cells were based on conventional semiconductors, such as silicon, copper indium gallium selenide (CIGS) or cadmium telluride (CdTe), with record efficiencies reaching 25.8%. Among them, the most efficient and by far the most common semiconductor material used is silicon, which can be found in approximately 90% of solar cells available on the market [11].

Yet, there are at least two reasons why these conventional silicon-based solar panels are still far from being the optimal solution. First of all, the process of making silicon wafers, which are needed for manufacturing of the most popular silicon-based solar cells, is costly and energy consuming. Moreover, the final stages of fabrication of planar silicon solar cells (SSCs), either crystalline or polycrystalline, are quite numerous and technically complicated. In addition, to ensure proper light absorption, silicon imposes a severe technological constraint concerning the cell thickness. Specifically, it means that the resulting SSCs are relatively thick and heavy, as well as rigid (non-flexible) and fragile, which makes them difficult to handle.

Account taken of the above, a search for alternative ways of harvesting solar energy has begun. Figure 1.2 shows the evolution of records of energy conversion efficiencies for various types of solar cells over the years up to 2019.

From this we can observe that until 1989 the crystalline SSCs were the undisputed leaders in terms of efficiencies; yet, 1990 saw a steep rise in performance of multi-junction cells, which eventually overtook the crystalline SSCs. Thin film cells never outperformed SSCs, but achieved efficiencies comparable to them. On the other hand, the emerging novel photovoltaic

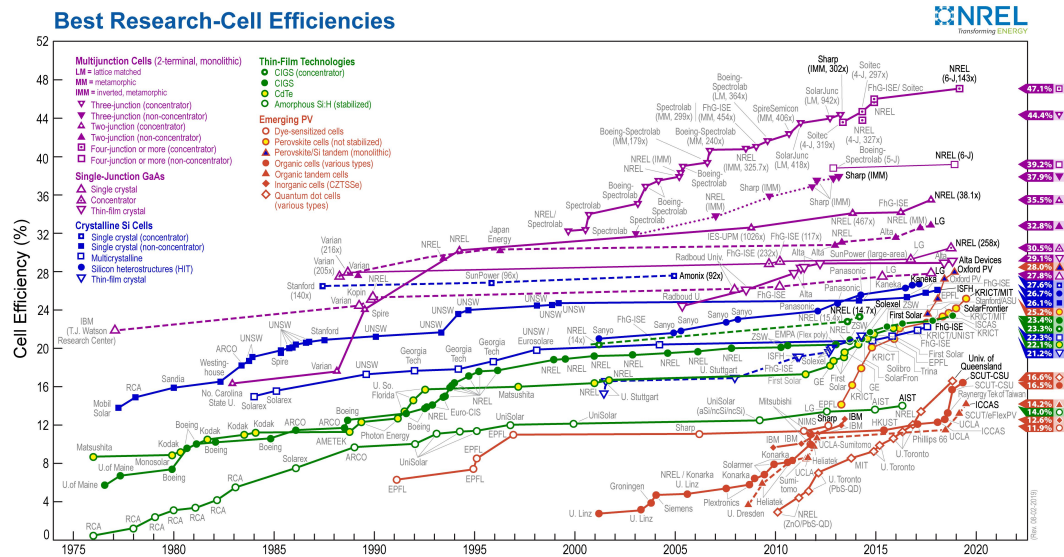


Figure 1.2 – Efficiency chart of the best research-cell energy conversion efficiencies by National Renewable Energy Laboratory (NREL) from 1976 till present, sorted into five groups: in purple – multi-junction cells; in blue – crystalline silicon cells; in green – thin-film-based cells and in red – emerging photovoltaic technology-based cells. Figure adapted from [12].

cells were boosted in 1991 by dye synthesized solar cells (DSSCs), developed by the group of Michael Grätzel at EPFL. They promised relatively high efficiency at a low cost and ease of production. Ultimately that was deemed not viable and new types of cells emerged along the way.

Among many contenders, the ones important for this thesis will be the perovskite solar cells (PSCs). These cells took off the initial 3.8% [13] and 9.7% [14] efficiencies of practically raw materials and almost by storm developed to cells with efficiencies higher than 21% in just 6 years. That was still not enough to beat the silicon-based cells. However, the most recent advancement are the tandem cells that combine the best of the two together, *i.e.* silicon and perovskites to reach up to ~27%, beating the *best-in-class* standalone silicon solar cells and coming close to the lower boundary of the multi-junction cells [12].

In the next sections the reader will be introduced to the material class of perovskites and more specifically, the organic-inorganic perovskites, which are archetypal materials for the entire perovskite-based photovoltaic technology.

## 1.2 Organic-inorganic perovskites

Perovskites are a class of materials first discovered in the Ural Mountains by the German mineralogist Gustav Rose in 1839 and named “perovskites” in honor of the Russian mineralogist Lev Perovski [15]. The materials have a general chemical formula of  $ABX_3$ , where A and B are

the positive cations and X is the anion.

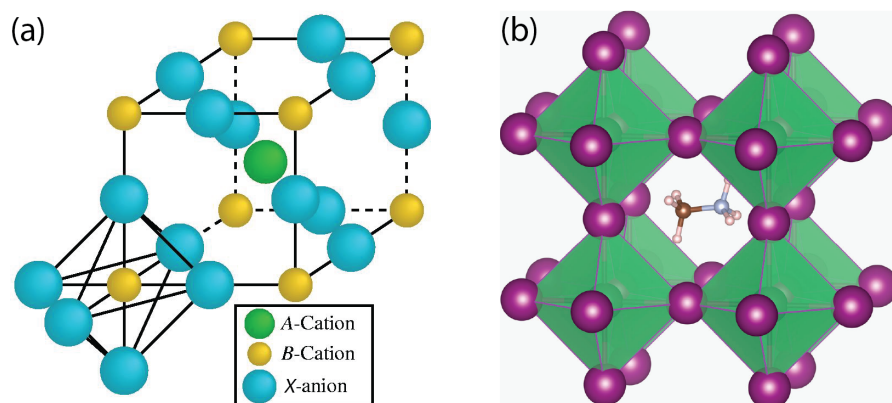


Figure 1.3 – Crystalline structures of perovskite materials. (a) General material structure with a chemical formula  $ABX_3$ . In this case shown here, the two cations, A and B, are depicted by green and yellow spheres respectively, while the anions are depicted by cyan spheres. (b) Structure of a organic-inorganic perovskite with a chemical formula  $CH_3NH_3PbX_3$ , where  $X = I, Br, Cl$ . In the case shown here, there is a methylammonium cation, depicted in silver-brown, surrounded by the octahedra (green faces) of  $PbX_6$ . The anions X are depicted by purple spheres. Images adapted from [16, 17], respectively.

Schematic representation of the crystalline structure of a general  $ABX_3$  perovskite can be seen in Figure 1.3(a), where green and yellow spheres represent the A and B cations, respectively, while the C anions are represented by cyan spheres.

Among many perovskite materials one important class is the materials used in the solar energy generation, *i.e.* organic-inorganic perovskites, otherwise known as metal-halide perovskites or MHPs. An archetypal example of such a MHP would be the methylammonium lead iodide. One has to note that extensive research has been devoted to studying the MHPs with iodine substituted by another halide and one of the most prominent examples of such substitution would be methylammonium lead bromide.

This thesis is focused on these two materials as they are the prime representatives of the MHPs compounds, as well as they possess the highest efficiencies of light-to-electricity conversion. Therefore, in the following, a more detailed characterization of these two MHPs will be presented.

Methylammonium lead iodide has two well known structural phase transitions, *i.e.* at 162 K and 327 K [18]. The first one, with increasing temperature, corresponds to transformation of the crystal unit cell from orthorhombic to tetragonal structure, while the second one transforms the crystal unit cell from tetragonal to cubic structure. Similarly, methylammonium lead bromide also has two structural transitions from orthogonal to tetragonal and then to cubic cell structures, with respective temperatures of 148 K and 235 K [19].

Due to the versatility of the embedded organic cations, the class of MHP materials is quite

vast. As mentioned above, the scope of this thesis encompasses the two archetypal MHPs, namely methylammonium lead iodide and bromide ( $\text{CH}_3\text{NH}_3\text{PbI}_3/\text{Br}_3$ ). To relate to the general chemical formula, in this case A = methylammonium (MA), B = lead (Pb) and X = I or Br, which in total can be abbreviated as  $\text{MAPbX}_3$  and  $\text{MAPbBr}_3$ , respectively. More specific crystalline structure of the  $\text{MAPbX}_3$  perovskite can be seen in Figure 1.3(b). In the case shown in this Figure, the center methylammonium cation ( $\text{CH}_3\text{NH}_3^+$ ) is surrounded by eight  $\text{PbX}_6$  octahedra.

In general, materials can be also classified from the perspective of the electronic properties by dividing them into three main classes – metals, insulators and semiconductors. The differences between these three classes of materials come from the electronic band structure (or simply band structure), which imposes the allowed and forbidden electron energy levels in the bulk of the crystalline materials. As a consequence of the crystal's periodicity, these energy levels form continuums called bands separated by band gaps. The upper band is called conduction band (CB) and the lower one – valence band (VB). A schematic of such classification showing the filling and relative position of bands and band gaps is shown in Figure 1.4(a). Insulators have a very large band gap and the bands are either filled or empty. In case of metals, the band gap is small or non-existent in case of overlapping bands and the filling of the bands is partial. For semiconductors there are multiple partially filled bands accompanied by a relatively narrow band gap.

Occupation probability over the bands is described by the Fermi-Dirac distribution function [20]:

$$f(E_i) = \frac{1}{1 + e^{\frac{E_i - E_f}{k_B T}}}, \quad (1.1)$$

where  $E_i$  is the energy of the  $i$ -th state,  $E_f$  is the Fermi level and  $k_B$  is the Boltzman constant.

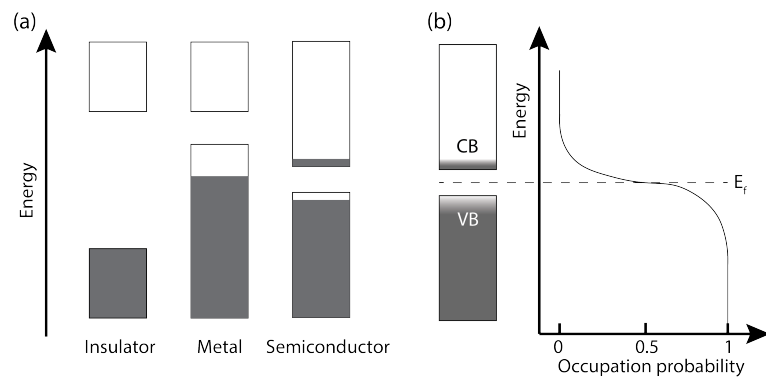


Figure 1.4 – Band filling of crystalline materials. (a) Energies of bands for insulators, metals and semiconductors. Grey color depicts the filling of the respective band for each type of material. (b) A scheme of band filling in semiconducting materials depicting the Fermi level,  $E_f$ , and the Fermi distribution of electrons leading to the probability of moving in between the valence and conduction bands.

From this perspective, MAPbX<sub>3</sub> materials fall into the category of semiconductors, the details of the band structure of which are illustrated in Figure 1.4(b). As evidenced by Equation 1.1, one can observe that due to the Fermi-Dirac nature of electron distribution, at temperature of 0 K for an intrinsic semiconductor (pure semiconductor, in which the Fermi level lies exactly in the middle of the band gap) such material will perform like an insulator with either filled or empty bands. Yet at room temperature, there is a sizable probability to find empty allowed states dubbed “holes” in the bottom of the conduction band that can be eventually filled by electrons hopping over the band gap, as the probability of that is non-zero. The physics of these charge carriers can be describe by applying the well-known principles from electrons and changing the sign of the charge.

There have been numerous reports on the values of the bandgaps of MAPbI<sub>3</sub> and MAPbBr<sub>3</sub>. The most commonly reported bandgaps are of 1.55 eV for the iodide [21] and of 2.32 eV for the bromide [22] perovskite, respectively.

### 1.3 General concepts of crystallization

The phenomenon of crystallization of MHPs has been studied extensively, yet given its complex nature it is still not fully understood. In general, there are three possibilities of formation of a new phase, *i.e.* from solution, from vapor or within a solid. Usually, the driving force of the crystallization is the difference of chemical potentials of the mother and the newly formed phases, called supersaturation [23].

According to the classical theory, the formation of a new phase begins with nucleation, which is defined as the formation of sufficiently large or supercritical particles from smaller ones named subcritical particles. This process of formation of the critical nuclei has an activated behavior, *i.e.* the growth of larger critical nuclei requires an input of energy to proceed [24, 25].

Two classes of nucleation can be distinguished – homogeneous and heterogeneous nucleation. In the homogeneous case, the formation of the minute particles of the new phase is spontaneous. On the other hand, in the heterogeneous case the formation of a new phase is occurring on top of foreign particles, which helps to lower the activation barrier energy of the nucleation.

Furthermore, nucleation can be classified based on its advancement as a function of time. Primary and secondary nucleation stages can be distinguished from this perspective. Primary nucleation occurs when there is spontaneous formation of supercritical particles in the homogeneous case or when the nucleation just begins on the foreign particles in heterogeneous case. Secondary nucleation, however only occurs when it is initiated by the crystallites of the new phase, already present in the solution [23].

From the perspective of rates of nucleation, one can find four distinctively different mechanisms. Namely, continuous nucleation, saturation by pre-existing nuclei, Avrami nucleation

and mixed nucleation [24]. Continuous nucleation occurs when the nucleation rate is constant at the fixed temperature and when initially, there were no nuclei present [24]. The saturation by the pre-existing nuclei mechanism is manifesting itself when there are some particles present in the solution, which can potentially become nuclei but due to the variation in their sizes, only those that are supercritical start growing. These supercritical particles are called pre-existing nuclei [24]. Avrami nucleation is akin of the continuous nucleation in the beginning, while resembling saturation by pre-existing nuclei closer to the end of the crystallization process. It can be characterized by the growth of supercritical particles from subcritical ones and keeping their total numbers constant [24]. The last mechanism is the mixed nucleation that can combine the processes mentioned above.

It has to be noted that one of the further possibilities for crystal growth after the nucleation phase might also involve Ostwald ripening. This is a thermodynamically guided process during which smaller crystallites or particles are absorbed by larger ones, based on the principle of energy minimization [26].

In this context, the crystallization of MHPs films generally follows a four-step transformation process (*i.e.*, diffusion  $\rightarrow$  reaction  $\rightarrow$  nucleation  $\rightarrow$  growth) [27]. In this process, the MHP nucleus is formed first and crystal growth begins at the MHP nucleus to form complete MHP crystals [28, 29]. Since a MHP nucleus basically provides a grain of the perovskite, a higher density of perovskite nuclei results in a larger number of grains, whereas a lower density of nuclei leads to a smaller number of grains, which are larger in size. Based on these facts, it is expected that controlling the nucleation density of the MHPs precursors should enable control over the morphological properties of the grains, such as crystallinity, size, and crystal facet orientation [30].

## 1.4 Fabrication methods of metal-halide perovskies

Various fabrication methods of MAPbI<sub>3</sub> and MAPbBr<sub>3</sub> thin films have been reported to date [31, 32]. In general, the most commonly used deposition techniques can be categorized into two categories: one-step precursor deposition methods [33] and two-step deposition methods [34]. It is customarily accepted that the two-step deposition provides better control of the composition, the thickness, and the morphology of the MAPbX<sub>3</sub>-based films, thus leading to higher photo-voltaic performances of the final devices [35]. On the other hand, one-step solution-casting protocols seem to be more suitable for manufacturing low-cost MAPbI<sub>3</sub>-based devices at large scale [36]. It has also been widely recognized that obtaining densely packed deposits of MAPbI<sub>3</sub> with small grain sizes in the range from hundreds of nanometers to micrometers can be beneficial for numerous prospective optoelectronic applications, including photo-optical gas sensors [37]. There are fewer reports on the preparation of MAPbBr<sub>3</sub> thin films using a two-step process. One such report demonstrates a way of obtaining dense layers of 5 – 10  $\mu\text{m}$  sized and perfectly oriented crystallites [38].

The two-step deposition route combining the solution process and vapor phase conversion

was used for growing polycrystalline MAPbI<sub>3</sub> microwires with length up to 80  $\mu\text{m}$  that revealed both an excellent light-guiding performance with very low optical loss and bandgap tunability [39]. The one-step solution-based synthesis of highly-photoactive MAPbI<sub>3</sub> nanowires with mean diameter of 50 to 400 nm and lengths up to 10  $\mu\text{m}$  has also been reported by Horvath *et al.* [40].

Although monolithic layers of organometallic perovskites are mostly used in photovoltaic applications, coatings having other morphological characteristics are also being intensively explored. In particular, high power conversion efficiency (PCE) of a coating formed by low-dimensional (1D) MAPbI<sub>3</sub> nano- and microstructures have recently been reported by Im *et al.* [41]. Specifically, thin layers consisting of nanowires having 100 nm in diameter and several  $\mu\text{m}$  in length were prepared by the two-step spin-coating procedure.

Another example might be a 400 nm thin film of MAPbBr<sub>3</sub> produced by spin-coating of HBr in a controlled manner over the perovskite precursor. Such technique has been used to create highly efficient green LEDs [42].

### 1.4.1 One-step methods: nucleation and growth

Classical theories and analyses of nucleation pertaining to solution-synthesis of nanoparticles can be invoked in the context of solution deposition of MHPs films.

Consider a precursor-solution film deposited onto a substrate, where removal of the solvent will cause supersaturation in the film. There are several methods, or a combination of methods, in which the solvent can be removed. The simplest and the most widely used method is isothermal heating to cause solvent evaporation [43, 44, 45, 46]. Another supersaturation method is the addition of an antisolvent which extracts the precursor solvent, and it can simultaneously reduce the solubility of the precursor solute [47, 48, 49, 50]. A more recent method is the degassing of a liquid precursor [51].

Assuming that the supersaturation of the precursor results in the appearance of MHPs species (commonly referred to as “monomers”, which can be atoms, ion, molecules, or formula units [52]), they can cluster together into single-crystal nuclei. These nuclei are likely to appear not only at the substrate/solution and colloidal particles/solution interfaces but also within the precursor solution.

### 1.4.2 Two-step methods: nucleation and growth

Typically, two-step methods entail deliberate reaction between two precursors on a substrate to result in the formation of solid state MHP thin films, where the precursors can be in solid, liquid, and vapor forms. The two-step methods are typically more involved compared to the one-step methods, but they were introduced to gain better control over the formation of MHPs by moderating the rapid reaction between the organic and the inorganic parts of the

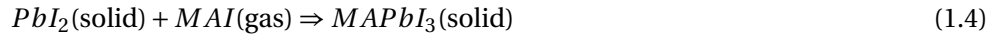
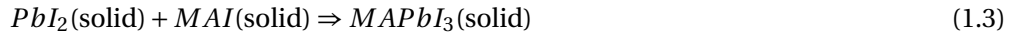
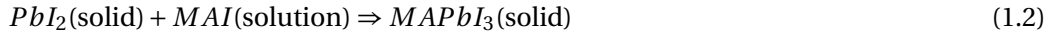


precursor [53, 54, 55].

The three representative two-step methods are:

1. solid-liquid by Burschka *et al.* [56],
2. solid-solid by Xiao *et al.* [57],
3. solid-vapor by Chen *et al.* [58],

Most of the other methods being some variation of these three. The simple reactions pertaining to these three methods, in the context of MAPbI<sub>3</sub> perovskite thin film deposition, respectively, are



In the first method, solid PbI<sub>2</sub> thin film is first deposited onto a substrate, which is then dipped into a liquid solution of MAI [56]. If the PbI<sub>2</sub> layer is dense, Reaction 1.2 is likely to start immediately at the top of the PbI<sub>2</sub> layer, resulting in the nucleation of MAPbI<sub>3</sub> there. However, the nature of this nucleation process is not clear. This is further compounded by the fact that this reaction can take a long time, and that the as-formed MAPbI<sub>3</sub> perovskite can dissolve back in the MAI solution [56, 58] resulting in rough films.

## 1.5 Point defects in semiconducting materials

Opposed to the ideal crystalline structure, in reality, crystals have defects. One way of classifying them would be their dimensionality: 0D or point defects, 1D – linear, 2D – interface defects and 3D or volume defects. Within the framework of this thesis, point defects, *i.e.* zero-dimensional crystal imperfections, seem to be the most important for the further discussion of the photo-physical properties of MHPs [59, 60].

Point defects can be intrinsic or extrinsic. Intrinsic defects are vacancies, interstitials and anti-site defects. Vacancies,  $V_A$ , are positions that are unoccupied but where atom  $A$  would normally reside. Interstitials,  $A_I$ , on the other hand are the positions where an atom  $A$  is sitting but would be absent in an ideal crystal. Anti-site defects,  $A_B$ , are positions where an atom  $A$  is residing instead of  $B$ . These types of defects are schematically illustrated in Figure 1.5. Extrinsic point defects are foreign atoms in the material and are called solutes in case they were added intentionally or impurities if the addition was unintentional.

As one would naturally expect, defects are charged entities. Yet that would contradict the charge-neutral nature of the whole crystalline solid. To avoid this, these defects appear in

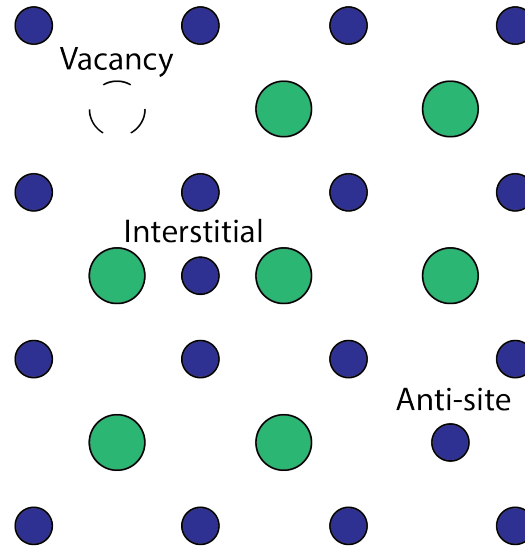


Figure 1.5 – Schematic representation of intrinsic point defects in a crystalline solid. Vacancy is depicted as a dashed circle in the top row; interstitial – as blue circle in the middle row and anti-site defect as a blue circle in the bottom row.

pairs, leading to their sum of charges being equal to zero. From this perspective, there are two types of defects, *i.e.* Frenkel defects and Schottky defects. The former are formed when an atom from the lattice is moved into an interstitial position. In the latter case, the defects form as pairs of positively and negatively charged atoms disappearing from two atomic positions at the same time.

Defects also affect the band structure of the solid. Each defect can be assigned with an energy level and placed in the energy level scheme of the material. Here we can distinguish between shallow and deep defects by the distance in energy from either valence or conduction bands. Shallow defects are found very close to either valence or conduction band edges, usually within  $3k_B T$ , where  $k_B$  is the Boltzmann constant and  $T$  is the absolute temperature. On the contrary, deep defects are found deep in the bandgap and far away from conduction or valence band edges. They are sometimes called “trap states” as they tend to prevent charge carriers from moving away and facilitate recombination.

## 1.6 Charge transfer materials

As it has been mentioned above in Section 1.1 on renewable materials, there has been a rapid emergence of the field of perovskite-based photovoltaics. For this reason the main application of the very efficient archetypal perovskite  $\text{MAPbI}_3$  has become a planar solar cell (designed on a flat substrate). Even though the efficiencies of transformation of sunlight into electricity were quite high from the start, reaching 3.8 % [13] and 9.7 % [14], some more sophisticated engineering was required to accommodate for effective transfer of the photo-

generated charges.

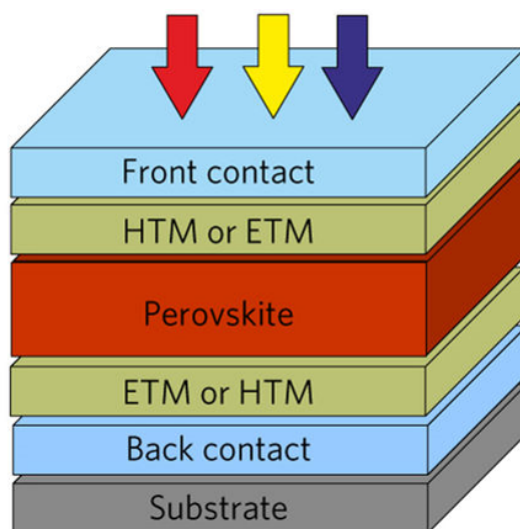


Figure 1.6 – Schematic representation of the material stack used in majority of perovskite-based devices. Light illumination is performed through the front contact and HTM/ETM towards the perovskite leading to generation of the photo-excited charge carriers, which in turn, are then transferred through the respective charge transfer material to the front/back contacts to generate electricity.

Schematic representation of the design of a conventional perovskite-based planar solar cell is shown in Figure 1.6. As can be seen, the solar cell consists of the stack of several thin layers of different functional materials [61, 62]. The incident light in this scheme is applied at the top of the stack and traverses two transparent layers of a front contact and a charge transfer material (CTM) before it reaches the perovskite, where the photo-generated charge carriers are produced. As can also be seen from the schematic representation in Figure 1.6, there are two types of CTM layers, *i.e.* electron and hole transport layers (hereinafter ETLs and HTLs).

The photo-generated charge carriers get selectively transferred to the back or front contact by the means of the respective ETLs and HTLs layers located above and beneath the perovskite. This process allows for generation of electricity.

Titanium dioxide ( $\text{TiO}_2$ ), due to its low cost, simple fabrication procedures, high charge mobilities and well-matched band structure with MHPs, has emerged as the most widely used material for designing planar ETL layers in MHPs-based photovoltaic devices [63]. The counterpart HTLs layers are commonly formed using organic conducting compounds, such as Spiro-OMeTAD [64] or PCBM [65].

As appears from the above,  $\text{TiO}_2$  has seen many implementations in the emerging MHPs-based photovoltaics. Therefore, there is a vital need to better understand the processes, which occur at the interface between the perovskite and  $\text{TiO}_2$ . One of the possible approaches, applied

in this thesis, is based on the technique of Electron Spin Resonance (ESR). Specifically, ESR allows for detection of unpaired electron spins, and thus it is capable of detecting the changes occurring in populations of structural defects. In the context of  $\text{TiO}_2$ -based ETL layer, ESR, by monitoring the changes in the population of  $\text{Ti}^{3+}$  paramagnetic defects in  $\text{TiO}_2$ , allows for detection and quantification of the photo-generated charges that are transferred over the MHP/ $\text{TiO}_2$  interface. The ESR-based methodological approach elaborated in this thesis can be helpful in further attempts to elucidate the processes and efficiencies of charge extraction from MHPs in perovskite-based photovoltaic devices.

### 1.7 Challenges of implementing perovskite materials

MHPs – the materials with extraordinary photo-physical properties, despite being cheap and easily prepared, also have some drawbacks. The three main challenges that hamper the direct implementation of MHPs in functional devices are: toxicity, stability to environmental factors and internal instabilities.

Toxicity of MHPs seems to be the most obvious, since  $\text{MAPbX}_3$  perovskite materials contain lead. On its own, it does not seem like a big issue as lead is permitted, for the time being, in the solar cell industry. Yet, in the long run, the fact that these materials easily react with water and are also relatively soluble, represents a serious problem of their potential heavy metal-related toxicity.

It is then clear, that to reduce the toxic impact of the MHPs on the environment, relatively complex technological efforts oriented towards device sealing as well as recycling, are necessary. In fact, to circumvent the problem of the heavy metal-related toxicity, there have been attempts to substitute lead with other elements, such as for example tin (Sn). Incorporated into the perovskite structure, tin does solve the heavy metal-related toxicity problem but has a drawback of its salts also being toxic. However, the overall drop in performance of devices based on Sn-substituted MHPs was too severe to rehabilitate such change in composition. On the other hand, one has to mention that Sn-substituted MHPs are quite well performing in the field of thermo-electricity.

Another issue, which was mentioned briefly above is the stability to environmental factors. These materials are highly susceptible to moisture and degrade very fast upon exposure. There have also been reports concerning the evidence that exposure to oxygen, accompanied by illumination causes degradation of these materials [66]. Normally, on its own, light does not harm the material; yet, at certain wavelengths, UV light can also degrade it. Moreover, the fact that MHPs are also fragile while exposed to numerous organic solvents and their vapors [67] renders them even harder to manufacture, process, form and store.

Lastly, the internal instabilities should be mentioned. Very often, these intrinsic material instabilities are responsible for the hysteretic behavior of the device performance. The underlying processes are ion movements [68], charge trapping and ferroelectric effects [69]. Clearly,

### **1.7. Challenges of implementing perovskite materials**

---

such non-stability of characteristics undermines the reproducibility and impacts the research progress. There have been attempts of standardization of procedures to facilitate comparisons [70, 71], but on fundamental level these processes can impede facile implementation of perovskites to devices.



## 2 Methodology and experimental techniques

### 2.1 Organic-inorganic perovskite material and sample preparation

The great majority of specimens investigated in this thesis were thin film deposits of MAPbI<sub>3</sub> and MAPbBr<sub>3</sub> coated onto cylindrical substrates having varying diameters in the range from 80 to 1800  $\mu\text{m}$ . Additionally, to complete the experimental analysis, single crystals of MAPbI<sub>3</sub> were also studied in some experiments.

Therefore, this section will cover in detail the techniques of deposition of thin film coatings of MAPbI<sub>3</sub> and MAPbBr<sub>3</sub>, as well as of preparation of single crystals of MAPbI<sub>3</sub>.

In the context of solution-casting of thin layers of MHPs onto the substrates having high curvatures, the most important technological steps included:

- preparation of MAPbI<sub>3</sub> and MAPbBr<sub>3</sub> precursor solutions;
- deposition of the precursor solutions onto the substrates;
- thermal annealing.

All chemicals for fabrication of MAPbI/Br<sub>3</sub> deposits and growing MAPbI/Br<sub>3</sub> single crystals were purchased from Sigma Aldrich and used as received, unless otherwise noted.

#### 2.1.1 Single-step solution-casting of MAPbI<sub>3</sub>/MAPbBr<sub>3</sub> on cylinder-shaped substrates: preparation of MAPbI<sub>3</sub>/MAPbBr<sub>3</sub> precursors in DMF solution

Prior to preparing the saturated DMF solutions of MAPbI<sub>3</sub> and MAPbBr<sub>3</sub>, it was necessary to grow stoichiometric single crystals of both MHPs. To this end, firstly, MAPbI<sub>3</sub> and MAPbBr<sub>3</sub> single crystals were grown by precipitation from aqueous solutions of concentrated hydroiodic acid (57 wt% in H<sub>2</sub>O) and hydrobromic acid (48 wt% in H<sub>2</sub>O), respectively, containing also stoichiometric amounts of lead(II) acetate trihydrate (Pb(ac)<sub>2</sub>·3H<sub>2</sub>O) and methylamine (CH<sub>3</sub>NH<sub>2</sub>),

40 wt% in H<sub>2</sub>O). MAPbI<sub>3</sub>/MAPbBr<sub>3</sub> crystals were grown and recrystallized in the saturated hydroiodic/hydrobromic acid solutions applying temperature gradient in the vessel. The crystals were dissolved at the higher temperature side of the vessel and re-crystallized at the lower temperature side of the vessel [72]. Finally, the obtained MAPbI<sub>3</sub>/MAPbBr<sub>3</sub> single crystals were harvested, dried at 120°C and dissolved in DMF, thus leading to a 50 wt%/30 wt% DMF stock solutions, respectively.

### 2.1.2 Single-step solution-casting of MAPbI/Br<sub>3</sub> on cylinder-shaped substrates: thin-film deposition

Thin polycrystalline MAPbI<sub>3</sub>/Br<sub>3</sub> layers were deposited *via* one-step solution-casting on cylinder-shaped quartz substrates (rods) having the following diameters: 80 μm, 330 μm, 400 μm, 700 μm, 1100 μm and 1800 μm.

Prior to performing solution-casting, the quartz rods were sequentially carefully washed in acetone and ethanol, rinsed with de-ionized water and dried in air. In addition, the quartz rods were also cleaned in O<sub>2</sub> plasma for 10 minutes. Subsequently, thus prepared substrates (cylinder-shaped quartz rods) were solution-casted using a doctor-blade technique from the stock solutions of stoichiometrically mixed MAPbI<sub>3</sub>/Br<sub>3</sub> precursors.

In the doctor-blading process, a precursor solution is deposited on a substrate beyond the doctor blade. By the means of a constant relative movement between the blade and the substrate, the precursor solution spreads on the substrate to form a thin layer which results in a film deposit upon drying.

Finally, the substrates were annealed on a laboratory hot plate at 110 °C for 10 minutes. During the curing process, the quartz rods were positioned at a small distance (3.0 mm) above the hotplate, thus allowing for circulation of the hot air all around the substrates. The corresponding scheme of the experimental setup is shown in Figure 2.1.

As mentioned in the introduction, one of the challenges facing the emerging MHPs-based photovoltaics is the thermodynamic stability against environmental conditions and the related long-term storage of these materials [73]. Therefore, in this work, to avoid interaction with air and moisture, the freshly prepared samples were always stored under an inert nitrogen atmosphere in sealed glass containers of a flow-through dry-box.

### 2.1.3 Preparation of single crystals of MAPbI<sub>3</sub>

Single crystals of MAPbI<sub>3</sub> were synthesized by solution growth. To this end, 3.3 mmol lead (II) acetate trihydrate (Pb(ac)<sub>2</sub> × 3H<sub>2</sub>O, >99.9%) was reacted with 6 ml of saturated hydroiodic acid solution (57 wt% HI in H<sub>2</sub>O). The formed PbI<sub>2</sub> precipitate was then dissolved in a gently heated acidic solution. The respective amount of methylamine (CH<sub>3</sub>NH<sub>2</sub>) solution (3.30 mmol, 40 wt% in H<sub>2</sub>O) was pipetted into the 5 °C ice cooled solution of PbI<sub>2</sub>.



## 2.2. MAPbI<sub>3</sub>/blue-TiO<sub>2</sub>NWs nanohybrid sample preparation

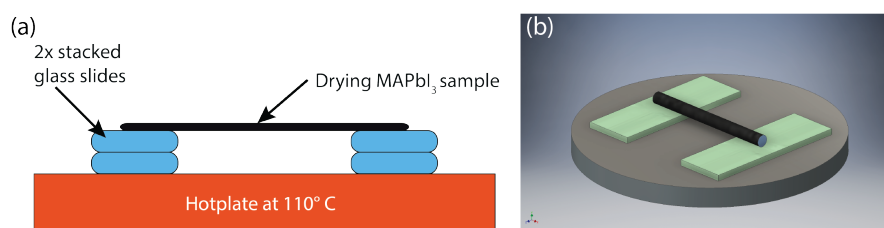


Figure 2.1 – Schematic representation of the experimental setup used for the thermal annealing of micro-crystalline MAPbI<sub>3</sub> deposited on cylinder-shaped quartz substrates with variable curvatures: (a) the side view and (b) the corresponding 3D overview of the experimental setup.

Maintaining the solution at low temperature (5°C) prevented evaporation of methylamine during the exothermic reaction of methylamine with hydroiodic acid. Black coloured micro-crystallites of CH<sub>3</sub>NH<sub>3</sub>PbI<sub>3</sub> were formed immediately and settled down at the bottom of the vessel. In a temperature gradient of 15°C in the acidic media, large (3 – 10 mm) intergrown dark crystals with metallic shine on the surface were formed in 7 – 10 days. The crystals were harvested and immediately wiped with laboratory paper wipes and further dried on hot plate at 100°C.

## 2.2 MAPbI<sub>3</sub>/blue-TiO<sub>2</sub>NWs nanohybrid sample preparation

### 2.2.1 Preparation of MAPbI<sub>3</sub>/TiO<sub>2</sub> nanohybrid material

The following forms of TiO<sub>2</sub> were selected to prepare various types of MAPbI<sub>3</sub>/TiO<sub>2</sub> hybrid materials:

- home-made white- and blue-TiO<sub>2</sub>NWs powders;
- crystalline powder obtained by grinding TiO<sub>2</sub> custom-made reduced anatase crystals;
- commercial Tayca Corp. AMT-600 anatase powder.

Firstly, to prepare a MAPbI<sub>3</sub>/TiO<sub>2</sub> hybrid material, 20 mg of one of the selected forms of TiO<sub>2</sub> were mixed with 100 µl of the MAPbI<sub>3</sub> precursor solution. Subsequently, thus obtained suspensions of TiO<sub>2</sub> in the MAPbI<sub>3</sub> precursor solution were sonicated for 5 minutes in an ultrasonic homogenizer and then directly deposited on the surface of the substrates (fused quartz rods, 2 mm in diameter). To obtain the final coatings of the hybrid MAPbI<sub>3</sub>/TiO<sub>2</sub> material, the deposits were annealed on a laboratory hot plate at 110°C for 10 minutes. Thanks to this approach, the 2 mm quartz rods could then serve both as the sample holders and light guides.

For preparing the reference deposits, which were composed exclusively of TiO<sub>2</sub>, 20 mg of one of the selected forms of TiO<sub>2</sub> were added to 100 µl volume of the solvent consisting of 90%

of ethanol and 10% distilled water, containing also the dissolved 1 mg of polyethylene oxide (PEO, 100'000 MW). Next, in a similar way as described above, thus prepared suspensions of TiO<sub>2</sub> were sonicated for 5 minutes in an ultrasonic homogenizer and then coated onto the surface of 2 mm diameter quartz rods. To obtain the final form of the TiO<sub>2</sub> deposits, the coatings were dried in air at room temperature for 2 hours. Also in this case, the 2 mm quartz rods (substrates) could then serve both as the sample holders and light guides.

### 2.2.2 MAPbI<sub>3</sub>/blue-TiO<sub>2</sub>NWs nanohybrid sample preparation for SEM and EDX

Firstly, a homogeneous suspension of blue-TiO<sub>2</sub>NWs in the stoichiometric solution of MAPbI<sub>3</sub> precursors in DMF was prepared. To this end, 2.0 mg of blue-TiO<sub>2</sub>NWs were added to 10  $\mu$ L of a stoichiometric solution of MAPbI<sub>3</sub> precursors in DMF. The thus prepared suspension was sonicated for 5 min in an ultrasonic homogenizer.

Subsequently, a thin layer of the MAPbI<sub>3</sub>/blue-TiO<sub>2</sub>NWs nanohybrid was deposited on a clean surface of a silicon wafer by dripping. To do this,  $\sim 1.0$   $\mu$ L volume of the suspension was dispensed from a micropipette (model ES-10, Eppendorf Research Plus – single channel pipette, 0.5 – 10  $\mu$ L) on a silicon wafer. Finally, the deposit of MAPbI<sub>3</sub>/blue-TiO<sub>2</sub>NWs nanohybrid was annealed at 110°C for 20 min on a hot plate.

### 2.2.3 Synthesis of reduced TiO<sub>2</sub> single crystals

High-quality single crystals of blue TiO<sub>2</sub> anatase were produced by a chemical transport method from anatase powder and ammonium chloride (NH<sub>4</sub>Cl) as a transport agent, using a modified procedure based on the one described in [74]. In brief,  $\sim 3.0$  g of high-purity sintered powder of anatase (99.6% pure, 3 – 6 mm sized grains, from Merck) were sealed together with  $\sim 0.4$  g of NH<sub>4</sub>Cl (Merck) in a  $\sim 20$ -cm long, 2.0 cm in diameter, quartz ampule. Before sealing, the reagents were thoroughly dried out and evacuated at pressure  $< 4 \cdot 10^{-6}$  mbar during one night.

Subsequently, the sealed ampule was placed in a horizontal tubular two-zone furnace and heated slowly to 750 °C and 600 °C, at the source and the deposition zones, respectively. After 5 – 8 weeks, millimeter-sized crystals ( $\sim 1.5 \times 1.5 \times 1.5$  mm<sup>3</sup>) with a bi-pyramidal shape were collected.

The microcrystalline powder (0.01 – 0.5 mm average grain sizes) of blue TiO<sub>2</sub> anatase was obtained by careful grinding of two-three small (*ca.*  $\sim 2 - 3$  mm<sup>3</sup>) single crystals of blue TiO<sub>2</sub> anatase in an agate mortar. The ground material conserved the same deep-blue color as the starting monocrystalline blue TiO<sub>2</sub> anatase.

### 2.3 Metal-halide perovskite material characterization techniques

This section will present an overview of various characterization and measurement techniques performed on samples studied in this work.

Several characterization techniques, such as optical microscopy, scanning electron microscopy (SEM) and X-ray diffraction (XRD) were utilized to study morphology, crystallinity and packing of the MHPs deposits, while atomic force microscopy (AFM) was used to verify the roughness of the substrates. Photoluminescence (PL) and photocurrent (PC) measurements were performed for the general photo-physical characterization of the MHPs deposits. Similarly, single crystals of MHPs were characterized with using XRD, photoluminescence and optical microscopy.

#### 2.3.1 Scanning electron microscopy imaging

Scanning electron microscopy (SEM) is a common technique used in material characterization [75]. It can provide a variety of information, including high-resolution images, through which the morphology and characteristic sizes can be inferred. In combination with energy dispersive X-ray analysis (EDX), this technique also yields elemental compositions and elemental maps of the studied specimens. A typical SEM microscope consists of a vertical vacuum chamber equipped with an electron gun and several electrostatic and magnetic condensers (lenses), which serve to form the high-energy electron beam (from 0.2 keV to 40 keV), as well to focus the incident electrons on a spot of  $\sim 0.4$  nm to  $\sim 5$  nm in diameter. Since the electron beam passes through pairs of scanning coils at the bottom of the electron-beam forming column, it can also be deflected in the  $x$  and  $y$  axes, so it scans in a raster fashion over a rectangular area of the sample surface. A schematic representation of a typical SEM microscope is shown in Figure 2.2.

There are three major pathways *via* which the electrons interact with the sample:

1. Elastic scattering otherwise called reflection;
2. Inelastic scattering, which causes secondary electrons to be emitted from the sample;
3. Electromagnetic radiation emission, which happens when an incident electron excites the sample intrinsic one, which upon relaxation emits a characteristic radiation.

In the two latter cases, when the focused beam of electrons hits the sample it creates an interaction volume which spreads into a teardrop shape inside the sample. The extent of this interaction volume is typically 100 nm to 5  $\mu$ m into the surface depending on the incident electron energy, atomic number of the element on the surface as well as the local density of the sample.

Finally, after interacting with the sample, electrons get detected by various detectors, like

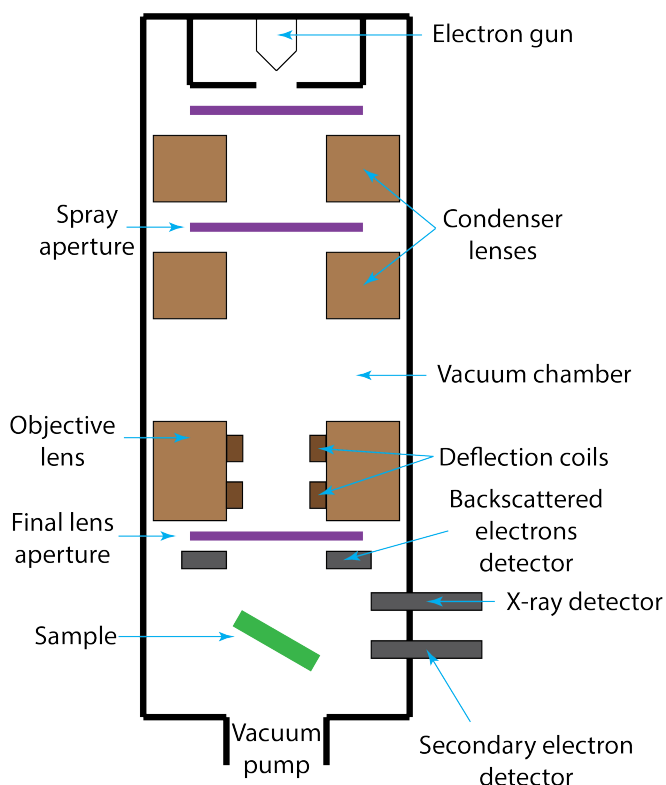


Figure 2.2 – Schematic representation of a scanning electron microscope (SEM). The outer shell represents the vacuum chamber inside of which the electron column and the sample (green) are placed. At the top, inside its own housing an electron gun is placed. Electron beam is then further collimated by the apertures depicted by black horizontal lines and focused by the means of condenser and objective lenses, depicted in light brown. Scanning over the sample surface is accommodated by the means of deflection coils (dark brown) placed in the objective lens. Detection of various electrons and X-rays emission is facilitated by three detectors, depicted in dark gray. The whole setup is being pumped down by a vacuum pump to achieve high vacuum.

back-scattered electron detectors, secondary electron detectors and X-ray detectors.

In this work, morphology of the polycrystalline  $\text{MAPbI}_3/\text{Br}_3$  layers deposited on cylinder-shaped quartz rods was investigated by SEM with the help of both secondary electron and in-lens detectors. All SEM images were collected with a high-performance Schottky field-emission electron microscope capable of resolution in 2 – 5 nm size range, Model LEO 1550 (Carl Zeiss AG, Jena, Germany), in the Center of MicroNanoTechnology (CMi) at the EPFL.

### 2.3.2 X-ray diffraction

X-ray diffraction (XRD) is another technique commonly used in materials science for determination of atomic and molecular structure. XRD is based on the process of interaction of X-rays

with atoms in the crystal lattice of the material under investigation. From this perspective, there are two ways of interaction of X-rays with the specimen, elastic and inelastic, which is then similar to the interactions of electrons incident on a studied target in a SEM microscope (as described in the subsection above).

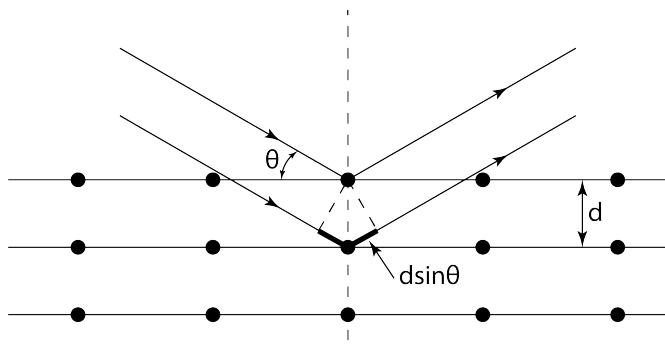


Figure 2.3 – Schematic representation of the mechanism underlying X-ray diffraction. An incoming X-ray beam at an angle  $\theta$  (from the top left) is reflected by the crystalline sites with separation  $d$  of the studied crystal. The outgoing beam (top right) forms reflections a collection of which is called a diffraction pattern according to Bragg's law.

Elastic interaction means that the X-rays do not change their energy upon interacting with the crystal, thus being effectively reflected. This is portrayed in Figure 2.3 – an incident X-ray beam is incoming from the top left side. If the positions of atoms are evenly spaced with inter-layer distance  $d$ , reflections occur according to the Bragg's law [76]:

$$n\lambda = 2d \sin \theta, \quad (2.1)$$

where  $n$  is the order of the reflection,  $d$  – the inter-layer spacing and  $\theta$  – the incidence angle of the X-ray beam. Moving the crystal, changing the relative position of the atomic planes with respect to the incident X-ray beam allows the experimentalist to acquire a set of reflections, otherwise known as the diffraction pattern. The diffraction pattern, in turn, can be treated *via* a Fourier transformation to obtain the electron density. The resulting data can be used to elucidate the mean atomic positions, chemical bonds, *etc.*

Inelastic interaction, on the other hand, implies that the incident X-ray beam either loses or acquires energy from the interaction with the crystal. An insight into inelastic scattering can be quite useful, as the energy loss or gain of the incident X-rays occurs due to the presence of specific types of excitations in the crystal lattice. These excitations might include: phonons – wavelike excitation of the lattice [77], plasmons – collective oscillations of the electron gas [78], polaritons – hybrid particles made up of a photon strongly coupled to an electric dipole (an electron-hole pair), or magnons – magnetic excitations of the spin lattice [79]. Therefore, the inelastic X-ray scattering technique can serve as a great tool to study these excitations.

The technique of X-ray scattering can be extended to a powder sample, which consists of

many crystallites of small sizes [80]. A major distinction from the above-described single crystal case is a markedly different crystallographic texture, which results from the relative “organization” of the crystalline grains in an anisotropic solid (powder). At the single crystal level, the crystallographic texture is strictly anisotropic, whereas in powders consisting of numerous randomly oriented small crystallites, the crystallographic texture becomes more isotropic. The X-ray powder diffraction technique takes advantage of this by assuming that an assembly of randomly oriented crystallites reveals a statistically significant number of diffraction planes with specific orientations – to diffract the incoming X-rays. This means that each of these crystallographic planes will be represented in the resulting diffraction pattern. Yet, it should be noted that there are cases when turning the sample is necessary to counter the effects of texturing.

As all the crystalline compounds have unique fingerprints when studied by XRD, in this work, this technique was mainly utilized to verify the crystalline phases of MHPs in polycrystalline deposits and single crystals of either  $\text{MAPbI}_3$  or  $\text{MAPbBr}_3$ . This allowed for a rapid and reliable confirmation of the quality of MHPs crystals and MHPs-based deposits, as well as to check for possible changes in the material due to the exposure to the environmental factors or prolonged storage (degradation).

### 2.3.3 Atomic force microscopy

Another common tool in the material characterization toolkit is atomic force microscopy (AFM). This method allows for imaging with particularity high precision, on the order of fraction of a nanometer, that is even higher than the spatial resolution of SEM. [81].

Three major applications of AFM are as follows:

- Force measurement, mainly utilized for studying mechanical properties of the samples;
- Imaging – obtaining high-resolution topography images of the samples;
- Manipulation – picking up ultra-small objects to arrange them in a specific configuration.

In the simplest realization of AFM (so-called static AFM mode) a sharp tip mounted on a flexible cantilever is interacting with the sample, which results in the deflection of the cantilever. The elastic deformation of the cantilever can be very precisely monitored by an optical detection system. Specifically, the back side of the cantilever reflects the laser beam onto a sector-sensitive photodiode (four-quadrant photodetector), which produces a variable voltage signal proportional to the deflection amplitude of the cantilever. A piezoelectric scanner moves the investigated specimen relative to the stationary position of the cantilever. This allows for either zig-zag or raster scanning pattern and provides information on the sample topography.

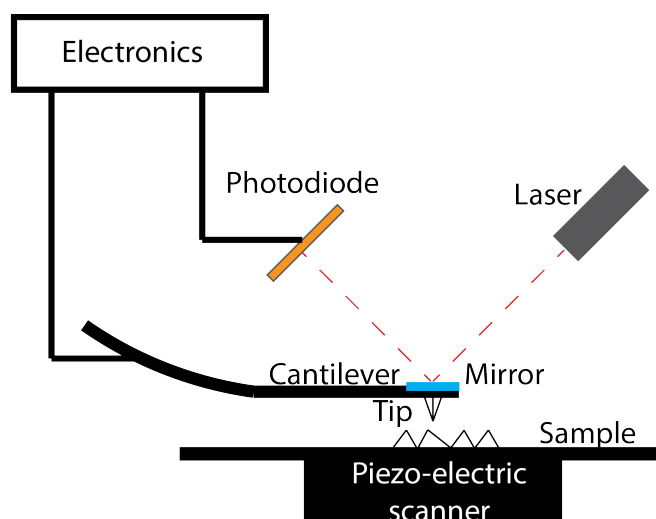


Figure 2.4 – Schematic representation of an atomic force microscope. A sample with a certain topology is mounted on a piezo-electric scanner to provide access to different parts of the surface. A very sharp tip is mounted on a cantilever and interacts with the surface of the sample distorting the cantilever geometry. A cantilever back-mounted mirror (cyan) reflects the incoming laser beam onto a sector-sensitive photodiode (orange) to track distortions of the cantilever. Utilizing the electronics this is, in turn, transformed into information about the sample topography.

Based on the type of interaction between the sample and the tip there are three main methods of conducting AFM measurements:

- Contact mode – the tip is in full contact with the sample;
- Tapping mode – the tip is occasionally in contact with the surface of the sample;
- Non-contact mode – the tip does not touch the sample.

In this work surface roughness of uncoated quartz rod substrates was investigated by AFM. Visualization of the surface topography and the 2D roughness profiles were done with an AFM XE-100 from Park Systems Inc. (Santa Clara, CA, USA). The measurements were performed under contact mode with the use of silicon cantilevers, model NSC36-10M (spring constant of 5.0 N/m), from Park Systems. The analysis of variation of the substrate roughness was conducted with a standard Park Systems software package, XEI.

### 2.3.4 Photoluminescence

Photoluminescence (PL) is the emission of light from a material following the absorption of light. This general phenomenon constitutes the basis of the PL spectroscopy – a nondestructive

and contactless method for characterization of the electronic structure of materials through excitation by light.

When the studied material is illuminated by light at certain wavelength (excitation wavelength) it can be either partially reflected or absorbed. The energy of the absorbed light gets deposited into the material, which, in turn, may cause excitation of the material. For example, in semiconductors, absorption of light of energy higher than the semiconductor bandgap ( $E_g$ ) can generate and excite charge carriers (electron-hole pairs). In this case, one of the possible ways the absorbed energy could dissipate is by relaxation of the excited charge carriers through light emission – hence the name “photoluminescence”.

When the charge carriers relax from their excited states into the equilibrium state, the corresponding processes can be either radiative or non-radiative. In the case of radiative recombination, the energy of the emitted light is directly related to the energy difference between the excited and equilibrium states. In general, the PL processes can be classified into three main categories:

- Resonant radiation – this type of radiation is characterized by resonant absorption and emission. In other words the incident energy of the photon is almost identical to the energy of the emitted one. This implies that there were no significant internal energy transfers occurring during the process. Such process occurs on a time scale of about tens of nanoseconds.
- Fluorescence – a relatively fast process occurring on time scales of  $10^{-8}$  to  $10^{-4}$  ns. Usually, this process involves an internal energy conversion, which precedes the photon emission. Therefore, as a portion of the exciting light energy is dissipated, the energy of the emitted light is lower than the one absorbed.
- Phosphorescence – a similar but much slower process than fluorescence. It occurs on the time scales of  $10^{-4}$  to  $10^{-2}$  ns and, independent of the internal energy conversion, involves also a change in spin multiplicity. Therefore, phosphorescence manifests itself less frequently than fluorescence. In fact, phosphorescence requires not only favorable conditions for the “*singlet-to-triplet*” inter-system crossing (ISC) transition, but also the corresponding radiative “*triplet-to-singlet*” transition is quantum-mechanically forbidden (in the absence of perturbations such as spin-orbit coupling or vibrational coupling). Therefore, the excited spin triplet state has a very high chance to relax through competing non-radiative processes.

A qualitative representation of the energy levels involved in excitation-relaxation processes in a light-excited semiconductor is presented in Figure 2.5(a). As can be seen in this Figure, when photons of the incident light have energy higher than the semiconductor’s bandgap ( $E_g$ ), the excitation wavelength is absorbed by the material and pairs of electrons and holes (excitons) are created. Within this mechanism, the electrons are promoted from the valence band (VB)



to the conduction band (CB), where they leave behind positively charged holes. Depending on the surplus of energy of the incident photons, electrons get excited either to the edge of the conduction band (CB) or to higher energy states. The electrons excited to higher energy states thermalize back to the CB edge by dissipating energy in the form of heat. Due to the fact that the a semiconductor has a continuum of states in both VB and CB bands, absorption can occur at multiple wavelengths which, in turn, leads to a very broad absorption spectrum with an onset at the  $E_g$ . This very prominent feature of semiconducting materials is depicted by the blue trace in Figure 2.5(b).

Following the process of absorption of light, electrons naturally recombine with holes left after the excitation in the VB. The process of recombination can be either radiative or non-radiative. In case of radiative recombination an emission of light (photoluminescence) can be observed. Typically, as depicted by the red trace in Figure 2.5(b), semiconductors exhibit one PL peak, which might be structured by additional transitions governed by the presence of shallow and deep states in the band gap.

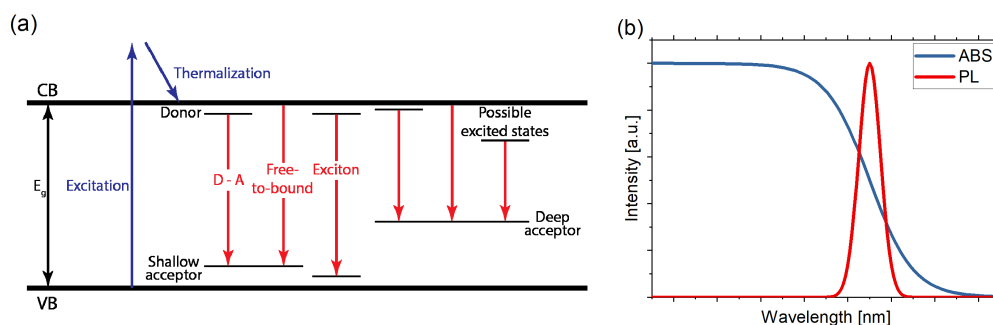


Figure 2.5 – (a) Qualitative energy level diagram and representation of the excitation-relaxation processes in semiconductors. (b) Qualitative schematic representation of typical absorption (blue trace) and PL emission (red trace) spectra of semiconducting materials.

The major peak of the PL spectrum comes from the transition over the  $E_g$ . Additional components of the PL spectrum can originate from several possible recombination pathways, including the *free-to-bound* recombination, donor-acceptor (D-A) or *3d* deep-lying electronic core orbitals when excited at energies below the  $E_g$  [82].

PL spectroscopy can be used for a variety of applications. In particular, it can serve to determine the band-gap energy of semiconductor materials, since the energy of the emitted light is related to the energies of the valence and conduction bands [83]. As such, the PL spectroscopy is a very useful tool for the general characterization of photovoltaic materials. Therefore, the PL spectroscopy has proven a very important technique for the topics discussed in this thesis.

Another area where the sensitivity of PL measurements is very useful is the detection of defects and impurity levels in semiconductors. As radiative transitions in semiconductors may occur through defect and impurity levels, a PL spectrum can be used to assign energies to certain defects and impurities. In this case the PL intensity is directly proportional to the

ratio of radiative to non-radiative transitions. Non-radiative transitions are mainly attributed to the presence of defects in the material. Therefore, the dependence of PL intensity on the excitation power and temperature may reveal the main dominating recombination processes in the material [83].

In some cases the defects can be found on the surface and here the PL spectroscopy is also extremely sensitive. Another interesting surface alteration process is adsorption of foreign species on the surface. Based on this, there is a possibility to monitor the electron-hole processes on the surface of the material. This particular issue, concerning tracking the changes in gaseous environments that influence the studied specimen [83], will be discussed in details in the subsequent chapters of this thesis.

With all its advantages, there is a general drawback to the PL spectroscopy as in general this technique is not quantitative. One should then be very careful in case a comparison of the absolute values is conducted.

### 2.3.5 Optical microscopy imaging and steady-state photoluminescence measurements

The workhorse of our experiments was the optical microscopy setup. Its versatility not only allowed us to obtain optical and fluorescent images but as well gather some valuable intuition of the morphology and packing changes of MHPs crystallites on cylindrical substrates. Furthermore, adding a special holder for samples allowed us to simultaneously track PC and PL responses in controlled gaseous media environments.

An overview of the whole microscopy setup used in the experiments throughout the work is presented in Figure 2.6. Optical microscopy imaging under visible light illumination, as well as the luminescence microscopy imaging and collection of the steady-state PL spectra, were performed with using a custom-designed setup, which combined an inverted biological epifluorescence microscope (TC5500, Meiji Techno, Japan) with a compact spectro-fluorometer (USB 2000+XR, Ocean Optics Inc., USA). A digital non-cooled CCD camera (Infinity 2, Lumenera Co., Ottawa, Canada) was used to capture the luminescence images of the studied deposits of MAPbI<sub>3</sub> and MAPbBr<sub>3</sub>.

PL spectra and fluorescence microscopy images were collected under the illumination with the excitation wavelengths of  $\lambda_{exc} = 470$  nm and  $\lambda_{exc} = 546$  nm, for the deposits of MAPbI<sub>3</sub> and MAPbBr<sub>3</sub>, respectively. The excitation wavelengths were filtered out from the emission spectrum of the microscope's Mercury vapor 100 W lamp by implementing two dedicated sets of Meiji Techno filters, Model 11001v2 Blue and Model 11002v2 Green, for the excitation wavelengths of  $\lambda_{exc} = 470$  nm and  $\lambda_{exc} = 546$  nm, respectively [84]), which provided photons with energy above the band gaps of both MHPs ( $E_{hv=470nm} = 2.64$  eV >  $E_{g\text{ MAPbBr}_3} = 2.32$  eV >  $E_{g\text{ MAPbI}_3} = 1.61$  eV) [85]. Specifically, three variants of the experimental setup were used for performing the PL and PC measurements, as well as the standard optical and fluorescence

## 2.3. Metal-halide perovskite material characterization techniques

microscopy. They are depicted in detail in Figures 2.8 and 2.9.

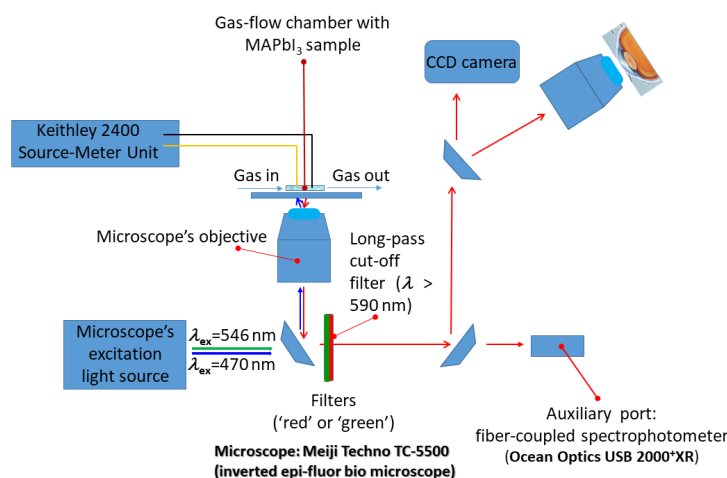


Figure 2.6 – Schematic overview of the setup used in photo-physical characterization experiments. A mercury lamp (bottom left) is used as a light source. The excitation wavelengths of 546 nm and 470 nm are selected from the spectrum of the mercury lamp by two dedicated sets of filters (filter box). The excitation light is focused by the objective onto the sample (middle) and the emitted light is gathered back by the same objective and guided either to the CCD camera and the microscope's ocular (top right) or, through an auxiliary port, to a compact spectro-fluorometer (Ocean Optics) to acquire the PL spectrum (bottom right). For the PC measurements a Keithley 2400 Source-Meter unit (top left) is used with the electrical connections to the measured sample provided by two copper wires. Standard plastic Luer-type connectors are used to accommodate gas intake and exhaust.

Spectral compositions of the excitation light after filtering with the respective filters, Model 11001v2 Blue and Model 11002v2 Green, for the excitation wavelengths of  $\lambda_{exc} = 470$  nm and  $\lambda_{exc} = 546$  nm, are shown Figures 2.7(a & b). It can be seen that the blue excitation light has a broader peak with 470 nm wavelength being its middle. The overall power density is calculated to be  $\sim 240$  mW/cm<sup>2</sup> and its visual representation is shown as a photo in Figure 2.7(c). The green excitation light has a narrower peak centered at 546 nm and higher power density of 480 mW/cm<sup>2</sup>. The photographs of the microscope sample stage under excitation of the studied sample with either the blue or green light are shown in Figure 2.7(c & d).

As depicted in Figure 2.8(a), prior to performing fluorescence microscopy imaging and collecting the PL spectra, the cylinder-shaped quartz substrates covered with either MAPbI<sub>3</sub> and MAPbBr<sub>3</sub> were inserted into and centrally positioned in a short section of a larger quartz tube (2.0 mm ID × 2.4 mm OD or 3.0 mm ID × 4.0 mm OD,  $\sim 50.0$  mm length), which served as external, light-transparent sample holder, hereinafter referred to as a gas-flow chamber. Centering of the cylinder-shaped quartz substrate inside the gas-flow chamber was achieved by implementing two plastic-made (PMMA) centering elements, to which the terminations of the substrates were glued. The gas-flow chamber was also equipped with the adequate gas inlets and outlets. Luer-type plastic connectors and thin polypropylene flexible tubes were

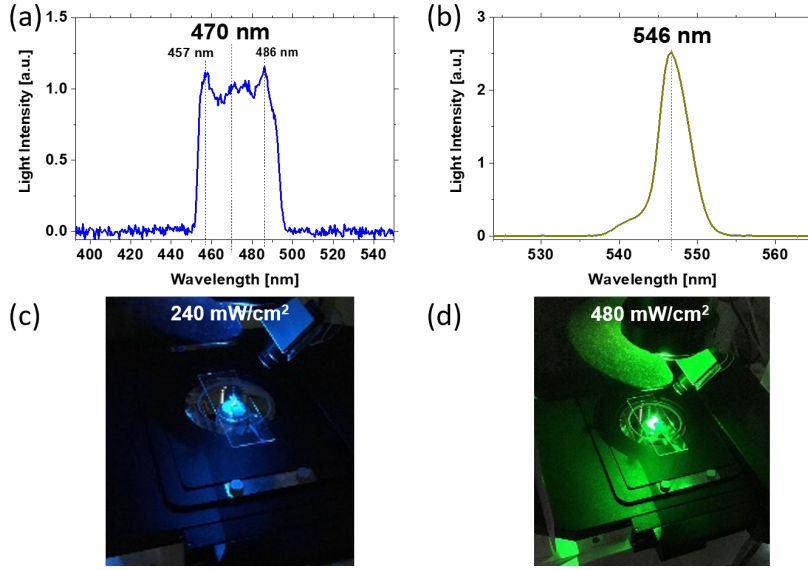


Figure 2.7 – Spectral compositions and the estimated power densities of the two main excitation lights:  $\lambda_{exc} = 470$  nm and  $\lambda_{exc} = 546$  nm. (a) Spectral composition of the blue excitation light,  $\lambda_{exc} = 470$  nm. (b) Spectral composition of the green excitation light,  $\lambda_{exc} = 546$  nm. Respective photographs of the microscope sample stage and estimated excitation power densities under excitation with:  $\lambda_{exc} = 470$  nm (c) and  $\lambda_{exc} = 546$  nm (d).

used to feed the gaseous media, *i.e.* oxygen ( $O_2$ ) and nitrogen ( $N_2$ ), into the gas-flow chamber. To perform fluorescence microscopy imaging and collecting the PL spectra the whole setup was then attached to a microscope sample holder plate and positioned on the XY stage of an inverted biological epi-fluorescence microscope, Meiji Techno TC5500, Japan, as shown in Figure 2.8(b).

For a controlled exposure of MHPs deposits to light and gaseous media, we also used another type of the gas-flow chamber, which was designed around a miniature hollow rectangular glass tube 1.0 mm height  $\times$  10.0 mm width, and 50 mm length (Model 4410, VitroCom Technical Glass, NJ, USA), seen in Figure 2.9. The flat geometry of this miniature gas-flow chamber allowed for an easy *side-by-side* parallel positioning of two cylinder-shape substrates coated with two different MHPs, *i.e.* MAPbI<sub>3</sub> and MAPbBr<sub>3</sub>. To achieve a good mechanical stability, before inserting into the gas-flow chamber, the two cylinder-shaped substrates (80  $\mu$ m DIA quartz rods) were positioned close to each other atop of a thin glass plate (150  $\mu$ m thick) and their terminations were glued to the glass surface with tiny drops of either nail-polish or Araldite.

For acquiring the PL spectra, the flat rectangular gas-flow chamber was also attached to a microscope slide holder and positioned on the XY stage of an inverted biological epi-fluorescence microscope. In particular, owing to small diameters of the cylindrical substrates as well as a relatively large light spot ( $\sim 55$   $\mu$ m DIA) used in our experimental setup, the *side-by-side*

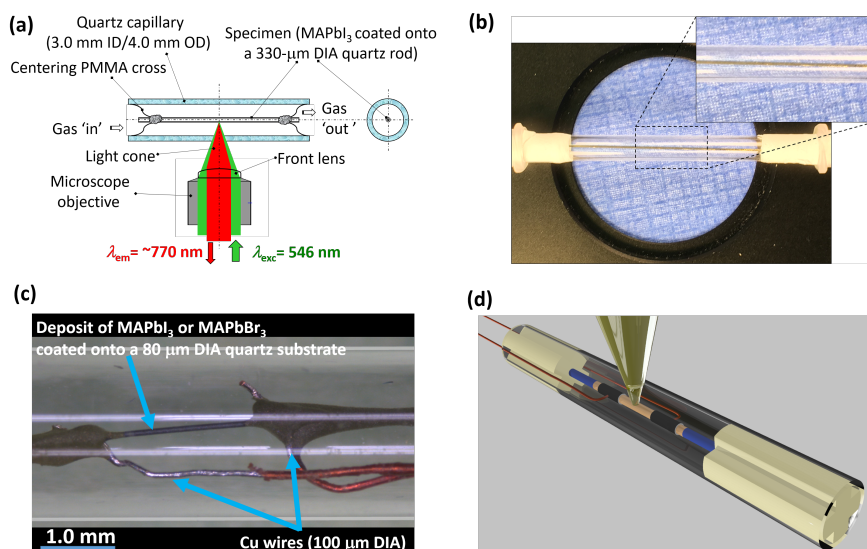


Figure 2.8 – Detailed scheme of the experimental setup used for photo-physical characterization of MHPs samples exposed to various gaseous media. (a) A cross-section view of the cylindrical gas-flow chamber containing the investigated sample and of the microscope's objective focusing the excitation light and gathering the emitted luminescence, depicted in green and red, respectively. (b) Photograph of the cylindrical gas-flow chamber mounted on a microscope plate with Luer-type connectors attached to it on either side. The blow-up shows the MHP sample inside the cylindrical gas-flow chamber. (c) Microscope image showing two copper wires connected to the MHP sample by carbon paste. (d) Schematic 3D representation of the complete gas-sensing device. The yellow cone represents the incoming excitation light.

*parallel* positioning of two substrates coated with different MHPs enabled us to perform the ultimate study comparing the PL responses of MAPbI<sub>3</sub> and MAPbBr<sub>3</sub> simultaneously exposed to exactly the same atmospheric conditions.

Gas delivery in this case was achieved by using a stainless needle (0.5 mm ID and 0.8 mm OD), which was protruding into the miniature flat gas-flow chamber through a rubber septum. The second stainless needle, protruding through the same rubber septum, provided an outlet port to allow the gas to be released from the chamber (Figure 2.9(b) in orange). The blow-up inserted into the photograph in Figure 2.9(b) shows the parallel *side-by-side* arrangement of two cylinder-shaped substrates coated with two different MHPs, *i.e.* MAPbI<sub>3</sub> and MAPbBr<sub>3</sub>, as well as a portion of the inlet stainless needle.

### 2.3.6 Measurements of the photocurrent for the deposits of MAPbI<sub>3</sub> and MAPbBr<sub>3</sub> intermittently exposed to the flow of either O<sub>2</sub> or N<sub>2</sub>

To measure the photocurrent (PC) responses of the deposits of MAPbI<sub>3</sub> and MAPbBr<sub>3</sub> to the intermittent flow of gaseous media, both MHPs were coated onto cylinder-shaped quartz substrates of 80 μm in diameter. After coating the substrates with MHPs deposits, two short

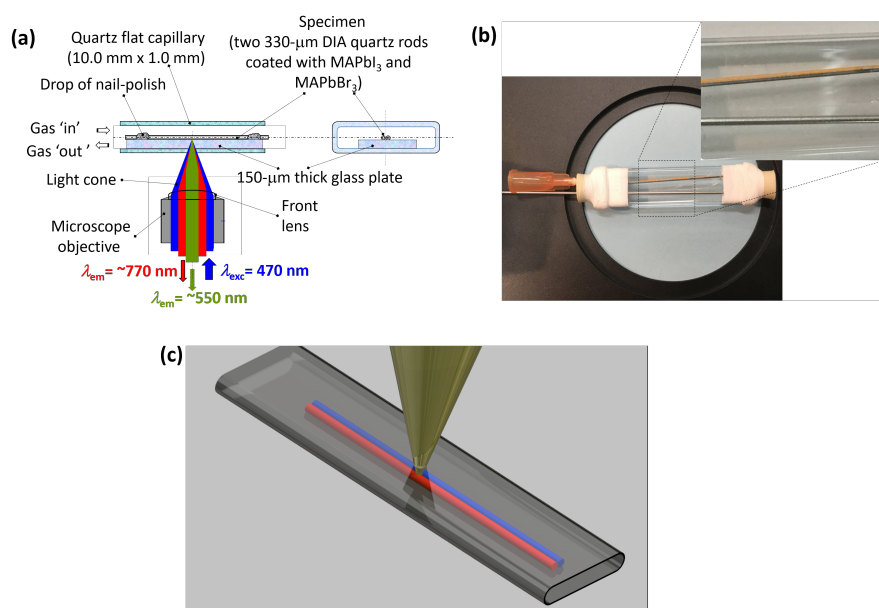


Figure 2.9 – Detailed scheme of the experimental setup based on a flat-cell gas-flow chamber used for photo-physical characterization of MHPs samples. (a) A cross-section view of the flat-cell gas-flow chamber containing two investigated samples and of the microscope's objective focusing the excitation light (depicted in blue) and gathering the emitted luminescence wavelengths, which are depicted in green and red, for the emissions from MAPbBr<sub>3</sub> and MAPbI<sub>3</sub>, respectively. (b) A flat-cell gas-flow chamber mounted on a microscope plate with needles used as gas inlet and outlet. Blow-up shows the two MHP samples positioned *side-by-side* inside the flat-cell gas-flow chamber. (c) Schematic 3D representation of the complete differential gas-sensing device. Two MHP samples are depicted in red and blue, while the yellow cone represents the incoming excitation light.

sections of thin copper wires (100  $\mu\text{m}$  in diameter) were attached with the conducting carbon paste (LeitC) to the quartz cylindrical substrates, thus providing the electrical contacts for the previously deposited thin layers of MAPbI<sub>3</sub> and MAPbBr<sub>3</sub> and can be seen in greater detail in Figure 2.8(c). The thus prepared samples were then encapsulated in short sections ( $\sim 50.0$  mm long) of a quartz tubes having a larger diameter (2 mm ID  $\times$  2.4 mm OD, Model CV2024, VitroCom Technical Glass, NJ, USA), which were also equipped with adequate gas inlets and outlets. The whole device is depicted in a render version in Figure 2.8(d) in previous section.

The configuration used in these measurements can be defined as a 2-terminal measurement. The difference from a more precise 4-terminal approach is that by having only two terminals we source current or voltage and measure the counterpart at the same two contacts. This is in contrast to the 4-terminal approach, in which the source and measurement terminals are separated into four independent contacts. Therefore, the 2-terminal measurements usually incorporate the resistances of the electrical leads and contacts. In the experiments reported herein, as mentioned above, carbon paste was used for contacting the samples.

## 2.4. Modified version of the experimental setup for performing PL measurements under photo-bleaching of MAPbI<sub>3</sub> with selective wavelengths

Moreover, the carbon paste has relatively high resistance of  $\sim 100\text{ k}\Omega$ , which would normally mask the contribution from the sample. However, in the case of MHPs samples, having intrinsically high resistances in the  $\text{M}\Omega$  range, the resistances originating from the contacts and electrical leads can practically be neglected.

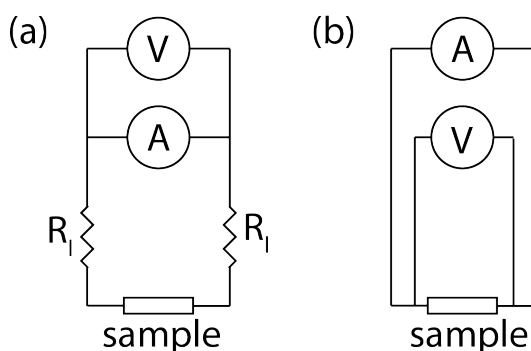


Figure 2.10 – Schematic representation of the experimental setup for PC measurements. (a) 2-terminal method, where A is the current source, V is the voltmeter providing the voltage measurement and  $R_l$  represents the lead and contact resistance. (b) 4-terminal method where the voltage is measured in parallel to the sample, thus eliminating the resistances of electrical leads and contacts.

## 2.4 Modified version of the experimental setup for performing PL measurements under photo-bleaching of MAPbI<sub>3</sub> with selective wavelengths

For the selective wavelength bleaching a slightly modified photo-physical characterization setup compared to the one described in one of the previous subsection (see Figure 2.6) has been used. In this experiment a technique of “co-excitation” was utilized, *i.e.* the sample was excited either exclusively at one wavelength, or it could be co-excited also with another excitation wavelength – added in parallel.

Specifically, we used the green light, at 532 nm wavelength and with power density of  $480\text{ mW/cm}^2$ , as the main excitation wavelength for MAPbI<sub>3</sub> samples. The specimens were positioned in identical cylindrical or rectangular (*flat-cell-based*) glass gas-flow chambers as described in previous sections. For co-excitation, the blue light at 470 nm wavelength and power density of  $25\text{ mW/cm}^2$  was applied from a  $400\text{ }\mu\text{m}$  fiber coupled laser, model MBL-III-473-50mW, with stability  $< 10\%$ . In addition, the experiments were also performed when the sample was excited exclusively by the blue light at 470 nm wavelength and power density of  $240\text{ mW/cm}^2$  (from the microscope mercury vapor lamp).



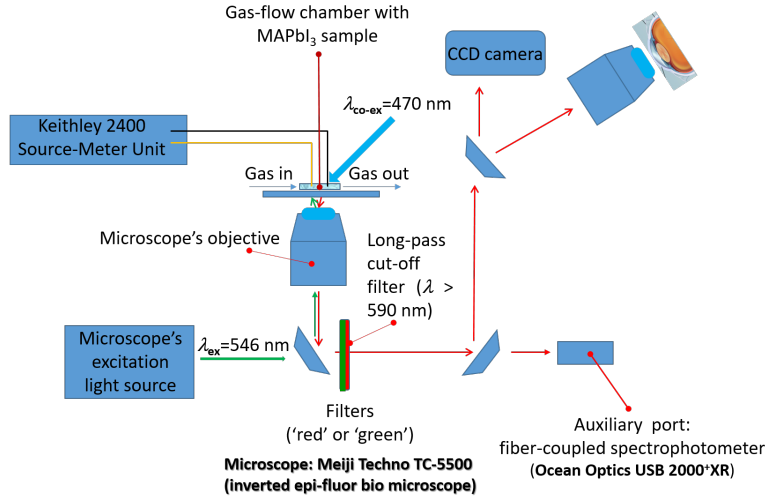


Figure 2.11 – Schematic overview of the experimental setup used for performing photo-physical characterization of MAPbI<sub>3</sub> deposits under photo-bleaching with selective wavelengths. The microscope mercury lamp (bottom left) was used as the primary excitation light source. The excitation wavelength of 546 nm was selected from the spectrum of the mercury lamp by a dedicated set of filters (filter box). Co-excitation was performed by shining the additional excitation wavelength of 470 nm from a fiber coupled laser pointed at the sample from above (middle). The main excitation light wavelength (546 nm) was focused by the microscope objective onto the sample (middle). The emitted light was gathered back by the same objective and guided either to the CCD camera and the microscope's ocular (top right) or, through an auxiliary port, to a compact spectro-fluorometer (Ocean Optics) to acquire the PL spectrum (bottom right). For the photocurrent measurements, a Keithley 2400 Source-Meter unit (top left) was used with the sample connected to it by two copper wires. Standard plastic Luer-type connectors are used to accommodate gas intake and exhaust.

## 2.5 Gas flow

### 2.5.1 Characterization of the type of flow of gaseous media in custom-made gas-flow chambers

It is worth mentioning that all the experiments concerning exposure of MHPs to the flow of gaseous media were performed under laminar flow conditions, which are characterized by low Reynolds numbers ( $R_n$ ), thus having values  $R_n < 2300$ .

The Reynolds number,  $R_n$ , for a fluid flow in a tube is generally expressed as

$$R_n = \frac{V\rho D}{\mu} \quad (2.2)$$

where  $V$  is the fluid velocity (m/s),  $\rho$  is the fluid density (kg/m<sup>3</sup>),  $D$  is the diameter (m) of the tube, and  $\mu$  is the dynamic viscosity (Pa.s). The fluid velocity is defined as  $V = Q/A$ , with flow rate  $Q$  in units of m<sup>3</sup>/s (or L/h), and the tube cross-section  $A = \pi(D/2)^2$ .



Oxygen (O <sub>2</sub> )			
	Tube 2.0 mm ID	Tube 3.0 mm ID	Rect. Tube (1.0 x 10.0 mm)
V (m/s)	6.05	1.37	1.9
R <sub>n</sub>	793.36	270.30	226.73
assuming $\rho = 1.331 \text{ kg/m}^3$ and $\mu = 0.0000203 \text{ Pa.s}$ for O <sub>2</sub> at 20°C			
Nitrogen (N <sub>2</sub> )			
	Tube 2.0 mm ID	Tube 3.0 mm ID	Rect. Tube (1.0 x 10.0 mm)
V (m/s)	6.05	1.37	1.9
R <sub>n</sub>	800.94	272.88	228.90
assuming $\rho = 1.165 \text{ kg/m}^3$ and $\mu = 0.0000176 \text{ Pa.s}$ for O <sub>2</sub> at 20°C			

Table 2.1 – Estimated Reynolds numbers (R<sub>n</sub>) for the flow of either of O<sub>2</sub> or N<sub>2</sub> in three types of gas-flow chambers used in this study

The estimated R<sub>n</sub> values for the three different gas-flow chambers and the fixed the gas-flow rate Q ~36 L/h, are indicated in Table 2.1.

As seen in Table 2.1, the calculated values of Reynolds numbers, R<sub>n</sub>, are low, being in the range of ~225 to ~800, thus well below R<sub>n</sub> ~2300, which is customarily considered as the threshold value from a laminar to transition (R<sub>n</sub> ~2300 – 4000) and turbulent (R<sub>n</sub> > 4000) types of flow. The low R<sub>n</sub> values in our experimental setups resulted from relatively low fluid velocities (in the range of ~1.4 to ~6.0 m/s for both O<sub>2</sub> and N<sub>2</sub>), as well as low cross-sectional areas of the gas-flow chambers.

Summarizing, in this work, all the experiments concerning exposure of MHPs to the flow of gaseous media were performed under laminar flow conditions, *i.e.* with R<sub>n</sub> < 2300.

### 2.5.2 Control of gas flow

In general, the standard gas-flow detecting instruments behave most reliably under laminar flow since a turbulent flow may affect the accuracy of measurements. Therefore, commercial gas-flow measuring devices are usually designed to condition the flow or are equipped with turbulence blocking filters. It is then worth mentioning that, in the present work, all the experiments concerning exposure of MHPs to the flow of gaseous media were performed under laminar flow conditions. Such flow conditions are characterized by low Reynolds numbers (R<sub>n</sub>), with the values of R<sub>n</sub> < 1000, thus well below R<sub>n</sub> ~2300, which is customarily considered as the threshold value from a laminar to transition (R<sub>n</sub> ~2300 – 4000) and turbulent (R<sub>n</sub> > 4000) types of flow. The low R<sub>n</sub> values, being in our experimental setup in the range of ~230 to ~800, were mostly due to relatively low fluid velocities (in the range of ~1.4 to ~6.0 m/s for both O<sub>2</sub> and N<sub>2</sub>), as well as low cross-sectional areas of the gas-flow chambers. More information concerning the characterization of the type of flow of gaseous media in custom-made gas-flow chambers used in this study can be found in Table 2.1.

Dry O<sub>2</sub> and N<sub>2</sub> with a flow rate of ~36 l/h were used in all experiments reported herein. The flow

rate was regulated and measured by a Swagelock Variable Area Flowmeter (VAF-G2-06M-1-0).

### 2.6 Electron spin resonance

Electron spin resonance (ESR) is a contactless spectroscopic technique developed in 1944 in Kazan (Russia) by Yevgeny Zavoisky [86]. From that time on, ESR finds its numerous applications in various research fields of biology, chemistry [87] and physics [88, 89, 90, 91, 92, 93]. Essentially, ESR detects the presence of unpaired electrons with ultra-high sensitivity, reaching as few as  $10^9 - 10^{10}$  unpaired spins in the investigated sample. In particular, ESR unambiguously detects free radicals [94], transition metals having odd number of electrons in partially filled **d**-shells, or excited states, *e.g.* triplet states. The fundamental physics of ESR is, in fact, identical to that of nuclear magnetic resonance (NMR), which is sensitive to the presence of magnetic moments related to atomic nuclei (like, *e.g.* protons). One important difference between NMR and ESR is that in ESR the resonant frequencies tend to be much higher, by virtue of the 659-times higher gyromagnetic ratio of an unpaired electron relative to a proton. For example, a typical frequency of electromagnetic radiation used in ESR spectroscopy is of  $\sim 9.8$  GHz (at the magnetic field strength of  $\sim 0.35$  T), thus roughly  $\sim 1000$  times higher than the corresponding NMR frequencies.

#### 2.6.1 Underlying principles of ESR

It is very well known that a magnetic moment,  $\vec{\mu}$ , placed in an external magnetic field,  $\vec{B}_0$  is described by a Zeeman hamiltonian [95, 96, 97]:

$$\hat{H}_{ext} = -\vec{\mu} \cdot \vec{B}_0 \quad (2.3)$$

For electrons in a solid, their magnetic moment,  $\vec{\mu}$ , is actually a sum of the orbital,  $\vec{L}$ , and the angular, otherwise known as spin,  $\vec{S}$ , momenta, hence:

$$\vec{\mu} = -\frac{\mu_B}{\hbar}(g_L\vec{L} + g_S\vec{S}) = -\frac{\mu_B}{\hbar}g_J\vec{J} \quad (2.4)$$

where  $\mu_B$  is the Bohr magneton,  $g_L = 1$  and  $g_S \approx 2.0023$  are the g-factors [98],  $g_J$  is the Lande factor and  $\vec{J} = \vec{L} + \vec{S}$  – the total angular momentum.

Thus, from Equations 2.3 and 2.4 one can compute the energy splitting of the degenerate energy levels of electrons in a solid under exposure to an external magnetic field,  $\vec{B}_0 = B_0\hat{z}$ . This energy splitting is called the Zeeman splitting and can be written as:

$$\Delta E = g_J\mu_B J_z B_0 \quad (2.5)$$

where  $J_z$  is the quantized projection of the total angular momentum on the z-axis and can

take values of:

$$J_z = -J, -J+1, \dots, J \quad (2.6)$$

Making use of Equations 2.3 and 2.4, the Ehrenfest theorem [99] and the gyromagnetic ratio,  $\gamma = \frac{\vec{\mu}}{\vec{J}}$ , the expectation value of  $\vec{J}$  can be calculated as follows:

$$\frac{d\langle \vec{J} \rangle}{dt} = \frac{i}{\hbar} \langle [\hat{H}_{ext}, \vec{J}] \rangle = \gamma \langle \vec{J} \rangle \times \vec{B}_0 \quad (2.7)$$

Equation 2.7 clearly shows that in conditions where a magnetic moment,  $\vec{J}$ , is placed in an external magnetic field,  $B_0$ , it would precess around the axis of the applied external field with a Larmor frequency:

$$\omega_L = \gamma B_0 \quad (2.8)$$

ESR spectroscopy takes advantage of the above-mentioned Zeeman splitting of the degenerate energy levels and probes them in a resonant fashion ( $\hbar\omega = \Delta E_z$ ) by applying microwave radiation on the sample.  $\vec{\mu}$  is rotating around the x-axis in a linearly polarized alternating magnetic field  $B_x$  and such oscillations would cause a continuous spin-flip in case no energy dissipation is occurring. The simplest model to describe such behavior with relaxation processes are the Bloch equations [100]:

$$\frac{dM_x}{dt} = \gamma[\vec{M} \times \vec{B}]_x - \frac{M_x}{T_2} \quad (2.9)$$

$$\frac{dM_y}{dt} = \gamma[\vec{M} \times \vec{B}]_y - \frac{M_y}{T_2} \quad (2.10)$$

$$\frac{dM_z}{dt} = \gamma[\vec{M} \times \vec{B}]_z + \frac{M_0 - M_z}{T_1} \quad (2.11)$$

where  $\vec{B}$  is the effective magnetic field,  $M_0$  – equilibrium magnetization through the z-axis,  $T_1$  – spin lattice or longitudinal relaxation time, describing the processes of energy transfer to the lattice and  $T_2$  – the spin-spin or transversal relaxation time, describing the loss of phase coherence of spins.

Solutions to Bloch equations 2.9 – 2.11 is the complex dynamic susceptibility,  $\chi$ :

$$\chi = \chi' - i\chi'' \quad (2.12)$$

In Equation 2.12,  $\chi'$  is the elastic or dispersive part of the relaxation process and  $\chi''$  is the inelastic or dissipative response of the system.  $\chi'$  and  $\chi''$  are related to each other *via* the Kramers-Kronig theorem [97].

### 2.6.2 Instrumentation

Among many scientific and technological advances that have been achieved during World War II one had to do with microwave technology. The progress in this field enabled the development of numerous techniques, such as of radar or microwave communication systems. The emergence of microwave generating sources has also greatly contributed to the development of several *high-frequency-based* spectroscopic techniques, including the continuous-wave (CW) ESR (in 1944) [86]. Implementation of the Fourier transform in the parent spectroscopic technique of NMR [101] (in 1965) [102] allowed transferring this approach also to the field of ESR and to develop the first pulsed [103] and high-field [104] ESR spectrometers in 1987 and 1996, respectively.

In this thesis, low-temperature CW ESR measurements in combination with in-situ sample illumination (photo-ESR) were performed to probe the charge transfer at the interface of  $\text{MAPbI}_3$  and  $\text{TiO}_2$ . These experiments were carried out with a Bruker ESR spectrometer E500 EleXsys Series (Bruker Biospin GmbH) equipped with a Gunn diode-based microwave bridge (model SuperX), a Bruker ER 4122 SHQE cavity and an Oxford Instruments Helium-gas continuous flow cryostat (ESR900).

The experimental setup for performing low-temperature photo-ESR measurements is shown in Figure 2.12(a) on the left. A conventional field modulation technique has been used for measurements in the dark with lock-in detection which resulted in the first derivative of the EPR absorption spectra.

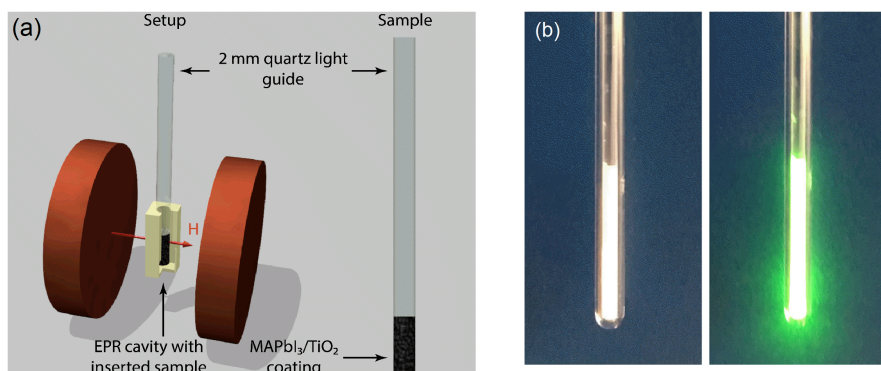


Figure 2.12 – (a) Schematic representation of the experimental setup used for the low-temperature Photo-EPR experiments (left) and the sample holder made of 2.0 mm diameter quartz rod, which served both as a sample holder and light guide (right). The thin film deposit of a sample under study was coated directly onto the outer surface of the sample holder at its bottom end protruding into the EPR resonator. b) Photographic images showing the concept of the light delivery to the studied samples: the sample holder coated at its bottom end with a thin film deposit of white- $\text{TiO}_2\text{NWs}$  (left) and the same sample holder under illumination with the green laser light,  $\lambda = 532 \text{ nm}$ ,  $P = 5.0 \text{ mW}$  (right). Both images were taken outside the EPR resonator.

The sample was coated onto a 2.0 mm diameter quartz rod, which served as both a sample

holder and light delivery guide. This is depicted schematically in Figure 2.12(a) on the right and an exemplary photo can be seen in Figure 2.12(b), where on the left the sample is not illuminated, whilst on the right it is illuminated by a green laser light,  $\lambda = 532$  nm, with power,  $P = 5.0$  mW.

## 2.7 3D printing

3D printing is a commonly used synonym of additive manufacturing – an umbrella term for manufacturing process where the material is added as opposed to machining where material is cut away. The impact of this technology is quite huge, opening ways to fabricate more complex shapes while making parts lighter due to the fact that only structurally necessary parts need to be produced as well improve the ecological footprint by spending less material and not disposing of the cut pieces.

The idea of a 3D printer is relatively simple – there are two main parts: the bed and the extruder. The bed is used to keep the part in place for next layers to be printed on top as well as to keep it at a certain temperature close to the glassy transition of the material to negate thermal expansion of each layer. Material, most commonly plastic filament is fed into the top of the extruder with its nozzle heated up sufficiently to fully melt the filament. A set of XYZ motors then move the bed and the extruder in such a way that a piece can be printed out in a layer-by-layer fashion. Upon extrusion in the current layer it solidifies and the next layer is printed on top. The resolution of such printing is determined by the accuracy of XYZ motors and the diameter of the nozzle.

To encode the above described actions of the 3D printer a software program has to be used to convert the CAD (.stl or .obj) file into compatible instruction code for the printer. Such program “slices” the 3D model into layers to be printed as well as can control various parameters. Among many of them, some examples are: filling factor, layer thickness, extrusion and bed temperatures, *etc.*

During my doctoral studies, I extensively used a Original Prusa i3 MK3 3D printer from PRUSA RESEARCH with a steel bed to fabricate certain elements, such as, *e.g.* gas inlets/outlet connectors and specialized microscope sample holders, which found their applications in several non-standard experiments oriented towards photo-physical characterization of MHPs under their exposure to various gaseous media.

Material utilized in the majority of cases was a silver PLA plastic filament with diameter of  $1.75 \pm 0.1$  mm in case of which all the extrusions were performed at 215 °C with the bed kept at 70 °C. Some of the smaller parts, which needed to be more flexible were printed with a Flexfill 98A filament with with diameter of  $1.75 \pm 0.1$  mm, nozzle extrusion temperature of 240 °C and bed at 50 °C.

3D CAD models have been designed with the help of Autodesk Inventor software and converted

into 3D printer code *via* PRUSA RESEARCH provided program Prusa Slic3r PE.

An overview of the full assemblies of the setups can be found in Figure 2.13. (a) and (c) are showing the renders of the microscope plates (grey) with the clips (ash) used to stabilize the gas inlets and outlets for cylindrical and flat-cell geometries of the gas-flow chambers. Note, however, that in Figure 2.13(c) there is also a 3D printed connector to the flat-cell accommodating either gas inlet and outlet stainless steel needles or a blank one depicted in cyan. Figures 2.13(b & d) show the corresponding parts as photographs after having been manufactured.

*Part-by-part* breakdown of the setups can be seen in Figures A.1 and A.4 followed by the respective detailed technical drawings of all the setup parts manufactured using the above-mentioned 3D printing technique in the Annex A. Specifically, the drawing of the slide and the holding clip for the connector/gas-flow chamber assembly can be seen in Figures A.2 and A.3, respectively. The microscope slide, clip, inlet/exhaust connector and blank connector can be seen in Figures A.5 – A.8, respectively.

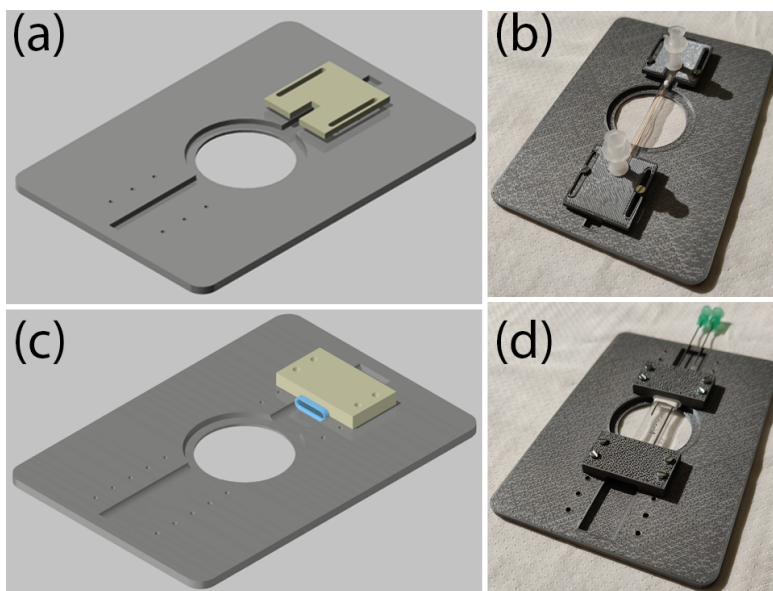


Figure 2.13 – 3D renders (left column) and photos of the full assemblies (right column) manufactured for the cylindrical (a & b) and flat-cell (c & d) geometry gas-flow chamber experiments. In (a & c), grey represents the microscope plate, ash – the clips used to affix the connectors with the gas-flow chamber to the plate and in (c), cyan represents the 3D-printed connector accommodating either gas inlet and outlet stainless steel needles or a blank one.

## 2.8 Experiment control software

The software to control the acquisition of the experimental data, namely the PL and PC responses has been written in Python. The script consisted of three main parts: a class library to interface with the measurement devices *via* PyVISA and two scripts to acquire, store and

plot the results. Full code can be found in Annex B.





# 3 Morphology and photoluminescence of thin film polycrystalline deposits of MAPbI<sub>3</sub> and MAPbBr<sub>3</sub> on non-planar, strongly curved substrates

## 3.1 Introduction

Recently, in the context of designing new generations of efficient cost-effective solar cells, significant effort has been devoted towards obtaining uniform and compact thin layers of both MAPbI<sub>3</sub> and MAPbBr<sub>3</sub>. In particular, there have been numerous reports on crystallinity and morphology, as well as PL properties of MAPbI<sub>3</sub> obtained either in the form of single-crystalline particles [105, 106] or polycrystalline films deposited on planar substrates [107, 108]. On the other hand a lot less information is available on the subject of thin film deposits of MAPbBr<sub>3</sub>. This, most likely, can be attributed to the fact that the bromide perovskite material has lower power conversion efficiency and therefore has gathered less interest from the solar cell oriented scientific community. Some of more recent studies of morphology, crystallinity and opto-electronic properties of MAPbBr<sub>3</sub> thin film deposits can be found at [38], while some of their applications like, *e.g.* high-performance LEDs prepared *via* precisely controlled film morphology, can be found in [42].

It has been generally accepted that due to the specific physicochemical properties of MAPbI<sub>3</sub>, the final photovoltaic characteristics of thin polycrystalline deposits of this material are strongly dependent on the coating process, which defines the crystallinity, grain sizes, uniformity and compactness of MAPbI<sub>3</sub> thin layers [109, 110]. Similarly, although being generally considered as more resilient to environmental factors than MAPbI<sub>3</sub>, the photovoltaic characteristics of MAPbBr<sub>3</sub>-based devices have also been found strongly dependent on the thin film fabrication process [111].

Various fabrication methods of MHP thin films have been reported to date [31, 32]. In general, the most commonly used deposition techniques can be categorized into the one-step precursor deposition methods [33] and two-step deposition methods [34, 38]. It is custom-

### Chapter 3. Morphology and photoluminescence of thin film polycrystalline deposits of MAPbI<sub>3</sub> and MAPbBr<sub>3</sub> on non-planar, strongly curved substrates

---

arily accepted that the two-step deposition provides better control of the composition, the thickness, and the morphology of the MAPbI<sub>3</sub>/Br<sub>3</sub>-based films, thus leading to higher photovoltaic performances of the final devices [35]. On the other hand, one-step solution-casting protocols seem to be more suitable for manufacturing low-cost MHPs-based devices at large scale [36, 42]. It has also been widely recognized that obtaining densely packed deposits of these perovskite materials with small grain sizes in the range from hundreds of nanometers to micrometers can be beneficial for numerous prospective optoelectronic applications, including photo-optical gas sensors [37].

Although monolithic layers of organometallic perovskites are mostly used in photovoltaic applications, coatings having other morphological characteristics are also being intensively explored. In particular, high power conversion efficiency (PCE) of a coating formed by low-dimensional (1D) MAPbI<sub>3</sub> nano- and microstructures have recently been reported by Im *et al.* [41]. Specifically, thin layers consisting of nanowires having 100 nm in diameter and several  $\mu\text{m}$  in length were obtained by two-steps spin-coating technology.

Two-step deposition route combining the solution process and vapor phase conversion was used for growing polycrystalline MAPbI<sub>3</sub> microwires with length up to 80  $\mu\text{m}$  that revealed both an excellent light-guiding performance with very low optical loss and bandgap tunability [39]. The one-step solution-based synthesis of highly-photoactive MAPbI<sub>3</sub> nanowires with mean diameter of 50 to 400 nm and lengths up to 10  $\mu\text{m}$  has also been reported by Horvath *et al.* [40].

In this context, this chapter covers fabrication and characterization of polycrystalline deposits of MAPbI<sub>3</sub> and MAPbBr<sub>3</sub> on non-planar, strongly curved substrates. In particular, using one-step solution-casting [112] on curved cylinder-shaped quartz substrates with diameters in the range from 80 to 1800  $\mu\text{m}$  we manufactured MAPbI<sub>3</sub> deposits consisting of polycrystalline microwires with average sizes of 100 nm to 8  $\mu\text{m}$  in width and up to  $\sim 150 \mu\text{m}$  in length [113] and MAPbBr<sub>3</sub> deposits consisting of microcubes with characteristic edge lengths in the range from 1  $\mu\text{m}$  up to  $\sim 100 \mu\text{m}$ .

Optical microscopy and scanning electron microscopy (SEM) imaging of the obtained deposits revealed a pronounced dependence of their morphology on the substrate curvature. Notably, a markedly enhanced surface grain packing, concomitant with smaller average microcrystallite sizes, was observed while coating MHPs on cylinder-shaped quartz substrates with the smallest diameters (*i.e.* of 80  $\mu\text{m}$  and 330  $\mu\text{m}$ ). Interestingly, however, micro-crystalline deposits of both MAPbI<sub>3</sub> and MAPbBr<sub>3</sub> conserved roughly the same thickness of 12 – 15  $\mu\text{m}$  throughout the whole range of variability of the substrate diameters.

## 3.2 Results and discussion

### 3.2.1 Morphology of MAPbI<sub>3</sub> deposits

Optical microscopy and scanning electron microscopy were used as essential analytical tools for characterization of morphology and crystallinity of MAPbI<sub>3</sub> deposits on cylinder-shaped quartz substrates. For more detailed technical information see Chapter 2.

A thin polycrystalline film of MAPbI<sub>3</sub> deposited on a planar substrate served as a reference sample in this study. This sample was prepared by solution casting of the stoichiometric stock solution (50 wt%) of MAPbI<sub>3</sub> precursors in DMF onto a flat surface of a glass microscope slide. The doctor-blading technique was used for casting as described in Chapter 2. An example microscopic image of such deposit is shown in Figure 3.1(a). When excited by the green light at 546 nm wavelength, this deposit of MAPbI<sub>3</sub> emits characteristic infra-red luminescence. This can be seen in Figure 3.1(b) together with a typical steady-state PL spectrum collected simultaneously with the luminescent imaging and peaking at ~770 nm (inset).

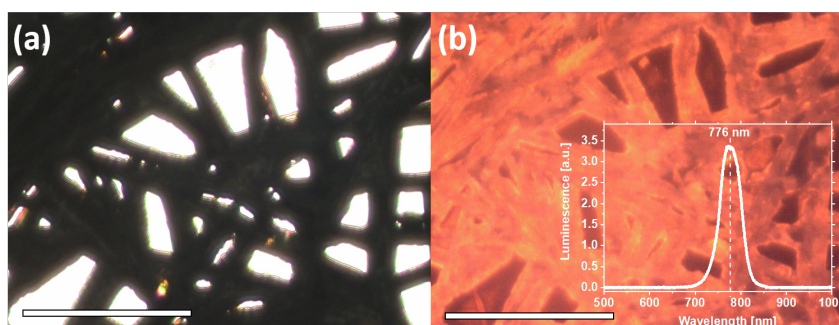


Figure 3.1 – Optical microscopy images of MAPbI<sub>3</sub> deposits obtained *via* one-step solution casting on a flat surface (glass microscope slide): (a) under illumination with visible light and (b) the corresponding luminescence image under the excitation with  $\lambda_{exc} = 546$  nm. Inset to (b): the steady-state PL spectrum collected simultaneously with the luminescent imaging. The scale bars are set to 50  $\mu$ m.

Combined, the two microscopic images in Figure 3.1 prove that, when a single-step solution casting is applied, well pronounced microwire-like crystallites of MAPbI<sub>3</sub> are formed on planar substrates. As can also be seen in Figure 3.1(a & b), the crystallite packing is not very dense – large voids can be observed on the deposit in between the microwires of MAPbI<sub>3</sub>.

Combined, the two images of Figure 3.1 show that on planar substrates we observe well pronounced fiber-like crystallites of MAPbI<sub>3</sub>. Yet the packing of these wire-like crystallites is not very dense – large voids can be observed on the deposit in-between the micro-wires of the perovskite.

Example optical microscopy images of MAPbI<sub>3</sub> deposits coated onto the curved surfaces are shown in Figure 3.2 – for two cylinder-shaped substrates with diameters of 330  $\mu$ m and 1800  $\mu$ m. As can be seen in this figure, morphology of the polycrystalline deposit on a 330  $\mu$ m

### Chapter 3. Morphology and photoluminescence of thin film polycrystalline deposits of MAPbI<sub>3</sub> and MAPbBr<sub>3</sub> on non-planar, strongly curved substrates

diameter substrate is distinctively different from the one deposited on a 1800  $\mu\text{m}$  diameter substrate. Moreover, both these deposits coated onto the curved surfaces are also very different from the MAPbI<sub>3</sub> deposit on planar substrate shown in Figure 3.1. In particular, the MAPbI<sub>3</sub> deposit on a 330  $\mu\text{m}$  diameter substrate consists of densely packed micrometer-sized wires, having average lengths of  $\sim 20$  to  $30\ \mu\text{m}$  and cross-sectional diameters (widths) of  $\sim 1.0\ \mu\text{m}$ . In contrast, the thin film of MAPbI<sub>3</sub>, deposited on a substrate with 1800  $\mu\text{m}$  diameter, consists of definitely larger, elongated and branched fibrous structures, having average lengths of  $\sim 50$  to  $70\ \mu\text{m}$  and cross-sectional dimensions of  $\sim 5$  to  $8\ \mu\text{m}$ .

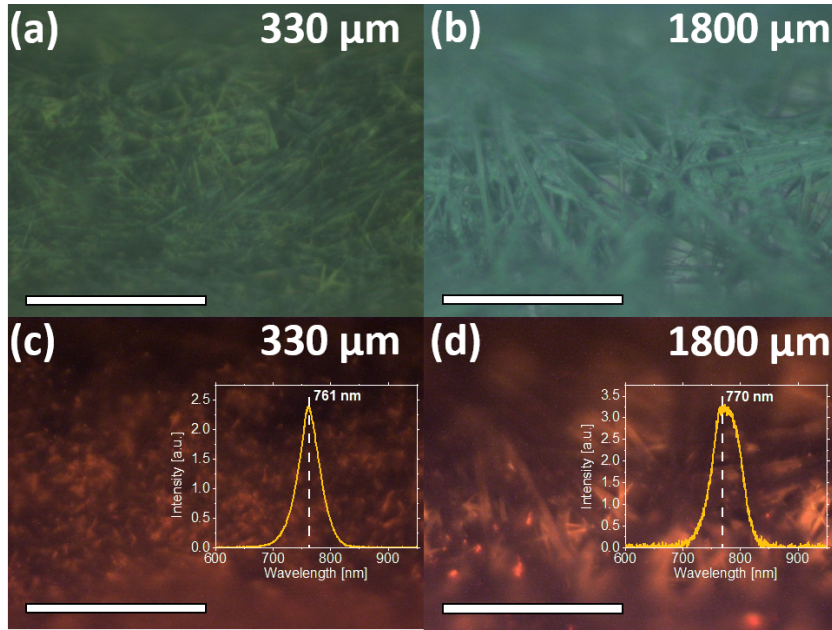


Figure 3.2 – Comparison of the optical microscopy images of MAPbI<sub>3</sub> deposits on cylinder-shaped quartz substrates having diameters of 330  $\mu\text{m}$  and 1800  $\mu\text{m}$ . The bright-field microscopic images acquired under the visible light illumination for the cylinder-shaped substrates with diameters of 330  $\mu\text{m}$  (a) and 1800  $\mu\text{m}$  (b). The corresponding luminescence images collected under the excitation with  $\lambda_{exc} = 546\ \text{nm}$  for the MAPbI<sub>3</sub> films deposited on the substrates with diameters 330  $\mu\text{m}$  (c) and 1800  $\mu\text{m}$  (d). Insets to (c) and (d): the steady-state PL spectra acquired simultaneously with luminescent imaging. In all images the scale bars are set to 50  $\mu\text{m}$ .

Luminescence microscopy images, acquired under the excitation of  $\lambda_{exc} = 546\ \text{nm}$  and shown in Figure 3.2(c & d), also point to the fact that MAPbI<sub>3</sub> deposits coated onto the substrates with 330  $\mu\text{m}$  and 1800  $\mu\text{m}$  diameters have markedly different morphologies. In particular, the strongly emitting bright spots correspond to the emission occurring essentially from the terminations of micrometer-sized wires, which are mostly longitudinally aligned on the surface of the 330  $\mu\text{m}$  DIA substrate (Figure 3.2(c)). In contrast, for the 1800  $\mu\text{m}$  DIA substrate (Figure 3.2(d)), the PL emission can also be seen from the numerous branch-crossing points, which facilitate the light emission from the otherwise elongated light-channeling structures [39].

It should be noted that the CCD camera used in our experimental setup for luminescence imaging was only able to detect the short-wavelength tail of the infra-red emission of MAPbI<sub>3</sub> emission. In contrast, the simultaneously acquired PL spectra provided the whole spectral information and can be seen in insets to Figures 3.2 (c & d).

In particular, the PL spectra shown in the insets to Figures 3.2(c & d), collected for samples deposited on cylinder-shaped substrates with diameters 330  $\mu\text{m}$  and 1800  $\mu\text{m}$  and peaking around  $\sim 760 - 770$  nm, are characteristic for polycrystalline thin films of MAPbI<sub>3</sub> [114]. The peak position at 770 nm of the PL spectrum acquired for the deposit coated onto the 1800  $\mu\text{m}$  substrate is slightly red-shifted as reference to the peak position at 761 nm collected for the deposit coated onto the 330  $\mu\text{m}$  substrate. Similarly red-shifted PL spectra have been often reported for larger sizes of MAPbI<sub>3</sub> crystallites [115, 116] and associated with enhanced self-absorption in the larger crystals [117].

The PL emission peaks shown in the insets to Figures 3.2(c & d) are also spectrally broadened and both reveal a shoulder at longer wavelength. Such broadening of the PL spectra and the presence of a long wavelength shoulder in PL emission peaks can be ascribed to the presence of the disordered crystalline phases and shallow trapping levels on the grain boundaries [118, 119].

Similar PL spectra were observed in this study for all MAPbI<sub>3</sub> deposits on cylinder-shaped substrates. An example steady-state PL spectrum collected for the micro-crystalline deposit of MAPbI<sub>3</sub> on a cylindrically shaped rod with 80  $\mu\text{m}$  diameter under excitation with  $\lambda_{exc} = 546$  nm is shown in Figure 3.3. The luminescence spectrum shown in Figure 3.3, peaking at

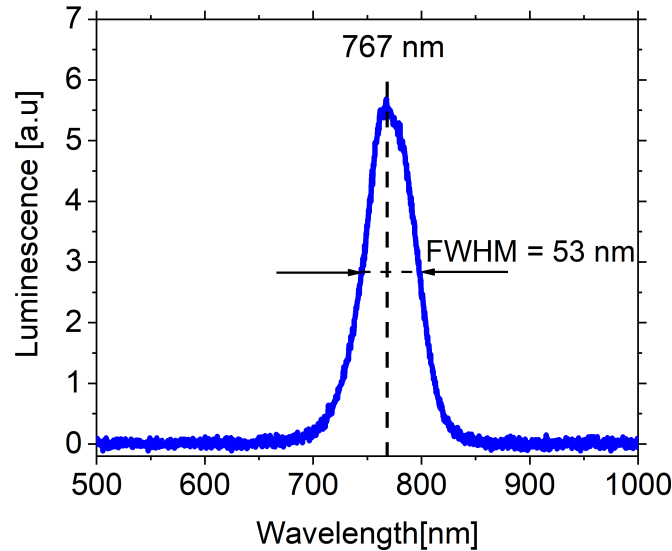


Figure 3.3 – An example of a typical PL spectrum acquired for MAPbI<sub>3</sub> coated *via* one step-solution casting onto cylinder-shaped substrates. This PL spectrum was collected under excitation at  $\lambda_{exc} = 546$  nm for the deposit of MAPbI<sub>3</sub> on a quartz rod having a diameter of 80  $\mu\text{m}$ .

### Chapter 3. Morphology and photoluminescence of thin film polycrystalline deposits of MAPbI<sub>3</sub> and MAPbBr<sub>3</sub> on non-planar, strongly curved substrates

770 nm, corresponds well to the PL spectra that are usually reported for micro-crystalline deposits of the tetragonal phase of MAPbI<sub>3</sub> at room temperature [114]. Thus, although the crystallite widths and lengths markedly decreased for substrates with higher curvatures, the PL spectral peak positions and the spectral shapes did not significantly evolve for deposits on substrates with different diameters.

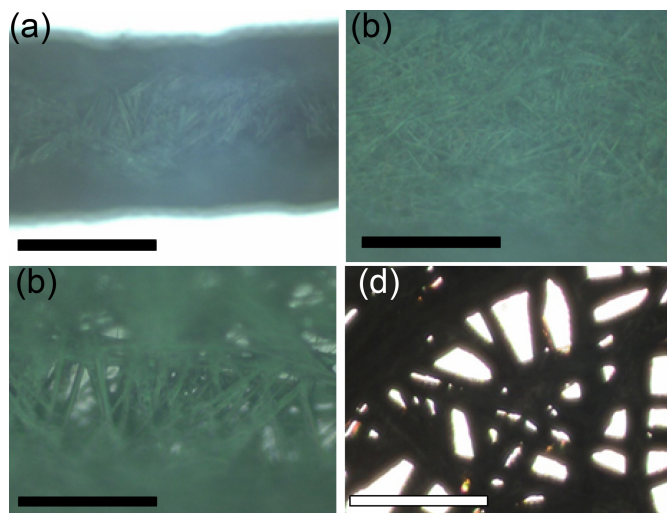


Figure 3.4 – Optical microscopy images of MAPbI<sub>3</sub> deposits coated *via* one-step solution casting onto three cylindrical substrates having different diameters of 80 μm (a), 330 μm (b), and 1800 μm (c) as well as on the flat surface of a microscope slide (d). The scale bars are set to 50 μm.

After gaining the first insight into the changes in morphology of MAPbI<sub>3</sub> deposits on the substrates with different curvatures (visible light and luminescence microscopy images in Figures 3.1 and 3.2), a direct comparison of morphological variability of thin film deposits of MAPbI<sub>3</sub> coated onto cylinder-shaped quartz substrates with various diameters is shown in Figure 3.4. The conventional SEM images shown in Figure 3.6 were collected for the entire range of the substrate diameters (*i.e.* 80 μm, 330 μm, 400 μm, 700 μm, 1100 μm, and 1800 μm).

As can be seen, the SEM images revealed a marked dependence of the crystallinity and morphology of the thus obtained MAPbI<sub>3</sub> deposits on the substrate diameter. In particular, for quartz rods with smallest diameters (80 μm – 330 μm), the MAPbI<sub>3</sub> thin films consisted of densely packed micrometer wires, whereas for the substrates with larger diameters (400 μm – 1800 μm) MAPbI<sub>3</sub> formed less densely packed polycrystalline branched and interconnected micrometer-sized ribbons structures, which contained also a large number of voids. Interestingly, however, the micro-crystalline MAPbI<sub>3</sub> films deposited on cylinder-shaped quartz substrates conserved roughly the same thickness of 12 – 15 μm throughout the whole range of variability of the substrate diameters.

Thus, in addition to elongated crystallites, which represent the major morphological feature of MAPbI<sub>3</sub> deposits in this study, we also observe other forms of polycrystalline MAPbI<sub>3</sub>,



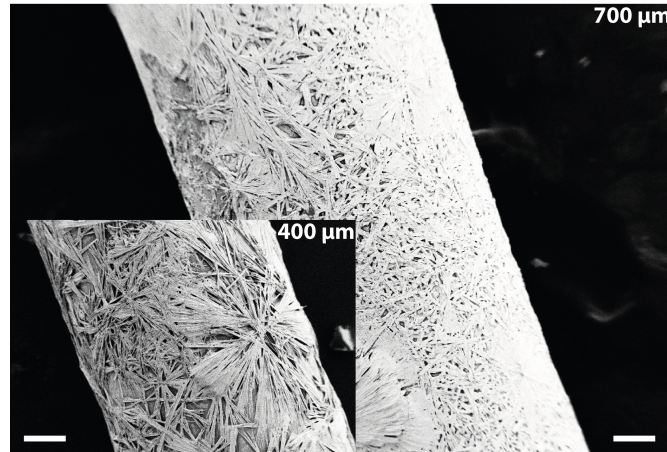


Figure 3.5 – SEM image of the MAPbI<sub>3</sub> deposits on two cylinder-shaped quartz rods having 700 μm diameter (main image) and 400 μm diameter (inset). The scale bars correspond to 100 μm in both images.

including small spheres, star-like, leaf-like or dandelion type structures. In particular, star-like structures systematically occur for MAPbI<sub>3</sub> deposits coated onto substrates with larger diameters (lower substrate curvatures). For example, such branched structures can be seen in Figure 3.5 for MAPbI<sub>3</sub> deposits on cylinder-shaped quartz rods having diameters of 400 μm and 700 μm.

In fact, the star-like structures present on cylindrical substrates with larger diameters are similar to these reported by Nie *et al.* for hot-casting of thin films of MAPbI<sub>3</sub> on flat substrates [116] or by Xu *et al.* for MAPbI<sub>3</sub> thin films deposited onto a flat glass substrate (ITO) covered with a compact layer of TiO<sub>2</sub> [120]. Moreover, the optical microscopy image in Figure 3.1(a) also shows the presence of branched and interconnected ribbons of MAPbI<sub>3</sub> deposited onto a flat glass surface, while employing the one step solution coating and analogous annealing conditions as used for coating the cylindrical substrates. It has to be stressed that the “voids”, which occur for practically all the deposits presented in Figure 3.6, are not really free of MAPbI<sub>3</sub>. As suggested by Xu *et al.*, the space in between the branched and interconnected micrometer-sized ribbons is also partially filled with smaller, more disordered “spherulitic” crystalline structures of MAPbI<sub>3</sub> [120].

Apart from the visual analysis, a thorough survey of the sizes, *i.e.* widths and lengths of the crystallites, was performed based on the above described SEM images. For this purpose, to gain a statistically significant result, a selection of several samples of MAPbI<sub>3</sub> deposits was investigated.

In principle, the crystallite dimensions, *i.e.* their lengths and widths, can be described using a Gaussian distribution:

$$f(x) = \frac{1}{\sqrt{2\pi}\sigma} e^{-\frac{(x-\mu)^2}{2\sigma^2}}, \quad (3.1)$$

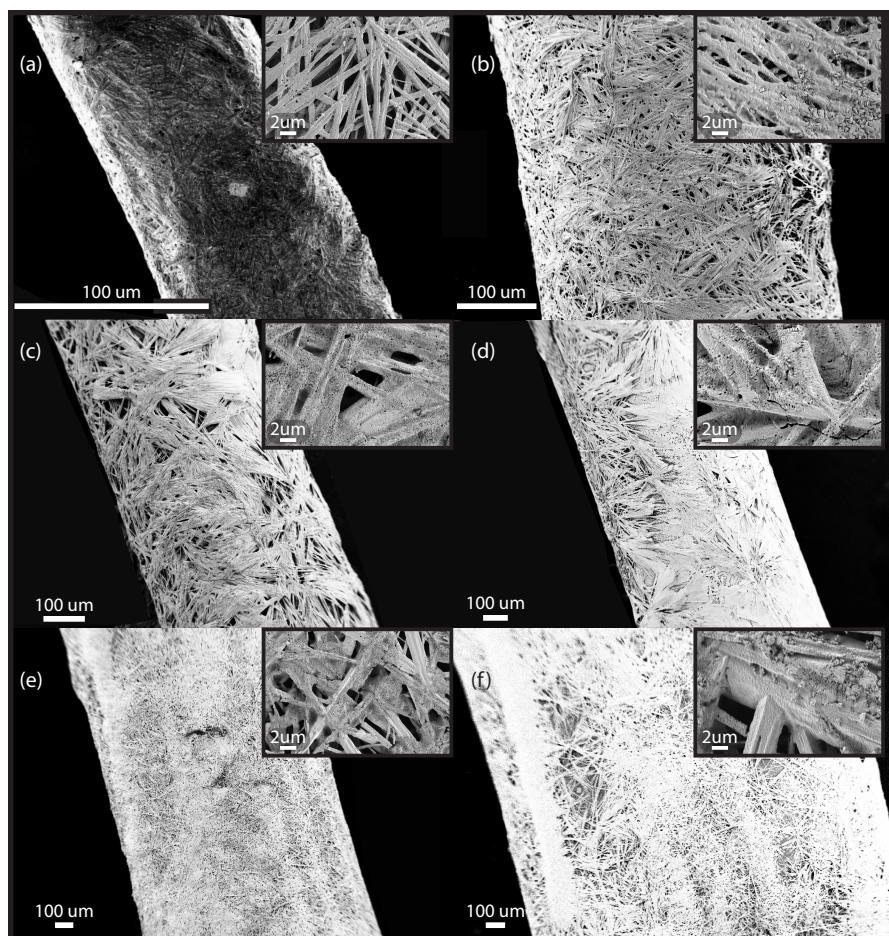


Figure 3.6 – SEM images of microcrystalline MAPbI<sub>3</sub> deposits on cylinder-shaped quartz substrates with varying diameters: (a) 80  $\mu\text{m}$ , (b) 330  $\mu\text{m}$ , (c) 400  $\mu\text{m}$ , (d) 700  $\mu\text{m}$ , (e) 1100  $\mu\text{m}$  and (f) 1800  $\mu\text{m}$ . The insets show the magnified image of the deposits on the rods of the same as the main figure.

where  $\mu$  is the mean or expected value,  $\sigma$  is the standard deviation and  $\sigma^2$  – the variance. These results are presented in a histogram form with Gaussians fitted on top for substrates of each diameter in Figure 3.7 and 3.8.

Overall, the SEM images presented in Figure 3.6 revealed a strong relationship between the morphology of MAPbI<sub>3</sub> deposits and the substrate curvature. In particular, for the cylinder-shaped quartz substrates with diameters within the range from 80 to 1800  $\mu\text{m}$ , the average sizes of polycrystalline microwires evolved from 100 nm to 8  $\mu\text{m}$  (width) and 5  $\mu\text{m}$  to 150  $\mu\text{m}$  (length).



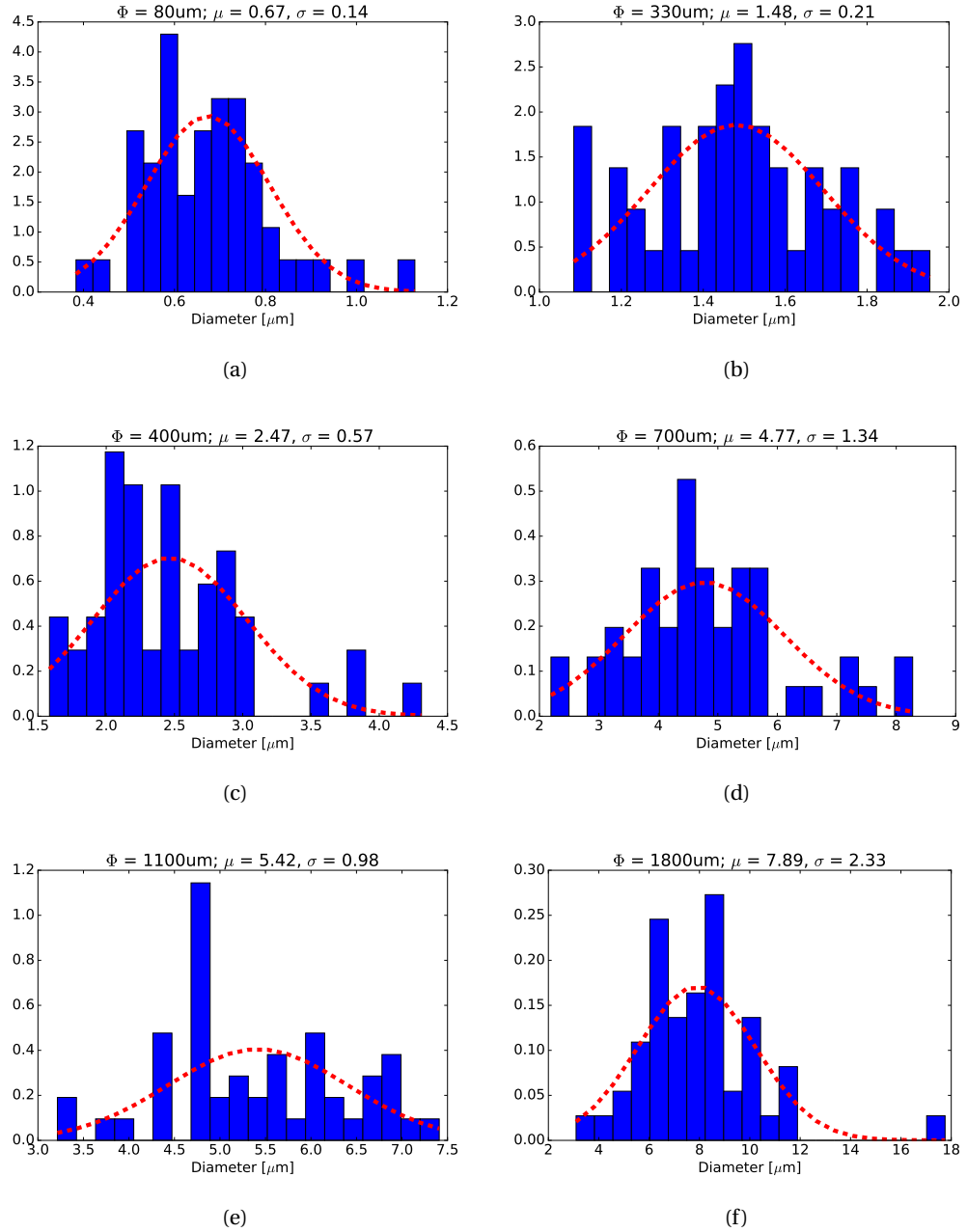


Figure 3.7 – The histograms of distributions of the crystallite widths of MAPbI<sub>3</sub> microwires in the deposits manufactured *via* one-step solution casting on cylinder-shaped quartz substrates with the following diameters: 80  $\mu\text{m}$  (a), 330  $\mu\text{m}$  (b), 400  $\mu\text{m}$  (c), 700  $\mu\text{m}$  (d), 1100  $\mu\text{m}$  and 1800  $\mu\text{m}$ .

### Chapter 3. Morphology and photoluminescence of thin film polycrystalline deposits of MAPbI<sub>3</sub> and MAPbBr<sub>3</sub> on non-planar, strongly curved substrates

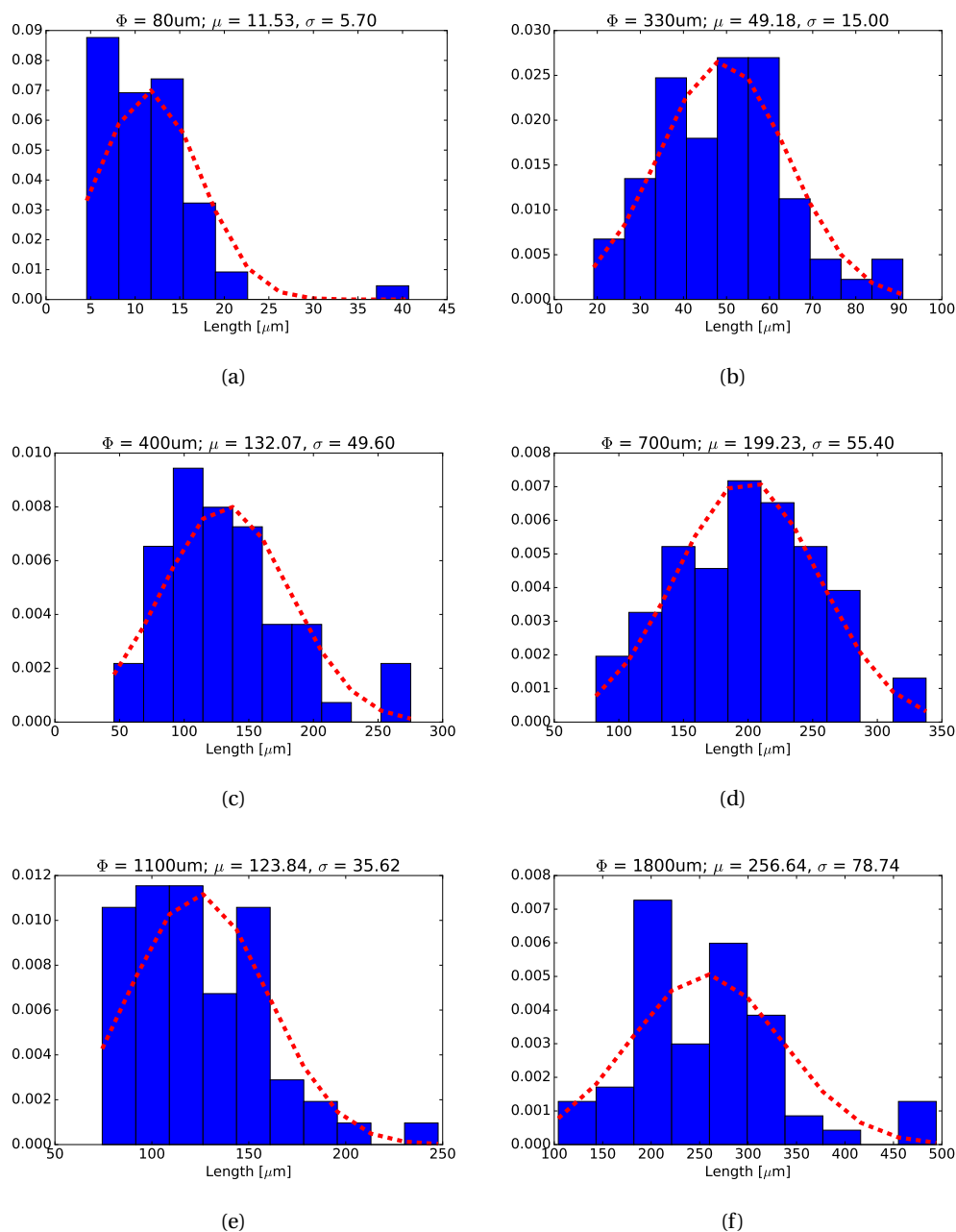


Figure 3.8 – The histograms of distributions of the crystallite lengths of MAPbI<sub>3</sub> microwires in the deposits manufactured *via* one-step solution casting on cylinder-shaped quartz substrates with the following diameters: 80  $\mu\text{m}$  (a), 330  $\mu\text{m}$  (b), 400  $\mu\text{m}$  (c), 700  $\mu\text{m}$  (d), 1100  $\mu\text{m}$  and 1800  $\mu\text{m}$ .

### 3.2.2 Morphology of MAPbBr<sub>3</sub> deposits

The same approach as described above for characterization of thin films of MAPbI<sub>3</sub> was also used to gather insight into the properties of polycrystalline thin film deposits of MAPbBr<sub>3</sub>. Optical imaging, PL measurements and SEM were used as three major techniques to study morphology and crystallinity of these coatings.

Thus, similarly as in the case of MAPbI<sub>3</sub>, a reference sample was prepared by coating MAPbBr<sub>3</sub> onto a flat surface. Optical images in visible light and a fluorescence microscopy image under 470 nm wavelength excitation can be seen in Figure 3.9(a & b) respectively. The inset to Figure 3.9(b) shows a typical PL spectrum obtained for the polycrystalline deposit of MAPbBr<sub>3</sub> on a planar substrate.

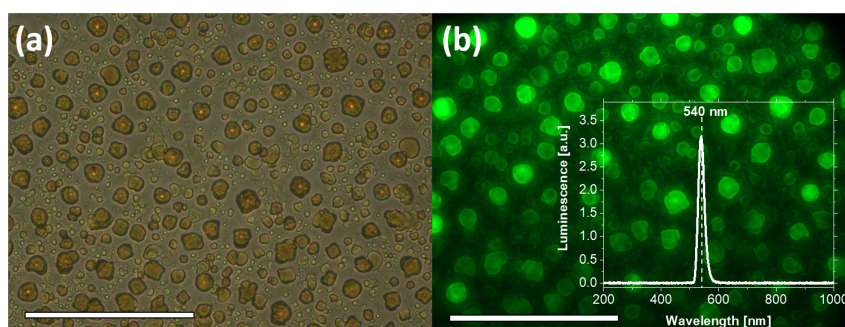


Figure 3.9 – Optical microscopy images of MAPbBr<sub>3</sub> deposits coated *via* one-step solution casting onto a planar substrate (glass microscope slide): (a) under illumination with visible light and (b) the corresponding luminescence image under the excitation with  $\lambda_{exc} = 470$  nm. Inset to (b): the steady-state PL spectrum collected simultaneously with the luminescent imaging. The scale bars are set to 50  $\mu$ m.

These images show that on flat surfaces, on average, there is no clearly defined shape of the crystallites and their size is on the order of 5  $\mu$ m. Even though the geometry of the microcrystallites is not well defined, they are markedly different from the ones observed for MAPbI<sub>3</sub> deposits on flat substrates, *i.e.* they form rather cuboidal or hexagonal prism microcrystals as compared to microwires of MAPbI<sub>3</sub> shown in Figure 3.1. Moreover, the coverage is also rather poor, with large voids in between the crystallites. Figure 3.10 shows a typical PL spectrum collected for the polycrystalline deposit of MAPbI<sub>3</sub> on a planar substrate under excitation at 470 nm. It can be seen that this deposit emits a characteristic green luminescence peaking at  $\sim 540$  nm.

It can be seen that morphology of the polycrystalline deposit on a cylindrical substrate with 330  $\mu$ m diameter is distinctively different from the one coated onto a substrate with 1100  $\mu$ m diameter (Figure 3.11(a & b)). Moreover, morphologies of these both deposits markedly differ from morphology of the deposit coated onto a planar surface (shown in Figure 3.9). Similar differences in morphology of MAPbI<sub>3</sub> deposits coated onto cylinder-shaped substrates and flat surfaces have been described in the preceding section.

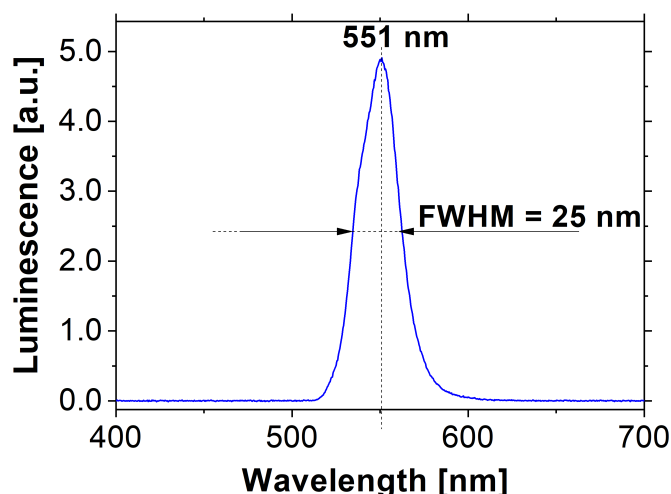


Figure 3.10 – An example of a typical PL spectrum acquired for polycrystalline thin films of MAPbBr<sub>3</sub> coated *via* one step-solution casting onto cylinder-shaped substrates. This PL spectrum was collected under excitation at  $\lambda_{exc} = 470$  nm for the deposit of MAPbBr<sub>3</sub> on a quartz rod with 80  $\mu\text{m}$  diameter.

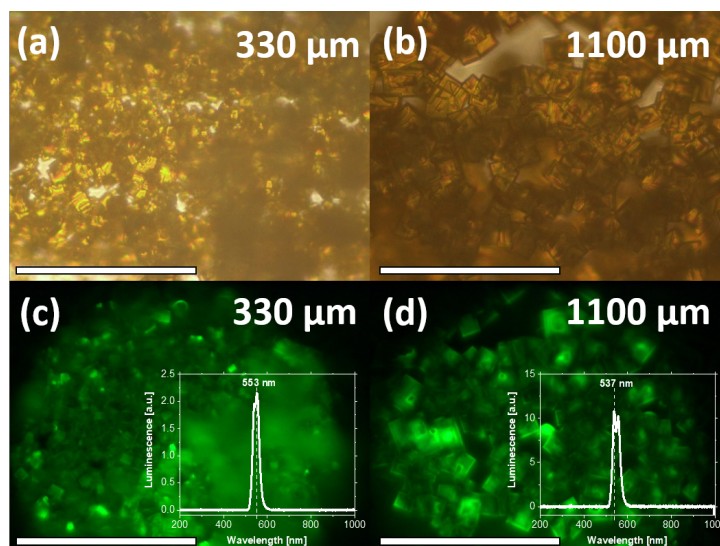


Figure 3.11 – Comparison of the optical microscopy images of MAPbBr<sub>3</sub> deposits on cylinder-shaped quartz substrates having diameters of 330  $\mu\text{m}$  and 1100  $\mu\text{m}$ . The bright-field microscopic images acquired under the visible light illumination for the cylinder-shaped substrates with diameters of 330  $\mu\text{m}$  (a) and 1100  $\mu\text{m}$  (b). The corresponding luminescence images collected under the excitation with  $\lambda_{exc} = 470$  nm for the MAPbI<sub>3</sub> films deposited on the substrates with diameters 330  $\mu\text{m}$  (c) and 1100  $\mu\text{m}$  (d). Insets to (c) and (d): the steady-state PL spectra acquired simultaneously with luminescent imaging. In all images the scale bars are set to 50  $\mu\text{m}$ .

One of the biggest morphological differences between the polycrystalline deposits of MAPbBr<sub>3</sub> and MAPbI<sub>3</sub> is that for practically all thin layers of MAPbBr<sub>3</sub> coated onto planar and curved

substrates, the overall crystallite geometry is much better defined, since the great majority of micro-crystallites are formed as micro-sized cubes. In particular, the MAPbBr<sub>3</sub> deposit on the 330  $\mu\text{m}$  DIA substrate consists of densely packed micrometer-sized cubes or microcubes, having average side length of  $\sim 5.0 \mu\text{m}$ . In contrast, the thin film of MAPbBr<sub>3</sub> deposited on the 1100  $\mu\text{m}$  DIA substrate consists of definitely larger microcubes having average side length of  $\sim 100.0 \mu\text{m}$ . Luminescence microscopy images, acquired under the excitation of  $\lambda_{exc} = 470 \text{ nm}$  and shown in Figure 3.11(c & d), also point to the formation of MAPbBr<sub>3</sub> deposit having markedly different morphologies for 330  $\mu\text{m}$  and 1100  $\mu\text{m}$  DIA substrates.

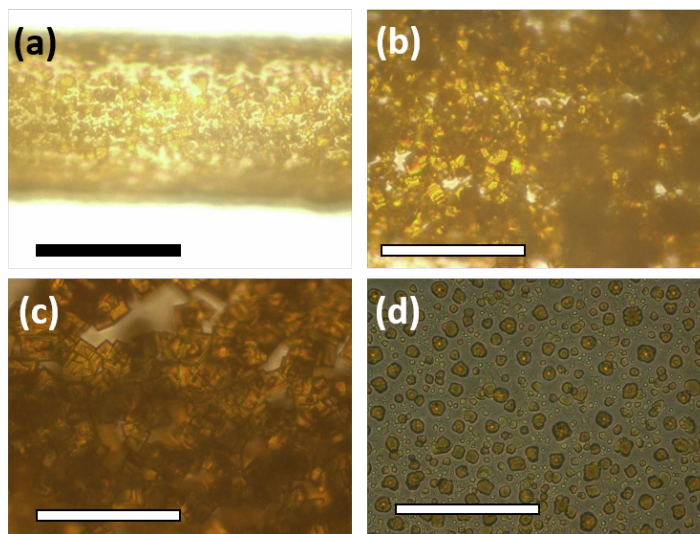


Figure 3.12 – Optical microscopy images of MAPbBr<sub>3</sub> deposits coated *via* one-step solution casting onto three cylindrical substrates having different diameters of 80  $\mu\text{m}$  (a), 330  $\mu\text{m}$  (b), and 1100  $\mu\text{m}$  (c) as well as on the flat surface of a microscope slide (d). The scale bars are set to 50  $\mu\text{m}$ .

Following the same experimental approach as for MAPbI<sub>3</sub> deposits, *i.e.* by analyzing the optical microscopy images shown in Figures 3.9 – 3.12, we gained the initial insight into the morphological variability of MAPbBr<sub>3</sub> deposits on substrates with different curvatures.

However, a more direct comparison of the morphological variability of thin film deposits of MAPbBr<sub>3</sub> on substrates with different curvatures was provided by SEM imaging. In particular, the conventional SEM images collected for the entire range of the substrate diameter (*i.e.* 80  $\mu\text{m}$ , 330  $\mu\text{m}$ , 400  $\mu\text{m}$ , 700  $\mu\text{m}$  and 1100  $\mu\text{m}$ ) are shown in Figure 3.13. As can be seen, the SEM images revealed a marked dependence of the crystallinity and morphology of the thus obtained MAPbBr<sub>3</sub> deposits on the substrate diameter. One can also see that with increasing substrate diameters, the average sizes of MAPbBr<sub>3</sub> micro-cubes markedly increased.

Specifically, for quartz rods with the smallest diameter (of 80  $\mu\text{m}$ ), the MAPbBr<sub>3</sub> thin films consisted of densely packed micrometer cubes, whereas for the substrates with larger diameters (330  $\mu\text{m}$  – 1100  $\mu\text{m}$ ) MAPbBr<sub>3</sub> formed markedly less densely packed polycrystalline micrometer-sized cubes deposits, which contained also a large number of voids.



### Chapter 3. Morphology and photoluminescence of thin film polycrystalline deposits of $\text{MAPbI}_3$ and $\text{MAPbBr}_3$ on non-planar, strongly curved substrates

The average edge lengths of the microcubes of  $\text{MAPbBr}_3$  have been obtained by the same method described in the previous section – by measuring a selection of micro-crystallites, building histograms based on the collected measurements and fitting a Gaussian distribution, according to Equation 3.1 to obtain the mean values. These histograms for  $\text{MAPbBr}_3$  deposits on substrates of all diameters can be found in Figure 3.14.

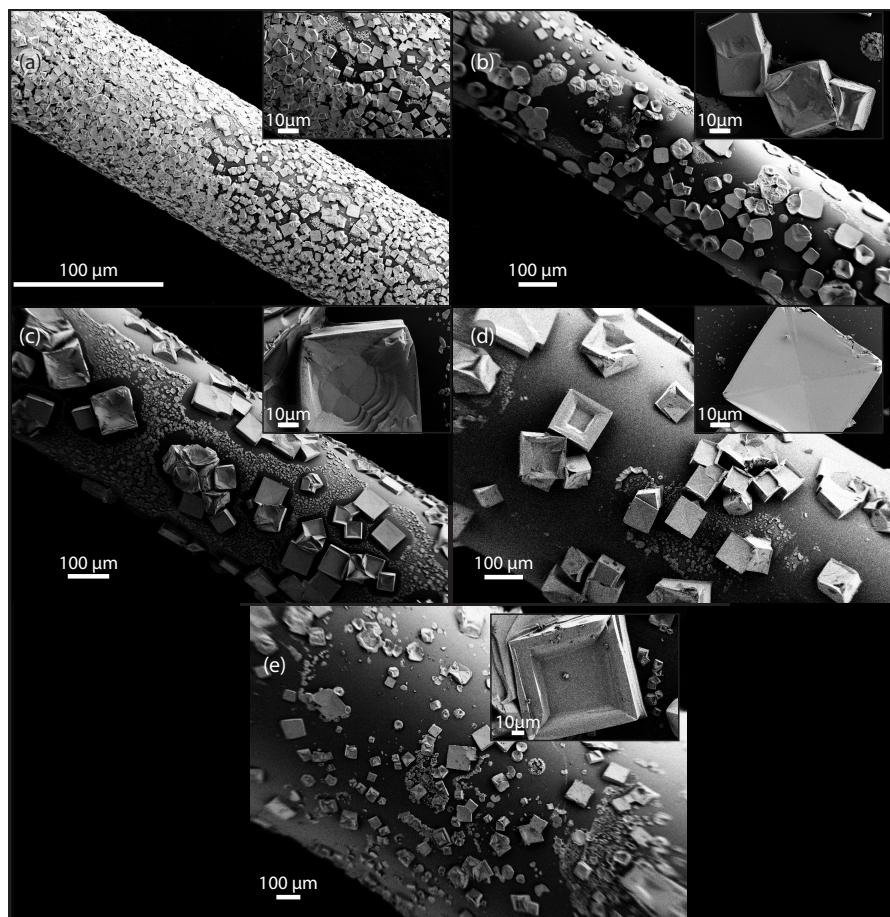


Figure 3.13 – SEM images of microcrystalline  $\text{MAPbBr}_3$  deposits on cylinder-shaped quartz substrates with varying diameters: (a)  $80\ \mu\text{m}$ , (b)  $330\ \mu\text{m}$ , (c)  $400\ \mu\text{m}$ , (d)  $700\ \mu\text{m}$  and (e)  $1100\ \mu\text{m}$ . The insets show the magnified image of the deposits on the same size rods as the main figure.

Even though the average side length of a  $\text{MAPbBr}_3$  microcube increased from  $1\ \mu\text{m}$  hundredfold, the micro-crystalline  $\text{MAPbBr}_3$  deposited on cylinder-shaped quartz substrates conserved roughly the same thickness of  $12 - 15\ \mu\text{m}$  throughout the whole range of variability of the substrate diameters.

In addition to the main micro-cube crystallites, which represent the major morphological feature of  $\text{MAPbBr}_3$  deposits in this study, we also observe other forms of polycrystalline  $\text{MAPbBr}_3$ , similar to the crystallites observed on the flat surface. These plate-like deposits can be seen in the voids between the larger micro-cubic crystallites in Figures 3.13(b – e). They

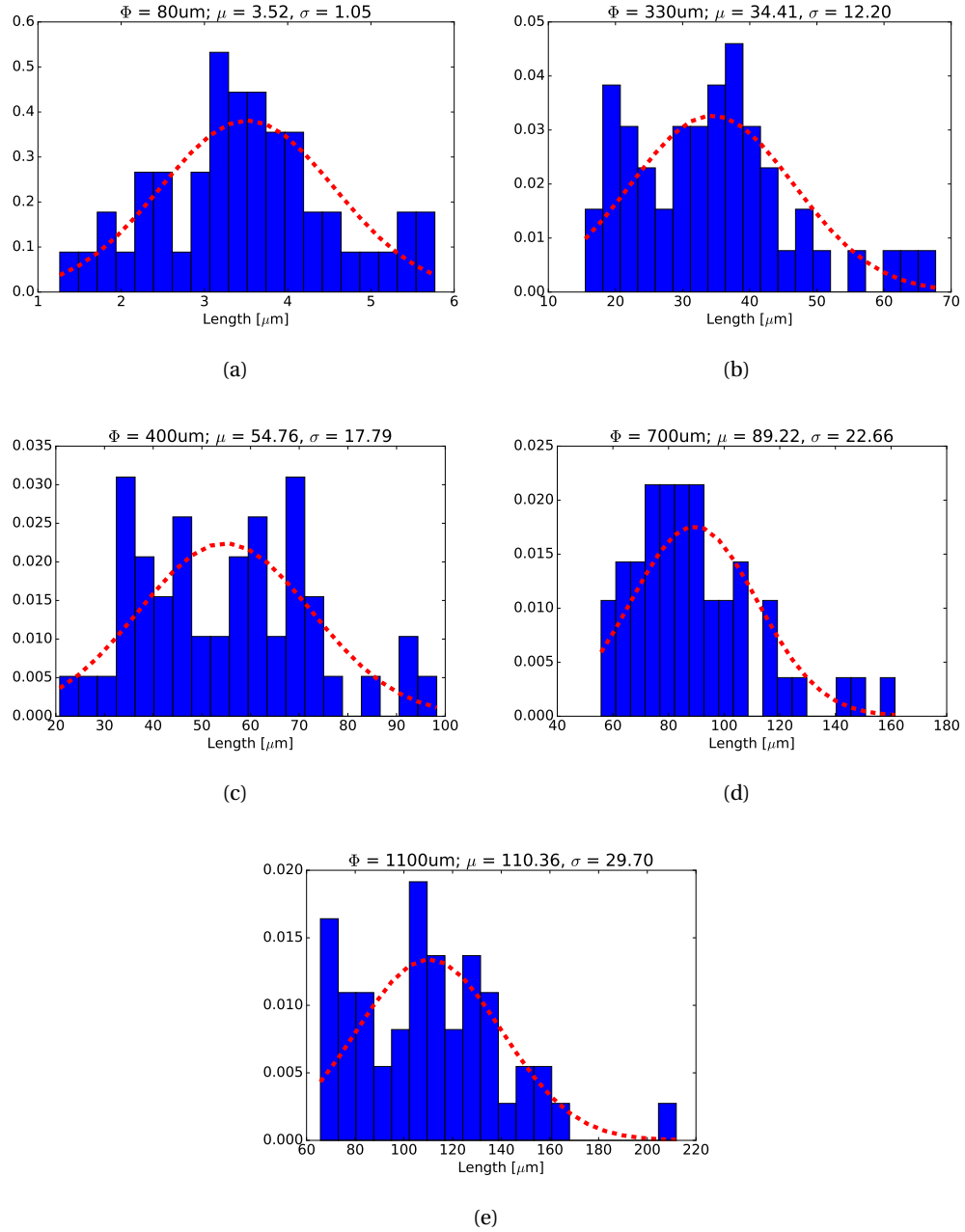


Figure 3.14 – The histograms of distributions of the crystallite lengths of MAPbBr<sub>3</sub> microcubes in the deposits manufactured *via* one-step solution casting on cylinder-shaped quartz substrates with the following diameters: 80  $\mu\text{m}$  (a), 330  $\mu\text{m}$  (b), 400  $\mu\text{m}$  (c), 700  $\mu\text{m}$  (d) and 1100  $\mu\text{m}$ .

seem to have a much smaller thickness than the micro-cubes as well as seem not to have a very well defined geometrical shape.

Photoluminescence spectra of MAPbBr<sub>3</sub> deposits, the same as with MAPbI<sub>3</sub> ones, have not

### Chapter 3. Morphology and photoluminescence of thin film polycrystalline deposits of MAPbI<sub>3</sub> and MAPbBr<sub>3</sub> on non-planar, strongly curved substrates

evolved and stayed very similar to the typical spectrum of MAPbBr<sub>3</sub> throughout the whole set of substrates.

Overall, we can conclude that for polycrystalline deposits of MAPbBr<sub>3</sub> there is a significant dependence of their morphology on the substrate curvature. Interestingly, the decrease in the packing density of crystallites is much more pronounced for the deposits of MAPbBr<sub>3</sub>. In particular, one can show that the deposits of MAPbI<sub>3</sub> on substrates with relatively high diameters (*e.g.* 400  $\mu\text{m}$ ) have definitely less voids and are packed more densely than the deposits of MAPbBr<sub>3</sub> on substrates having even smaller diameters (*e.g.* 330  $\mu\text{m}$ ).

#### 3.2.3 Mechanisms behind the morphological changes in crystallinity of MHPs

Mechanisms behind the morphological changes in crystallinity of MHPs deposits as a function of the substrate curvature are complex and may involve quite a number of contributions, such as variability of the heat capacities and substrate surface roughness of quartz rods, surface wetting properties [121], substrate curvature dependent evaporation rates of the solvent (DMF) as well as the local changes in the air flow during annealing of the deposits.

It is generally accepted that the morphology of solution-processed perovskite films is governed by nucleation and crystal growth processes. In particular, the substrate surface roughness and the distribution of the surface defects can markedly influence the nucleation processes. To determine the potential variability of the surface roughness, we used two high-resolution imaging techniques, *i.e.* SEM and atomic force microscopy (AFM). The SEM images acquired for the uncoated cylindrical quartz substrates of different diameters revealed statistically similar densities of surface defects. As can be seen in the SEM images in Figure 3.15 (a – e), the surface of the substrates is smooth and void of major contaminations.

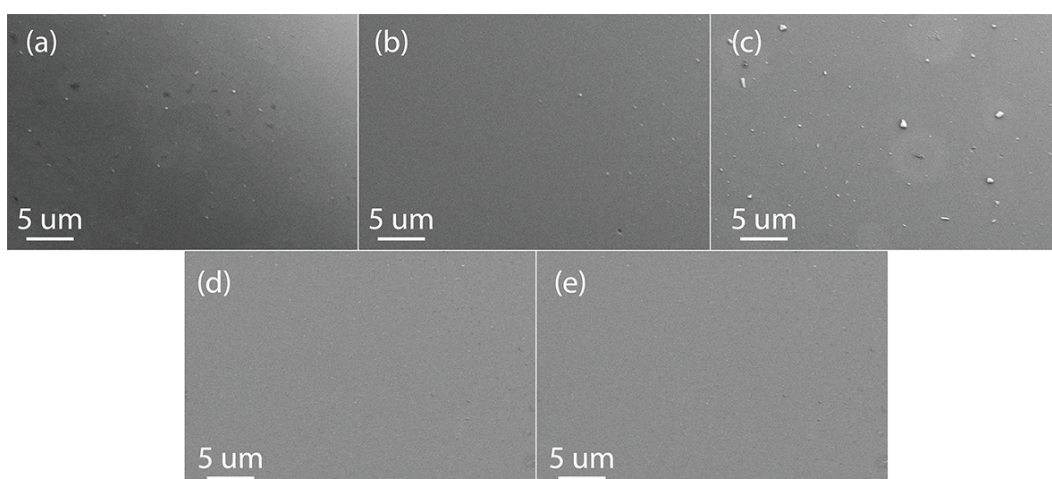


Figure 3.15 – SEM images of clean (uncoated) quartz cylindrical substrates of different diameters: (a) 80  $\mu\text{m}$ , (b) 330  $\mu\text{m}$ , (c) 400  $\mu\text{m}$ , (d) 700  $\mu\text{m}$ , (e) 1100  $\mu\text{m}$ .



Concomitantly, the AFM measurements pointed to a rather low and similar surface roughness ( $<1.0$  nm) for all the quartz substrates. To gather additional information concerning the variability of the surface roughness, we performed the AFM visualization of the surface topography and acquired the 2D roughness profiles for the quartz cylindrical substrates having different diameters. Thus, the AFM topography images and 2D roughness profiles shown in Figure 3.16 revealed that the cylindrical quartz substrates used in this study had a similar surface roughness. It has then been inferred that the variability of the surface roughness could not sufficiently influence the nucleation and subsequent crystallization process of MHPs deposits.

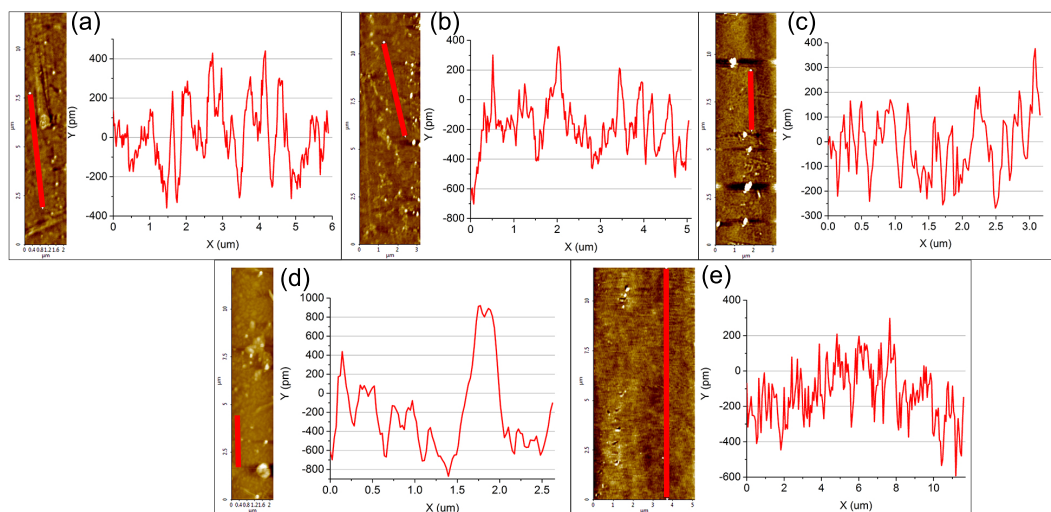


Figure 3.16 – AFM topography images and the 2D roughness profiles of the surface of uncoated quartz cylindrical substrates of different diameters: (a)  $80\ \mu\text{m}$ , (b)  $330\ \mu\text{m}$ , (c)  $400\ \mu\text{m}$ , (d)  $700\ \mu\text{m}$ , (e)  $1100\ \mu\text{m}$ . The red lines in the AFM topography images correspond to the acquired 2D roughness profiles.

Since in our experimental setup the cylindrical substrates are not in direct contact with the heat source during the annealing process (Figure 2.1), we also investigated the influence of the variability of substrate heat capacities on the crystallization of MHPs deposits. A rough estimate of the difference in the heat capacities for the substrate diameter range used in this study ( $80 - 1800\ \mu\text{m}$ ) yields a relatively large factor of 500. Therefore, to gain further insight into the contribution of the variability of substrate heat capacities, the annealing process at  $110^\circ\text{C}$  was performed for both non-preheated and preheated substrates. To this end, two cylindrical quartz rods with diameters of  $80\ \mu\text{m}$  and  $400\ \mu\text{m}$  were simultaneously wetted with the same volumes ( $\sim 2.5\ \mu\text{L}$ ) of the stoichiometric solution of  $\text{MAPbI}_3$  precursors in DMF either outside of the hot plate (non-preheated substrates) or when the rods were already positioned on the hot plate (preheated substrates). The example results of annealing of the  $\text{MAPbI}_3$  deposits with using these two different scenarios can be viewed as frame sequences in Figures 3.17 and 3.18, for non-preheated and preheated substrates, respectively.

These frame sequences reveal that for both scenarios of annealing the crystallization pro-

### Chapter 3. Morphology and photoluminescence of thin film polycrystalline deposits of MAPbI<sub>3</sub> and MAPbBr<sub>3</sub> on non-planar, strongly curved substrates



Figure 3.17 – Frame sequence showing the annealing process of MAPbI<sub>3</sub> on non-preheated substrates with diameters of 400  $\mu\text{m}$  (left) and 80  $\mu\text{m}$  (right). This sequence shows the marked differences in crystallization processes on the surfaces of substrates with 400  $\mu\text{m}$  and 80  $\mu\text{m}$  diameter, which occur much faster for the substrates with smaller diameter.

cess was definitely much faster for thinner substrates. In particular, for the non-preheated substrates, the estimated times of MAPbI<sub>3</sub> crystallization were of 1 sec 120 msec and 12 sec 520 msec, for quartz rods diameters of 80  $\mu\text{m}$  and 400  $\mu\text{m}$ , respectively, whereas for the preheated substrates the corresponding time lapses were of 880 ms and 5 sec. Thus the corresponding crystallization time ratios were of  $\sim 12$  and  $\sim 5$ , for the non-preheated and preheated substrates, respectively. Interestingly, a rough calculation of the difference in the heat capacities for the two quartz substrates with diameters of 80  $\mu\text{m}$  and 400  $\mu\text{m}$  suggests a factor of  $\sim 25$ .

It should also be noted that in our experimental setup for annealing the coated quartz rods are positioned at a small distance ( $\sim 3.0$  mm) from the hot plate (Figure 2.1). Therefore, concomitantly with a rather large diameter of the hot plate itself ( $\sim 25.0$  cm), the herein used annealing setup provided comparable air-flow conditions for the quartz cylindrical substrates

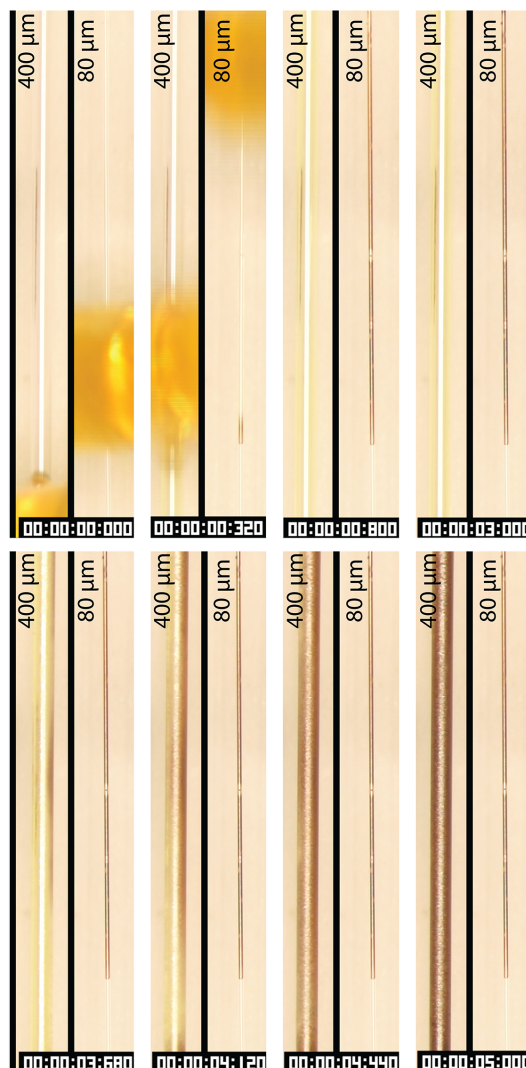


Figure 3.18 – Frame sequence showing the annealing process of MAPbI<sub>3</sub> on preheated substrates with diameters of 400  $\mu\text{m}$  (left) and 80  $\mu\text{m}$  (right). This sequence shows the marked differences in crystallization processes on the surfaces of substrates with 400  $\mu\text{m}$  and 80  $\mu\text{m}$  diameter, which occur much faster for the substrates with smaller diameter.

having different diameters.

We additionally checked the influence of the increasing substrate curvature on the solvent evaporation rate during the thermal annealing of the solution-processed MAPbI<sub>3</sub> deposits. The actual influence of the substrate curvature on liquid evaporation rates had been investigated theoretically by William Thomson (also known as Lord Kelvin), who derived the relevant formulas. In principle, the most general form of the Kelvin law (Equation 3.2) is dependent only upon thermodynamic principles and does involve specific properties of materials. It describes the change in vapor pressure due to a curved liquid-vapor interface, such as, *e.g.* the

### Chapter 3. Morphology and photoluminescence of thin film polycrystalline deposits of MAPbI<sub>3</sub> and MAPbBr<sub>3</sub> on non-planar, strongly curved substrates

---

surface of a droplet:

$$\frac{RT}{M} \ln \left( \frac{P}{P_0} \right) = \pm 2 \frac{\sigma}{d} \left( \frac{1}{r} - \frac{1}{r_0} \right), \quad (3.2)$$

where  $R$  is the gas constant;  $T$  is the absolute temperature;  $M$  – the molecular weight;  $\sigma$  – the surface energy;  $d$  – the density of the liquid;  $P$  – the escaping tendency of the substance from a curved surface with radius  $r$ ; and  $P_0$  – the escaping tendency from a surface with radius  $r_0$ , where  $r_0$  may be infinitely large, namely, in a flat surface. Thus as suggested by the Kelvin equation (Equation 3.2), under the same experimental conditions for the thermal annealing, the actual evaporation rate of the solvent from strongly curved convex substrates (like, *e.g.* quartz rods with very small diameters) should be higher than from substrates with smaller curvatures [122, 123]. In fact, similar phenomena to these observed herein have been reported for numerous systems where the curved geometry of the substrates influenced the solvent evaporation rate at both micro- and macro-scales [124, 125].

To further analyze the size variability of polycrystalline MAPbI<sub>3</sub> microwires on substrates with different radii ( $r$ ), while based solely on the Kelvin's law, the following assumptions can be made:

1. As evidenced by Equation 3.2, the solvent evaporation rate is proportional to  $\sim \exp(1/r)$ ;
2. The nucleation rate of MAPbI<sub>3</sub> crystallites should correlate with the solvent evaporation rate.

These assumptions suggest that the average sizes of the formed microwires should also correlate, at least partially, with the substrate radii. Therefore, one should expect crystallites with smaller sizes for the cylindrical substrates with the decreasing substrate radii (*i.e.* the increasing substrate curvatures,  $1/2r$ ). Thus, the average sizes of MAPbI<sub>3</sub> microwires should correlate with  $\sim \exp(-1/r)$ . Based on these assumptions, the estimated vapor pressure change, while varying the substrate diameters in the range of 80 to 1800 micrometers, is of the order of  $\sim 2.5\%$ .

The experimentally measured dependencies of average characteristic sizes (widths and lengths) of MAPbI<sub>3</sub> microwires and MAPbBr<sub>3</sub> micro-cube side lengths on the substrate curvature are plotted in Figure 3.19. The corresponding histograms of the crystallite size distributions for each substrate diameter can be found in the Figures 3.7, 3.7 and 3.14. Thus, the exponential decays shown in Figure 3.19 point to a strong correlation of the characteristic crystallite sizes of MAPbI<sub>3</sub> microwires and MAPbBr<sub>3</sub> micro-cubes with the substrate curvature.

Overall, these findings have implications for the field of solution-processed deposition of micro-crystalline organometallic perovskites, because they demonstrate that casting and crystallization processes conducted under the same reaction conditions, with the same re-

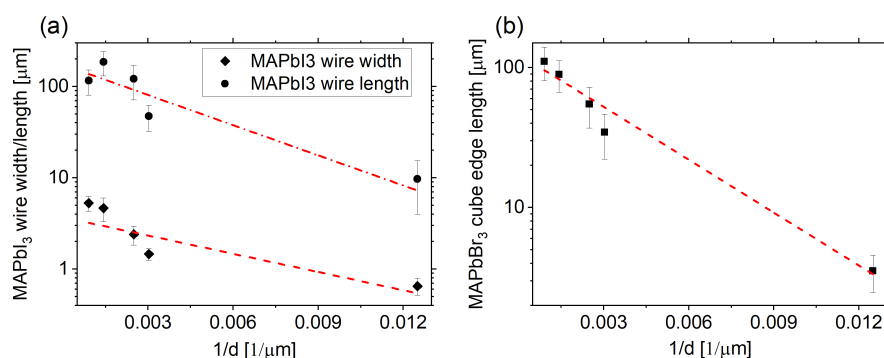


Figure 3.19 – The average characteristic sizes of (a) MAPbI<sub>3</sub> microwires, black diamonds and dots for widths and lengths, respectively and (b) MAPbBr<sub>3</sub> micro-cube side lengths as black squares, plotted as a function of the substrate curvature ( $1/d$ ). The solid line corresponds to the fit with an exponential function.

action time do not produce equivalent deposits; rather, they are dependent on the substrate geometry.

### 3.3 Conclusion

In brief, this part of the presented PhD work demonstrates, for the first time, the marked influence of the substrate curvature on the crystallinity and morphology of microcrystalline deposits of MAPbI<sub>3</sub> and MAPbBr<sub>3</sub> prepared *via* one-step solution casting.

In particular, MAPbI<sub>3</sub> layers deposited on cylinder-shaped quartz substrates with small diameters (80 μm and 330 μm) proved to be densely-packed and consisted of micrometer-sized, needle-shaped wires (1 μm thick and 20 μm long). In contrast, for the larger-diameter substrates (from 400 μm to 1800 μm), the variability in the texture of the polycrystalline layers of MAPbI<sub>3</sub> with respect to the substrate curvature was substantially less pronounced.

Similar dependencies were observed for MAPbBr<sub>3</sub> deposits. The thin polycrystalline films of MAPbBr<sub>3</sub> coated onto cylinder-shaped quartz substrates with smallest diameters (80 μm) proved to be densely-packed and consisted of micrometer-sized cubes with characteristic side length of ~1 μm. Deposits coated onto the larger-diameter substrates proved to have voids as well as increasing crystallite sizes up to ~100 μm (especially for the substrate diameter of 1100 μm and larger). The thickness variability of polycrystalline layers of MAPbBr<sub>3</sub> with respect to the substrate curvature was substantially less pronounced than in the case of MAPbI<sub>3</sub> counterparts.

The herein observed size reduction of micro-crystallites concomitant with denser coverage of organometallic perovskite deposits coated onto quartz cylindrical substrates with diminishing diameters was attributed to both the diminishing substrate heat capacities and, albeit to a lesser extent, the enhanced evaporation rates of the solvent for the substrates with increasing

### **Chapter 3. Morphology and photoluminescence of thin film polycrystalline deposits of MAPbI<sub>3</sub> and MAPbBr<sub>3</sub> on non-planar, strongly curved substrates**

---

curvatures.

This portion of the research was thoroughly discussed in K. Mantulnikovs *et al.*, *ACS Photonics* 2018, 5, 4, 1476 – 1485 [113].

## 4 Impact of gaseous media on photoluminescence and photocurrent of polycrystalline MAPbI<sub>3</sub> and MAPbBr<sub>3</sub>.

Originally, the research reported in this thesis started from the study of morphology and crystallinity of thin films of MAPbI<sub>3</sub> deposited on cylinder-shaped substrates in the form of quartz rods. As reported in Chapter 3, densely packed deposits consisting of micrometer-sized crystallites, concomitant with large *surface-to-volume* ratios, were obtained when MAPbI<sub>3</sub> was coated onto the substrates with the smallest diameters, *i.e.* of 80  $\mu\text{m}$  and 330  $\mu\text{m}$ . The elongated cylinder-shaped geometry of the thus prepared deposits encouraged us to combine them with simple tubular, light-transparent gas-flow chambers. This, in turn, opened an easy route to monitor the PL and PC responses of MAPbI<sub>3</sub> to the impact of various gaseous media with using our experimental setup based on an epi-fluorescence microscope.

Since densely packed polycrystalline deposits were also obtained when the second archetypal MHP, MAPbBr<sub>3</sub>, was coated onto the cylindrical substrates with the smallest diameters (of 80  $\mu\text{m}$  and 300  $\mu\text{m}$ ), the study of interaction with gaseous media was enlarged to encompass this perovskite as well. Thus, in a similar way as for coatings of MAPbI<sub>3</sub>, the PL and PC responses could be acquired for polycrystalline deposits of MAPbBr<sub>3</sub> exposed to a precisely controlled recurrent flow of either O<sub>2</sub> or N<sub>2</sub>.

The subsequent combination of two archetypal MHPs, MAPbI<sub>3</sub>, and MAPbBr<sub>3</sub>, positioned *side-by-side* in the same gas-flow chamber and simultaneously exposed to identical atmospheric conditions, enabled us to demonstrate, for the first time, their strongly differential PL and PC responses to exposure to O<sub>2</sub> and N<sub>2</sub>.

Overall, this part of the thesis points to the fact that implementation of an elongated cylinder-shaped geometry of densely-packed micro-crystalline deposits of the two MHPs, MAPbI<sub>3</sub> and MAPbBr<sub>3</sub>, concomitant with their strongly differential PL and PC responses to the environmental gaseous media, such as O<sub>2</sub> and N<sub>2</sub>, offers a novel route towards designing simple and low-cost photo-electronic devices, including differential gas sensors.

## **4.1 Introduction**

It has been widely accepted that, independent of the preparation method of thin polycrystalline deposits of MHPs, their structural, photo-physical and long-term stability properties strongly depend on the exposure to most important environmental gaseous media, such as oxygen (O<sub>2</sub>) and nitrogen (N<sub>2</sub>) [126, 127, 109, 110]. In particular, Burschka *et al.* found that MAPbI<sub>3</sub>-based devices should be fabricated under the controlled atmospheric conditions with the relative humidity below 1% [56]. It has also been concluded that exposure to O<sub>2</sub> and light can be considered as a major source of instability in these materials and that, in general, MAPbBr<sub>3</sub> has a better stability in air than MAPbI<sub>3</sub> [128, 129]. Moreover, it has also been reported that O<sub>2</sub> can strongly and partially reversibly modulate the photo-physical properties of both MHPs [130, 131]. Recently, reversible and very rapid (<400 ms) responses of the photocurrent (PC) to even minute changes of O<sub>2</sub> concentrations (~70 ppm) have been reported by M.-A. Stoeckel *et al.* for nano-structured polycrystalline films of MAPbI<sub>3</sub> [132].

Fang *et al.* found that MAPbBr<sub>3</sub> single crystals were ultrasensitive to their environment and their PL efficiency markedly increased in O<sub>2</sub> [133]. It has been suggested, based on implementing a deeply penetrating two-photon excitation (800 nm), that the most efficient trap states, which interact with the environmental gases and modulate the PL, are localized near the MAPbBr<sub>3</sub> crystal surface.

However, notwithstanding the constantly growing evidence of the impact of the gaseous atmosphere on both the long-term stability and photo-physical properties of MHPs, the actual mechanisms underlying their interactions with environmental gaseous media, including O<sub>2</sub> and N<sub>2</sub>, still remain the subject of debate.

In this context, here, we report on the pronounced differences in PL and PC responses of polycrystalline deposits of two archetypical MHPs, MAPbI<sub>3</sub> and MAPbBr<sub>3</sub>, coated onto strongly curved substrates, to the impact of the recurring exposures to two gaseous media, *i.e.* O<sub>2</sub> and N<sub>2</sub>.

To manufacture polycrystalline deposits of MHPs, we employed a simple approach of single-step solution-casting [134, 33, 112], which has recently been modified in our laboratory to allow for coating polycrystalline films of MAPbI<sub>3</sub> directly onto cylindrical substrates having high curvatures [113]. Briefly, we performed single-step solution coating of MAPbI<sub>3</sub> and MAPbBr<sub>3</sub> onto cylinder-shaped quartz substrates (rods) with diameters in the range of 80  $\mu\text{m}$  to 1100  $\mu\text{m}$ . In particular, densely packed polycrystalline films with high *surface-to-volume* ratio, consisting of microwires for MAPbI<sub>3</sub> and microcubes for MAPbBr<sub>3</sub>, were obtained for the smallest substrate diameters, *i.e.* of 80  $\mu\text{m}$  and 330  $\mu\text{m}$ .

We took advantage of the longitudinal geometry, dense packing and uniform morphology of the MHPs deposits coated onto these quartz rods (80  $\mu\text{m}$  and 330  $\mu\text{m}$  in diameter) to design simple, optically-transparent devices, which enabled us to monitor the variations of PL and PC of MAPbI<sub>3</sub> and MAPbBr<sub>3</sub> in response to the intermittent exposures to either O<sub>2</sub> or N<sub>2</sub>. To



this end, the MHPs-coated quartz rods were encapsulated either in short sections of slightly larger quartz capillary tubes [113] or in miniature flat rectangle glass capillaries. The latter arrangement enabled us to position the quartz substrates coated with MAPbI<sub>3</sub> and MAPbBr<sub>3</sub> *side-by-side* very close one to each other, thus providing an easy way to simultaneously monitor the PL responses from the two different MHPs under exposure to exactly the same environmental conditions.

The herein reported markedly opposite trends in the simultaneously acquired PL and PC responses of polycrystalline deposits of MAPbI<sub>3</sub> and MAPbBr<sub>3</sub>, under exposure to two important environmental gaseous media, O<sub>2</sub> and N<sub>2</sub>, point to the possibility of applying our approach in sensitive differential gas sensing. In fact, the advantages of differential sensing have already been demonstrated for both industrially-used photo-optical or resistive gas- and pressure-sensing devices, as well as for emerging nano- and micro-sensing systems based on specific and differential responses of optical and electronic properties of novel materials, such as carbon nanotubes [135] or inorganic quantum dots [136, 137].

Taken together, our approach based on simultaneous exposure of two archetypal MHPs, MAPbI<sub>3</sub> and MAPbBr<sub>3</sub>, coated onto cylinder-shaped substrates with high curvatures, to O<sub>2</sub> and N<sub>2</sub>, can serve as a model for developing uncomplicated differential MHPs-based gas sensors.

## 4.2 Results and discussion

### 4.2.1 Influence of the gas flow on photoluminescence of polycrystalline deposits of MAPbI<sub>3</sub>

Since the cylinder-shaped geometry of MAPbI<sub>3</sub> deposits facilitate the design of sealed housings, we explored a possibility of implementing the obtained micro-crystalline densely packed MAPbI<sub>3</sub> films as prospective photo-optical gas sensors. To this end, a cylindrical substrate having 330  $\mu\text{m}$  in diameter was covered with MAPbI<sub>3</sub> and encapsulated in a section of a slightly larger quartz capillary (3.0 mm ID/4.0 mm OD), which served as an external, light-transparent sample holder and gas-flow chamber. This setup has been described in greater detail in Chapter 2 (for more information see Figure 2.8(a)&(b)). This approach provided an easy way for a direct exposure of a MAPbI<sub>3</sub>-covered substrate to gaseous media, such as O<sub>2</sub>, N<sub>2</sub> and Ar. Moreover, it also made it possible to detect gas-dependent changes in the characteristic PL emission of MAPbI<sub>3</sub>. Overall, this construction revealed its usefulness for photo-optical sensing of gaseous media and may serve a model of uncomplicated MAPbI<sub>3</sub>-based gas sensors.

The motivation to study the impact of exposure of polycrystalline deposits of MHPs to the environmentally-important gaseous media, O<sub>2</sub> and N<sub>2</sub>, stems from the fact that perovskite-based photovoltaic devices might be exploited under an air atmosphere. In particular, O<sub>2</sub> is known to be highly reactive and, as such, it can affect the material electronic structure and, subsequently, its photo-physical properties.

## Chapter 4. Impact of gaseous media on photoluminescence and photocurrent of polycrystalline MAPbI<sub>3</sub> and MAPbBr<sub>3</sub>.

First observations were made when statically gathering photoluminescence and observing it in the optical image *via* the camera, while switching gasses from N<sub>2</sub> to O<sub>2</sub>. This is demonstrated in Figure 4.1(b & c) – switching of the gas flow from N<sub>2</sub> to O<sub>2</sub> results in a rapid drop of photoluminescence of the MAPbI<sub>3</sub> deposit. To verify this we have collected the PL spectra while the sample was under flow of either of the two gases – concomitantly collected PL spectra confirm this observation. In particular, looking at the variation of PL over time in Figure 4.1(d), upon switching from N<sub>2</sub> to O<sub>2</sub>, a rapid drop of the PL signal, occurring on the time scale of ~25 sec, is observed. The corresponding individual PL spectra, collected at characteristic points of switching the gas flow marked by the green and blue circles are shown in Figure 4.1(e). The observed change in their amplitudes points to a decrease in PL signal of ~46% under exposure to the flow of O<sub>2</sub>. The subsequent switching to the flow of N<sub>2</sub> results in the renewed, although definitely slower, recovery of the PL signal emission as can be seen in Figure 4.1(d).

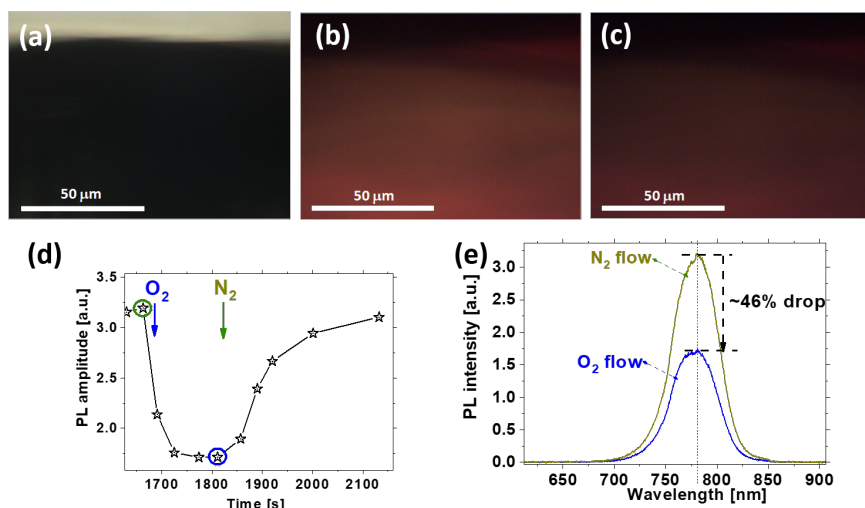


Figure 4.1 – The microscopic images of the MAPbI<sub>3</sub> deposit on the 330 μm DIA substrate in an off-center position as reference to the detecting optics during collecting the PL emission under the intermittent exposure to the flow of N<sub>2</sub> or O<sub>2</sub>. (a) The visible light microscopic image of the edge fragment of 330 μm DIA substrate. (b) The microscopic luminescent image ( $\lambda_{exc} = 546$  nm) of the sample exposed to the flow of N<sub>2</sub>. (c) The microscopic luminescent image ( $\lambda_{exc} = 546$  nm) of the sample exposed to the flow of O<sub>2</sub>. (d) A portion of the time-evolution of the PL amplitude highlighting the characteristic points of switching the gas flow N<sub>2</sub> to O<sub>2</sub> and from O<sub>2</sub> to N<sub>2</sub>, marked by the blue and green arrows, respectively. (e) The corresponding PL spectra collected at characteristic switching points shown in (d) under the flow of N<sub>2</sub> and O<sub>2</sub>, marked by the green and blue circles, respectively.

It is well known that under exposure of MAPbI<sub>3</sub> deposits to the visible light their overall PL intensity increases slowly over time [66]. Such process is usually referred to “light-soaking” or “photo-brightening”. The time-evolution of the PL intensity of the polycrystalline deposit of MAPbI<sub>3</sub> corresponding to such a typical “light-soaking” process, lasting approximately one hour, is shown in Figure 4.2(a) [130, 138].

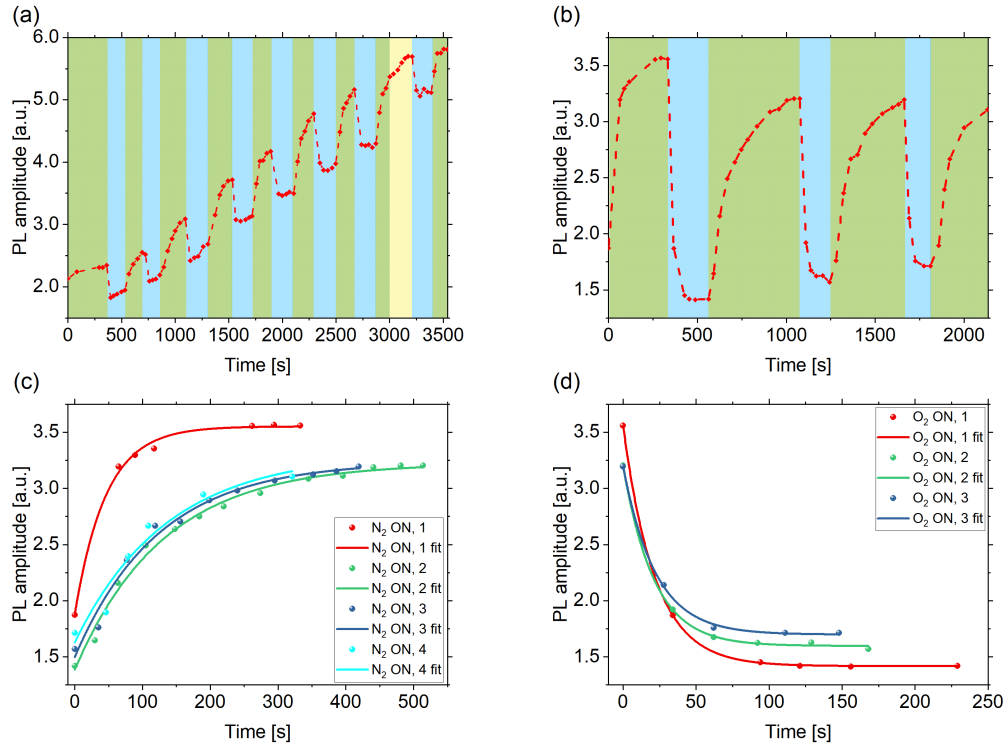


Figure 4.2 – (a) The time evolution of the PL signal acquired for the deposit of MAPbI<sub>3</sub> coated onto a cylinder-shaped quartz rod (330  $\mu\text{m}$  in diameter) under continuous excitation at  $\lambda_{exc} = 546$  nm and intermittent exposure to various gaseous media (O<sub>2</sub>, N<sub>2</sub> and Ar) during the “light-soaking” treatment. (b) The typical time-evolution of the PL signal acquired for MAPbI<sub>3</sub> deposited onto a cylinder-shaped substrate (quartz rod, 330  $\mu\text{m}$  in diameter) under the continuous excitation at  $\lambda_{exc} = 546$  nm and intermittent exposure to N<sub>2</sub> and O<sub>2</sub>. The time intervals of alternating exposures to different gaseous media are highlighted in (a & b) by the green, yellow and blue background colors, for N<sub>2</sub>, Ar and O<sub>2</sub>, respectively. (c) The overlapped plots of the increasing portions of the photoluminescent response under exposure to N<sub>2</sub>. (d) The overlapped plots of the decreasing portions of the photoluminescent response under exposure to O<sub>2</sub>. The solid lines correspond to the exponential fits. The steepest plot in (d) corresponds to the initial exposure of the sample to the flow of O<sub>2</sub>, just following completion of the “light-soaking” process (red trace).

The example time-evolution of the PL response in steady-state regime (*i.e.* when the PL signal remains relatively stable following completion of the “light-soaking” process), acquired for a freshly-prepared MAPbI<sub>3</sub> deposit on a 330  $\mu\text{m}$  diameter quartz rod under continuous illumination with green light ( $\lambda_{exc} = 546$  nm) and intermittent exposure to O<sub>2</sub> and N<sub>2</sub>, is shown in Figure 4.2(b).

As can be seen in Figure 4.2(b), while interchanging successively the gas flow from N<sub>2</sub> to O<sub>2</sub>, the PL response of the MAPbI<sub>3</sub> deposit markedly changes. Specifically, under the intermittent exposures to N<sub>2</sub> and O<sub>2</sub>, the corresponding PL signals undergo a pronounced intensity increase or decrease, respectively. For easier comparison, the overlapped plots of the decreasing and

#### Chapter 4. Impact of gaseous media on photoluminescence and photocurrent of polycrystalline MAPbI<sub>3</sub> and MAPbBr<sub>3</sub>.

---

increasing portions of the photoluminescent responses under the intermittent flows of O<sub>2</sub> and N<sub>2</sub>, are shown in Figure 4.2(c & d), respectively. The partial decay and the subsequent partial recovery of the PL signal under exposure to the flow of O<sub>2</sub> and N<sub>2</sub>, respectively, was reproducible and could be observed several times during the experiment.

Even though the times of exposure to the two above-mentioned gaseous media were not the same, fitting the exponential decaying (rising) function allowed us to extract the characteristic times corresponding to a decrease (increase) of the PL signal amplitude by *ca.* 2.7 times. It is then evident that the subsequent exposures to O<sub>2</sub> result in rapid decays of the PL emission, which occur on a time scale of ~20 seconds (Figure 4.2(d)). In contrast, after switching back to N<sub>2</sub>, the photoluminescent response undergoes a phase of recovery, *i.e.* restores the initial PL amplitude as in the previous cycle. This process is definitely slower and occurs on a time scale of ~130 seconds (Figure 4.2(c)). It is worth pointing out that the plot with the steepest slope (red trace in Figure 4.2(c)) and the corresponding rise time of ~45 seconds, was recorded during the first exposure to the flow of N<sub>2</sub>, just following completion of the “light-soaking” process. The relative changes in the PL signal intensity shown in Figure 4.2(b) were found to be of 50 – 60%.

Some of the previously reported gas sensors have shown weaker performance in terms of the response times as well as they usually required a more sophisticated engineering. For example, Addabbo *et al.* [139] reported on YCoO<sub>3</sub>-based sensor of CO, NO and NO<sub>2</sub> *via* resistivity measurements. In their device, they used a heated sensing material. In particular, the corresponding working temperatures were of 180°C for sensing NO<sub>x</sub> and more than 200°C for CO. At their best, these devices had the response times of 0.5 – 1.5 minutes and recovery times of 0.6 – 4.7 minutes. Another report on gas sensing, this time with using a perovskite material MAPbBr<sub>3</sub>, has been reported by Fang *et al.* [133]. Their device was based on the intensity of the PL signal and was sensitive to air, dry O<sub>2</sub> and moist N<sub>2</sub>. The response times reported for this device were of the order of ~1000 seconds or longer. Compared to the above mentioned reports, the response times reported herein are definitely shorter, being in the same range as those reported for more sophisticated devices and having heated substrates [140].

The phenomenon of the partial decay of the PL signal under exposure to O<sub>2</sub> has been often reported in the context of the studies of the influence of light and oxygen on the stability of MAPbI<sub>3</sub>-based photo-active layers. Although there is a consensus that, in combination with light, oxygen molecules mainly contribute to quenching of the PL emission in microcrystalline deposits of MAPbI<sub>3</sub> [141], the proposed plausible mechanisms explain only partially the corresponding phenomena [142, 143]. Moreover, there is also growing experimental evidence that, in the context of the monocrystalline MAPbI<sub>3</sub>, an opposite effect, *i.e.* the PL enhancement, upon exposure to O<sub>2</sub>, can also be observed [130, 144].

The rapid diffusion of oxygen into the microcrystalline deposits of MAPbI<sub>3</sub> in combination with photo-excited carriers are considered to be the dominant factors resulting in an enhancement of trapping sites responsible for non-radiative charge recombination [128, 145]. In particular,

the total diffusion times into thin layers (typically 500 nm thick) of MAPbI<sub>3</sub> have been found to occur on a time scale of 5 – 10 minutes [145].

Moreover, as can also be seen in Figure 4.2(b), the subsequent cycles of gas switching from N<sub>2</sub> to O<sub>2</sub> result in an overall decrease of the photoluminescent response observed during the recovery phase (exposure to N<sub>2</sub>), as well as in an overall increase of the PL signals acquired at the end of the rapid decay phase (exposure to O<sub>2</sub>). This might suggest that although the observed changes in the photoluminescent responses upon successive exposures to O<sub>2</sub> are largely reversible, there is a long-term oxygen-induced photo-degradation of MAPbI<sub>3</sub>.

Thus, at least two different scenarios of oxygen interactions with microcrystalline deposits of MAPbI<sub>3</sub> can be invoked. Firstly, a rapid penetration and diffusion of O<sub>2</sub> in parallel with continuous illumination with above-bandgap photons ( $h\nu > 1.6$  eV), can activate deep trap centers of the photo-excited carriers, thus leading to an efficient and reversible PL quenching. Secondly, the diffusion of oxygen molecules into polycrystals of MAPbI<sub>3</sub> and their interaction with the photo-excited carriers (electrons) may result in formation of superoxide radical species (O<sub>2</sub><sup>•-</sup>), which are critical to both the oxygen-induced degradation of the host lattice and concomitant irreversible decrease of the PL emission of MAPbI<sub>3</sub> [145].

#### 4.2.2 Photoluminescence response of polycrystalline deposits of MAPbI<sub>3</sub> and MAPbBr<sub>3</sub> under recurrent exposures to the flow of either O<sub>2</sub> or N<sub>2</sub>

Example results illustrating the markedly differential PL responses of the polycrystalline deposits of MAPbI<sub>3</sub> and MAPbBr<sub>3</sub> under the simultaneous exposure either to air or to the recurrent gas-flow of either O<sub>2</sub> or N<sub>2</sub> are shown in Figure 4.3(a – d). Specifically, Figure 4.3(a – c) shows the optical and fluorescence microscopy images of the two polycrystalline deposits of MAPbI<sub>3</sub> and MAPbBr<sub>3</sub> coated onto 330  $\mu$ m diameter substrates positioned *side-by-side* in a custom-made gas-flow chamber (for more technical details, see Figure 2.9 in Chapter 2). The first fluorescence microscopy image in Figure 4.3(b) collected under the excitation wavelength of  $\lambda_{exc} = 470$  nm shows the characteristic green luminescence of the substrate coated with polycrystalline MAPbBr<sub>3</sub> (lower specimen) and a rather weak red-near IR luminescence of the substrate coated with polycrystalline MAPbI<sub>3</sub> (upper specimen). The second fluorescence microscopy image in Figure 4.3(c), recorded under the excitation wavelength of  $\lambda_{exc} = 546$  nm, shows a stronger red-near IR luminescence of the substrate coated with polycrystalline MAPbI<sub>3</sub> (upper specimen). It also points to a lack of the green luminescence of MAPbBr<sub>3</sub> (lower specimen), which remains insensitive to the sub-bandgap excitation at  $\lambda_{exc} = 546$  nm. The corresponding steady-state PL spectra, collected simultaneously for the two specimens at the excitation wavelengths of  $\lambda_{exc} = 470$  nm (blue trace) and  $\lambda_{exc} = 546$  nm (green trace) are shown in Figure 4.3(d). These PL spectra acquired for two MHPs samples positioned *side-by-side* close each other confirm the PL responses of MAPbI<sub>3</sub> and MAPbBr<sub>3</sub>, which can be seen in luminescence microscopy images in Figures 4.3(b & c). Specifically, the two PL maxima peaking at 553 nm and 768 nm can be observed under excitation at  $\lambda_{exc} = 470$  nm, corresponding to the characteristic

## Chapter 4. Impact of gaseous media on photoluminescence and photocurrent of polycrystalline MAPbI<sub>3</sub> and MAPbBr<sub>3</sub>.

PL emissions of MAPbBr<sub>3</sub> and MAPbI<sub>3</sub>, respectively (blue trace in Figure 4.3(d)). In contrast, only one PL maximum, peaking at 768 nm and corresponding to the characteristic emission of MAPbI<sub>3</sub> is observed under excitation at  $\lambda_{exc} = 546$  nm wavelength (green trace in Figure 4.3(d))

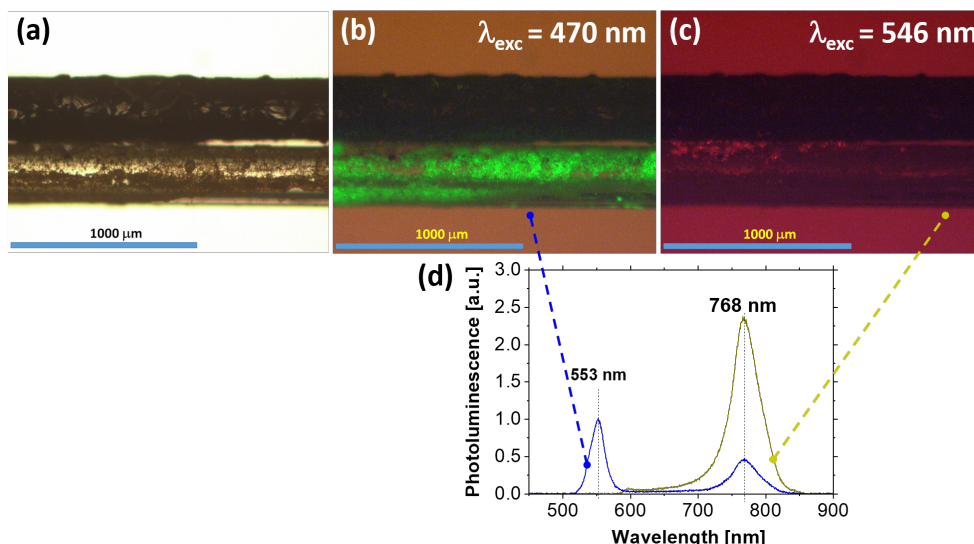


Figure 4.3 – Optical and fluorescence microscopy images of the deposits of MAPbI<sub>3</sub> and MAPbBr<sub>3</sub> coated onto 330 μm diameter substrates positioned *side-by-side* in a custom-made gas-flow chamber (see Figure 2.9 for technical details). (a) The bright-field optical microscopy image of the two cylinder-shaped substrates coated with two different MHPs. (b) The fluorescence microscopy image of the two substrates observed under the excitation at  $\lambda_{exc} = 470$  nm. (c) The fluorescence microscopy image of the two substrates observed under the excitation at  $\lambda_{exc} = 546$  nm. (d) Steady-state PL spectra acquired simultaneously for two cylinder-shaped substrates coated with two different MHPs excited at  $\lambda_{exc} = 470$  nm (blue trace) and  $\lambda_{exc} = 546$  nm (green trace). The dashed blue and green lines associate the steady-state PL spectra shown in (d) with the corresponding fluorescence microscopy images shown in (b) and (c).

As one can also see from the blue trace in Figure 4.3(d), the PL amplitude of MAPbI<sub>3</sub> is markedly lower under excitation at  $\lambda_{exc} = 470$  nm, than at  $\lambda_{exc} = 546$  nm. Such differences in the PL amplitudes have been reported for MAPbI<sub>3</sub> under excitation with the visible light with either shorter (460 to 480 nm) or longer wavelengths (>500 nm) [146, 147] and were attributed to inter-band transitions due to the splitting of the valence and conduction bands, thus leading to either “photo-bleaching” under excitation at  $\lambda_{exc} = 460$  to 480 nm, or “photo-brightening” under excitation at  $\lambda_{exc} > 500$  nm [148]. Recently, a rapid, blue light-induced ( $\lambda_{exc} = 457$  nm) “photo-bleaching”, concomitant with a partial degradation of polycrystalline deposits of MAPbI<sub>3</sub> has also been reported [149].

A comprehensive overview of the markedly distinctive PL responses of polycrystalline deposits of MAPbI<sub>3</sub> and MAPbBr<sub>3</sub>, coated onto substrates of 330 μm in diameter, positioned *side-by-side* in a miniature gas-flow chamber and recurrently exposed to the flow of either N<sub>2</sub> or O<sub>2</sub>, is shown in Figure 4.4 (for technical details see Figure 2.9 in Chapter 2). For clarity reasons,

Figure 4.4(a) shows, once again, the steady-state PL spectra, collected simultaneously for the two specimens of MAPbI<sub>3</sub> and MAPbBr<sub>3</sub> at the excitation wavelengths of  $\lambda_{exc} = 470$  nm (blue trace) and  $\lambda_{exc} = 546$  nm (green trace). Subsequently, the 3D plot in Figure 4.4(b) summarizes the overall differential behavior of the PL responses of the polycrystalline deposits of MAPbI<sub>3</sub> and MAPbBr<sub>3</sub> exposed to the intermittent exposures to two gaseous media, O<sub>2</sub> and N<sub>2</sub>. From the set of steady-state PL spectra collected at  $\lambda_{exc} = 470$  nm wavelength (Figure 4.4(b)) one can see that the PL peak of MAPbI<sub>3</sub> increases, whereas the PL peak of MAPbBr<sub>3</sub> decreases as a function of time of exposure to N<sub>2</sub>. In contrast, under exposure to O<sub>2</sub>, the PL responses reveal the opposite behavior, that is the PL peak of MAPbI<sub>3</sub> rapidly decreases, whereas the PL peak of MAPbBr<sub>3</sub> markedly increases.

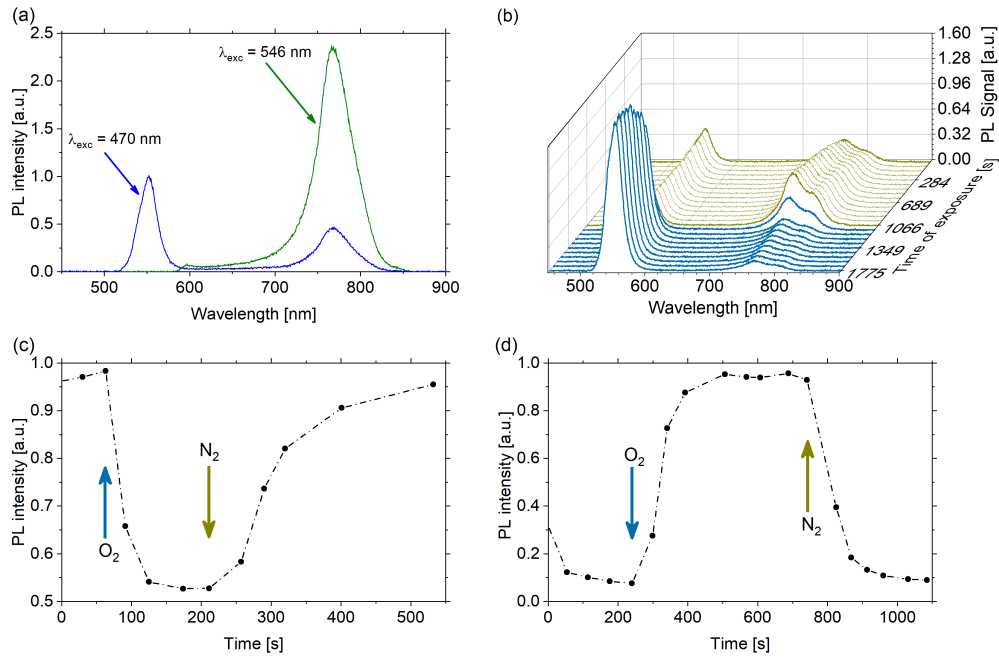


Figure 4.4 – PL responses of the polycrystalline deposits of MAPbI<sub>3</sub> and MAPbBr<sub>3</sub> drop-casted onto cylindrical substrates exposed either to air or to the recurrent flows of two gaseous media, O<sub>2</sub> or N<sub>2</sub>. (a) PL traces acquired for the *side-by-side* arrangement of MAPbI<sub>3</sub> and MAPbBr<sub>3</sub>, under excitation at  $\lambda_{exc} = 470$  nm (blue trace) peaking at 553 nm and 768 nm, respectively. Under the excitation at  $\lambda_{exc} = 546$  nm (green trace) only the peak of MAPbI<sub>3</sub> (at 768 nm) can be seen. (b) The 3D plot of steady state PL spectra excited at  $\lambda_{exc} = 470$  nm and collected simultaneously for the *side-by-side* arrangement of MAPbI<sub>3</sub> and MAPbBr<sub>3</sub> samples positioned in a miniature gas-flow chamber (rectangular glass tube) under intermittent exposures to N<sub>2</sub> (green traces) and O<sub>2</sub> (blue traces). (c) The time evolution of the PL signal excited at  $\lambda_{exc} = 546$  nm for an individual sample of MAPbI<sub>3</sub> coated onto a cylindrical substrate (330  $\mu$ m in diameter, assembly in a 2.0 mm ID  $\times$  2.4 mm OD quartz tube). (d) The time evolution of the PL signal excited at  $\lambda_{exc} = 470$  nm for an individual sample of MAPbBr<sub>3</sub> coated onto a cylindrical substrate (330  $\mu$ m in diameter, assembly in a 2.0 mm ID  $\times$  2.4 mm OD quartz tube).

The dynamic time-resolved PL responses of polycrystalline deposits on substrates of 330  $\mu$ m



## Chapter 4. Impact of gaseous media on photoluminescence and photocurrent of polycrystalline MAPbI<sub>3</sub> and MAPbBr<sub>3</sub>.

for two different MHPs, exposed to switching of the chemical environment from pure N<sub>2</sub> to pure O<sub>2</sub>, are shown in Figures 4.4(c & d), for MAPbI<sub>3</sub> and MAPbBr<sub>3</sub>, respectively. The analysis of the PL response dynamics for MAPbI<sub>3</sub> (Figure 4.4(c)) shows that under exposure to O<sub>2</sub>, the PL intensity decays relatively rapidly, on a time scale of ~20 seconds (the time lapse corresponding to ~2.7 times decrease of the PL signal amplitude). In contrast, after the subsequent switching back to N<sub>2</sub>, the PL signal restores its initial level. The recovery process is slower and occurs on a time scale of ~130 seconds (the time lapse corresponding to ~2.7 times increase of the PL signal amplitude). Typically, the relative changes in the PL signal amplitude for the deposits of MAPbI<sub>3</sub>, recurrently exposed to the flow of either N<sub>2</sub> or O<sub>2</sub>, were found to be ~50 – 60%. It is also evident that the PL response dynamics for MAPbBr<sub>3</sub> (Figure 4.4(d)) undergoes the opposite changes under intermittent exposures to N<sub>2</sub> and O<sub>2</sub>.

The time resolved kinetics of the changes in the PL emission for the polycrystalline deposit of MAPbBr<sub>3</sub>, under exposure to either O<sub>2</sub> or N<sub>2</sub>, are shown in Figures 4.5(a & b). In particular, under exposure to O<sub>2</sub>, the PL signal intensity rapidly increases (on a time scale of ~85 seconds) (Figure 4.5(a)), whereas under exposure to N<sub>2</sub>, the PL signal intensity decreases on a roughly the same time scale (~90 seconds) detailed in (Figure 4.5(b)). Interestingly, for the deposits of MAPbBr<sub>3</sub>, recurrently exposed to the flow of either N<sub>2</sub> or O<sub>2</sub>, the relative changes in the PL signal intensity were found to be higher than for the deposits of MAPbI<sub>3</sub>, reaching ~90%.

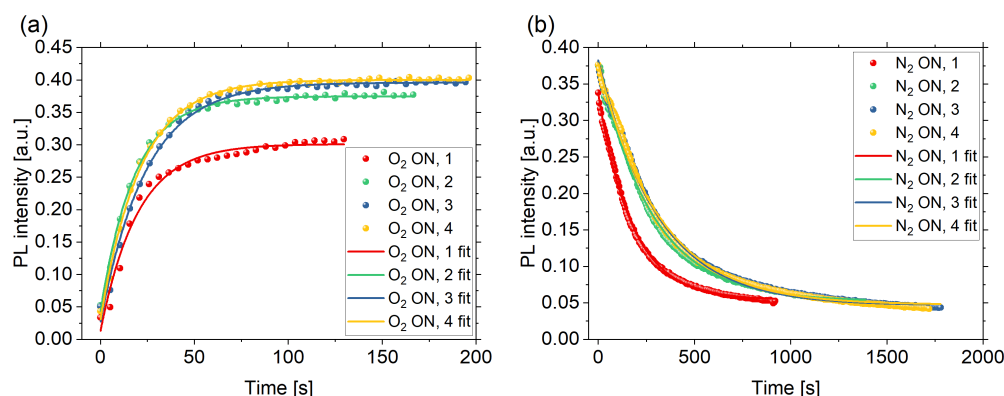


Figure 4.5 – (a) The overlapped plots of the increasing portions of the photoluminescent response of MAPbBr<sub>3</sub> under exposure to O<sub>2</sub>. (b) The overlapped plots of the decreasing portions of the photoluminescent response of MAPbBr<sub>2</sub> under exposure to N<sub>2</sub>. The solid lines correspond to the exponential fits.

The herein observed changes in the PL intensity for the polycrystalline deposits of MAPbI<sub>3</sub> and MAPbBr<sub>3</sub> are very high, and thus macroscopically visible. An example of such “photo-brightening” for the deposit of MAPbBr<sub>3</sub> coated onto an 80  $\mu$ m diameter substrate can clearly be visible in Figure 4.6(b – e).

It is also worth mentioning that all these intensity variations under subsequent exposures to N<sub>2</sub> or O<sub>2</sub> occur with essentially no difference in the wavelength and shape of the emission peaks for both MAPbI<sub>3</sub> and MAPbBr<sub>3</sub>. Concomitantly, the time-evolutions of the PL signals



presented in Figures 4.4(c & d) reproduce the PL variations shown in the cumulative 3D plot (Figure 4.4(b)), which was gathered for two MHPs samples positioned *side-by-side* and simultaneously exposed to the same environmental conditions. Thus, as evidenced by the graphs in Figure 4.4(b – d), while recurrently switching the chemical environment from pure N<sub>2</sub> to pure O<sub>2</sub>, the corresponding PL responses of the deposits of MAPbI<sub>3</sub> and MAPbBr<sub>3</sub> are totally dissimilar.

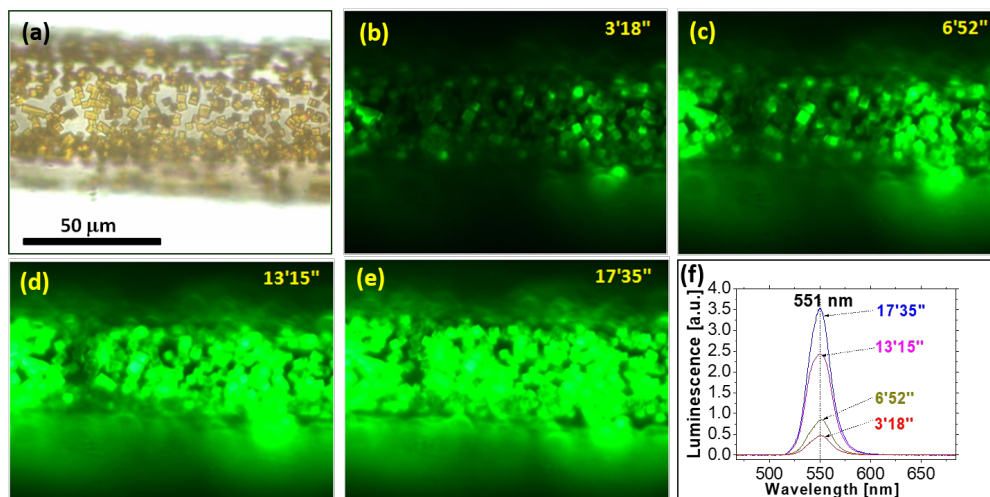


Figure 4.6 – Macroscopically observable changes in the PL intensity for the polycrystalline deposit of MAPbBr<sub>3</sub> coated onto a cylinder-shaped quartz substrate with 80 μm DIA under exposure to air and at the excitation wavelength  $\lambda_{exc} = 470$  nm. (a) The bright-field visible light optical microscopy image of the sample. (b – d) Selected fluorescence microscopy time-lapse images acquired at four different time moments after turning on the excitation illumination, *i.e.* at 3'18'', 6'52'', 13'15'' and 17'35''. (f) The time evolution of the steady-state luminescence spectra collected for the deposit of MAPbBr<sub>3</sub> deposit collected at the same time moments as the time-lapse fluorescence microscopy images.

To exclude the effects of structural changes under exposures to pure gaseous N<sub>2</sub> and O<sub>2</sub> a set of XRD measurements was performed. To this end, the samples were exposed to a combination of gaseous N<sub>2</sub> and O<sub>2</sub> and illumination by green light ( $\lambda_{exc} = 546$  nm) for ~15 minutes, which was the typical time of exposure during our experiments. As can be seen in Figures 4.7(a & b), the obtained XRD spectra did not reveal any structural changes in both MAPbI<sub>3</sub> and MAPbBr<sub>3</sub>.

Altogether, the above findings demonstrate that under the experimental conditions used in this study, the PL responses of polycrystalline deposits of MAPbI<sub>3</sub> and MAPbBr<sub>3</sub> to the exposure to N<sub>2</sub> to O<sub>2</sub> are distinctively different. In addition, notwithstanding the observed differences, the actual temporal changes in the PL signal intensities occur at approximately the same time scales for both MHPs.

## Chapter 4. Impact of gaseous media on photoluminescence and photocurrent of polycrystalline MAPbI<sub>3</sub> and MAPbBr<sub>3</sub>.

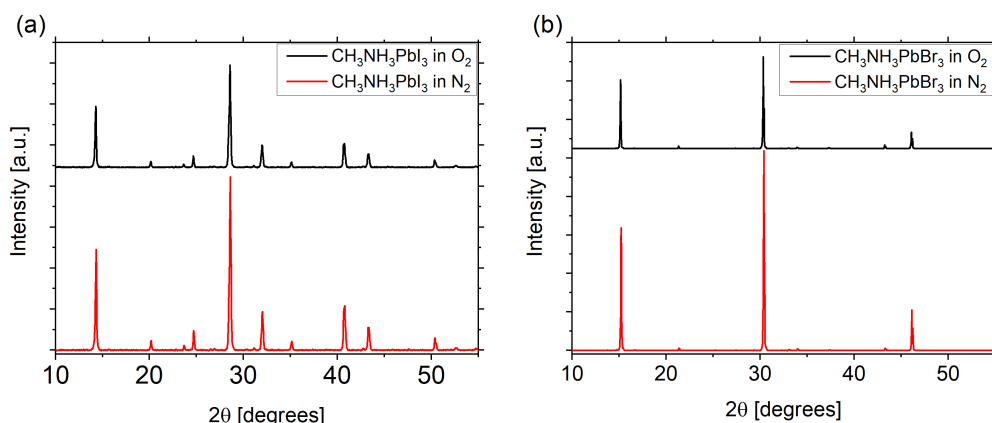


Figure 4.7 – XRD patterns for (a) MAPbI<sub>3</sub> and (b) MAPbBr<sub>3</sub> after the exposure to N<sub>2</sub> (red traces) and O<sub>2</sub> (black traces).

### 4.2.3 Correlations between the photoluminescence and the photocurrent for polycrystalline deposits of MAPbI<sub>3</sub> and MAPbBr<sub>3</sub> during intermittent exposures to either O<sub>2</sub> or N<sub>2</sub>

It is worth noting that our custom-built miniature gas-flow chambers, in addition to being capable of exposing the samples to the flow of well-controlled high-purity gases and enabling the collection of PL spectra, provided also a possibility for electrical contacting the MHPs deposits. Therefore, during the intermittent exposures of the polycrystalline samples of MAPbI<sub>3</sub> and MAPbBr<sub>3</sub> to the flow of either O<sub>2</sub> or N<sub>2</sub>, we could also measure their PC responses. Figure 2.8 shows the schematic representation of the experimental setup employed for the simultaneous monitoring of PL and PC responses of polycrystalline deposits of MHPs coated onto cylinder-shaped substrates of 80  $\mu\text{m}$  in diameter.

Simultaneously acquired time-evolutions of the PL and PC responses for the polycrystalline deposits of MHPs coated onto quartz substrates of 80  $\mu\text{m}$  in diameter, during the intermittent exposures to the flow of either O<sub>2</sub> or N<sub>2</sub>, are shown in Figure 4.8(a & b), for MAPbI<sub>3</sub> and MAPbBr<sub>3</sub>, respectively. In both Figures, the time intervals of alternating exposures to two different gaseous media, N<sub>2</sub> and O<sub>2</sub>, are highlighted by the green and blue background colors, respectively.

As can be seen from the graphs presented in Figure 4.8, the PL responses during the recurrent exposures to the flow of either O<sub>2</sub> or N<sub>2</sub> (highlighted by the black traces) follow the distinctly different time evolutions for MAPbI<sub>3</sub> and MAPbBr<sub>3</sub>, as discussed in the previous section. In particular, upon exposure to O<sub>2</sub>, the PL intensity for MAPbI<sub>3</sub> decreases, whereas the PL intensity of MAPbBr<sub>3</sub> markedly increases. Surprisingly, however, the PC responses (highlighted by the red scattered points) acquired during intermittent exposures to the flow of either O<sub>2</sub> or N<sub>2</sub>, are markedly different for the deposits of MAPbI<sub>3</sub> and MAPbBr<sub>3</sub>. In particular, the time evolutions of PC and PL responses clearly anti-correlate for MAPbI<sub>3</sub> (Figure 4.8(b)), whereas they remain correlated for MAPbBr<sub>3</sub> (Figure 4.8(c)). An overview of the correlations between

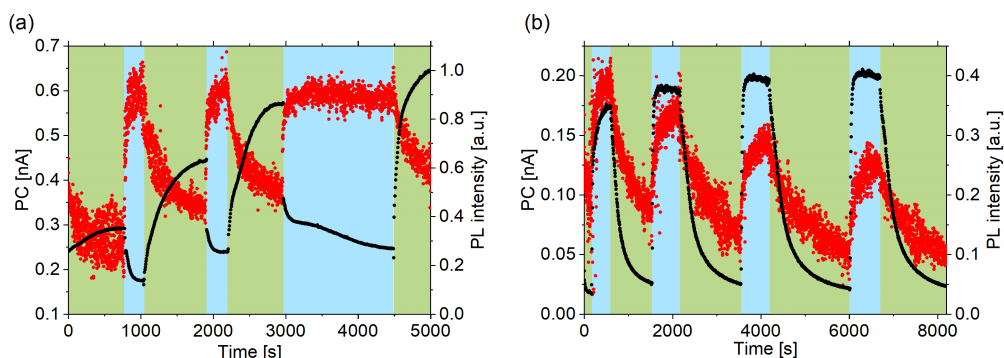


Figure 4.8 – Time-resolved PL and PC responses of the polycrystalline deposits of MAPbI<sub>3</sub> and MAPbBr<sub>3</sub> coated onto cylinder-shaped quartz substrates under exposure to recurrent switching of the chemical environment from pure N<sub>2</sub> to pure O<sub>2</sub>. (a) Simultaneously acquired time-evolutions of PC (red scattered points) and PL (black scattered points) for a polycrystalline deposit of MAPbI<sub>3</sub> under recurrent exposures to the flow of either N<sub>2</sub> or O<sub>2</sub>. (b) Simultaneously acquired time-evolutions of PC (red scattered points) and PL (black scattered points) for a polycrystalline deposit of MAPbBr<sub>3</sub> under recurrent exposures to the flow of either N<sub>2</sub> or O<sub>2</sub>. The time intervals of alternating exposures to two different gaseous media are highlighted by the green and blue background colors, for N<sub>2</sub> and O<sub>2</sub>, respectively.

Feature	Gas	MAPbI <sub>3</sub>	MAPbBr <sub>3</sub>
PL	O <sub>2</sub>	↓	↑
	N <sub>2</sub>	↑	↓
PC	O <sub>2</sub>	↑	↑
	N <sub>2</sub>	↓	↓

Table 4.1 – Correlations between the photoluminescence (PL) and the photocurrent (PC) of the polycrystalline deposits of MAPbI<sub>3</sub> and MAPbBr<sub>3</sub> observed during intermittent exposures to either O<sub>2</sub> or N<sub>2</sub>. The arrowheads pointing “upwards” and “downwards” correspond to a trend of PL or PC to increasing or decreasing.

the PL and PC responses for the polycrystalline deposits of MAPbI<sub>3</sub> and MAPbBr<sub>3</sub> observed during intermittent exposures to the flow of either O<sub>2</sub> or N<sub>2</sub> is presented in Table 4.1.

There is a general belief that the photophysical characteristics of MHPs, including the changes in PL and PC responses to the modifications of the external environment (*e.g.* exposure to various gaseous media, moisture, or temperature), strongly depend on both bulk and surface shallow- or deep-level defect centers formed during the process of crystal formation [150, 151]. It is also well established that these low-temperature, solution-processed materials, contrary to the expectations, possess in general an apparently low density of trapping defects [152, 153], which might have both negative and positive impacts on their optoelectronic properties. However, despite numerous previous studies, the nature, density and activity of trap states in MHPs, as well as the exact mechanisms of their possible contributions to the radiative and non-radiative recombination mechanisms of photogenerated carriers have remained elusive.

#### Chapter 4. Impact of gaseous media on photoluminescence and photocurrent of polycrystalline MAPbI<sub>3</sub> and MAPbBr<sub>3</sub>.

---

In the context of exposure to environmental gaseous media, much recent research made it evident that the PL intensity observed for thin polycrystalline deposits of MHPs can vary dramatically upon exposure to O<sub>2</sub> or N<sub>2</sub> [130]. It has also been shown that, the actual impact of light and gaseous media on the PL intensity (enhancement or diminishment) strongly depends on how the MHPs samples were prepared in different laboratories [151].

In general, many possible bulk and surface defects can occur in crystalline materials such as MHPs (as described in Chapter 1. These defects include various types of deep and shallow defects/traps, which can potentially interact with environmental gaseous media and are believed to form efficient non-radiative quenching centers [154, 155]. In particular, Uratani *et al.* [156] and Zhang *et al.* [157] put forward the importance of deep intra-band states for MAPbI<sub>3</sub> and shallow traps for MAPbBr<sub>3</sub> as non-radiative recombination centers.

According to Uratani *et al.*, the PL of MAPbI<sub>3</sub> is quenched due to the O<sub>2</sub>-mediated re-activation of deep intra-band traps. Specifically, adhering O<sub>2</sub> molecules, upon their interaction with the surface of MAPbI<sub>3</sub> microcrystals, extract electrons from these defects, thus leading to repopulation of deep non-radiative quenching centers, which results in the PL diminishment [156].

In this context, recently, Meggiolaro *et al.* identified the iodine-related defects as the source of photo-chemically activated deep electron and hole traps in MAPbI<sub>3</sub> [158]. Furthermore, Hong *et al.* suggested that the light-mediated interplay between lead- and iodine-related structural interstitial defects, *i.e.* Pb<sup>2+</sup> and I<sup>1+</sup> (in the dark) and Pb<sup>0</sup> and I<sup>1-</sup> (under illumination), can modify the relative contributions of radiative and non-radiative recombination processes in MAPbI<sub>3</sub> microcrystals [159]. Specifically, it has been hypothesized that, due to the light-induced charging with valence-band electrons the population of deep intra-band trap states I<sup>1+</sup>, which are responsible for efficient non-radiative recombination, can be largely reduced. It has also been pointed out that the charged state of this defect, I<sup>1-</sup>, hybridizes with the valence band and therefore should not contribute to the efficient non-radiative recombination. On the other hand, the light-generated carriers can also increase the population of the intra-band Pb<sup>0</sup> centers (by charging the shallow Pb<sup>2+</sup> states), thus potentially leading to the PL decrease.

Since, as demonstrated by Mosconi *et al.* [160], iodine-related interstitial bulk and surface defects at all charge states (-1, 0, +1) should be more abundant than other types of defects in solution-processed polycrystalline perovskite films, in the following discussion we mostly focused on the role of iodine surface defects. In particular, it is then quite plausible that, in addition to light, the populations of bulk and especially surface defects can also be modified in the presence of a strong gaseous electron acceptor, such as molecular O<sub>2</sub>. Specifically, adhering O<sub>2</sub> molecules might compete with the light-mediated process of charging the deep intra-band trap states (I<sup>1+</sup> → I<sup>1-</sup>). In other words, in the presence of O<sub>2</sub>, the deep non-radiative recombination centers (I<sup>1+</sup>) cannot be efficiently deactivated by the light-generated charges. Thus, the competition of O<sub>2</sub> molecules with light-induced deactivation of I<sup>1+</sup>-related deep intra-band centers preserves their population, which results in the PL diminishment, as observed in this study for the polycrystalline deposits of MAPbI<sub>3</sub> exposed to O<sub>2</sub>.

In the case of MAPbBr<sub>3</sub>, Fang *et al.* reported on the ultrahigh sensitivity of single crystals of MAPbBr<sub>3</sub>, to environmental gases, including O<sub>2</sub> [133]. Specifically, it has been observed that the amplitude of the PL signal increased by more than two orders of magnitude after changing the environment from vacuum to air. It has then been concluded that physisorption or desorption of O<sub>2</sub> molecules could reversibly modulate the PL response of MAPbBr<sub>3</sub> single crystals. In this context, Zhang *et al.* found that discharging of the shallow surface trap states in grains of MAPbBr<sub>3</sub> by O<sub>2</sub> molecules allowed for more radiative recombination transitions to occur, thus leading to the PL enhancement [157].

The proposed schematic interpretation of the mechanisms underlying the diversified PL responses of the polycrystalline deposits of MAPbI<sub>3</sub> and MAPbBr<sub>3</sub> under exposure to light and O<sub>2</sub>, as observed in this study, is shown in Figure 4.9.

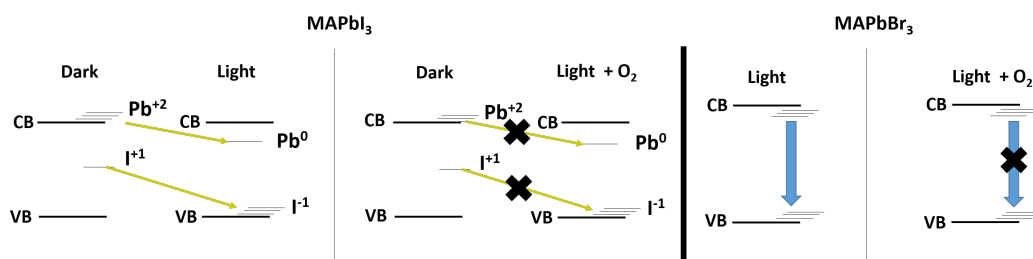


Figure 4.9 – Schematic representation of the energy levels of shallow and deep quenching centers governing the processes of radiative and non-radiative recombinations in MAPbI<sub>3</sub> (left panel) and MAPbBr<sub>3</sub> (right panel) under the combined exposure to above the band gap energy photons and O<sub>2</sub>. The yellow arrows in the left panel indicate an interplay between the shallow Pb<sup>2+</sup> and deep I<sup>1+</sup> defects in the dark, and deep Pb<sup>0+</sup> and shallow I<sup>1-</sup> defects under illumination for MAPbI<sub>3</sub>. The blue arrows in the right panel indicate the major non-radiative recombination channels in MAPbBr<sub>3</sub>. The black crosses indicate the counteraction of the gaseous O<sub>2</sub> against the processes of: (left panel) light-induced charging of Pb<sup>2+</sup> and I<sup>1+</sup> defects in MAPbI<sub>3</sub> (highlighted by the yellow arrows), and (right panel) major non-radiative recombination channels in MAPbBr<sub>3</sub> (highlighted by the blue arrows).

#### 4.2.4 Stability of photoluminescence of MAPbI<sub>3</sub> and MAPbBr<sub>3</sub> under exposure to a constant gas pressure: towards gas sensing

Since the herein observed differential PL and PC responses can possibly allow for designing sensors for detecting the presence and measuring the concentration of environmental gaseous media, including O<sub>2</sub>, the stability of levels of measured features represent a very important issue for a prospective long-term operation of a device. Figure 4.10 shows the results of the experiment where the PL level was monitored for polycrystalline deposits of both MHPs, coated onto 80 μm substrates and exposed for longer periods of time to N<sub>2</sub> and O<sub>2</sub>, for MAPbI<sub>3</sub> and MAPbBr<sub>3</sub>, respectively. It is worth noting that, under the experimental conditions used in the present study, the PL responses of MAPbI<sub>3</sub> and MAPbBr<sub>3</sub> were reaching their high levels whilst exposed to N<sub>2</sub> and O<sub>2</sub>, respectively.

## Chapter 4. Impact of gaseous media on photoluminescence and photocurrent of polycrystalline MAPbI<sub>3</sub> and MAPbBr<sub>3</sub>.

As can be seen in Figure 4.10, under exposure to gaseous media at constant pressures and intermittent exposures to dark periods (for 10 – 15 min), the high PL levels of both MAPbI<sub>3</sub> and MAPbBr<sub>3</sub> were very well preserved. Moreover, each time after switching back the illumination with above band gap photons ( $\lambda_{exc} = 546$  nm for MAPbI<sub>3</sub> and  $\lambda_{exc} = 470$  nm for MAPbBr<sub>3</sub>), the recovered PL intensities were very close to their corresponding values at the end of the preceding light cycle. It is also worth mentioning that the recovery time of the PL signal upon illumination was very rapid, being below 5 s, for both MAPbI<sub>3</sub> and MAPbBr<sub>3</sub>.

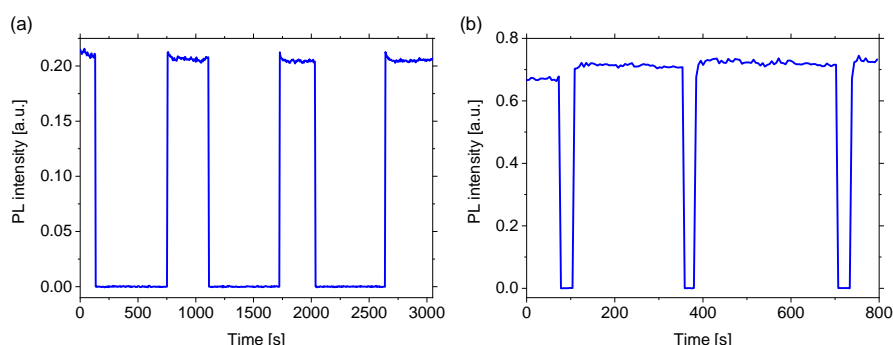


Figure 4.10 – Long-term stability of the PL responses of polycrystalline deposits of MHPs coated onto 80  $\mu$ m DIA substrates under intermittent exposures to light and dark periods for: (a) MAPbI<sub>3</sub> under the constant gas pressure of N<sub>2</sub>, and (b) MAPbBr<sub>3</sub> under the constant gas pressure of O<sub>2</sub>. The PL was excited with above-band gap photons, at excitation wavelengths of  $\lambda_{exc} = 546$  nm and  $\lambda_{exc} = 470$  nm, for MAPbI<sub>3</sub> and MAPbBr<sub>3</sub>, respectively.

Overall, the above-mentioned findings demonstrated that the PL responses of the polycrystalline deposits of MAPbI<sub>3</sub> and MAPbBr<sub>3</sub> coated onto cylinder-shaped substrates having small diameters (80  $\mu$ m or 330  $\mu$ m) and exposed to environmental gaseous media at constant pressures were remarkably stable and reproducible. We associate this remarkable reproducibility of the observed PL enhancements or diminishments to a simple approach adopted in this study, in which the deposits of MAPbI<sub>3</sub> and MAPbBr<sub>3</sub> were characterized without any extra additional layers or interfaces. Therefore, upon dynamic switching of the chemical environment, concomitant with relatively short time exposures (<1 hour for a single cycle), the time-resolved PL responses were exclusively dependent on the properties of MHPs themselves and their interactions with environmental gaseous media at constant pressures. However, notwithstanding the aforementioned results, further studies are necessary to shed more light on the practical feasibility of gas sensing with using MHPs. In particular, recently, Senocrate *et al.* reported a severe material degradation caused by light-enhanced diffusion and dissolution of oxygen in the bulk of polycrystalline deposits of MAPbI<sub>3</sub> under long times of exposures (>10 h) [129].

## 4.3 Conclusion

In conclusion, we have systematically studied photophysical properties of the two archetypal metal-halide perovskites, MAPbI<sub>3</sub> and MAPbBr<sub>3</sub>, under exposure to various gaseous media. To the best of our knowledge, this is the first report showing strongly differential responses of photoluminescence (PL) and photocurrent (PC) for these two polycrystalline MHPs materials deposited onto cylinder-shaped substrates having small diameters (80  $\mu\text{m}$  or 330  $\mu\text{m}$ ) and simultaneously exposed to two important environmental gaseous media, such as oxygen (O<sub>2</sub>) and nitrogen (N<sub>2</sub>).

Specifically, we show that for polycrystalline samples of MAPbI<sub>3</sub> and MAPbBr<sub>3</sub> prepared in such way, *i.e.* having longitudinal-cylindrical geometries and high *surface-to-volume* ratios, their PL responses undergo pronouncedly opposite changes, while they are positioned *side-by-side* in a miniature custom-built gas-flow chamber and simultaneously exposed to the flow of either O<sub>2</sub> or N<sub>2</sub>.

In particular, under exposure to O<sub>2</sub>, the PL signal intensity of MAPbI<sub>3</sub> rapidly decreased (on a time scale of  $\sim 50$  s), whereas it markedly increased for MAPbBr<sub>3</sub> (on a much faster time scale of  $\sim 21$  s). In contrast, under exposure to N<sub>2</sub>, the PL response of MAPbI<sub>3</sub> raised back and restored its initial level (on a time scale of  $\sim 260$  s), whereas the PL signal of MAPbBr<sub>3</sub> decreased (on a similar time scale of  $\sim 300$  s). The corresponding relative (although opposite) changes in the PL signal amplitudes under recurrent exposures to the flow of either N<sub>2</sub> or O<sub>2</sub> were found to be of  $\sim 73$  % and of  $\sim 87$  %, for the deposits of MAPbI<sub>3</sub> and MAPbBr<sub>3</sub>, respectively.

Interestingly, the PC response of the MAPbBr<sub>3</sub> deposit recurrently exposed to the flow of either N<sub>2</sub> or O<sub>2</sub> largely correlated with the evolution of the PL signal. In contrast, for the deposits of MAPbI<sub>3</sub>, recurrently exposed to the flow of either N<sub>2</sub> or O<sub>2</sub>, the PC response revealed an anti-correlated behavior as compared to the changes in PL.

The herein observed marked differential evolution of the PL responses of the deposits of MHPs upon their exposure to the intermittent flow of various environmental gaseous media have been associated with different interaction mechanisms of shallow- and deep-level surface defect centers in these materials with physisorbed molecules of a strong gaseous electron acceptor, that is molecular O<sub>2</sub>.

This portion of the research was presented in details in K. Mantulnikovs *et al.*, "Differential response of the photoluminescence and photocurrent of polycrystalline CH<sub>3</sub>NH<sub>3</sub>PbI<sub>3</sub> and CH<sub>3</sub>NH<sub>3</sub>PbBr<sub>3</sub> to the exposure to Oxygen and Nitrogen", published in *ACS Appl. Electron. Mater.* on September the 4<sup>th</sup> 2019 [161].





## 5 Wavelength-dependent selective photo-bleaching in MAPbI<sub>3</sub> – impact of the variable oxygen/nitrogen atmosphere

### 5.1 Introduction

Over the last ten years, solar cells based on organic–inorganic metal halide perovskites (MHPs), usually represented by methylammonium lead triiodide (MAPbI<sub>3</sub>), have witnessed impressive increase in power conversion efficiencies (PCE) and draw tremendous attention of the scientific community. However, practical relevance of MAPbI<sub>3</sub> and parent MHP compounds still remains unclear owing to the poor long-term stability and notorious short device operation time. So far, the longest life-time reported for MHP-based photovoltaic devices is roughly one year [162], which is much shorter than 25 years – as expected for the already well-established and commercialized silicon-based technologies. In particular, long-term functioning of MHPs-based devices, operating in real conditions, under exposure to elevated temperatures, oxygen, moisture, and UV-VIS light, still remains a challenge and severely limits the field of their applications [163, 164].

One of the critical issues concerning the long-term stability of MHP-based photovoltaic devices is their interaction with the second major constituent of the atmosphere that is molecular oxygen (O<sub>2</sub>). In this context, there have been numerous publications [165, 130, 131, 133, 166] reporting on both beneficial and harmful effects of the combined action of the atmospheric O<sub>2</sub> and light.

Specifically, the PL enhancement, also called “photo-brightening”, was reported for crystals and polycrystalline films of MAPbI<sub>3</sub> in the presence of molecular O<sub>2</sub>, especially at low levels of photo-excitation [130]. The observed increase in the quantum yield of the PL emission of MAPbI<sub>3</sub> samples in oxygen-rich environments was associated with the oxygen-mediated passivation of the surface electronic trap states. One of the possible explanation of this oxygen-mediated passivation of defects in oxygen-rich environments was ascribed to the process

## Chapter 5. Wavelength-dependent selective photo-bleaching in MAPbI<sub>3</sub> – impact of the variable oxygen/nitrogen atmosphere

---

of physisorption of oxygen at the MAPbI<sub>3</sub> surface, followed by diffusion of O<sub>2</sub> molecules toward the iodine vacancies [145]. On the other hand, rapid “photo-degradation” has also been reported for MAPbI<sub>3</sub> deposits exposed to prolonged illumination in the presence of molecular O<sub>2</sub>, in particular when higher light intensities were used. This latter phenomenon was associated to the photo-generation of superoxide radicals (O<sub>2</sub><sup>-</sup>) at the surface of MAPbI<sub>3</sub> crystallites [145]. In addition, recently, a strong efficiency dependence of photo-induced processes of activation/deactivation of traps on the power of photo-excitation was reported D. Hong *et al.*, who observed both PL enhancement and PL decline for the same MAPbI<sub>3</sub> crystal [159].

Another important phenomenon that needs further attention is the selective, wavelength-dependent, photo-bleaching mechanism in MHPs, such as MAPbI<sub>3</sub>, since they seem to behave inhomogeneously when exposed to different excitation wavelengths. Specifically, there has been a recent report by Quitsch *et al.* [149] demonstrating distinctively opposite processes of either photo-brightening or photo-bleaching in thin film deposits of MAPbI<sub>3</sub> under illumination with either 532 nm or 457 nm wavelengths, respectively. The authors also found a critical excitation wavelength of ~520 nm, around which the photo-brightening and photo-bleaching effects compensated each other. This latter phenomenon was associated with matching of the excitation wavelength of ~520 nm to the residual band gap of PbI<sub>2</sub> (~2.38 eV at room temperature) [167]. In their publication, Quitsch *et al.* also suggested a partial reversibility of the photo-bleaching induced by the short-wavelength ( $\lambda_{exc} < 520$  nm) illumination, *e.g.* by short storage periods in the dark.

Overall, recent reports concerning the long-term stability of MHP-based photovoltaic devices suggest a rather complex and not totally well-understood mechanisms, which, depending on the variability of the experimental conditions, lead to either PL enhancement or PL decline. Therefore, further studies are needed to shed more light on the dependence of the photo-physical and photo-chemical properties of MHPs, while implementing a whole variety of wavelengths and power of photo-excitation as well as under precisely controlled components and content of the gaseous atmosphere.

In this context, in this work, we focused on checking the concurrent light-induced processes of photo-brightening and photo-bleaching in MAPbI<sub>3</sub> thin film deposits and single crystals. The experiments were performed under the well-controlled dry gaseous media atmosphere, consisting of either O<sub>2</sub> or N<sub>2</sub>. In particular, our experimental setup enabled us to perform repeatable photo-bleaching and partial photo-recovery cycles in polycrystalline deposits of MAPbI<sub>3</sub>, which were induced by the intermittent illumination with a strong flux of visible light at two wavelengths: 545 nm and 470 nm. In addition, we could also perform co-excitation experiments, when MAPbI<sub>3</sub> thin film deposits or single crystals were photo-excited simultaneously with two different wavelengths (of 545 nm and 470 nm). In this unique experimental approach we could probe the two competing processes of photo-brightening and photo-bleaching at the same time.

Overall, this chapter presents novel observations related to photo-brightening or photo-bleaching (photo-degradation) in MAPbI<sub>3</sub> thin film deposits and single crystals as well as shows the dependence of these processes on the content of the gaseous atmosphere and the photo-excitation wavelength. These findings might help to gather a better insight into charge generation and recombination processes and can help in achieving rational design and tailored properties of MAPbI<sub>3</sub>-based optoelectronic and photovoltaic devices.

## 5.2 Results and discussion

### 5.2.1 Co-excitation experiments on the polycrystalline deposits of MAPbI<sub>3</sub> under controlled atmosphere

MAPbI<sub>3</sub> deposits coated onto 80  $\mu$ m diameter cylindrical quartz substrates were used for measurements of the changes in the PL intensity under intermittent excitation with two different excitation wavelengths, of 546 nm and 470 nm. As described in more details in Chapter 3, the MAPbI<sub>3</sub> deposits coated onto cylindrical quartz substrates having small diameters (80 and 330  $\mu$ m) consisted of densely packed microwires. The experiments were performed under precisely controlled atmosphere of dry gases, either in O<sub>2</sub> or N<sub>2</sub>. The samples were placed in a miniature gas-flow chamber with a volume of  $\sim$ 160  $\mu$ l (for more technical details see Chapter 2).

The PL intensity kinetics were acquired under the excitation wavelengths of either 546 nm or 470 nm. The obtained PL time evolutions collected in O<sub>2</sub> and N<sub>2</sub> are shown in Figure 5.1. Similar results have been obtained by Quitsch *et al.*, with a major difference that their experiments were performed in air and the ratios between the green and blue light excitation powers were of  $\sim$ 30, as compared to  $\sim$ 2 in our experiments. Authors attribute the decay in the PL intensity under excitation with blue light (457 nm) to photo-degradation, while the PL increase under excitation at 532 nm, in a relatively short timescale, is believed to be the typical photo-brightening.

Figure 5.1(a) illustrates a similar overall behavior of the kinetics of PL to that reported by Quitsch *et al.* [149]. Under the controlled atmosphere of either pure O<sub>2</sub> or N<sub>2</sub>, initially, the PL intensity experiences a relatively rapid “photo-brightening” phase on a time scale of  $\sim$ 890 seconds, which is then followed by a slower “photo-degradation”. At the moment of switching the excitation from 546 nm to 470 nm, both time traces show a significant and very quick drop (of  $\sim$ 2 to 20 times) in intensity with a minor recovery and stabilization of the PL intensity level. When the wavelength of excitation is changed, a fast recovery occurs and the PL time-evolution is continued, *i.e.* it decays during the prolonged exposure. The blow-up of the transition dynamics can be seen in Figure 5.1(b), from which we can deduce that the initial major part of the recovered intensity is restored in less than 5 seconds in both atmospheres.

It should be noted, that, as mentioned in Chapter 2, the intensities of the two excitations were different, *i.e.* 480 mW/cm<sup>2</sup> and 240 mW/cm<sup>2</sup> for 546 nm and 470 nm excitations respectively.

## Chapter 5. Wavelength-dependent selective photo-bleaching in MAPbI<sub>3</sub> – impact of the variable oxygen/nitrogen atmosphere

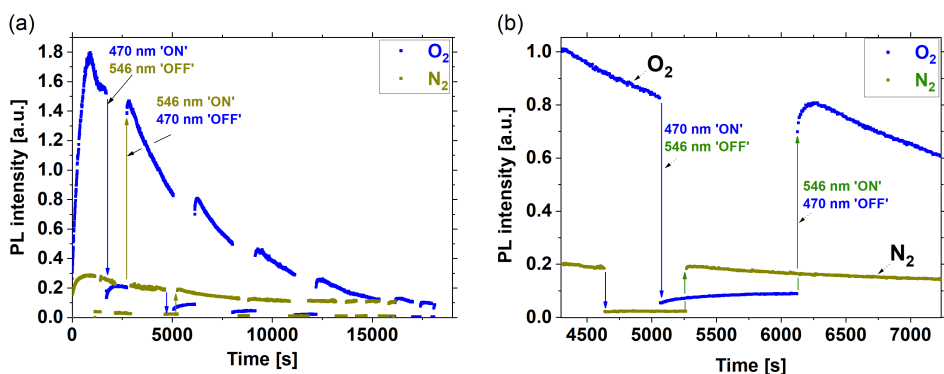


Figure 5.1 – Kinetic traces of the photoluminescence (PL) intensity collected for a polycrystalline deposit of MAPbI<sub>3</sub> coated onto an 80  $\mu$ m diameter substrate under exposure to the flow of pure gaseous media of either O<sub>2</sub> (blue trace) or N<sub>2</sub> (green trace) and intermittent changes of the excitation light wavelengths between 546 nm and 470 nm. The onset and offset moments of turning on the excitation wavelength of either 470 nm “ON” (546 nm “OFF”) or 546 nm “ON” (470 nm “OFF”), are indicated by blue and green vertical arrows, respectively. The “down” and “up” arrowheads point to the respective instantaneous decrease or increase in the PL intensity upon switching the excitation wavelength from 546 nm to 470 nm. (a) The complete kinetic traces of the PL intensity acquired in the presence of either O<sub>2</sub> (blue trace) or N<sub>2</sub> (green trace) indicating that an initial rapid “photo-brightening” is followed by a slower “photo-degradation”. (b) The blow-up of (a) showing the details of the kinetic traces corresponding to two events of switching of the excitation wavelength: from 546 nm to 470 nm (indicated by blue arrows) and from 470 nm to 546 nm (indicated by green arrows). The blow-up shown in (b) was chosen for the time lapse between  $\sim$ 4300 seconds and  $\sim$ 7230 seconds. The light excitation power densities were of 480 mW/cm<sup>2</sup> and 240 mW/cm<sup>2</sup>, for 546 nm and 470 nm wavelengths, respectively.

This 2 times difference in the excitation powers cannot be solely accounted for such a large drops in the PL intensity.

To elucidate this phenomenon, we performed the first experiment of its kind, based on co-excitation of MAPbI<sub>3</sub> samples with the green light at 546 nm in parallel with the blue light at 470 nm and a lower power ( $\sim$ 25 mW/cm<sup>2</sup>). The results of such exposure to a single wavelength excitation, intermittent with a co-excitation periods are shown in Figure 5.2.

Figures 5.2(a & c) show that upon co-exciting the sample with two wavelengths, the PL intensity experiences a drop in both cases, under O<sub>2</sub> and N<sub>2</sub> respectively. This is very counter-intuitive, as the additional flux of photons should normally lead to an increased PL intensity. This gives us a hint that the co-excitation with the additional wavelength of 470 nm might have a previously unreported diminishing effect on the properties of MAPbI<sub>3</sub> and the devices based on it.

In particular, Figure 5.2(b) shows the details of a single co-excitation cycle when the additional excitation at 470 nm wavelength is turned on at  $\sim$ 8725 seconds in parallel to the main exci-

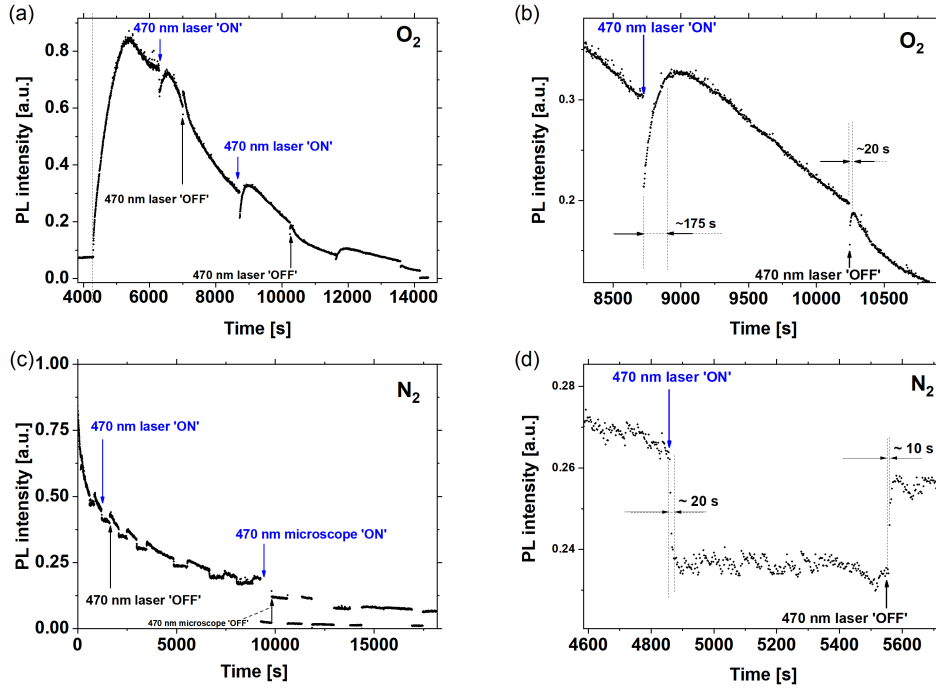


Figure 5.2 – Photoluminescence intensity time traces of a polycrystalline film of MAPbI<sub>3</sub> coated onto a 80  $\mu\text{m}$  under controlled atmospheres of O<sub>2</sub> (a) and (b) or N<sub>2</sub> (c) and (d) and intermittent switching between excitation at 546 nm and co-excitation at 546 nm and 470 nm laser denoted by “470 nm laser ON” markings. (b) and (d) demonstrate the dynamics of such switching event in a zoom-in of the experimental timespan. The zoomed region in (b) and (d) was chosen for the time lapse between ~8300 seconds and from ~10900 seconds to ~4600 seconds and ~5700 seconds, respectively.

tation wavelength of 546 nm and is turned off at 10245 seconds. It can be seen that after the above-described drop in O<sub>2</sub>, the PL intensity recovers with a time constant of about 180 seconds, overshoots the previous level and subsequently continues the overall trend of the PL intensity decay during a long-time exposure. Interestingly, at the moment of switching the co-exciting wavelength, the PL intensity drops, as one would expect, due to decreased photon flux and then recovers relatively fast on the timescale of ~20 seconds to continue the overall trend.

In contrast, a slightly different process dynamics is observed in N<sub>2</sub>, as can be seen in Figure 5.2(d), which shows the details of a single co-excitation cycle when the additional excitation at 470 nm wavelength is turned on at ~4860 seconds and turned off at ~5555 seconds. Here, both the PL intensity drop upon turning co-excitation on (at 470 nm) and the recovery after switching the co-excitation off are relatively fast, occurring on timescales of ~10 to ~20 seconds. There are no other features observed for the recovery dynamics in N<sub>2</sub>. Yet, the biggest difference from the corresponding dynamics in O<sub>2</sub> is that instead of recovery under co-excitation, the PL intensity is actually stable during the whole co-excitation time.

### 5.2.2 Co-excitation experiments on single crystals of MAPbI<sub>3</sub> under controlled atmosphere

To have a better insight into the phenomenon, we expanded our study also to single crystals of MAPbI<sub>3</sub> to check for the differences brought by the change of morphology between single crystals and films.

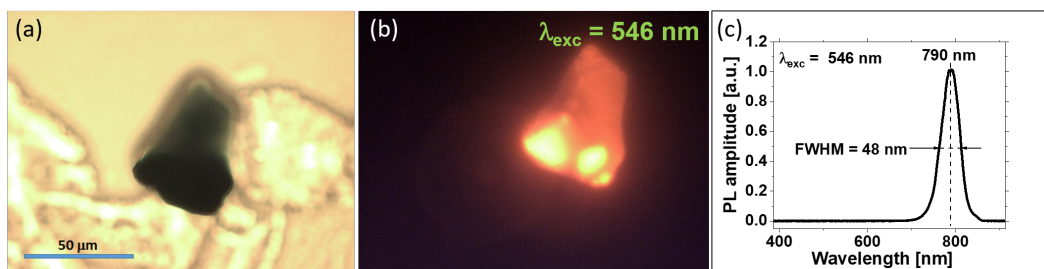


Figure 5.3 – (a) Visible light and (b) photoluminescent photo of the single crystal of MAPbI<sub>3</sub> under controlled atmosphere used in PL measurements. (c) The corresponding PL spectrum under excitation at 546 nm.

The microscopic images of the MAPbI<sub>3</sub> single crystal used in this part of the study are shown in Figure 5.3(a & b). Specifically, Figure 5.3(a) shows the bright-field visible light image, while Figure 5.3(b) depicts the corresponding luminescence image under excitation of 546 nm. Figure 5.3(c) shows a typical single crystal PL spectrum, peaking around 790 nm. Results of the co-excitation experiment on a single crystal of MAPbI<sub>3</sub> under controlled atmosphere of either O<sub>2</sub> or N<sub>2</sub> can be seen in Figures 5.4(a & b).

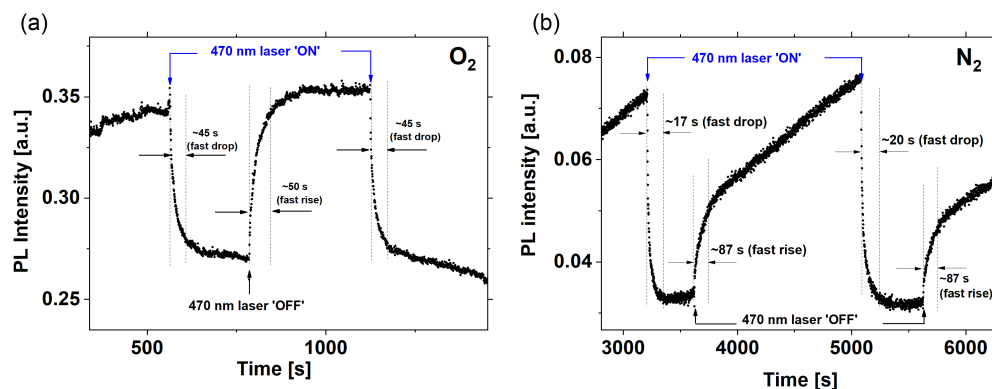


Figure 5.4 – PL intensity time traces collected for a single crystal of MAPbI<sub>3</sub> under controlled atmospheres of O<sub>2</sub> (a) or N<sub>2</sub> (b) and intermittent switching between excitation at 546 nm and co-excitation at 546 nm and 470 nm, denoted by “470 nm laser ON” markings.

Once again, the steady-state level of the PL intensity was achieved by exciting the MAPbI<sub>3</sub> crystal at 546 nm. As for the experiments with the polycrystalline deposits, a similar drop in the PL intensity in both atmospheres was observed upon turning on the co-exciting wavelength (470 nm). As shown in Figures 5.4(a & b), there are slight differences in the timescales of these

drops, *i.e.* they are of  $\sim 45$  and  $\sim 17$  seconds, in  $O_2$  and  $N_2$ , respectively.

In contrast, bigger differences arise upon removal of the co-exciting light that is during the recovery phase. While in  $O_2$ , upon removal of the co-exciting light, the intensity reaches saturation after  $\sim 50$  seconds, thus being quite fast, in  $N_2$ , we observe a much longer timescale of the recovery phase ( $\sim 90$  seconds) and the lack of saturation, concomitant with a linear increase in the PL intensity.

We infer that such behavior could stem from the competition of the processes brought upon by  $O_2$  and the co-exciting blue light at 470 nm. When comparing Figures 5.4 and 5.2, we attribute at least some part of the observed differences in timescales of the PL intensity drops and recoveries to the distinctively different *surface-to-volume* ratios of crystals and polycrystalline deposits.

### 5.3 Conclusion

Taken together, these observations suggest that, for thin films of  $MAPbI_3$ , the excitation at 470 nm and interactions with  $O_2$  molecules trigger competitive mechanisms. It seems that these two factors influence and modulate the overall fate of photo-generated carriers in  $MAPbI_3$  through markedly diversified processes as schematically shown in Figure 5.5. Specifically,  $O_2$  molecules neutralize the charged surface defects (non-radiative traps), whereas excitation at 470 nm provides a competitive pathway, which re-populates the non-radiative recombination centers. Molecular oxygen,  $O_2$ , an electron acceptor, might compete with the light-mediated process of charging the  $I^{+1}$  deep intra-band trap states ( $I^{+1} \rightarrow I^{-1}$ ). This would preserve the non-radiative deep recombination centers ( $I^{+1}$ ), thus leading to the PL depletion. On the other hand, molecules of  $O_2$  can also compete with the light-activation of  $Pb^0$  intra-band recombination centers, contributing, in contrast, to higher PL levels.

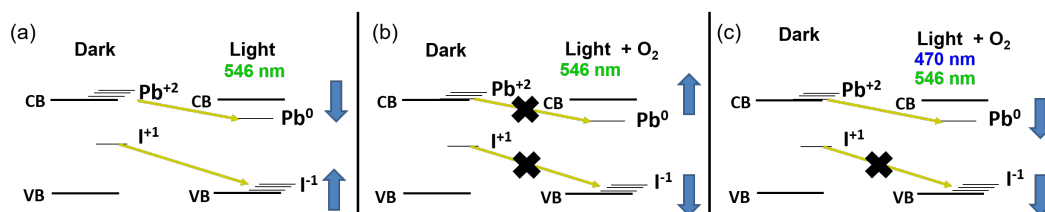


Figure 5.5 – Schematic representations of the electronic energy level alignments under different light excitation conditions showing the concurrent processes: (a) in the dark and under single-wavelength excitation (546 nm); (b) in the dark and under single-wavelength excitation (546 nm) in  $O_2$ ; (c) in the dark and under co-excitation at 546 nm and 470 nm in  $O_2$ .





## 6 Light-induced charge transfer at the MAPbI<sub>3</sub>/TiO<sub>2</sub> interface – a low-temperature Photo-ESR assay

### 6.1 Introduction

In parallel to applications of MHPs in photovoltaics, a number of studies have also investigated a variety of MHPs-based detectors and sensors, including X-ray detecting devices [72], near-ultraviolet to near-infrared (330 – 800 nm) light detectors [168, 169, 170, 171], tactile sensors [172], as well as gas [37], and even high-energy particle detectors [173].

In general, the above-mentioned devices have been designed as stacked-planar structures. Therefore, for the purpose of performing specific applications, their architectures required a stack of various kinds of functional thin layers. In consequence, besides MHP-based light-harvesting layers and device terminal electrodes, the remaining most investigated elements of the stacked-planar architectures have been the electron transport layers (ETLs) and hole transport layers (HTLs).

To date, among various compounds suitable for applications in MHP-based photovoltaic devices, TiO<sub>2</sub> remains the most widely used material for preparing ETLs [63]. In particular, TiO<sub>2</sub> offers a number of important advantages, including chemical stability, nontoxicity, high charge mobilities, well-matched band structure with MHPs, low cost and simple fabrication procedures [174].

It has been shown that the performance of TiO<sub>2</sub>-based ETLs could be largely improved through bandgap-engineering by doping TiO<sub>2</sub> with transition metal [175] or nonmetal elements [176, 177], surface functionalization [178], photosensitization [179] and heterojunction preparation [180]. In fact, the recent surge of interest in MHPs-based photovoltaics opened a new research area oriented towards improvement of the physicochemical properties of TiO<sub>2</sub>, as well as morphology optimization of TiO<sub>2</sub>/MHPs interfaces [181].

MAPbI<sub>3</sub>, the archetypal and also the first successfully employed MHP in solar cells, is continuing to be used as a model material to study the transfer mechanisms of light-generated

## Chapter 6. Light-induced charge transfer at the MAPbI<sub>3</sub>/TiO<sub>2</sub> interface – a low-temperature Photo-ESR assay

---

carriers in various types of bilayer MHP/ETL or MHP/ HTL systems [182, 183, 184].

In this context, there have been several reports on the transfer mechanisms of photogenerated carriers at the interfaces between MHPs and the ETL materials, such as TiO<sub>2</sub>, or HTL materials, such as Spiro-OMeTAD or PCBM [185, 186, 187]. In these investigations, time-resolved spectroscopic techniques, including transient absorption (TA), photoluminescence (TRPL), and terahertz absorption (TRTS), as well as time-resolved microwave photoconductivity (TRMC), have been the most widely implemented methodological approaches [188].

Despite intensive research, direct observation of the transfer of photogenerated carriers at the MHP/ETL interface still remains a challenge. This complicates gaining insight into the role of surface and bulk defects at the MHP/ETL interface and to better understand their influence on the device performance. Therefore, one of the goals of this PhD thesis was trying to tackle the problem of the charge transfer of light-generated carriers in bilayer MHP/ETL systems. In particular, in our attempt to gain insight into this process, we implemented the technique of low-temperature electron spin resonance (ESR) in combination with *in situ* illumination (photo-ESR). The results of this study demonstrate that the above-mentioned approach can be used to directly monitor the charge transfer from MAPbI<sub>3</sub> to TiO<sub>2</sub>, as well as to determine the exact number of trapped electrons by the TiO<sub>2</sub> surface defects.

Specifically, we report a low-temperature photo-ESR study performed on a model nanohybrid system consisting of TiO<sub>2</sub> nanowires (TiO<sub>2</sub>NWs) dispersed in a polycrystalline MAPbI<sub>3</sub> matrix. Our approach is based on observation of the light-induced decrease in intensity of the ESR signal of paramagnetic defects of trivalent titanium (Ti<sup>3+</sup>,  $S = 1/2$ ) in TiO<sub>2</sub>NWs. Prior to low-temperature ESR measurements, in order to enhance the concentration of Ti<sup>3+</sup> defects, TiO<sub>2</sub>NWs were thermally reduced in hydrogen (H<sub>2</sub>) atmosphere. The thermal reduction process resulted not only in the formation of a large concentration of Ti<sup>3+</sup> defect centers, but was also accompanied by a marked color change of the TiO<sub>2</sub>NWs; from white to blue. Therefore, hereinafter, non-reduced (oxidized) TiO<sub>2</sub>NWs and thermally reduced TiO<sub>2</sub>NWs, are referred to as white-TiO<sub>2</sub>NWs and blue-TiO<sub>2</sub>NWs, respectively.

The observed diminishment of the ESR signal upon illumination with the green laser light ( $\lambda_{exc} = 532$  nm) is associated with the photo-excited electrons that cross the MHP/ETL interface between the grains of polycrystalline MAPbI<sub>3</sub> and dispersed blue-TiO<sub>2</sub>NWs, thus leading to the conversion of paramagnetic states of Ti<sup>3+</sup> to the ESR-silent Ti<sup>2+</sup> states.

### 6.2 Results and discussion

To quantify the effect of the charge transfer at the interface between MAPbI<sub>3</sub> and TiO<sub>2</sub> and to gain insight into the underlying mechanisms, we performed low-temperature photo-ESR measurements on a model nanohybrid system consisting of blue-TiO<sub>2</sub>NWs dispersed in a polycrystalline MAPbI<sub>3</sub> matrix. In this approach, thermally-reduced TiO<sub>2</sub>NWs (blue-TiO<sub>2</sub>NWs), containing a large concentration of paramagnetic defects of trivalent titanium (Ti<sup>3+</sup>,  $S = 1/2$ ),

were used as a representative ETL material. Moreover, the dispersion of blue-TiO<sub>2</sub>NWs in polycrystalline MAPbI<sub>3</sub> ensured a large distributed surface of the MAPbI<sub>3</sub>/blue-TiO<sub>2</sub>NWs interface.

### 6.2.1 Morphological and elemental characterization of the MAPbI<sub>3</sub>/blue-TiO<sub>2</sub>NWs nanohybrid material

Morphological characterization of blue-TiO<sub>2</sub>NWs and the MAPbI<sub>3</sub>/blue-TiO<sub>2</sub>NWs nanohybrid material is presented in Figure 6.1. Specifically, Figure 6.1(a) shows the SEM image of a thin film deposit consisting solely of blue-TiO<sub>2</sub>NWs. As can be seen, blue-TiO<sub>2</sub>NWs form a highly interlaced pattern made up of a large number of entangled individual nanowires with a high length-to-width aspect-ratio and average dimensions of  $\sim 10$  nm in width and  $\sim 5 - 10$   $\mu\text{m}$  in length (Figure 6.1(a)).

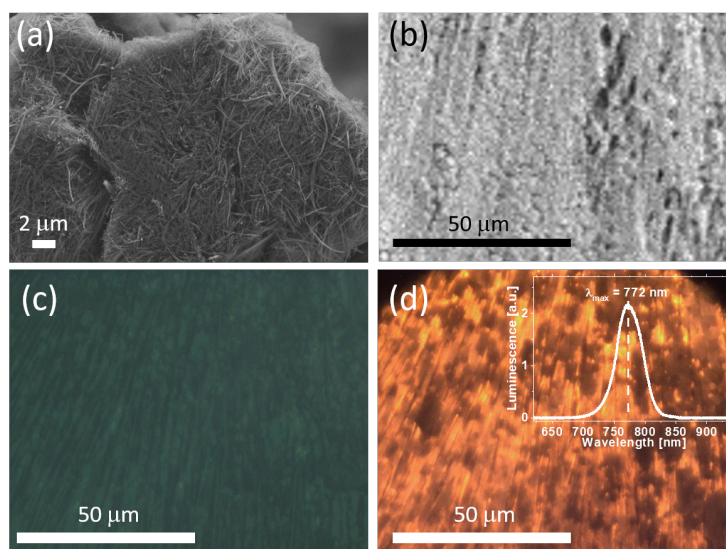


Figure 6.1 – Morphological characterization of blue-TiO<sub>2</sub>NWs and the MAPbI<sub>3</sub>/blue-TiO<sub>2</sub>NWs. (a) SEM image of the blue-TiO<sub>2</sub>NWs deposit. (b) SEM, (c) optical and (d) luminescence (under excitation with  $\lambda_{exc} = 546$  nm) microscopy images of the MAPbI<sub>3</sub>/blue-TiO<sub>2</sub>NWs nanohybrid coated onto a planar surface of a microscope slide showing the MAPbI<sub>3</sub> wire-like morphology and inclusions of blue-TiO<sub>2</sub>NWs (dark, non-luminescent spots in (d)). Inset: The PL spectrum acquired for the MAPbI<sub>3</sub>/blue-TiO<sub>2</sub>NWs nanohybrid material.

The morphological features of the MAPbI<sub>3</sub>/blue-TiO<sub>2</sub>NWs nanohybrid coated onto a planar surface of a glass microscope slide are shown in Figures 6.1(b – d). In particular, Figure 6.1(b) shows that the deposit the MAPbI<sub>3</sub>/blue-TiO<sub>2</sub>NWs nanohybrid is made up of a parallel array of MAPbI<sub>3</sub> microwires having average widths and lengths of  $\sim 5$   $\mu\text{m}$  and  $\sim 50$   $\mu\text{m}$ , respectively. Although the aligned in parallel MAPbI<sub>3</sub> microwires dominate the SEM image in Figure 6.1(b), the presence of numerous agglomerates of blue-TiO<sub>2</sub>NWs can also be seen. They form randomly distributed protuberances on a more regular pattern of MAPbI<sub>3</sub> microwires and can

## Chapter 6. Light-induced charge transfer at the MAPbI<sub>3</sub>/TiO<sub>2</sub> interface – a low-temperature Photo-ESR assay

also be seen in Figure 6.1(d) as dark, non-emitting spots in the luminescence microscopy image (collected under excitation with  $\lambda_{exc} = 546$  nm wavelength). The inset to Figure 6.1(d) shows the corresponding PL spectrum. This spectrum, peaking at  $\sim 770$  nm and having a relatively narrow full width half maximum (FWHM) of  $\sim 48$  nm, is characteristic for MAPbI<sub>3</sub> and points to a high-quality of this MHP in the deposit of MAPbI<sub>3</sub>/blue-TiO<sub>2</sub>NWs nanohybrid.

The results of the SEM/EDX elemental analysis of MAPbI<sub>3</sub>/blue-TiO<sub>2</sub>NWs nanohybrid are shown in Figure 6.2. The elemental analysis was performed for a selected surface fragment (with dimensions  $75\ \mu\text{m} \times 75\ \mu\text{m}$ ) of the deposit and focused on the presence of three elements, iodine, lead, and titanium. The overlapped EDX-detected traces of these three elements can be seen in Figure 6.2(a). The comprehensive EDX-analysis spectrum and the element distribution histogram are shown in Figure 6.2(b). The individual element distribution maps for iodine, lead and titanium are presented in Figure 6.2(c), Figure 6.2(d) and Figure 6.2(e), respectively. The element distribution maps shown in Figures 6.2(c & d), correspond to iodine and lead (both present in MAPbI<sub>3</sub>), whereas the distribution map shown in Figure 6.2(e) corresponds to titanium, which is present in the second component of the nanohybrid material, *i.e.* blue-TiO<sub>2</sub>NWs.

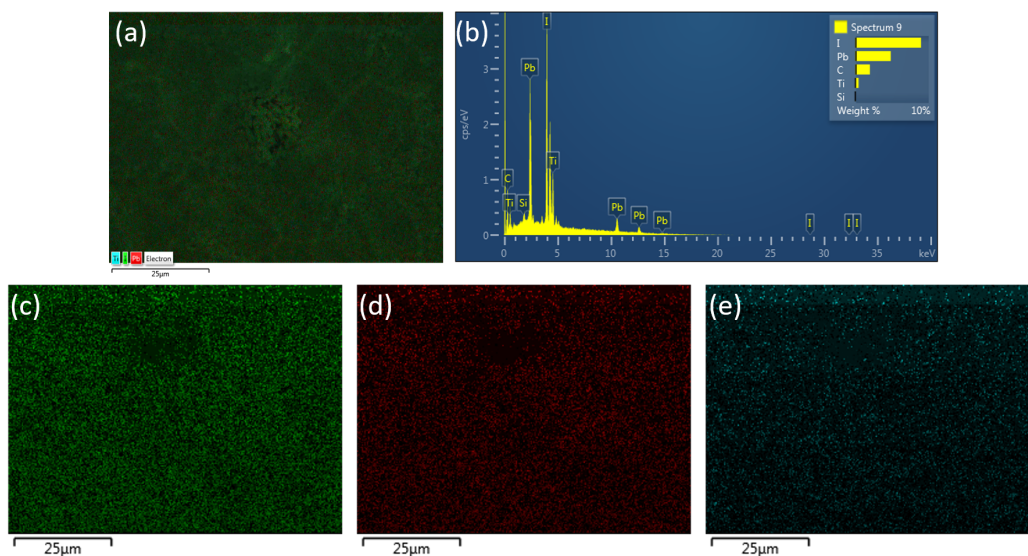


Figure 6.2 – The SEM/EDX elemental mapping analysis performed for a selected surface fragment ( $75\ \mu\text{m} \times 75\ \mu\text{m}$ ) of a thin film deposit of the MAPbI<sub>3</sub>/blue-TiO<sub>2</sub>NWs nanohybrid, showing: (a) overlapped EDX-detected traces of three elements, iodine (green dots), lead (red dots), and titanium (cyan dots); (b) the comprehensive EDX-analysis spectrum and the element distribution histogram; and the individual element distribution maps of iodine (c), lead (d) and titanium (e).

The SEM/EDX elemental mapping analysis clearly indicates a homogeneous distribution of the three above-mentioned elements and provides evidence for a uniform spread of blue-TiO<sub>2</sub>NWs and MAPbI<sub>3</sub> microwires within the selected fragment of the MAPbI<sub>3</sub>/blue-TiO<sub>2</sub>NWs

nanohybrid deposit.

It is noteworthy to mention that thin film deposits of MAPbI<sub>3</sub> coated by single-step solution casting from neat DMF solutions very often have microwire- or fibre-like morphological structures [189]. We also have previously reported a similar microwire-like morphology and practically identical luminescence characteristics for single-step solution casted deposits of MAPbI<sub>3</sub> on various types of both curved and flat substrates. In particular, microwires with sizes of  $\sim 8 \mu\text{m}$  in diameter and up to  $\sim 150 \mu\text{m}$  in length were observed for small substrates' curvatures or flat surfaces [113]. Therefore, one can conclude that the presence of blue-TiO<sub>2</sub>NWs does not significantly modify nucleation and crystal growth of MAPbI<sub>3</sub> microwires during deposition of the MAPbI<sub>3</sub>/blue-TiO<sub>2</sub>NWs nanohybrid from stoichiometric solutions of MAPbI<sub>3</sub> in DMF.

### 6.2.2 Spin state configurations of Ti defect centers in blue-TiO<sub>2</sub>NWs

As already mentioned in Section 6.1, the transfer of light-excited non-equilibrium electrons from MAPbI<sub>3</sub> to the reduced TiO<sub>2</sub> (blue-TiO<sub>2</sub>NWs) should result in a partial modification of the population of the paramagnetic electron-trapping Ti<sup>3+</sup> centers. It is then inferred that electrons generated by light in MAPbI<sub>3</sub> traverse the interface MAPbI<sub>3</sub>/blue-TiO<sub>2</sub>NWs and are partially trapped by paramagnetic Ti<sup>3+</sup> defect centers ( $3d^1$ ,  $S = 1/2$ ). As a result, a fraction of the Ti<sup>3+</sup> paramagnetic species is being reduced to Ti<sup>2+</sup> ESR silent states. This offers the opportunity to track the electron transfer process by monitoring the decrease of the ESR signal of Ti<sup>3+</sup>.

The herein suggested process of one-electron reduction of Ti<sup>3+</sup> paramagnetic defects deserves an additional comment. In principle, Ti<sup>2+</sup> has a  $3d^2$  electronic configuration. Therefore, the spin state configuration of Ti<sup>2+</sup> can adopt either a high-spin ( $S = 1$ ) or a low-spin ( $S = 0$ ). The former was observed in early ESR studies in zinc-fired ZnSe, in CdTe, and in ZnS [190, 191, 192]. Recently, high-spin ( $S = 1$ ) Ti<sup>2+</sup> species were also reported in strongly reduced TiO<sub>2</sub>, which formed core-shell nanostructures consisting of titanium monoxide (TiO) encapsulated in titania with lower oxygen deficiency (TiO<sub>1+x</sub>), *i.e.* TiO@TiO<sub>1+x</sub> [193]. The presence of high-spin ( $S = 1$ ) Ti<sup>2+</sup> species in TiO@TiO<sub>1+x</sub> was confirmed by the ESR feature at *g*-factor of  $\sim 1.92$ . In this context, the detailed low-temperature ESR investigation performed for the herein studied samples of the reduced TiO<sub>2</sub> (blue-TiO<sub>2</sub>NWs) failed to identify the ESR signal of Ti<sup>2+</sup> both in the dark and upon illumination. Given a large concentration of Ti defects in blue-TiO<sub>2</sub>NWs, this may be explained either by a strong broadening of the corresponding ESR signal or the absence of ESR signal due to its plausible low-spin state configuration ( $S = 0$ ). In particular, since a large number of titanium-related defects occur in tetragonally-distorted octahedral environments, there is only one d orbital available, which, being of the lowest energy, is expected to be filled up first [194, 195, 196]. This may favor stabilization of a low-spin state configuration ( $S = 0$ ) for the Ti<sup>2+</sup> defect centers in blue-TiO<sub>2</sub>NWs.

### **6.2.3 Photo-ESR study of the commercial nanocrystalline TiO<sub>2</sub> anatase – a control experiment**

Commercial TiO<sub>2</sub> anatase (AMT600, Tayca Corp.) was used as a control material to validate our approach of using low-temperature photo-ESR to monitor the light-excited charge transfer at the interface MAPbI<sub>3</sub>/blue-TiO<sub>2</sub>NWs. To this end, a thin layer of anatase AMT600 was deposited directly on a 2 mm-diameter quartz rod (sample holder) by dip-coating, as described in Section 2.2 (see also Figure 2.12(b)).

Figure 6.3 depicts the ESR spectra acquired at 5 K for this sample under dark conditions (black trace) and under illumination with: the green laser,  $\lambda_{\text{exc}} = 532$  nm,  $P = 20.0$  mW (green trace), and the red laser LED,  $\lambda_{\text{exc}} = 650$  nm,  $P = 20.0$  mW (blue trace). Overall, the ESR features observed in Figure 6.3 can be associated with the presence of low concentrations of oxygen vacancies ( $g \sim 1.992$ ), Ti<sup>3+</sup> paramagnetic states ( $g \sim 1.94 - 1.97$ ), as well as oxygen-related radicals (superoxide O<sub>2</sub><sup>-</sup> / oxygen O<sup>-</sup>) at  $g > 2.0$ .

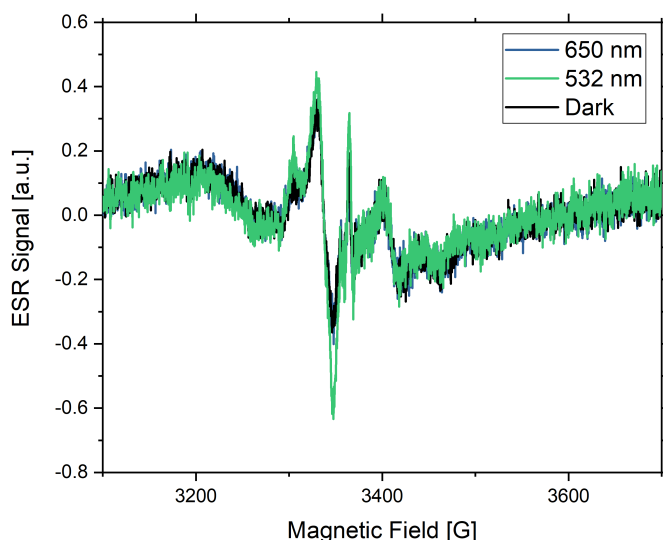


Figure 6.3 – ESR spectra recorded at 5 K for the commercial anatase powder (AMT600, Tayca Corp.) under dark conditions (black trace) and illumination with: green laser,  $\lambda_{\text{exc}} = 532$  nm,  $P = 20.0$  mW (green trace) and red laser LED,  $\lambda_{\text{exc}} = 650$  nm,  $P = 20.0$  mW (blue trace).

It can clearly be seen that, under illumination with 532 nm and 650 nm wavelengths, the ESR spectra do not change as compared to the ESR spectrum recorded in dark conditions. Thus, independent of the differences in the spectral properties of the illuminating wavelengths, this result also points to the absence of heat-induced effects in our experiment (*i.e.* with using the light intensities up to 20 mW).

In contrast to the results observed under illumination with 532 nm and 660 nm wavelengths, under exposure of the same sample to UVA light ( $\lambda_{\text{exc}} = 365$  nm,  $P = 20.0$  mW), the ESR spectra revealed pronounced time-dependent changes. In particular, as shown in Figure 6.4, all the above-mentioned ESR features, present as very weak traces in the initial spectrum recorded in

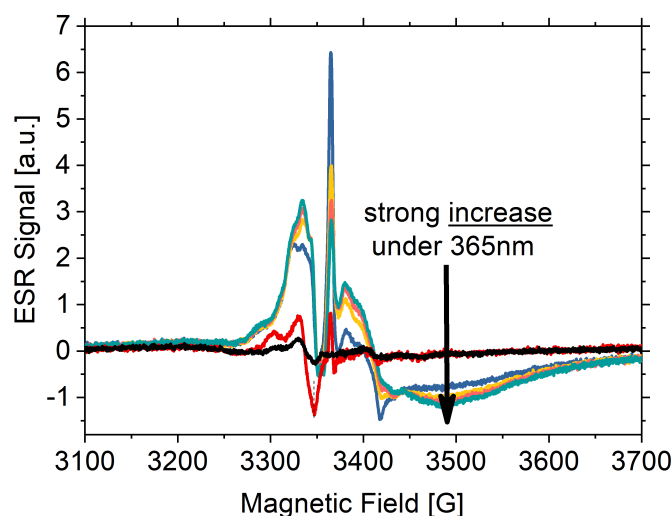


Figure 6.4 – Time-evolution of the ESR spectra recorded at 5 K for the commercial anatase powder (AMT600, Tayca Corp.) under photo-excitation with UVA,  $\lambda_{\text{exc}} = 365$  nm,  $P = 20.0$ : the initial ESR spectrum under dark conditions (black trace) and several progressively increasing ESR spectra with increasing illumination time (color traces).

the dark (black trace in Figure 6.4), markedly grow up under illumination with  $\lambda_{\text{exc}} = 365$  nm. The fastest growth occurred for the ESR signals related to oxygen radicals (superoxide  $\text{O}_2^-$  / oxygen  $\text{O}^-$ , at  $g > 2.0$ ) and to oxygen vacancies ( $\text{V}_\text{O}^-$ , narrow signal at  $g \sim 1.992$ ). In parallel, under illumination with  $\lambda_{\text{exc}} = 365$  nm, the ESR signal related to the paramagnetic states of  $\text{Ti}^{3+}$  (at  $g \sim 1.94 - 1.97$ ) also considerably grows up. The growth of the ESR signal related to  $\text{Ti}^{3+}$  occurred progressively with the illumination time (for up to 15 min of illumination), whereas the narrow ESR signal corresponding to oxygen vacancies ( $\text{V}_\text{O}^-$ ,  $g \sim 1.992$ ) grew up very rapidly at the beginning of illumination (during the first 5 min of exposure to UVA) and then slowly diminished.

Similar behaviors of photo-induced changes in the ESR spectra for either anatase or rutile samples under broad-band illumination (320 – 900 nm) at cryogenic temperatures have been reported earlier [197]. In particular, it has been pointed out that the dynamics of electron trapping at Ti-related defects, as well as de-trapping under dark and continuous illumination conditions depend on the wavelength of illumination and the photon flux intensity. Moreover, the overall electron trapping/de-trapping dynamics strictly depends on the type and density of defect states available. Therefore, the character of the light-induced changes depends also on the crystal phase (anatase or rutile), morphology, crystallinity, and the possible presence of impurities [198].

Taken together, the low-temperature photo-ESR measurements performed for the commercial anatase (AMT600) revealed that the ESR spectra were not sensitive to illumination with the wavelengths of 660 nm and 532 nm, *i.e.* for photon energies lower than the band-gap of  $\text{TiO}_2$  anatase ( $E_g \text{ TiO}_2 = 3.2$  eV). In contrast, the ESR signals recorded for this control material

## Chapter 6. Light-induced charge transfer at the MAPbI<sub>3</sub>/TiO<sub>2</sub> interface – a low-temperature Photo-ESR assay

---

evolved rapidly when the illumination wavelength was changed to 365 nm (the photon energy of 3.4 eV). Specifically, under illumination with  $\lambda_{\text{exc}} = 365$  nm, we observed the growth of ESR features related to the paramagnetic states of Ti<sup>3+</sup> (at  $g \sim 1.94 - 1.97$ ). This is in sharp contrast to the major finding of this work obtained for the model MHP/ETL interface, which was embodied in our study by the MAPbI<sub>3</sub>/blue-TiO<sub>2</sub>NWs hybrid material. Specifically, as discussed later in Section 6.2.6, for this model MHP/ETL interface we observed a significant light-induced diminishment of the Ti<sup>3+</sup>-related signal under excitation at 532 nm (photon energy of 2.33 eV <  $E_{\text{g TiO}_2}$ ).

Overall, the results provided by the low-temperature photo-ESR measurements performed for the commercial TiO<sub>2</sub> anatase validate the choice of the strongly reduced anatase-like TiO<sub>2</sub>, *i.e.* blue-TiO<sub>2</sub>NWs, as a representative ETL material, and the illumination wavelength of 532 nm (photon energy lower than  $E_{\text{g TiO}_2}$ ), to study the light-induced charge-transfer at the model interface MAPbI<sub>3</sub>/blue-TiO<sub>2</sub>NWs.

### 6.2.4 Low-temperature photo-ESR measurements of a strongly reduced (self-doped) crystalline TiO<sub>2</sub> anatase

The validity of our experimental approach based on addressing the paramagnetic Ti<sup>3+</sup> defect centers in TiO<sub>2</sub> as charge-transfer sensitive targets was also proved by performing low-temperature photo-ESR measurements under different illumination conditions for single-crystals of reduced (self-doped) TiO<sub>2</sub> anatase (hereinafter blue-TiO<sub>2</sub>SCs) as well as for a composite material consisting of MAPbI<sub>3</sub> and the micro-crystalline phase of blue-TiO<sub>2</sub>SCs (hereinafter MC-blue-TiO<sub>2</sub>), *i.e.* MAPbI<sub>3</sub>/MC-blue-TiO<sub>2</sub>.

Blue-TiO<sub>2</sub>-SCs were synthesized using the technological route described in Subsection 2.2.3. The synthesis yielded blue-colored millimeter-sized crystals ( $1.5 \times 1.5 \times 1.5$  mm<sup>3</sup>) with a bi-pyramidal shape. The micro-crystalline phase was obtained by grinding several small blue-TiO<sub>2</sub>-SCs in an agate mortar (for more details see Subsection 2.2.3).

The most representative results obtained for blue-TiO<sub>2</sub>-SCs and the composite material consisting of MAPbI<sub>3</sub> and the micro-crystalline phase of blue-TiO<sub>2</sub>-SCs (MC-blue-TiO<sub>2</sub>), *i.e.* MAPbI<sub>3</sub>/MC-blue-TiO<sub>2</sub>, are shown in Figure 6.5.

Figure 6.5(a) presents the typical low-temperature ESR spectra recorded at 10 K and 30 K for an individual blue-TiO<sub>2</sub>SC. The observed ESR signals are dominated by the strong features at  $g$ -factors of  $\sim 1.98$  and  $\sim 1.95$ , which correspond to Ti<sup>3+</sup> paramagnetic species with significant local crystal lattice distortions. In the temperature range 5 – 100 K, the paramagnetic susceptibility of these centers evolves according to the Curie's law. At higher temperatures, their ESR lines rapidly broaden out due to dipole-dipole interactions. Therefore, the further temperature dependence of the paramagnetic susceptibility of Ti<sup>3+</sup> centers could not be observed.

As shown in Figure 6.5(b), the ESR spectra acquired for the composite MAPbI<sub>3</sub>/MC-blue-TiO<sub>2</sub> material (consisting of MAPbI<sub>3</sub> and the micro-crystalline phase of blue-TiO<sub>2</sub>SCs) markedly



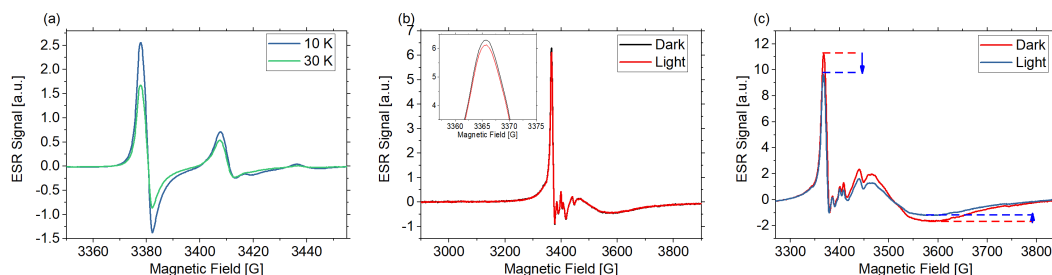


Figure 6.5 – (a) The ESR spectra acquired at 10 K (blue trace) and 30 K (green trace) for a single crystal of reduced (self-doped)  $\text{TiO}_2$  anatase (blue- $\text{TiO}_2$ -SC). (b) The ESR spectra (recorded at 5 K) for the composite  $\text{MAPbI}_3/\text{MC-blue-TiO}_2$  (consisting of  $\text{MAPbI}_3$  and micro-crystalline phase of blue- $\text{TiO}_2$ -SC, *i.e.* MC-blue- $\text{TiO}_2$ ) acquired under dark conditions (black trace) and illumination with visible light from a tungsten halogen light source (red trace). Inset: Zoom at the ESR signal maximum at  $g \sim 1.994$  ( $H = 3366$  G), showing the amplitude difference of light-OFF and light-ON ESR signals. (c) The ESR spectra (recorded at 5 K) for the composite material  $\text{MAPbI}_3/\text{MC-blue-TiO}_2$  acquired under dark conditions (red trace) and illumination with UVA light,  $\lambda_{\text{exc}} = 365$  nm, 20.0 mW (blue trace). The blue arrows mark the diminishment of the ESR signal under illumination with UVA light.

differ from the spectra recorded for an individual single crystal of reduced  $\text{TiO}_2$  anatase (blue- $\text{TiO}_2$ SC). In fact, the ESR signals collected for the composite material originate from  $\text{Ti}^{3+}$  defect centers distributed over the whole assembly of small crystallites. Therefore, their overall ESR spectrum corresponds to the sum of narrow components with  $g$ -factor values in the range from  $\sim 1.99$  to  $\sim 1.95$ , thus representing similar spreading of  $g$ -factors as those found in bulk  $\text{Ti}^{3+}$  defects.

It can also be seen that the ESR spectra recorded for the composite  $\text{MAPbI}_3/\text{MC-blue-TiO}_2$  material do not significantly change under illumination with visible light. In contrast, as documented in Figure 6.5(c), the ESR signal markedly diminish for this sample under illumination with UVA light ( $\lambda_{\text{exc}} = 365$  nm, 20.0 mW).

This is in agreement with the suggested model, which infers that the ESR-detectable changes in the population of  $\text{Ti}^{3+}$  defect centers occur either due the electron transfer from  $\text{MAPbI}_3$  or due to a direct excitation of  $\text{TiO}_2$  with light having photon energies exceeding the band-gap of anatase ( $E_g \text{TiO}_2 = 3.2$  eV). This latter condition is fulfilled under illumination conditions with UVA light at  $\lambda_{\text{exc}} = 365$  nm (3.4 eV) and results in direct removal of electrons from  $\text{Ti}^{3+}$  states. In contrast, under illumination with less energetic photons (*e.g.* VIS light), the direct excitation of both  $\text{TiO}_2$  and  $\text{MAPbI}_3$  is less efficient and does not lead to detectable changes in the population of  $\text{Ti}^{3+}$  defect centers.

Overall, the ESR measurements performed for blue- $\text{TiO}_2$ -SCs point to the presence of a large population of internal  $\text{Ti}^{3+}$  defect centers in the crystalline phase of the strongly reduced (self-doped)  $\text{TiO}_2$  anatase. Moreover, we show that photo-ESR is capable of detecting changes in the population of  $\text{Ti}^{3+}$  defect centers in the composite  $\text{MAPbI}_3/\text{MC-blue-TiO}_2$  material,

which can serve as a very simple model of MAPbI<sub>3</sub>/TiO<sub>2</sub> interface.

### 6.2.5 ESR characterization of blue-TiO<sub>2</sub>NWs

The results of the low-temperature ESR measurements performed for blue-TiO<sub>2</sub>NWs are shown in Figure 6.6. In particular, Figure 6.6(a) shows the temperature dependence of the inverse of the spin-susceptibility,  $1/\chi$ , in the temperature range from 5 to 90 K. The spin-susceptibility measured by ESR,  $\chi$ , is proportional to the ESR signal intensity (*i.e.* the doubly-integrated ESR signal). As can be seen in Figure 6.6(a), the plot of  $1/\chi$  is linear as a function of temperature and intersects the temperature axis close to absolute zero. Thus, in this temperature range, the spin-susceptibility of blue-TiO<sub>2</sub>NWs, originating from the existence of Ti<sup>3+</sup> defects centers, has a fully paramagnetic character and evolves in accordance with the expected Curie-type behavior *i.e.*, as  $\chi \propto 1/T$ .

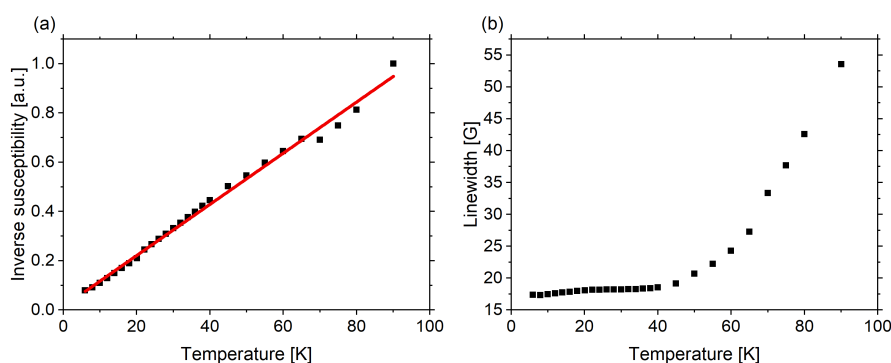


Figure 6.6 – The results of the low-temperature ESR measurements performed for blue-TiO<sub>2</sub>NWs in the temperature range from 5 to 90 K. (a) The temperature evolution of the inverse ESR signal intensity ( $1/\chi$ ). (b) The plot of the ESR *peak-to-peak* linewidth as a function of temperature.

The rapid broadening of the ESR linewidth above ~50 K, concomitant with the very fast diminishment of the ESR signal amplitude, were the reasons for performing the herein reported photo-ESR study at cryogenic temperatures, *i.e.* at  $T < 50$  K.

### 6.2.6 Photo-ESR study of the MAPbI<sub>3</sub>/blue-TiO<sub>2</sub>NWs nanohybrid interface

The experimental setup used for low-temperature photo-ESR measurements oriented towards the detection and quantization of photo-generated charges at the MAPbI<sub>3</sub>/blue-TiO<sub>2</sub>NWs interface is depicted in Figure 2.12. As schematically shown, a 2 mm-diameter rod made of clear fused quartz was implemented to position the sample and deliver light into the ESR cylindrical cavity (TE<sub>011</sub>) resonator (Figure 2.12(a)). The deposits of all the studied materials, including the MAPbI<sub>3</sub>/blue-TiO<sub>2</sub>NWs nanohybrid, were directly coated on the outer surface of the quartz rod by dip-coating. Only the bottom part of the quartz rod, which protruded into the ESR resonator, was coated. Thin film deposits of the commercially available anatase

(AMT600, Tayca Corp.), as well as of white-TiO<sub>2</sub>NWs and blue-TiO<sub>2</sub>NWs, were deposited from aqueous suspensions incorporating also small amounts of poly(ethylene)oxide (PEO) and ethanol, while, as discussed above, the MAPbI<sub>3</sub>/blue-TiO<sub>2</sub>NWs nanohybrid was coated from the stoichiometric solution of MAPbI<sub>3</sub> in DMF, which contained suspended blue-TiO<sub>2</sub>NWs.

Due to a substantial difference in refractive indices between MAPbI<sub>3</sub> ( $n \approx 2.8$ ) [199], TiO<sub>2</sub> ( $n \approx 2.6$ ) [200] and quartz ( $n \approx 1.46$ ) [201] our approach made it possible to efficiently extract light from the quartz light guide to the whole surface of the deposited material. Figure 2.12(b) provides a comprehensive proof of a very efficient extraction of the green laser light ( $\lambda_{exc} = 532$  nm) from the sample holder (quartz rod) to the thin deposit of white-TiO<sub>2</sub>NWs.

The most important findings of this work, stemming from the low-temperature photo-ESR study of photo-generated charges at the model MHP/ETL interface, are summarized in Figure 6.7.

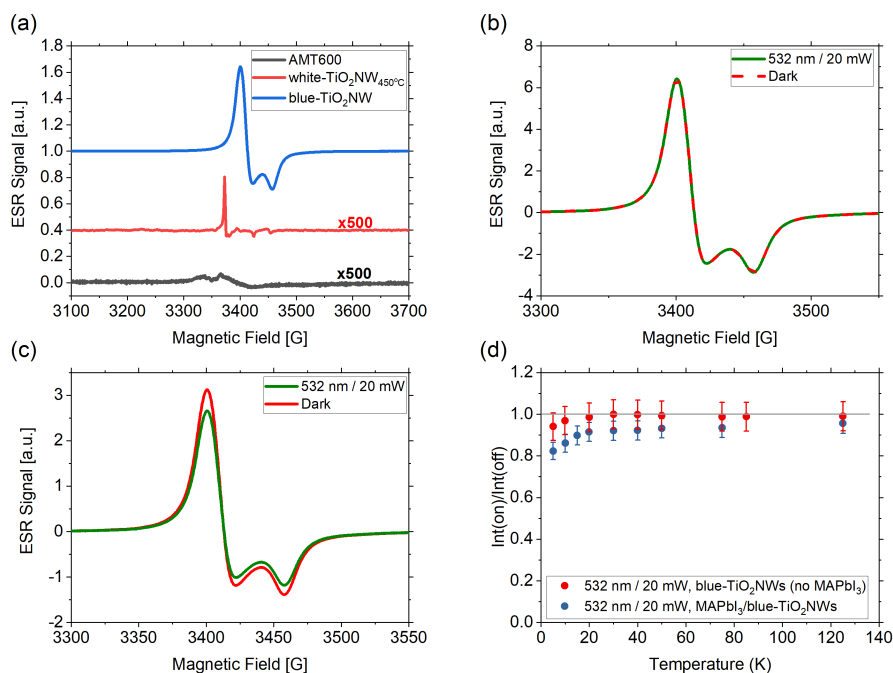


Figure 6.7 – Low-temperature photo-ESR detection of photo-generated charges at the interface between MAPbI<sub>3</sub> and blue-TiO<sub>2</sub>NWs (MAPbI<sub>3</sub>/Blue-TiO<sub>2</sub>NWs). (a) The comparison of ESR spectra acquired at 20 K for the commercial anatase (AMT600, Tayca Corp.) – black trace, white-TiO<sub>2</sub>NWs – red trace, and blue-TiO<sub>2</sub>NWs – blue trace. (b) The ESR spectra acquired for blue-TiO<sub>2</sub>NWs in the dark (red broken trace) and under illumination with the green laser light,  $\lambda_{exc} = 532$  nm,  $P = 20.0$  mW (green trace). (c) The ESR spectra acquired for the MAPbI<sub>3</sub>/blue-TiO<sub>2</sub>NWs nanohybrid in the dark (red trace) and under illumination with the green laser light,  $\lambda_{exc} = 532$  nm,  $P = 20.0$  mW (green trace). (d) The temperature-evolution plots of the ratios of the ESR signal intensities acquired under illumination (green laser light,  $\lambda_{exc} = 532$  nm,  $P = 20.0$  mW) and in the dark conditions for: blue-TiO<sub>2</sub>NWs (red dots) and the MAPbI<sub>3</sub>/blue-TiO<sub>2</sub>NWs nanohybrid material (blue dots).

## Chapter 6. Light-induced charge transfer at the MAPbI<sub>3</sub>/TiO<sub>2</sub> interface – a low-temperature Photo-ESR assay

---

The comparative ESR evaluation of three TiO<sub>2</sub>-based materials having the potential for applications in a model MAPbI<sub>3</sub>/TiO<sub>2</sub> system is shown in Figure 6.7(a). Specifically, the stacked plot in this figure compiles normalized ESR spectra acquired at 20 K for the commercially available anatase (black trace), white-TiO<sub>2</sub>NWs (red trace) and blue-TiO<sub>2</sub>NWs (blue trace).

Although all three spectra reveal the presence of paramagnetic species, it can be concluded that blue-TiO<sub>2</sub>NWs provide the strongest ESR-detectable feature (blue trace). In particular, as discussed in details in Ref. [89], the strong ESR signal observed for blue-TiO<sub>2</sub>NWs corresponds to a powder ESR spectrum of the surface-located Ti<sup>3+</sup> paramagnetic centers. For distorted (tetragonally-elongated) octahedral sites this signal can be fitted with a uniaxial powder distribution having two *g*-factor components: parallel (*g*<sub>||</sub> = 1.94) and perpendicular (*g*<sub>⊥</sub> = 1.97) (Ref. [89] and references therein). The temperature dependence of the ESR signal intensity confirmed the Curie-type behavior for these Ti<sup>3+</sup>-related paramagnetic centers in blue-TiO<sub>2</sub>NWs (see Figure 6.6). The overall concentration of paramagnetic Ti<sup>3+</sup> centers in blue-TiO<sub>2</sub>NWs, estimated in our previous work, was found to be of ~0.4% of all the surface Ti cations [196].

The much weaker ESR spectrum recorded for white-TiO<sub>2</sub>NWs (red trace) can be interpreted as originating mostly from paramagnetic oxygen vacancies, V<sub>O</sub><sup>-</sup> (the narrow peak at *g* ≈ 2.003) [202], and a low concentration of bulk-located Ti<sup>3+</sup> centers (at *g*-factor values of ≈ 1.99 and ≈ 1.96).

Interestingly, the traces of Ti<sup>3+</sup> paramagnetic centers can also be observed for the untreated commercial anatase (weak signals at *g*-factor values of ≈ 1.97 and ≈ 1.94). However, the overall ESR spectrum of this material (black trace) is clearly dominated by a broadened signal with *g*-factor values of ≈ 2.029, ≈ 2.011 and ≈ 2.003, which can be ascribed to the adsorbed reduced oxygen molecules and structural oxygen defects, *i.e.* superoxide and oxygen (O<sub>2</sub><sup>-</sup> / O<sup>-</sup>) radicals [203, 204].

Figure 6.7(b) reports the ESR spectra acquired for the deposit of blue-TiO<sub>2</sub>NWs under illumination with the green laser light ( $\lambda_{exc} = 532$  nm, P= 20.0 mW) and in the dark conditions. In the present study, this sample, consisting solely of the thermally-reduced TiO<sub>2</sub>NWs, served as reference for the MAPbI<sub>3</sub>/blue-TiO<sub>2</sub>NWs nanohybrid material. It can be seen that the ESR spectra recorded for blue-TiO<sub>2</sub>NWs in the dark and under illumination do not differ and perfectly overlap each other. As discussed before, both ESR spectra correspond to Ti<sup>3+</sup> paramagnetic centers with their characteristic powder distribution with *g*-factor values of *g*<sub>||</sub> = 1.94 and *g*<sub>⊥</sub> = 1.97.

In contrast, as shown in Figure 6.7(c), the ESR signal of Ti<sup>3+</sup> centers in the thin film deposit of the MAPbI<sub>3</sub>/blue-TiO<sub>2</sub>NWs nanohybrid material markedly diminishes under identical illumination conditions. Thus, the observed reduction of the ESR signal upon illumination can be associated with the transfer of photo-excited electrons from MAPbI<sub>3</sub> to blue-TiO<sub>2</sub>NWs. In particular, the light-excited non-equilibrium electrons in MAPbI<sub>3</sub> cross the interface between MAPbI<sub>3</sub> polycrystals and dispersed blue-TiO<sub>2</sub>NWs, thus leading to change in the spin

state configuration from  $\text{Ti}^{3+}$  ESR-active ( $3d^1$ ,  $S = 1/2$ ) to ESR-silent  $\text{Ti}^{2+}$  ( $3d^2$ ,  $S = 0$ ). The light-induced drop in the ESR signal intensity for the herein studied  $\text{MAPbI}_3/\text{blue-TiO}_2\text{NWs}$  nanohybrid material was  $\sim 20\%$  at 20 K.

The temperature evolutions of the ESR-detected charge transfer for the deposit of  $\text{MAPbI}_3/\text{blue-TiO}_2\text{NWs}$  nanohybrid material and the reference sample, *i.e.* the deposit consisting solely of blue- $\text{TiO}_2\text{NWs}$ , are shown in Figure 6.7(d). It can be seen that the ratio of the ESR signal intensities acquired for the deposit of  $\text{MAPbI}_3/\text{blue-TiO}_2\text{NWs}$  nanohybrid material under illumination and dark conditions is markedly lower than unity, adapting values from  $\sim 0.8$  to  $\sim 0.9$  in the temperature range of 5 K to 80 K (blue dots). In contrast, the corresponding ESR signal intensity ratio for the reference sample remains close to unity and is practically independent of temperature (red dots). As already mentioned, with increasing temperatures, the ESR signal line-width for  $\text{Ti}^{3+}$ -related defect centers rapidly broadens up, thus rendering difficult the ESR measurements at temperatures higher than 100 K (for more details see in Figure 6.6(b)).

The observed light-induced changes were fully reversible and the ESR signal recovered its initial amplitude under dark conditions. These phenomena were observed for the  $\text{MAPbI}_3/\text{blue-TiO}_2\text{NWs}$  nanohybrid deposit under illumination with various wavelengths having photon energies lower than  $E_{g\text{ TiO}_2} = 3.2\text{ eV}$ . However, the most prominent effect, corresponding to *ca.* 20% drop of the ESR signal intensity, occurred under illumination with the green laser light at  $\lambda_{exc} = 532\text{ nm}$  (2.33 eV).

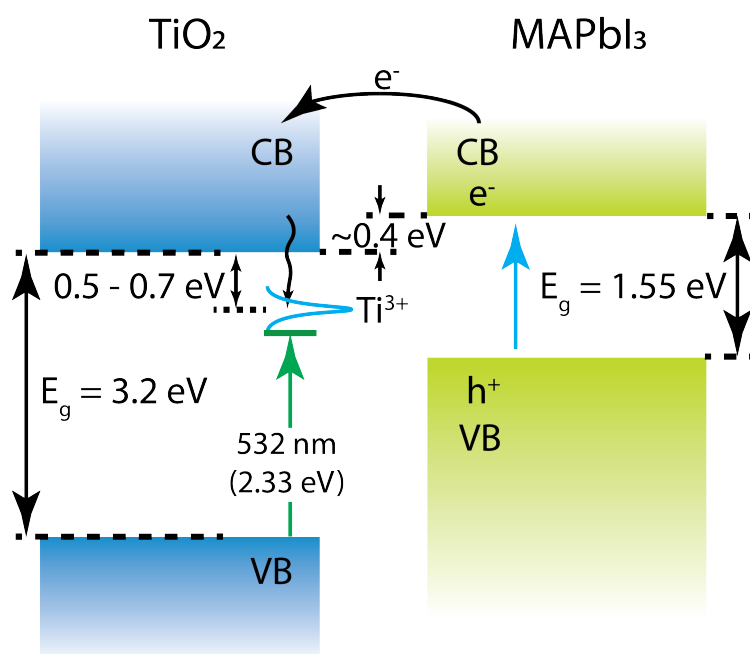


Figure 6.8 – Schematic representation of the energy band alignment diagram at the  $\text{MAPbI}_3/\text{blue-TiO}_2\text{NWs}$  interface.

## Chapter 6. Light-induced charge transfer at the MAPbI<sub>3</sub>/TiO<sub>2</sub> interface – a low-temperature Photo-ESR assay

---

As can be deduced from the schematic energy band alignment diagram for the MAPbI<sub>3</sub>/blue-TiO<sub>2</sub>NWs interface (Figure 6.8), the photon energy of the green laser light (2.33 eV) is lower than the energy of the intra-band Ti<sup>3+</sup> defects states, which are located *ca.* 0.5 – 0.7 eV below the edge of the conduction band of TiO<sub>2</sub>. Therefore, we hypothesize that the green laser light-induced excitation of charge carriers essentially takes place within the narrow-band semiconductor, MAPbI<sub>3</sub>, whereas blue-TiO<sub>2</sub>NWs serve as a unidirectional electron sink with an enhanced electron trapping efficiency due to the presence of Ti<sup>3+</sup> defects.

### 6.3 Conclusion

Taken together, we report a contactless method to directly track light-excited carriers at the ETL/MHP interface in a model system consisting of TiO<sub>2</sub>-based nanowires (TiO<sub>2</sub>NWs) dispersed in the polycrystalline MAPbI<sub>3</sub> matrix. Specifically, thermally-reduced TiO<sub>2</sub>NWs (blue-TiO<sub>2</sub>NWs), containing a large concentration of Ti<sup>3+</sup> paramagnetic centers, were used as the representative material for the ETL. The dispersion of blue-TiO<sub>2</sub>NWs in polycrystalline MAPbI<sub>3</sub> ensured a large distributed surface of the MAPbI<sub>3</sub>/blue-TiO<sub>2</sub>NWs interface.

The technique of low-temperature ESR in combination with *in situ* illumination (photo-ESR) was implemented to monitor the light-induced changes in the population of Ti<sup>3+</sup> paramagnetic centers in blue-TiO<sub>2</sub>NWs. In particular, we find that under illumination with the green laser light ( $\lambda_{exc} = 532$  nm) the concentration of Ti<sup>3+</sup> defects in blue-TiO<sub>2</sub>NWs drops by ~20%. This process can be understood in terms of the transfer of light-excited non-equilibrium electrons from MAPbI<sub>3</sub> to blue-TiO<sub>2</sub>NWs, which, in turn, leads to conversion of ESR-active Ti<sup>3+</sup> centers ( $3d^1$ ,  $S = 1/2$ ) to ESR-silent Ti<sup>2+</sup> states ( $3d^2$ ,  $S = 0$ ). Moreover, for the herein studied model ETL/MHP interface, the low-temperature photo-ESR measurements confirm that blue-TiO<sub>2</sub>NWs serve as a unidirectional electron sink with an enhanced electron trapping efficiency due to the presence of Ti<sup>3+</sup> defects.

Finally, we also infer that the technique of low-temperature photo-ESR is an effective strategy to study the transfer mechanisms of photogenerated carriers at the ETL/MHP interface in MAPbI<sub>3</sub>-based photovoltaic and photoelectronic systems.

These findings are the subject of the paper by K. Mantulnikovs et al., “Light-induced charge transfer at the CH<sub>3</sub>NH<sub>3</sub>PbI<sub>3</sub>/TiO<sub>2</sub> interface – a low-temperature Photo-EPR assay” submitted to *Journal of Physics: Photonics* [205].

## 7 Conclusion and outlook

### 7.1 Conclusion

Over the last couple of years, the research field concerning metal-halide perovskites (MHPs) has evolved quite significantly. The major developments have been achieved in thin film material processing, solar cell physics and underpinned power conversion efficiencies (PCEs), as well as long-term stability, which, in fact, still remains a key problem prior to commercialization of this exciting technology. In particular, within the duration of this PhD thesis, which started in 2015, the greatest research emphasis has still been oriented toward the increase of PCEs of MHPs-based solar cells, which, over the last four years have been boosted from  $\sim 3\%$  to  $\sim 17\%$  and from  $\sim 20\%$  to  $\sim 25.2\%$ , for inorganic metal-halide perovskites and organic-inorganic metal-halide perovskites, respectively [12, 206, 207].

Evidently, this remarkable progress in constantly increasing PCEs lead to novel fabrication methods of MHPs thin films, better control and optimization of their morphology, as well as to more complex solar cell architectures, such as, *e.g.*, MHP/silicon tandem cells or structures implementing MHPs quantum dots (QDs) and luminescent solar concentrators. Overall, with the latest record PCE exceeding  $25.2\%$  [12], MHPs-based solar cell can rival the established silicon and other inorganic thin-film photovoltaic technologies, which are currently present on the market.

Alongside with these astounding developments in MHPs-based photovoltaics, another research direction has been thriving, namely of prospective applications of MHPs materials in optical detection and sensing. To date, there have been numerous successful attempts to implement MHPs as novel optically-sensitive materials in a whole variety of detectors and sensors, such as X-ray detecting devices, UV-VIS-near-IR (330 – 800 nm) light detectors, as well as gas and even high-energy radiation detectors [206, 208].

Thus, the research related to this PhD thesis started at the moment when the scientific landscape has already been well marked with relatively matured technologies of fabrication of MHPs-based photovoltaic devices, including solar cells and photo-optical sensors. In par-

ticular, the initial research topic of this dissertation was inspired by a random observation pointing to the fact that the morphology and quality of thin MHPs deposits coated onto different types of substrates, while using the simplest, one-step solution-casting method, were strongly dependent on the substrate curvature.

Therefore, instead of exploring various solution processing techniques, such as, *e.g.*, two-step spin-coating sequential deposition, double-source co-evaporation, or vapor deposition methods, this work initially focused on shedding light on the morphology dependence of thin deposits of an archetypal MHP, methylammonium lead iodide,  $\text{CH}_3\text{NH}_3\text{PbI}_3$  (MAPbI<sub>3</sub>), coated on cylinder-shaped elongated substrates.

With using optical microscopy, luminescence spectroscopy and imaging, scanning electron microscopy (SEM), X-ray diffraction and atomic force microscopy (AFM), we studied the variability of morphology, crystallinity and coverage of thin deposits of polycrystalline MAPbI<sub>3</sub> coated via one-step solution method onto thin quartz rods having diameters in the range from 80 to 1800  $\mu\text{m}$ . In particular, MAPbI<sub>3</sub> layers coated onto quartz rods with the smallest diameters (80  $\mu\text{m}$  and 330  $\mu\text{m}$ ) proved to be of the best quality, being densely-packed and consisting of micrometer-sized, needle-shaped wires (1  $\mu\text{m}$  thick and 20  $\mu\text{m}$  long). In contrast, deposits coated onto the larger-diameter substrates proved to have numerous voids, as well as increasing crystallites sizes, with lengths of the microwires up to  $\sim 100$   $\mu\text{m}$  (especially for the substrate diameter of 400  $\mu\text{m}$  and larger). Moreover, for the larger-diameter substrates (from 400  $\mu\text{m}$  to 1800  $\mu\text{m}$ ), the variability in the texture of the polycrystalline layers of MAPbI<sub>3</sub> with respect to the substrate curvature was less marked. This portion of the research was thoroughly discussed in Chapter 3 of this dissertation, as well as in K. Mantulnikovs *et al.*, *ACS Photonics* 2018, 5, 4, 1476-1485 [113].

The above-mentioned methodological approach was then extended to the morphology dependence on the substrate curvature for the second archetypal MHP, *i.e.* methylammonium lead bromide,  $\text{CH}_3\text{NH}_3\text{PbBr}_3$  (MAPbBr<sub>3</sub>). In a similar way as for MAPbI<sub>3</sub>, the thin films of polycrystalline MAPbBr<sub>3</sub> coated onto cylinder-shaped quartz substrates with smallest diameters (80  $\mu\text{m}$ ) proved to be very densely-packed and consisted of micrometer-sized cuboid-shape crystallites with characteristic side length of  $\sim 5$   $\mu\text{m}$ . MAPbBr<sub>3</sub> deposits coated onto the larger-diameter substrates had voids and also increasing crystallite sizes up to  $\sim 100$   $\mu\text{m}$  (especially for the substrate diameter of 1100  $\mu\text{m}$ ). Overall, the morphological variability of polycrystalline layers of MAPbBr<sub>3</sub> with respect to the substrate curvature was substantially less pronounced than in the case of MAPbI<sub>3</sub> counterparts. This portion of the research was presented in details in Chapter 3 of this dissertation, as well as in K. Mantulnikovs *et al.*, "Differential response of the photo-luminescence and photocurrent of polycrystalline  $\text{CH}_3\text{NH}_3\text{PbI}_3$  and  $\text{CH}_3\text{NH}_3\text{PbBr}_3$  to the exposure to Oxygen and Nitrogen", published in *ACS Appl. Electron. Mater.* on September the 4<sup>th</sup> 2019 [161].

The advantages of densely-packed polycrystalline thin films, concomitant with large *surface-to-volume* ratios, offered by small cross-sectional dimensions and the cylindrical and elon-



gated geometry of MAPbI<sub>3</sub> and MAPbBr<sub>3</sub> deposits coated onto the substrates with the smallest diameters (80  $\mu\text{m}$  and 330  $\mu\text{m}$ ), encouraged us to implement them as model gas-sensing elements. To this end, we combined these MHPs deposits with custom-made tubular, light-transparent gas-flow chambers. Thanks to this approach, we got a possibility to monitor the photoluminescence (PL) and photocurrent (PC) responses of both archetypal MHPs, MAPbI<sub>3</sub> and MAPbBr<sub>3</sub>, to the impact of various gaseous media with using a relatively simple experimental setup based on a modified epi-fluorescence microscope. In particular, we could perform a systematic study of photo-physical properties of these both MHPs exposed to two important environmental gaseous media, *i.e.* oxygen (O<sub>2</sub>) and nitrogen (N<sub>2</sub>). Independent of observing characteristic processes of the initial photo-brightening for both MHPs exposed to the combined action of light and O<sub>2</sub>, we could also monitor strongly diverse responses of photo-bleaching for MAPbI<sub>3</sub> and systematic photo-brightening for MAPbBr<sub>3</sub> under prolonged exposure to these two factors.

This approach made it also possible to demonstrate the differential behavior of the PL emission from MAPbI<sub>3</sub> and MAPbBr<sub>3</sub> when the samples were positioned *side-by-side* in a miniature custom-built gas-flow chamber and simultaneously exposed to the flow of either O<sub>2</sub> or N<sub>2</sub>. To the best of our knowledge, this is the first report showing strongly differential responses of PL and PC for these two polycrystalline MHPs materials deposited onto cylinder-shaped substrates having small diameters (80  $\mu\text{m}$  or 330  $\mu\text{m}$ ) and simultaneously exposed to the identical illumination and environmental conditions, defined by the presence of either O<sub>2</sub> or N<sub>2</sub>. This portion of the research was comprehensively presented in Chapter 4 of this dissertation as well as in K. Mantulnikovs *et al.*, “Differential response of the photo-luminescence and photocurrent of polycrystalline CH<sub>3</sub>NH<sub>3</sub>PbI<sub>3</sub> and CH<sub>3</sub>NH<sub>3</sub>PbBr<sub>3</sub> to the exposure to Oxygen and Nitrogen”, published in *ACS Appl. Electron. Mater.* on September the 4<sup>th</sup> 2019 [161].

In this PhD thesis, we also tackled an important issue of the selective, wavelength-dependent, photo-bleaching in MAPbI<sub>3</sub>, which has been reported earlier, but still is not fully understood. Specifically, we focused on checking the concurrent light-induced processes of photo-brightening and photo-bleaching in thin film deposits and single crystals of MAPbI<sub>3</sub> exposed to different excitation wavelengths. The competing light-induced processes of photo-brightening and photo-bleaching in MAPbI<sub>3</sub> were observed under the well-controlled dry gaseous media atmosphere, consisting of either O<sub>2</sub> or N<sub>2</sub>. Overall, the results related to photo-brightening or photo-bleaching in MAPbI<sub>3</sub> show the dependence of these processes on the content of the gaseous atmosphere and the photo-excitation wavelength, *i.e.* 546 nm and 470 nm, for photo-brightening and photo-bleaching, respectively. These findings might help to gather a better insight into charge generation and recombination processes and can help in achieving rational design and tailored properties of MAPbI<sub>3</sub>-based optoelectronic and photovoltaic devices. This research was discussed exhaustively in Chapter 5 of this PhD thesis.

One of the goals of this PhD thesis was to shed more light on the topic of the charge transfer mechanism of light-generated carriers at the interface of MAPbI<sub>3</sub> and TiO<sub>2</sub>. This is still a very important issue, since the great majority of MHPs-based photovoltaic devices, designed in

the form of stacked-planar structures, contain an interface between MHPs and the electron transport layer (ETL). In this study, thermally-reduced  $\text{TiO}_2$ NWs (blue- $\text{TiO}_2$ NWs), containing a large population of  $\text{Ti}^{3+}$  defect centers, were used as a representative ETL material. The presence of paramagnetic defects of trivalent titanium ( $\text{Ti}^{3+}$ ,  $S = 1/2$ ) in the ETL material enabled us to implement the technique of low-temperature electron spin resonance (ESR) in combination with *in situ* illumination (photo-ESR) to follow the transfer of light-excited electrons from  $\text{MAPbI}_3$  to the ETL layer (blue- $\text{TiO}_2$ NWs). The results of this study demonstrate that the above-mentioned approach can be used to directly monitor the charge transfer from  $\text{MAPbI}_3$  to  $\text{TiO}_2$ , as well as to determine the exact number of trapped electrons by the surface defects in  $\text{TiO}_2$ . These findings were presented in details in Chapter 6 of this PhD thesis and are the subject of the paper by K. Mantulnikovs et al., “Light-induced charge transfer at the  $\text{CH}_3\text{NH}_3\text{PbI}_3/\text{TiO}_2$  interface – a low-temperature Photo-EPR assay” submitted to *Journal of Physics: Photonics* [205].

## 7.2 Outlook

Both  $\text{MAPbI}_3$  and  $\text{MAPbBr}_3$  are not the simplest materials to study or to employ due to their vulnerabilities to the environmental factors, as well as the underlying complicated physicochemical processes. Although, in the recent years, there have been significant advances in reducing degradation of these materials under exposure to various environmental extremes, yet, there is still much room for improvement. In the context of this PhD thesis, a potential roadmap might then suggest to prioritize two directions: chemistry of MHPs and physics behind the processes occurring in them.

Specifically, there are still chemical stability problems related mostly to  $\text{MAPbI}_3$ , with some of those also relevant to  $\text{MAPbBr}_3$ . It would then be a great challenge to synthesize these perovskite materials in a reproducible and reliable fashion, providing researchers and engineers with high quality materials – towards better understanding of the basic science behind and bringing the MHPs-based photovoltaics closer to real-world applications.

Having chemistry under control, a diligent and systematic study of the band structure, the electronic processes and ionic movement, potentially on different morphologies of MHPs might lead to a major breakthrough in the solar cell industry and the perovskite-based branch of applied research. This may include implementation of impedance spectroscopy and time-resolved photoluminescence techniques, both under controlled atmospheres, to further confirm the observations and theoretical hypothesis of this thesis.

From the engineering point of view, a plausible continuation of the developments of this thesis would be to employ the longitudinal-cylindrical geometries of MHPs deposits and their *side-by-side* configuration to design more complex differential gas sensors, possibly calibrated for being sensitive to variable partial oxygen pressures.

For real-world applications of MHPs-based solar cells, more insight is still needed into the

concurrent processes of the selective-wavelength photo-bleaching and exposure to oxygen. This also includes the understanding of the degradation mechanisms under light and oxygen exposures.

Finally, the scientific community would need to address the issue of toxicity of MHPs. Even though this problem remains highly challenging, it definitely does not impede any of the above-mentioned perspectives.



# A Technical drawings of parts used in the experiments

## A.1 Cylindrical geometry gas-flow chamber setup

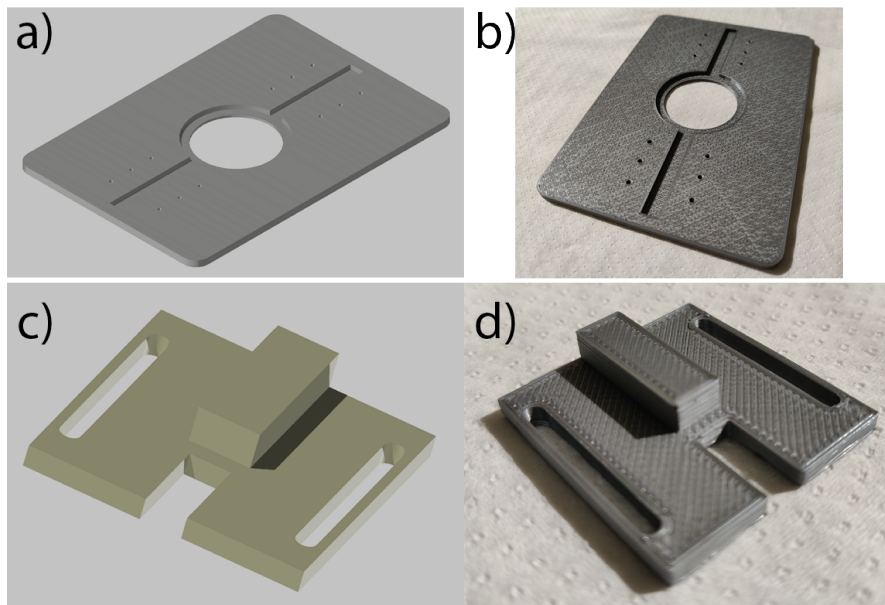


Figure A.1 – 3D renders (left column) and photos (right column) of the each substituting part of the setup assemblies shown in Figure 2.13 (a & b). a) shows a 3D render of the microscope slide and b) shows a photo of a 3D-printed part. c) shows the clip to hold the gas inlet and outlet connectors and d) a photo of the same part in plastic. Grey represents the microscope plate and ash – the clip used to affix the connectors with the gas-flow chamber to the plate.

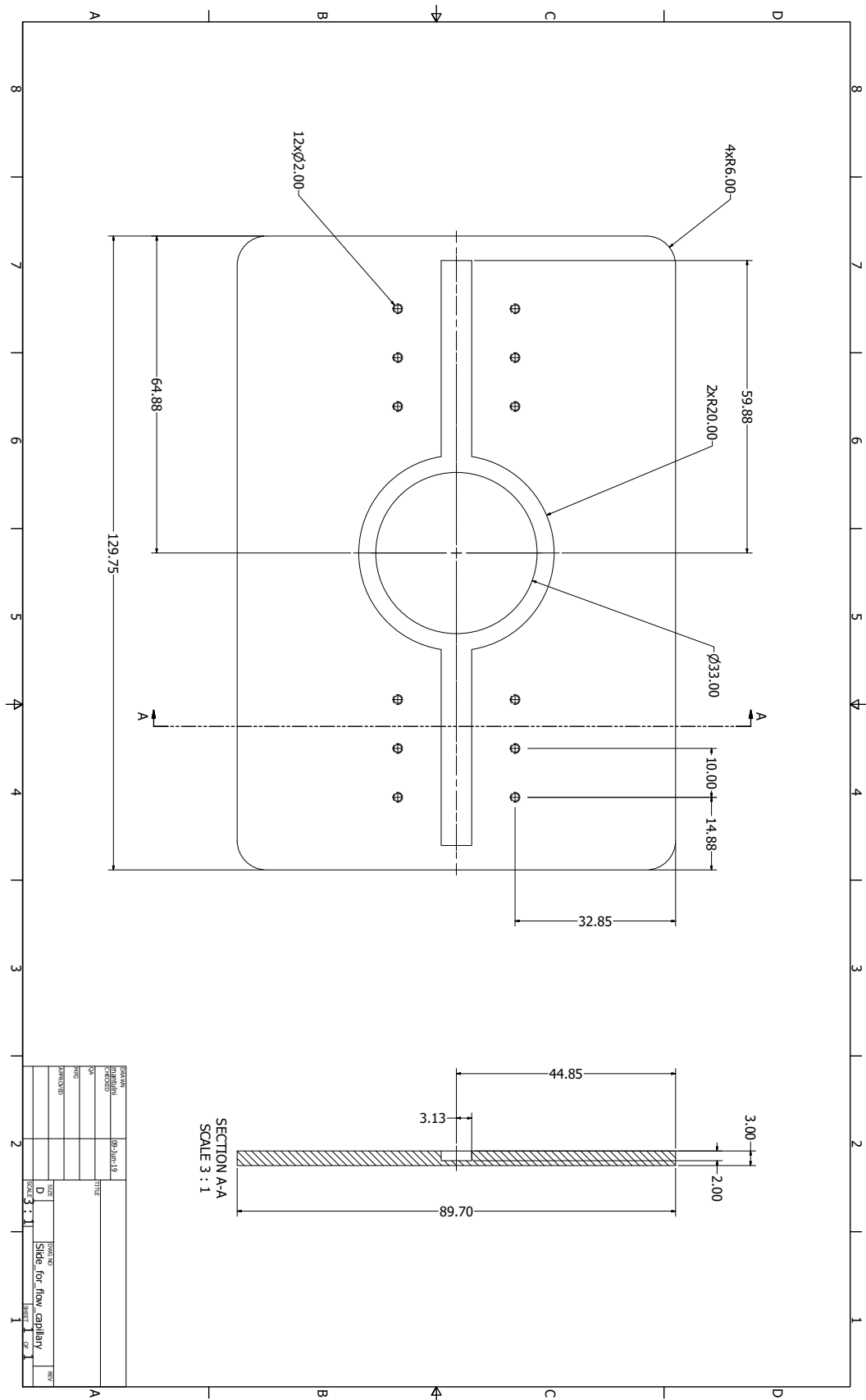


Figure A.2



## A.2 Flat-cell geometry gas-flow chamber setup

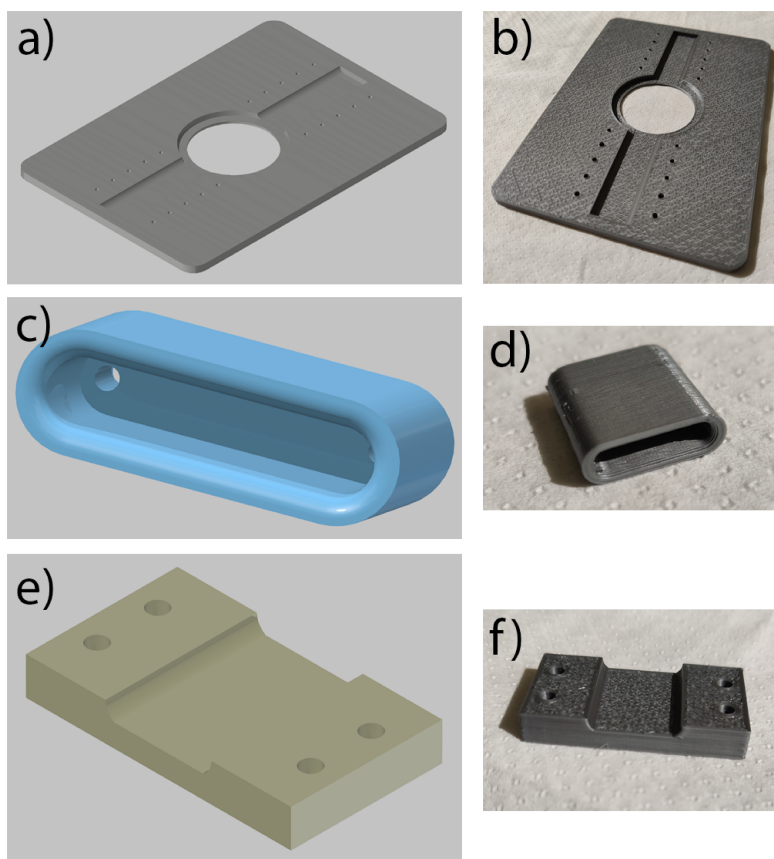


Figure A.4 – 3D renders (left column) and photos (right column) of the each substituting part of the setup assemblies shown in Figure 2.13 (c & d). a) shows a 3D render of the microscope slide and b) shows a photo of a 3D-printed part. In c) the connector used to interface with the gas lines. A blank version was also produced for symmetry reasons. d) the same gas inlet/outlet connector manufactured in plastic. e) shows the clip to hold the gas inlet and outlet connectors and f) a photo of the same part in plastic. Here, grey represents the microscope plate, ash – the clips used to affix the connectors with the gas-flow chamber to the plate and cyan – the 3D-printed connector accommodating either gas inlet and outlet stainless steel needles or a blank one.



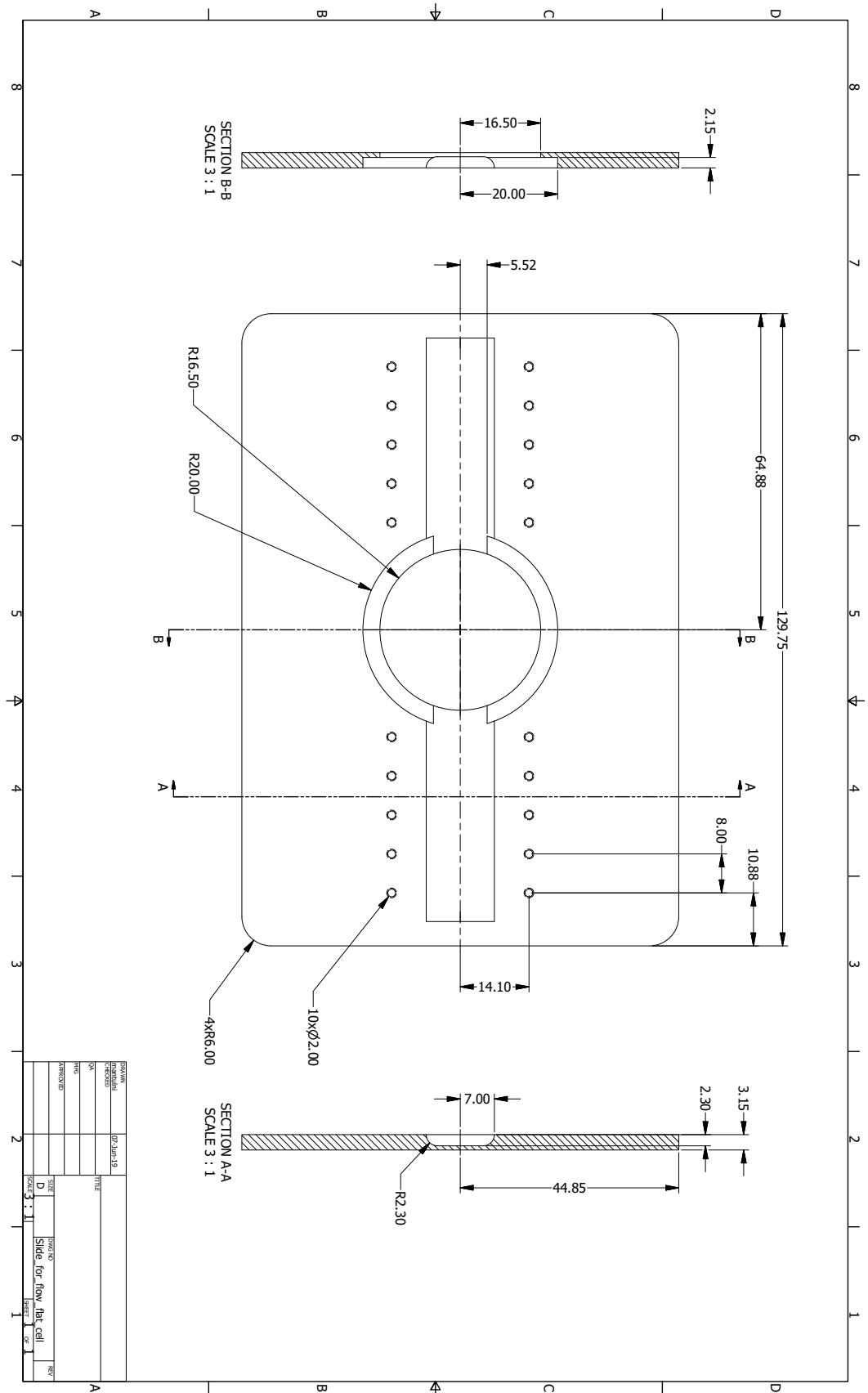


Figure A.5

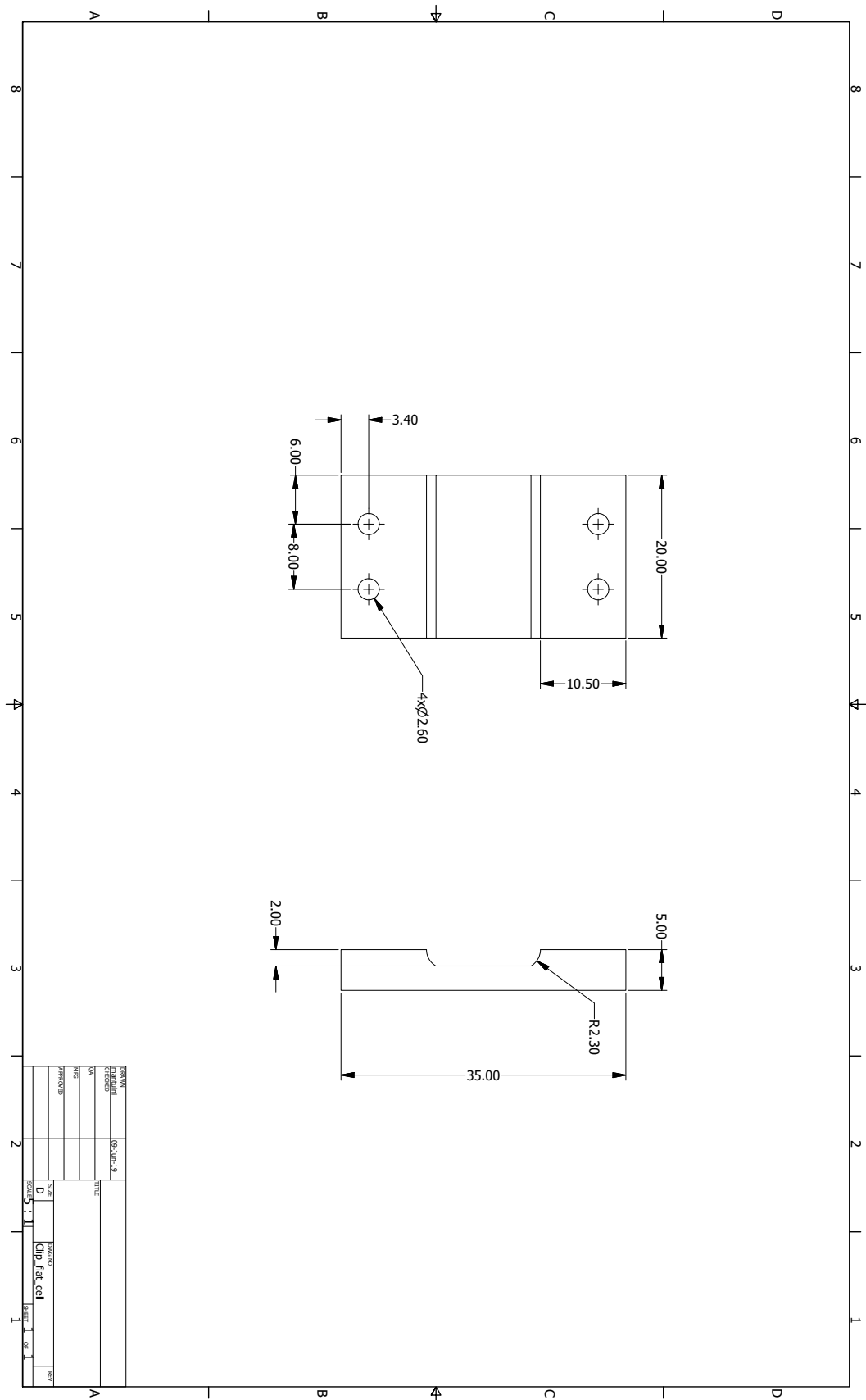
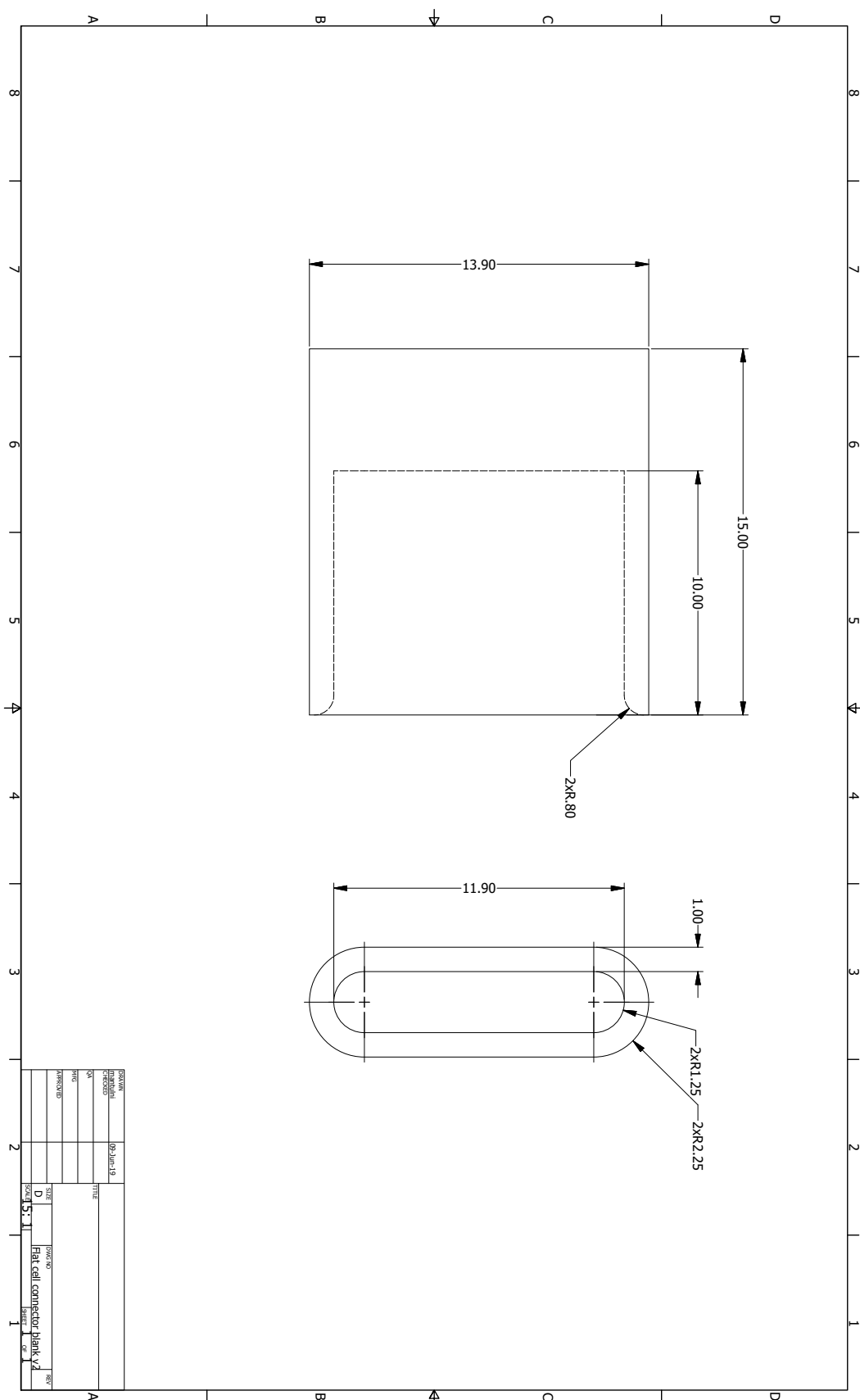


Figure A.6

---





## B Experiment control code

### B.1 Data management class

```
1         import visa
2         import re
3         import time
4         import logging
5         import sys
6
7         class data_manager(object):
8             """Data management class"""
9         def __init__(self, in_str = "data.dat"):
10             """Data management class constructor."""
11             self.filename = in_str
12
13         def file_input(self, file_in = "0"):
14             """Writes the input list to a file"""
15             with open(self.filename, 'a') as data_file:
16                 data_file.write(file_in)
17                 data_file.write("\n")
18                 data_file.close()
19
20         @staticmethod
21         def data_str_create(data_in):
22             """Static method creating a list."""
23             data_to_write = ' '.join(map(str,data_in))
24             return data_to_write
```

### B.2 Photocurrent measurement script

```
1      import Instrument_classes as ins
2      import time
3      import matplotlib.pyplot as plt
4      import os
5      #import Functions as func
6      import numpy as np
7      import visa
8
9      rm=visa.ResourceManager()
10     K2400 = rm.open_resource("GPIB::9::INSTR")
11     K2400.write(':SOUR:FUNC VOLT')
12     K2400.write(':SOUR:VOLT 10')
13     K2400.write(':SENS:CURREN:PROT 100e-6')
14
15
16     save_path = 'C:/Users/nn/Documents/DATA/Konstanteen/2018_10/MAPbI3_DPPH/
17     Run_2/'
18     #data_file = ins.data_manager("data_18-04-30_N2_02_GREEN_PL.dat")
19     name_of_file = "I_181015_MAPbI.dat"
20     data_file = ins.data_manager(os.path.join(save_path, name_of_file))
21
22
23     n = n_pts = 10000
24     delay = 0.1
25     #I_list = []
26     #t_list = []
27
28     plt.close("all")
29     fig = plt.gcf()
30     fig.show()
31     fig.canvas.draw()
32     fig.canvas.set_window_title('Photocurrent vs time')
33
34     plt.xlabel('time [s]')
35     plt.ylabel('Current [A]')
36
37     # Customize the major grid
38     plt.grid(which='major', linestyle='-', linewidth='0.5', color='red')
39
40
41
42     K2400.write(':OUTP:STAT ON')
43
44     #K2400.write(':FORM:ELEM TIME')
45     #time.sleep(.25)
46     #K2400.write(':INIT')
47     #time.sleep(.25)
48     #t_0 = K2400.query(':FETCH?').split(",")
49
50     t_0 = time.time()
51
52
53     while n>0:
54         K2400.write(':FORM:ELEM VOLT, CURREN')
55         K2400.write(':INIT')
56         time.sleep(.25)
57         data = K2400.query(':FETCH?').split(",")
```

## B.2. Photocurrent measurement script

---

```
58     time.sleep(.25)
59     t = time.time()-t_0
60     t_file = time.time()
61     #     t = float(data[2].strip())-float(t_0[0])
62     print('Point {0} of {4}; V = {1} V; I = {2} A, t = {3} s'.format(n_pts-n,
        float(data[0].strip()), float(data[1].strip()), round(t,4), n_pts))
63     #     print(n, data)
64     #     I_list.append(float(data[1].strip()))
65     #     t_list.append(float(data[2].strip())-float(t_0[0]))
66
67
68
69     #     plt.plot(t_list,I_list,'bx-')
70     plt.plot(t,float(data[1].strip()), color='b', marker='.')
71     fig.canvas.draw()
72     plt.pause(0.05)
73
74     write_str_down = [float(data[0].strip()), float(data[1].strip()), t_file]
75     data_file.file_input(data_file.data_str_create(write_str_down))
76
77     n = n-1
78     time.sleep(delay)
79
80     K2400.write(':OUTP:STAT OFF')
81     print('Measurement finished')
```

### B.3 Photoluminescence measurement script

```
1      import Instrument_classes as ins
2      import seabreeze.spectrometers as sb
3      import matplotlib.pyplot as plt
4      import numpy as np
5      import os
6      import time
7
8      n = f_n = 20000
9      delay = 2
10     int_time = 100e-3
11
12     #MAPbI3
13     int_start = 940
14     int_stop = 1695
15
16     #MAPbBr3
17     #int_start = 600
18     #int_stop = 1200
19
20
21
22     save_path = 'C:/Users/nn/Documents/DATA/Konstanteen/2018_12/Sunglasses/
23     Run_10_02_Cap2_B_kinetics/'
24     name_of_int_file = "int_Cap2_kinetics_02_181221.dat"
25     int_file = ins.data_manager(os.path.join(save_path, name_of_int_file))
26
27     plt.close("all")
28     fig = plt.gcf()
29     fig.show()
30     fig.canvas.draw()
31     fig.canvas.set_window_title('PL Intensity vs time')
32
33     plt.xlabel('time [s]')
34     plt.ylabel('Signal [a.u.]')
35     plt.grid(which='major', linestyle='-', linewidth='0.5', color='red')
36
37     spec = sb.Spectrometer.from_serial_number()
38     spec.integration_time_micros(int_time*1e6)
39
40     print('Close the shutter to take the background spectrum and press any
41     key.')
42     os.system("pause")
43     bckgrd = (spec.intensities()).transpose()
44     print('Background spectrum acquired. Open the shutter and press any key
45     to continue the acquisition.')
46     np.savetxt(os.path.join(save_path, 'PL_bcg.dat'), bckgrd, delimiter="\t",
47     newline=os.linesep)
48     print('Background spectrum saved to {}'.format('PL_bcg.dat'))
49     os.system("pause")
50
51     WL = (spec.wavelengths())
52     WL_int = WL[2:]
53
54     np.savetxt(os.path.join(save_path, 'PL_WL.dat'), WL, delimiter="\t",
```



### B.3. Photoluminescence measurement script

```

        newline=os.linesep)
55     print('Wavelengths saved to {0}'.format('PL_WL.dat'))
56
57     t_0 = time.time()
58     while n>0:
59         integral = 0
60         print('Acquiring spectrum {0} of {1}. Time: {2}'.format(f_n - n, f_n,
        round(time.time()-t_0, 3)))
61         spectrum = (spec.intensities())
62         cor_spec = spectrum[2:]-bckgrd[2:]
63         debug_cor_sp = spectrum[2:]
64         #     integral = np.trapz((spectrum[2:]-bckgrd[2:])[int_start:int_stop],x=
        p, dx = dx)
65         #     debug_int = np.trapz(debug_cor_sp[int_start:int_stop],x=WL_int[
        int_start:int_stop])
66         integral = np.trapz(cor_spec[int_start:int_stop],x=WL_int[int_start:
        int_stop])
67         name_of_file = 'PL_{0}.dat'.format(f_n - n)
68         HeaderTXT = str(time.time())
69         completeName = os.path.join(save_path, name_of_file)
70         np.savetxt(completeName,spectrum, delimiter="\t", newline=os.linesep,
        header=HeaderTXT)
71         n = n-1
72
73         plt.plot(time.time()-t_0, integral, color='b', marker='.',linestyle = '
        None')
74         #     plt.plot(time.time()-t_0, debug_int, color='g', marker='.',linestyle
        = 'None')
75         fig.canvas.draw()
76         plt.pause(0.05)
77
78         write_str = [time.time(), integral]
79         int_file.file_input(int_file.data_str_create(write_str))
80         print('t = {0}; Integral = {1}'.format(round(time.time()-t_0, 3),
        integral))
81
82         time.sleep(delay)
83
84         spec.close()
85         print('Measurement finished')
```



## Bibliography

- [1] “National climate assessment.” Onilne, 2014. (accessed 25 June 2019).
- [2] P. L. Kapitsa, “Doklad na nauchnoi sessii, posvyashonnoi 250-letiyu Akademii nauk CCCP: Energiia i Fizika,” *Vestnik, AS of USSR*, vol. 1, pp. 34–43, 1976.
- [3] “What is ITER?.” Onilne. (accessed 07 August 2019).
- [4] “The demonstration power plant: DEMO.” Onilne. (accessed 07 August 2019).
- [5] N. U. of Science and Technology, “Norway could be europe’s green battery,” *Phys.org*, 2015. <https://phys.org/news/2015-07-norway-europe-green-battery.html>.
- [6] H. Ritchie and M. Roser, “Renewable energy,” *Our World in Data*, 2019. <https://ourworldindata.org/renewable-energy>.
- [7] W. G. Adams and R. E. Day, “V. The action of light on selenium,” *Proceedings of the Royal Society of London*, vol. 25, no. 171-178, pp. 113–117, 1877.
- [8] D. M. Chapin, C. S. Fuller, and G. L. Pearson, “A new silicon p-n junction photocell for converting solar radiation into electrical power,” *Journal of Applied Physics*, vol. 25, no. 5, pp. 676–677, 1954.
- [9] J. Pelrin, *From Space to Earth: The Story of Solar Electricity*. aatec publications, 1999.
- [10] S. Buckley, “Thermic diode solar panels for space heating,” *Solar Energy*, vol. 20, no. 6, pp. 495 – 503, 1978.
- [11] Fraunhofer Institute for Solar Energy Systems, “I. Photovoltaics Report,” 2017.
- [12] “NREL Efficiency Chart.” Onilne, 04 2018. (accessed 13 August 2019).
- [13] A. Kojima, K. Teshima, Y. Shirai, and T. Miyasaka, “Organometal halide perovskites as visible-light sensitizers for photovoltaic cells,” *J. Am. Chem. Soc.*, vol. 131, no. 17, pp. 6050–6051, 2009.
- [14] H.-S. Kim, C.-R. Lee, J.-H. Im, K.-B. Lee, T. Moehl, A. Marchioro, S.-J. Moon, R. Humphry-Baker, J.-H. Yum, J. E. Moser, M. Grätzel, and N.-G. Park, “Lead iodide perovskite sensitized all-solid-state submicron thin film mesoscopic solar cell with efficiency exceeding 9%,” *Sci. Rep.*, vol. 2, p. 591, Aug 2012.

## Bibliography

---

- [15] A. Navrotsky and D. J. Weidner, *Perovskite: A Structure of Great Interest to Geophysics and Materials Science, Volume 45*. aatec publications, 1989.
- [16] "Perovskite structure." Onilne. (accessed 27 June 2019).
- [17] "File:CH3NH3PbI3 structure.png." Onilne. (accessed 27 June 2019).
- [18] C. Quarti, E. Mosconi, J. M. Ball, V. D'Innocenzo, C. Tao, S. Pathak, H. J. Snaith, A. Petrozza, and F. De Angelis, "Structural and optical properties of methylammonium lead iodide across the tetragonal to cubic phase transition: implications for perovskite solar cells," *Energy Environ. Sci.*, vol. 9, pp. 155–163, 2016.
- [19] F. Chen, C. Zhu, C. Xu, P. Fan, F. Qin, A. Gowri Manohari, J. Lu, Z. Shi, Q. Xu, and A. Pan, "Crystal structure and electron transition underlying photoluminescence of methylammonium lead bromide perovskites," *J. Mater. Chem. C*, vol. 5, pp. 7739–7745, 2017.
- [20] L. Landau and E. Lifshitz, "Chapter V - The Fermi and Bose Distributions," in *Statistical Physics (Third Edition)* (L. Landau and E. Lifshitz, eds.), pp. 158 – 190, Oxford: Butterworth-Heinemann, third edition ed., 1980.
- [21] C. C. Stoumpos, C. D. Malliakas, and M. G. Kanatzidis, "Semiconducting tin and lead iodide perovskites with organic cations: Phase transitions, high mobilities, and near-infrared photoluminescent properties," *Inorganic Chemistry*, vol. 52, no. 15, pp. 9019–9038, 2013.
- [22] E. Edri, S. Kirmayer, D. Cahen, and G. Hodes, "High open-circuit voltage solar cells based on organic–inorganic lead bromide perovskite," *The Journal of Physical Chemistry Letters*, vol. 4, no. 6, pp. 897–902, 2013.
- [23] K.-W. Benz, W. Neumann, and A. Mogilatenko, *Introduction to Crystal Growth and Characterization*. WILEY-VCH Verlag, 2014.
- [24] F. Liu, F. Sommer, C. Bos, and E. J. Mittemeijer, "Analysis of solid state phase transformation kinetics: models and recipes," *International Materials Reviews*, vol. 52, no. 4, pp. 193–212, 2007.
- [25] I. V. Markov, *Crystal Growth for Beginners: Fundamentals of Nucleation, Crystal Growth and Epitaxy*. World Scientific Press, June 1995.
- [26] C. V. Thompson, "Grain growth in thin films," *Annual Review of Materials Science*, vol. 20, no. 1, pp. 245–268, 1990.
- [27] Y. Zhou, O. S. Game, S. Pang, and N. P. Padture, "Microstructures of organometal trihalide perovskites for solar cells: Their evolution from solutions and characterization," *The Journal of Physical Chemistry Letters*, vol. 6, no. 23, pp. 4827–4839, 2015.

- [28] Y. Zhao, H. Tan, H. Yuan, Z. Yang, J. Z. Fan, J. Kim, O. Voznyy, X. Gong, L. N. Quan, C. S. Tan, J. Hofkens, D. Yu, Q. Zhao, and E. H. Sargent, "Perovskite seeding growth of formamidinium-lead-iodide-based perovskites for efficient and stable solar cells," *Nature Communications*, vol. 9, no. 1, p. 1607, 2018.
- [29] M. Xiao, L. Zhao, M. Geng, Y. Li, B. Dong, Z. Xu, L. Wan, W. Li, and S. Wang, "Selection of an anti-solvent for efficient and stable cesium-containing triple cation planar perovskite solar cells," *Nanoscale*, vol. 10, pp. 12141–12148, 2018.
- [30] H. Dong, Z. Wu, J. Xi, X. Xu, L. Zuo, T. Lei, X. Zhao, L. Zhang, X. Hou, and A. K.-Y. Jen, "Pseudohalide-induced recrystallization engineering for  $\text{CH}_3\text{NH}_3\text{PbI}_3$  film and its application in highly efficient inverted planar heterojunction perovskite solar cells," *Advanced Functional Materials*, vol. 28, no. 2, p. 1704836, 2018.
- [31] Y. Liang, Y. Yao, X. Zhang, W.-L. Hsu, Y. Gong, J. Shin, E. D. Wachsman, M. Dagenais, and I. Takeuchi, "Fabrication of organic-inorganic perovskite thin films for planar solar cells via pulsed laser deposition," *AIP Adv.*, vol. 6, no. 1, p. 015001, 2016.
- [32] S. Pang, H. Hu, J. Zhang, S. Lv, Y. Yu, F. Wei, T. Qin, H. Xu, Z. Liu, and G. Cui, " $\text{NH}_2\text{CH}=\text{NH}_2\text{PbI}_3$ : An alternative organolead iodide perovskite sensitizer for mesoscopic solar cells," *Chem. Mater.*, vol. 26, no. 3, pp. 1485–1491, 2014.
- [33] G. E. Eperon, V. M. Burlakov, P. Docampo, A. Goriely, and H. J. Snaith, "Morphological control for high performance, solution-processed planar heterojunction perovskite solar cells," *Adv. Funct. Mater.*, vol. 24, no. 1, pp. 151–157, 2014.
- [34] A. H. Ip, L. N. Quan, M. M. Adachi, J. J. McDowell, J. Xu, D. H. Kim, and E. H. Sargent, "A two-step route to planar perovskite cells exhibiting reduced hysteresis," *Appl. Phys. Lett.*, vol. 106, no. 14, p. 143902, 2015.
- [35] A. Barrows, A. Pearson, C. Kwak, A. Dunbar, A. Buckley, and D. Lidzey, "Efficient planar heterojunction mixed-halide perovskite solar cells deposited via spray-deposition," *Energy Environ. Sci.*, vol. 7, pp. 1–7, 2014.
- [36] D. Wang, Z. Liu, Z. Zhou, H. Zhu, Y. Zhou, C. Huang, Z. Wang, H. Xu, Y. Jin, B. Fan, S. Pang, and G. Cui, "Reproducible one-step fabrication of compact  $\text{MAPbI}_{3-x}\text{Cl}_x$  thin films derived from mixed-lead-halide precursors," *Chem. Mater.*, vol. 26, no. 24, pp. 7145–7150, 2014.
- [37] C. Bao, J. Yang, W. Zhu, X. Zhou, H. Gao, F. Li, G. Fu, T. Yu, and Z. Zou, "A resistance change effect in perovskite  $\text{CH}_3\text{NH}_3\text{PbI}_3$  films induced by ammonia," *Chem. Commun.*, vol. 51, no. 84, pp. 15426–15429, 2015.
- [38] N. Giesbrecht, J. Schlipf, L. Oesinghaus, A. Binek, T. Bein, P. Müller-Buschbaum, and P. Docampo, "Synthesis of perfectly oriented and micrometer-sized  $\text{MAPbBr}_3$  perovskite crystals for thin-film photovoltaic applications," *ACS Energy Letters*, vol. 1, no. 1, pp. 150–154, 2016.

- [39] Z. Wang, J. Liu, Z.-q. Xu, Y. Xue, L. Jiang, J. C. Song, F. Huang, Y. Wang, Y. L. Zhong, Y. Zhang, Y.-B. Cheng, and Q. Bao, "Wavelength-tunable waveguides based on polycrystalline organic-inorganic perovskite microwires," *Nanoscale*, vol. 8, pp. 6258–6264, 2015.
- [40] E. Horváth, M. Spina, Z. Szekrényes, K. Kamarás, R. Gaal, D. Gachet, and L. Forró, "Nanowires of methylammonium lead iodide ( $\text{CH}_3\text{NH}_3\text{PbI}_3$ ) prepared by low temperature solution-mediated crystallization," *Nano Lett.*, vol. 14, no. 12, pp. 6761–6766, 2014.
- [41] J.-H. Im, J. Luo, M. Franckevičius, N. Pellet, P. Gao, T. Moehl, S. M. Zakeeruddin, M. K. Nazeeruddin, M. Grätzel, and N.-G. Park, "Nanowire perovskite solar cell," *Nano Lett.*, vol. 15, no. 3, pp. 2120–2126, 2015.
- [42] J. C. Yu, D. B. Kim, E. D. Jung, B. R. Lee, and M. H. Song, "High-performance perovskite light-emitting diodes via morphological control of perovskite films," *Nanoscale*, vol. 8, pp. 7036–7042, 2016.
- [43] H. S. Jung and N.-G. Park, "Perovskite solar cells: From materials to devices," *Small*, vol. 11, no. 1, pp. 10–25, 2015.
- [44] Y. Zhao and K. Zhu, "Solution chemistry engineering toward high-efficiency perovskite solar cells," *The Journal of Physical Chemistry Letters*, vol. 5, no. 23, pp. 4175–4186, 2014.
- [45] S. D. Stranks, P. K. Nayak, W. Zhang, T. Stergiopoulos, and H. J. Snaith, "Formation of thin films of organic-inorganic perovskites for high-efficiency solar cells," *Angewandte Chemie International Edition*, vol. 54, no. 11, pp. 3240–3248, 2015.
- [46] J.-H. Im, H.-S. Kim, and N.-G. Park, "Morphology-photovoltaic property correlation in perovskite solar cells: One-step versus two-step deposition of  $\text{CH}_3\text{NH}_3\text{PbI}_3$ ," *APL Materials*, vol. 2, no. 8, p. 081510, 2014.
- [47] N. J. Jeon, J. H. Noh, Y. C. Kim, W. S. Yang, S. Ryu, and S. I. Seok, "Solvent engineering for high-performance inorganic-organic hybrid perovskite solar cells," *Nature Materials*, vol. 13, pp. 897–903, Jul 2014. Article.
- [48] M. Xiao, F. Huang, W. Huang, Y. Dkhissi, Y. Zhu, J. Etheridge, A. Gray-Weale, U. Bach, Y.-B. Cheng, and L. Spiccia, "A fast deposition-crystallization procedure for highly efficient lead iodide perovskite thin-film solar cells," *Angewandte Chemie International Edition*, vol. 53, no. 37, pp. 9898–9903, 2014.
- [49] Y. Zhou, M. Yang, W. Wu, A. L. Vasiliev, K. Zhu, and N. P. Padture, "Room-temperature crystallization of hybrid-perovskite thin films via solvent-solvent extraction for high-performance solar cells," *J. Mater. Chem. A*, vol. 3, pp. 8178–8184, 2015.
- [50] D. Shi, V. Adinolfi, R. Comin, M. Yuan, E. Alarousu, A. Buin, Y. Chen, S. Hoogland, A. Rothenberger, K. Katsiev, Y. Losovj, X. Zhang, P. A. Dowben, O. F. Mohammed, E. H.

- Sargent, and O. M. Bakr, "Low trap-state density and long carrier diffusion in organolead trihalide perovskite single crystals," *Science*, vol. 347, no. 6221, pp. 519–522, 2015.
- [51] Z. Zhou, Z. Wang, Y. Zhou, S. Pang, D. Wang, H. Xu, Z. Liu, N. P. Padture, and G. Cui, "Methylamine-gas-induced defect-healing behavior of  $\text{CH}_3\text{NH}_3\text{PbI}_3$  thin films for perovskite solar cells," *Angewandte Chemie International Edition*, vol. 54, no. 33, pp. 9705–9709, 2015.
- [52] J. J. De Yoreo, P. U. P. A. Gilbert, N. A. J. M. Sommerdijk, R. L. Penn, S. Whitelam, D. Joester, H. Zhang, J. D. Rimer, A. Navrotsky, J. F. Banfield, A. F. Wallace, F. M. Michel, F. C. Meldrum, H. Cölfen, and P. M. Dove, "Crystallization by particle attachment in synthetic, biogenic, and geologic environments," *Science*, vol. 349, no. 6247, 2015.
- [53] H. Hu, D. Wang, Y. Zhou, J. Zhang, S. Lv, S. Pang, X. Chen, Z. Liu, N. P. Padture, and G. Cui, "Vapour-based processing of hole-conductor-free  $\text{CH}_3\text{NH}_3\text{PbI}_3$  perovskite/C60 fullerene planar solar cells," *RSC Adv.*, vol. 4, pp. 28964–28967, 2014.
- [54] Y. Zhou, M. Yang, J. Kwun, O. S. Game, Y. Zhao, S. Pang, N. P. Padture, and K. Zhu, "Intercalation crystallization of phase-pure  $\alpha\text{-HC}(\text{NH}_2)_2\text{PbI}_3$  upon microstructurally engineered  $\text{PbI}_2$  thin films for planar perovskite solar cells," *Nanoscale*, vol. 8, pp. 6265–6270, 2016.
- [55] J.-W. Lee and N.-G. Park, "Two-step deposition method for high-efficiency perovskite solar cells," *MRS Bulletin*, vol. 40, no. 8, p. 654–659, 2015.
- [56] J. Burschka, N. Pellet, S.-J. Moon, R. Humphry-Baker, P. Gao, M. K. Nazeeruddin, and M. Grätzel, "Sequential deposition as a route to high-performance perovskite-sensitized solar cells," *Nature*, vol. 499, pp. 316–319, Jul 2013.
- [57] Z. Xiao, C. Bi, Y. Shao, Q. Dong, Q. Wang, Y. Yuan, C. Wang, Y. Gao, and J. Huang, "Efficient, high yield perovskite photovoltaic devices grown by interdiffusion of solution-processed precursor stacking layers," *Energy Environ. Sci.*, vol. 7, pp. 2619–2623, 2014.
- [58] Q. Chen, H. Zhou, Z. Hong, S. Luo, H.-S. Duan, H.-H. Wang, Y. Liu, G. Li, and Y. Yang, "Planar heterojunction perovskite solar cells via vapor-assisted solution process," *Journal of the American Chemical Society*, vol. 136, no. 2, pp. 622–625, 2014.
- [59] J. J. W. Morris, "Chapter 4: Defects in crystals." Onilne.
- [60] O. D. Hentz, *The Uncommon Nature of Point Defects in Organic-Inorganic Perovskite Solar Cells*. PhD thesis, Massachusetts Institute of Technology, 2018.
- [61] M. A. Green, A. Ho-Baillie, and H. J. Snaith, "The emergence of perovskite solar cells," *Nature Photonics*, vol. 8, p. 506–514, Jun 2014. Review Article.
- [62] H. Zhou, Q. Chen, G. Li, S. Luo, T.-b. Song, H.-S. Duan, Z. Hong, J. You, Y. Liu, and Y. Yang, "Interface engineering of highly efficient perovskite solar cells," *Science*, vol. 345, no. 6196, pp. 542–546, 2014.

- [63] K. Mahmood, S. Sarwar, and M. T. Mehran, "Current status of electron transport layers in perovskite solar cells: materials and properties," *RSC Adv.*, vol. 7, pp. 17044–17062, 2017.
- [64] U. Bach, D. Lupo, P. Comte, J. E. Moser, F. Weissörtel, J. Salbeck, H. Spreitzer, and M. Grätzel, "Solid-state dye-sensitized mesoporous TiO<sub>2</sub> solar cells with high photon-to-electron conversion efficiencies," *Nature*, vol. 395, no. 6702, pp. 583–585, 1998.
- [65] C.-H. Chiang and C.-G. Wu, "Bulk heterojunction perovskite-pcbm solar cells with high fill factor," *Nature Photonics*, vol. 10, p. 196–200, Feb 2016. Article.
- [66] G. Abdelmageed, L. Jewell, K. Hellier, L. Seymour, B. Luo, F. Bridges, J. Z. Zhang, and S. Carter, "Mechanisms for light induced degradation in mapbi3 perovskite thin films and solar cells," *Applied Physics Letters*, vol. 109, no. 23, p. 233905, 2016.
- [67] E. Smecca, Y. Numata, I. Deretzi, G. Pellegrino, S. Boninelli, T. Miyasaka, A. La Magna, and A. Alberti, "Stability of solution-processed MAPbI<sub>3</sub> and FAPbI<sub>3</sub> layers," *Phys. Chem. Chem. Phys.*, vol. 18, pp. 13413–13422, 2016.
- [68] J. Xing, Q. Wang, Q. Dong, Y. Yuan, Y. Fang, and J. Huang, "Ultrafast ion migration in hybrid perovskite polycrystalline thin films under light and suppression in single crystals," *Phys. Chem. Chem. Phys.*, vol. 18, pp. 30484–30490, 2016.
- [69] Y. Kutes, L. Ye, Y. Zhou, S. Pang, B. D. Huey, and N. P. Padture, "Direct observation of ferroelectric domains in solution-processed CH<sub>3</sub>NH<sub>3</sub>PbI<sub>3</sub> perovskite thin films," *The Journal of Physical Chemistry Letters*, vol. 5, no. 19, pp. 3335–3339, 2014.
- [70] N.-G. Park, M. Grätzel, T. Miyasaka, K. Zhu, and K. Emery, "Towards stable and commercially available perovskite solar cells," *Nature Energy*, vol. 1, p. 16152, Oct 2016. Perspective.
- [71] X. Zhao and N.-G. Park, "Stability issues on perovskite solar cells," *Photonics*, vol. 2, no. 4, pp. 1139–1151, 2015.
- [72] B. Náfrádi, G. Náfrádi, L. Forró, and E. Horváth, "Methylammonium Lead Iodide for Efficient X-ray Energy Conversion," *J. Phys. Chem. C*, vol. 119, no. 45, pp. 25204–25208, 2015.
- [73] Y. Zhou and Y. Zhao, "Chemical stability and instability of inorganic halide perovskites," *Energy Environ. Sci.*, vol. 12, pp. 1495–1511, 2019.
- [74] H. Berger, H. Tang, and F. Lévy, "Growth and raman spectroscopic characterization of tio<sub>2</sub> anatase single crystals," *Journal of Crystal Growth*, vol. 130, no. 1, pp. 108 – 112, 1993.
- [75] D. McMullan, "Scanning electron microscopy 1928–1965," *Scanning*, vol. 17, no. 3, pp. 175–185, 1995.



- 
- [76] W. H. Bragg and W. L. Bragg, "The reflection of x-rays by crystals," *Proceedings of the Royal Society of London. Series A, Containing Papers of a Mathematical and Physical Character*, vol. 88, no. 605, pp. 428–438, 1913.
- [77] E. Burkel, "Phonon spectroscopy by inelastic x-ray scattering," *Reports on Progress in Physics*, vol. 63, pp. 171–232, January 2000.
- [78] M. Upton, D. Casa, T. Gog, J. Misewich, J. P. Hill, D. Lowndes, and G. Eres, "Inelastic x-ray scattering studies of plasmons in carbon nanotubes," *American Physical Society, APS March Meeting*, p. abstract ID. D28.001, 03 2007.
- [79] L. Chaix, E. W. Huang, S. Gerber, X. Lu, C. Jia, Y. Huang, D. E. McNally, Y. Wang, F. H. Vernay, A. Keren, M. Shi, B. Moritz, Z.-X. Shen, T. Schmitt, T. P. Devereaux, and W.-S. Lee, "Resonant inelastic x-ray scattering studies of magnons and bimagnons in the lightly doped cuprate  $\text{La}_{2-x}\text{Sr}_x\text{CuO}_4$ ," *Phys. Rev. B*, vol. 97, p. 155144, Apr 2018.
- [80] H. P. Klug and L. E. Alexander, *X-Ray Diffraction Procedures: For Polycrystalline and Amorphous Materials, 2nd Edition*. aatec publications, 1974.
- [81] G. Binnig, C. F. Quate, and C. Gerber, "Atomic force microscope," *Phys. Rev. Lett.*, vol. 56, pp. 930–933, Mar 1986.
- [82] S. G. Bishop, "Characterization Of Semiconductors By Photoluminescence And Photoluminescence Excitation Spectroscopy," in *Optical Characterization Techniques for Semiconductor Technology* (D. E. Aspnes, R. F. Potter, and S. S. So, eds.), vol. 0276, pp. 2 – 10, International Society for Optics and Photonics, SPIE, 1981.
- [83] G. Davies, "The optical properties of luminescence centres in silicon," *Physics Reports*, vol. 176, no. 3, pp. 83 – 188, 1989.
- [84] F. M. Mor, A. Sienkiewicz, A. Magrez, L. Forró, and S. Jeney, "Single potassium niobate nano/microsized particles as local mechano-optical Brownian probes," *Nanoscale*, vol. 8, no. 12, pp. 6810–6819, 2016.
- [85] P. F. Ndione, Z. Li, and K. Zhu, "Effects of alloying on the optical properties of organic–inorganic lead halide perovskite thin films," *J. Mater. Chem. C*, vol. 4, pp. 7775–7782, 2016.
- [86] E. K. Zavoisky, *Paramagnetic Absorption in Orthogonal and Parallel Fields for Salts, Solutions and Metals*. PhD thesis, Kazan University, Kazan, Russia, 1944.
- [87] B. Náfrádi, M. Choucair, K.-P. Dinse, and L. Forró, "Room temperature manipulation of long lifetime spins in metallic-like carbon nanospheres," *Nature Communications*, vol. 7, p. 12232, 2016.
- [88] C. P. Poole, *Relaxation in magnetic resonance*. Academic Press, 1971.

## Bibliography

---

- [89] P. Szirmai, G. Fábián, B. Dóra, J. Koltai, V. Zólyomi, J. Kürti, N. M. Nemes, L. Forró, and F. Simon, “Density of states deduced from ESR measurements on low-dimensional nanostructures; benchmarks to identify the ESR signals of graphene and SWCNTs,” *physica status solidi (b)*, vol. 248, no. 11, pp. 2688–2691, 2011.
- [90] O. Chauvet, G. Oszlányi, L. Forro, P. W. Stephens, M. Tegze, G. Faigel, and A. Jànossy, “Quasi-one-dimensional electronic structure in orthorhombic  $\text{RbC}_{60}$ ,” *Physical Review Letters*, vol. 72, no. 17, pp. 2721–2724, 1994.
- [91] D. P. DiVincenzo, “Quantum computation,” *Science*, vol. 270, no. 5234, p. 255, 1995.
- [92] T. Takui, L. Berliner, and G. Hanson, *Electron Spin Resonance (ESR) Based Quantum Computing*, vol. 31. Springer, 2016.
- [93] P. Szirmai, *Frustration and Randomness: Magnetic Studies of Organic Quantum Spin Liquids*. PhD thesis, EPFL, 2017.
- [94] J. L. Zweier, “Measurement of superoxide-derived free radicals in the reperfused heart. Evidence for a free radical mechanism of reperfusion injury,” *Journal of Biological Chemistry*, vol. 263, no. 3, pp. 1353–1357, 1988.
- [95] P. Zeeman, “The effect of magnetisation on the nature of light emitted by a substance,” *Nature*, vol. 55, no. 1424, p. 347, 1897.
- [96] P. Szirmai, “Electron spin resonance spectroscopy in boron-doped diamond,” Master’s thesis, Budapest University of Technology and Economics, 2013.
- [97] C. P. Slichter, *Principles of magnetic resonance*, vol. 1. Springer Science & Business Media, 2013.
- [98] N. Ashcroft and N. Mermin, *Solid State Physics*. HRW international editions, Holt, Rinehart and Winston, 1976.
- [99] P. Ehrenfest, “Bemerkung über die angenäherte gültigkeit der klassischen mechanik innerhalb der quantenmechanik,” *Zeitschrift für Physik*, vol. 45, no. 7-8, pp. 455–457, 1927.
- [100] F. Bloch, “Nuclear induction,” *Physical Review*, vol. 70, no. 7-8, p. 460, 1946.
- [101] E. M. Purcell, H. Torrey, and R. V. Pound, “Resonance absorption by nuclear magnetic moments in a solid,” *Physical Review*, vol. 69, no. 1-2, p. 37, 1946.
- [102] R. R. Ernst and W. A. Anderson, “Application of Fourier transform spectroscopy to magnetic resonance,” *Review of Scientific Instruments*, vol. 37, no. 1, pp. 93–102, 1966.
- [103] K.-D. Schmalbein and K. Holczer, “Electron spin resonance spectrometer,” Nov. 1 1988. US Patent 4,782,296.

- [104] K. Holczer, D. Schmalbein, and P. Hofer, "Method of measuring pulsed electron spin resonance signals and pulsed electron spin resonance spectrometer," Apr. 30 1996. US Patent 5,512,829.
- [105] G. Grancini, V. D'Innocenzo, E. R. Dohner, N. Martino, A. R. Srimath Kandada, E. Mosconi, F. De Angelis, H. I. Karunadasa, E. T. Hoke, and A. Petrozza, "CH<sub>3</sub>NH<sub>3</sub>PbI<sub>3</sub> perovskite single crystals: surface photophysics and their interaction with the environment," *Chem. Sci.*, vol. 6, no. 12, pp. 7305–7310, 2015.
- [106] C. Zhao, W. Tian, J. Leng, R. Cui, W. Liu, and S. Jin, "Diffusion-correlated local photoluminescence kinetics in CH<sub>3</sub>NH<sub>3</sub>PbI<sub>3</sub> perovskite single-crystalline particles," *Sci. Bull.*, vol. 61, no. 9, pp. 665–669, 2016.
- [107] A. D. Wright, C. Verdi, R. L. Milot, G. E. Eperon, M. A. Pérez-Osorio, H. J. Snaith, F. Giustino, M. B. Johnston, and L. M. Herz, "Electron–phonon coupling in hybrid lead halide perovskites," *Nat. Commun.*, vol. 7, no. May, p. 11755, 2016.
- [108] C. Li, Y. Zhong, C. A. M. Luna, T. Unger, K. Deichsel, A. Gräser, J. Köhler, A. Köhler, R. Hildner, and S. Huettner, "Emission enhancement and intermittency in polycrystalline organolead halide perovskite films," *Molecules*, vol. 21, no. 8, pp. 1–12, 2016.
- [109] Z. Tang, S. Tanaka, S. Ito, S. Ikeda, K. Taguchi, and T. Minemoto, "Investigating relation of photovoltaic factors with properties of perovskite films based on various solvents," *Nano Energy*, vol. 21, pp. 51–61, 2016.
- [110] Y. Zhou, M. Yang, A. L. Vasiliev, H. F. Garces, Y. Zhao, D. Wang, S. Pang, K. Zhu, and N. P. Padture, "Growth control of compact CH<sub>3</sub>NH<sub>3</sub>PbI<sub>3</sub> thin films via enhanced solid-state precursor reaction for efficient planar perovskite solar cells," *J. Mater. Chem. A*, vol. 3, no. 17, pp. 9249–9256, 2015.
- [111] A. Elseman, "Chapter 11 - coatings and thin-film technologies," in *Organometal Halide Perovskites Thin Film and Their Impact on the Efficiency of Perovskite Solar Cells* (A. Taborda and A. Avila, eds.), IntechOpen, 2019.
- [112] M. Spina, E. Bonvin, A. Sienkiewicz, L. Forró, and E. Horváth, "Controlled growth of CH<sub>3</sub>NH<sub>3</sub>PbI<sub>3</sub> nanowires in arrays of open nanofluidic channels," *Sci. Rep.*, vol. 6, no. January, p. 19834, 2016.
- [113] K. Mantulnikovs, A. Glushkova, P. Matus, L. Ćirić, M. Kollár, L. Forró, E. Horváth, and A. Sienkiewicz, "Morphology and Photoluminescence of CH<sub>3</sub>NH<sub>3</sub>PbI<sub>3</sub> Deposits on Nonplanar, Strongly Curved Substrates," *ACS Photonics*, vol. 5, no. 4, pp. 1476–1485, 2018.
- [114] A. R. Srimath Kandada and A. Petrozza, "Photophysics of hybrid lead halide perovskites: The role of microstructure," *Acc. Chem. Res.*, vol. 49, no. 3, pp. 536–544, 2016.

## Bibliography

---

- [115] V. D’Innocenzo, A. R. Srimath Kandada, M. De Bastiani, M. Gandini, and A. Petrozza, “Tuning the light emission properties by band gap engineering in hybrid lead-halide perovskite,” *J. Am. Chem. Soc.*, vol. 136, no. 51, pp. 17730–17733, 2014.
- [116] W. Nie, H. Tsai, R. Asadpour, J.-C. Blancon, A. J. Neukirch, G. Gupta, J. J. Crochet, M. Chhowalla, S. Tretiak, M. A. Alam, H.-L. Wang, and A. D. Mohite, “High-efficiency solution-processed perovskite solar cells with millimeter-scale grains,” *Science*, vol. 347, no. 6221, pp. 522–525, 2015.
- [117] Y. Tian, A. Merdasa, E. Unger, M. Abdellah, K. Zheng, S. McKibbin, A. Mikkelsen, T. Pullerits, A. Yartsev, V. Sundström, and I. G. Scheblykin, “Enhanced organo-metal halide perovskite photoluminescence from nanosized defect-free crystallites and emitting sites,” *J. Phys. Chem. Lett.*, vol. 6, no. 20, pp. 4171–4177, 2015.
- [118] D. W. de Quilettes, S. M. Vorpahl, S. D. Stranks, H. Nagaoka, G. E. Eperon, M. E. Ziffer, H. J. Snaith, and D. S. Ginger, “Impact of microstructure on local carrier lifetime in perovskite solar cells,” *Science*, vol. 348, no. 6235, pp. 683–686, 2015.
- [119] S. De Wolf, J. Holovsky, S.-J. Moon, P. Löper, B. Niesen, M. Ledinsky, F.-J. Haug, J.-H. Yum, and C. Ballif, “Organometallic halide perovskites: Sharp optical absorption edge and its relation to photovoltaic performance,” *J. Phys. Chem. Lett.*, vol. 5, no. 6, pp. 1035–1039, 2014.
- [120] Z. Xu, A. Edgeton, and S. Costello, “Spatially inhomogeneous photoluminescence-voltage hysteresis in planar heterojunction perovskite-based solar cells,” *Appl. Phys. Lett.*, vol. 111, no. 22, p. 223901, 2017.
- [121] K. Kondiparty, A. Nikolov, S. Wu, and D. Wasan, “Wetting and spreading of nanofluids on solid surfaces driven by the structural disjoining pressure: Statics analysis and experiments,” *Langmuir*, vol. 27, no. 7, pp. 3324–3335, 2011.
- [122] D. J. Woodland and E. Mack, “The Effect of Curvature of Surface on Surface Energy. Rate of Evaporation of Liquid Droplets. Thickness of Saturated Vapor Films,” *J. Am. Chem. Soc.*, vol. 55, no. 8, pp. 3149–3161, 1933.
- [123] D. S. Kim, Y. J. Cha, M. H. Kim, O. D. Lavrentovich, and D. K. Yoon, “Controlling Gaussian and mean curvatures at microscale by sublimation and condensation of smectic liquid crystals,” *Nat. Commun.*, vol. 7, p. 10236, 2016.
- [124] P. J. Sáenz, A. W. Wray, Z. Che, O. K. Matar, P. Valluri, J. Kim, and K. Sefiane, “Dynamics and universal scaling law in geometrically-controlled sessile drop evaporation,” *Nat. Commun.*, vol. 8, p. 14783, 2017.
- [125] H. Gao, J. Feng, B. Zhang, C. Xiao, Y. Wu, X. Kan, B. Su, Z. Wang, W. Hu, Y. Sun, L. Jiang, and A. J. Heeger, “Capillary-Bridge Mediated Assembly of Conjugated Polymer Arrays toward Organic Photodetectors,” *Adv. Funct. Mater.*, vol. 1701347, p. 1701347, 2017.

- [126] C. Wang, B. R. Ecker, H. Wei, J. Huang, and Y. Gao, "Environmental Surface Stability of the MAPbBr<sub>3</sub> Single Crystal," *The Journal of Physical Chemistry C*, vol. 122, no. 6, pp. 3513–3522, 2018.
- [127] K.-H. Wang, L.-C. Li, M. Shellaiah, and K. Wen Sun, "Structural and Photophysical Properties of Methylammonium Lead Tribromide (MAPbBr<sub>3</sub>) Single Crystals," *Scientific Reports*, vol. 7, no. 1, p. 13643, 2017.
- [128] N. Aristidou, I. Sanchez-Molina, T. Chotchuangchutchaval, M. Brown, L. Martinez, T. Rath, and S. A. Haque, "The role of oxygen in the degradation of methylammonium lead trihalide perovskite photoactive layers," *Angew. Chem.*, vol. 54, no. 28, pp. 8208–8212, 2015.
- [129] A. Senocrate, T. Acartürk, G. Y. Kim, R. Merkle, U. Starke, M. Grätzel, and J. Maier, "Interaction of oxygen with halide perovskites," *J. Mater. Chem. A*, vol. 6, pp. 10847–10855, 2018.
- [130] Y. Tian, M. Peter, E. Unger, M. Abdellah, K. Zheng, T. Pullerits, A. Yartsev, V. Sundström, and I. G. Scheblykin, "Mechanistic insights into perovskite photoluminescence enhancement: light curing with oxygen can boost yield thousandfold," *Phys. Chem. Chem. Phys.*, vol. 17, no. 38, pp. 24978–24987, 2015.
- [131] J. F. Galisteo-López, M. Anaya, M. E. Calvo, and H. Míguez, "Environmental effects on the photophysics of organic–inorganic halide perovskites," *The Journal of Physical Chemistry Letters*, vol. 6, no. 12, pp. 2200–2205, 2015.
- [132] M.-A. Stoeckel, M. Gobbi, S. Bonacchi, F. Liscio, L. Ferlauto, E. Orgiu, and P. Samorì, "Reversible, fast, and wide-range oxygen sensor based on nanostructured organometal halide perovskite," *Advanced Materials*, vol. 29, no. 38, p. 1702469, 2017.
- [133] H.-H. Fang, S. Adjokatse, H. Wei, J. Yang, G. R. Blake, J. Huang, J. Even, and M. A. Loi, "Ultrahigh sensitivity of methylammonium lead tribromide perovskite single crystals to environmental gases," *Sci. Adv.*, vol. 2, no. 7, 2016.
- [134] J. M. Ball, M. M. Lee, A. Hey, and H. J. Snaith, "Low-temperature processed meso-superstructured to thin-film perovskite solar cells," *Energy Environ. Sci.*, vol. 6, pp. 1739–1743, 2013.
- [135] B. Yann, D. Olivier, T. Philippe, S. Toma, K. E. I., and L. Annick, "Selective differential ammonia gas sensor based on n-doped swcnt films," *Physica Status Solidi (b)*, vol. 248, no. 11, pp. 2462–2466, 2011.
- [136] H. Xia, J. Hu, J. Tang, K. Xu, X. Hou, and P. Wu, "A rgb-type quantum dot-based sensor array for sensitive visual detection of trace formaldehyde in air," *Scientific Reports*, vol. 6, p. 36794, Nov 2016. Article.

## Bibliography

---

- [137] Z. Jiang, X. Yu, S. Zhai, and Y. Hao, "Ratiometric dissolved oxygen sensors based on ruthenium complex doped with silver nanoparticles," *Sensors*, vol. 17, no. 3, 2017.
- [138] A. M. A. Leguy, P. Azarhoosh, M. I. Alonso, M. Campoy-Quiles, O. J. Weber, J. Yao, D. Bryant, M. T. Weller, J. Nelson, A. Walsh, M. van Schilfgaarde, and P. R. F. Barnes, "Experimental and theoretical optical properties of methylammonium lead halide perovskites," *Nanoscale*, vol. 8, no. 12, pp. 6317–6327, 2016.
- [139] T. Addabbo, F. Bertocci, A. Fort, M. Mugnaini, L. Shahin, V. Vignoli, R. Spinicci, S. Rocchi, and M. Gregorkiewitz, "An artificial olfactory system (aos) for detection of highly toxic gases in air based on  $\text{YCoO}_3$ ," *Procedia Eng.*, vol. 87, no. Supplement C, pp. 1095 – 1098, 2014.
- [140] G. Korotcenkov, V. Brinzari, and B. K. Cho, " $\text{In}_2\text{O}_3$ - and  $\text{SnO}_2$ -based thin film ozone sensors: Fundamentals," *J. Sens.*, vol. 2016, p. 31, 2016.
- [141] D. Bryant, N. Aristidou, S. Pont, I. Sanchez-Molina, T. Chotchunangatchaval, S. Wheeler, J. R. Durrant, and S. A. Haque, "Light and oxygen induced degradation limits the operational stability of methylammonium lead triiodide perovskite solar cells," *Energy Environ. Sci.*, vol. 9, pp. 1655–1660, 2016.
- [142] S. Yuan, Z. Qiu, H. Zhang, H. Gong, Y. Hao, and B. Cao, "Oxygen influencing the photocarriers lifetime of  $\text{CH}_3\text{NH}_3\text{PbI}_{3-x}\text{Cl}_x$  film grown by two-step interdiffusion method and its photovoltaic performance," *Appl. Phys. Lett.*, vol. 108, no. 3, p. 033904, 2016.
- [143] E. Climent-Pascual, B. C. Hames, J. S. Moreno-Ramirez, A. L. Alvarez, E. J. Juarez-Perez, E. Mas-Marza, I. Mora-Sero, A. de Andres, and C. Coya, "Influence of the substrate on the bulk properties of hybrid lead halide perovskite films," *J. Mater. Chem. A*, vol. 4, pp. 18153–18163, 2016.
- [144] X. Feng, H. Su, Y. Wu, H. Wu, J. Xie, X. Liu, J. Fan, J. Dai, and Z. He, "Photon-generated carriers excite superoxide species inducing long-term photoluminescence enhancement of  $\text{MAPbI}_3$  perovskite single crystals," *J. Mater. Chem. A*, vol. 5, pp. 12048–12053, 2017.
- [145] N. Aristidou, C. Eames, I. Sanchez-Molina, X. Bu, J. Kosco, M. S. Islam, and S. A. Haque, "Fast oxygen diffusion and iodide defects mediate oxygen-induced degradation of perovskite solar cells," *Nat. Commun.*, vol. 8, no. May, p. 15218, 2017.
- [146] J. S. Manser and P. V. Kamat, "Band filling with free charge carriers in organometal halide perovskites," *Nature Photonics*, vol. 8, pp. 737 – 743, Aug 2014. Article.
- [147] J. A. Christians, J. S. Manser, and P. V. Kamat, "Multifaceted Excited State of  $\text{CH}_3\text{NH}_3\text{PbI}_3$ . Charge Separation, Recombination, and Trapping," *The Journal of Physical Chemistry Letters*, vol. 6, no. 11, pp. 2086–2095, 2015.

- [148] A. M. A. Leguy, P. Azarhoosh, M. I. Alonso, M. Campoy-Quiles, O. J. Weber, J. Yao, D. Bryant, M. T. Weller, J. Nelson, A. Walsh, M. van Schilfgaarde, and P. R. F. Barnes, "Experimental and theoretical optical properties of methylammonium lead halide perovskites," *Nanoscale*, vol. 8, pp. 6317–6327, 2016.
- [149] W.-A. Quitsch, D. W. deQuilettes, O. Pfingsten, A. Schmitz, S. Ognjanovic, S. Jariwala, S. Koch, M. Winterer, D. S. Ginger, and G. Bacher, "The role of excitation energy in photobrightening and photodegradation of halide perovskite thin films," *The Journal of Physical Chemistry Letters*, vol. 9, no. 8, pp. 2062–2069, 2018.
- [150] J. S. Manser, J. A. Christians, and P. V. Kamat, "Intriguing optoelectronic properties of metal halide perovskites," *Chemical Reviews*, vol. 116, no. 21, pp. 12956–13008, 2016.
- [151] C. Ran, J. Xu, W. Gao, C. Huang, and S. Dou, "Defects in metal triiodide perovskite materials towards high-performance solar cells: origin, impact, characterization, and engineering," *Chem. Soc. Rev.*, vol. 47, pp. 4581–4610, 2018.
- [152] Y. Chen, H. T. Yi, X. Wu, R. Haroldson, Y. N. Gartstein, Y. I. Rodionov, K. S. Tikhonov, A. Zakhidov, X.-Y. Zhu, and V. Podzorov, "Extended carrier lifetimes and diffusion in hybrid perovskites revealed by hall effect and photoconductivity measurements," *Nature Communications*, vol. 7, p. 12253, Aug 2016.
- [153] T. Leijtens, G. E. Eperon, A. J. Barker, G. Grancini, W. Zhang, J. M. Ball, A. R. S. Kandada, H. J. Snaith, and A. Petrozza, "Carrier trapping and recombination: the role of defect physics in enhancing the open circuit voltage of metal halide perovskite solar cells," *Energy Environ. Sci.*, vol. 9, pp. 3472–3481, 2016.
- [154] J. M. Ball and A. Petrozza, "Defects in perovskite-halides and their effects in solar cells," *Nature Energy*, vol. 1, p. 16149, Oct 2016. Review Article.
- [155] A. Buin, P. Pietsch, J. Xu, O. Voznyy, A. H. Ip, R. Comin, and E. H. Sargent, "Materials processing routes to trap-free halide perovskites," *Nano Letters*, vol. 14, no. 11, pp. 6281–6286, 2014.
- [156] H. Uratani and K. Yamashita, "Charge carrier trapping at surface defects of perovskite solar cell absorbers: A first-principles study," *The Journal of Physical Chemistry Letters*, vol. 8, no. 4, pp. 742–746, 2017.
- [157] H. Zhang, Y. Liu, H. Lu, W. Deng, K. Yang, Z. Deng, X. Zhang, S. Yuan, J. Wang, J. Niu, X. Zhang, Q. Jin, H. Feng, Y. Zhan, and L. Zheng, "Reversible air-induced optical and electrical modulation of methylammonium lead bromide (MAPbBr<sub>3</sub>) single crystals," *Applied Physics Letters*, vol. 111, no. 10, p. 103904, 2017.
- [158] D. Meggiolaro, S. G. Motti, E. Mosconi, A. J. Barker, J. Ball, C. Andrea Riccardo Perini, F. Deschler, A. Petrozza, and F. De Angelis, "Iodine chemistry determines the defect tolerance of lead-halide perovskites," *Energy Environ. Sci.*, vol. 11, pp. 702–713, 2018.

## Bibliography

---

- [159] D. Hong, Y. Zhou, S. Wan, X. Hu, D. Xie, and Y. Tian, "Nature of photoinduced quenching traps in methylammonium lead triiodide perovskite revealed by reversible photoluminescence decline," *ACS Photonics*, vol. 5, no. 5, pp. 2034–2043, 2018.
- [160] E. Mosconi, D. Meggiolaro, H. J. Snaith, S. D. Stranks, and F. De Angelis, "Light-induced annihilation of frenkel defects in organo-lead halide perovskites," *Energy Environ. Sci.*, vol. 9, pp. 3180–3187, 2016.
- [161] K. Mantulnikovs, A. Glushkova, M. Kollár, L. Forró, E. Horváth, and A. Sienkiewicz, "Differential response of the photoluminescence and photocurrent of polycrystalline  $\text{CH}_3\text{NH}_3\text{PbI}_3$  and  $\text{CH}_3\text{NH}_3\text{PbBr}_3$  to the exposure to Oxygen and Nitrogen," *ACS Appl. Electron. Mater.*, 2019. 10.1021/acsaelm.9b00329.
- [162] G. Grancini, C. Roldán-Carmona, I. Zimmermann, E. Mosconi, X. Lee, D. Martineau, S. Narbey, F. Oswald, F. De Angelis, M. Graetzel, and M. K. Nazeeruddin, "One-year stable perovskite solar cells by 2d/3d interface engineering," *Nature Communications*, vol. 8, p. 15684, Jun 2017.
- [163] Z. Yi, N. H. Ladi, X. Shai, H. Li, Y. Shen, and M. Wang, "Will organic–inorganic hybrid halide lead perovskites be eliminated from optoelectronic applications?," *Nanoscale Adv.*, vol. 1, pp. 1276–1289, 2019.
- [164] L. Meng, J. You, and Y. Yang, "Addressing the stability issue of perovskite solar cells for commercial applications," *Nature Communications*, vol. 9, no. 1, p. 5265, 2018.
- [165] R. Brenes, C. Eames, V. Bulović, M. S. Islam, and S. D. Stranks, "The impact of atmosphere on the local luminescence properties of metal halide perovskite grains," *Advanced Materials*, vol. 30, no. 15, p. 1706208, 2018.
- [166] S. G. Motti, M. Gandini, A. J. Barker, J. M. Ball, A. R. Srimath Kandada, and A. Petrozza, "Photoinduced emissive trap states in lead halide perovskite semiconductors," *ACS Energy Letters*, vol. 1, no. 4, pp. 726–730, 2016.
- [167] R. Ahuja, H. Arwin, A. Ferreira da Silva, C. Persson, J. M. Osorio-Guillén, J. Souza de Almeida, C. Moyses Araujo, E. Veje, N. Veissid, C. Y. An, I. Pepe, and B. Johansson, "Electronic and optical properties of lead iodide," *Journal of Applied Physics*, vol. 92, no. 12, pp. 7219–7224, 2002.
- [168] S. A. Veldhuis, P. P. Boix, N. Yantara, M. Li, T. C. Sum, N. Mathews, and S. G. Mhaisalkar, "Perovskite materials for light-emitting diodes and lasers," *Advanced Materials*, vol. 28, no. 32, pp. 6804–6834, 2016.
- [169] P. Andričević, M. Kollár, X. Mettan, B. Náfrádi, A. Sienkiewicz, D. Fejes, K. Hernádi, L. Forró, and E. Horváth, "Three-dimensionally enlarged photoelectrodes by a protogenetic inclusion of vertically aligned carbon nanotubes into  $\text{CH}_3\text{NH}_3\text{PbBr}_3$  single crystals," *J. Phys. Chem. C*, vol. 121, no. 25, pp. 13549–13556, 2017.



- [170] M. Spina, M. Lehmann, B. Náfrádi, L. Bernard, E. Bonvin, R. Gaál, A. Magrez, L. Forró, and E. Horváth, "Microengineered  $\text{CH}_3\text{NH}_3\text{PbI}_3$  nanowire/graphene phototransistor for low-intensity light detection at room temperature," *Small*, vol. 11, no. 37, pp. 4824–4828, 2015.
- [171] M. Zhang, F. Zhang, Y. Wang, L. Zhu, Y. Hu, Z. Lou, Y. Hou, and F. Teng, "High-performance photodiode-type photodetectors based on polycrystalline formamidinium lead iodide perovskite thin films," *Scientific Reports*, vol. 8, no. 1, p. 11157, 2018.
- [172] R. Saraf, L. Pu, and V. Maheshwari, "A light harvesting, self-powered monolith tactile sensor based on electric field induced effects in  $\text{MAPbI}_3$  perovskite," *Advanced Materials*, vol. 30, no. 9, p. 1705778, 2018.
- [173] S. Yakunin, D. N. Dirin, Y. Shynkarenko, V. Morad, I. Cherniukh, O. Nazarenko, D. Kreil, T. Nauser, and M. V. Kovalenko, "Detection of gamma photons using solution-grown single crystals of hybrid lead halide perovskites," *Nature Photonics*, vol. 10, p. 585–589, Jul 2016.
- [174] R. Ranjan, A. Prakash, A. Singh, A. Singh, A. Garg, and R. K. Gupta, "Effect of tantalum doping in a  $\text{TiO}_2$  compact layer on the performance of planar spiro-ometad free perovskite solar cells," *J. Mater. Chem. A*, vol. 6, pp. 1037–1047, 2018.
- [175] T. Umebayashi, T. Yamaki, H. Itoh, and K. Asai, "Analysis of electronic structures of 3d transition metal-doped  $\text{TiO}_2$  based on band calculations," *Journal of Physics and Chemistry of Solids*, vol. 63, no. 10, pp. 1909 – 1920, 2002.
- [176] O. Teruhisa, M. Takahiro, and M. Michio, "Photocatalytic activity of s-doped  $\text{TiO}_2$  photocatalyst under visible light," *Chemistry Letters*, vol. 32, no. 4, pp. 364–365, 2003.
- [177] A. Murphy, "Does carbon doping of  $\text{TiO}_2$  allow water splitting in visible light? comments on "nanotube enhanced photoresponse of carbon modified (CM)-n- $\text{TiO}_2$  for efficient water splitting"," *Solar Energy Materials and Solar Cells*, vol. 92, no. 3, pp. 363 – 367, 2008.
- [178] I. Paramasivam, J. Macak, and P. Schmuki, "Photocatalytic activity of  $\text{TiO}_2$  nanotube layers loaded with ag and au nanoparticles," *Electrochemistry Communications*, vol. 10, no. 1, pp. 71–75, 2008.
- [179] S. Ghafoor, S. Ata, N. Mahmood, and S. N. Arshad, "Photosensitization of  $\text{TiO}_2$  nanofibers by  $\text{Ag}_2\text{S}$  with the synergistic effect of excess surface  $\text{Ti}^{3+}$  states for enhanced photocatalytic activity under simulated sunlight," *Sci Rep*, vol. 7, p. 255, Mar 2017.
- [180] J. Xue, Q. Shen, W. Liang, X. Liu, and F. Yang, "Photosensitization of  $\text{TiO}_2$  nanotube arrays with cdse nanoparticles and their photoelectrochemical performance under visible light," *Electrochimica Acta*, vol. 97, pp. 10 – 16, 2013.

## Bibliography

---

- [181] Y. An, A. Shang, G. Cao, S. Wu, D. Ma, and X. Li, "Perovskite solar cells: Optoelectronic simulation and optimization," *Solar RRL*, vol. 2, no. 11, p. 1800126, 2018.
- [182] D. Pérez-del Rey, P. P. Boix, M. Sessolo, A. Hadipour, and H. J. Bolink, "Interfacial modification for high-efficiency vapor-phase-deposited perovskite solar cells based on a metal oxide buffer layer," *The Journal of Physical Chemistry Letters*, vol. 9, no. 5, pp. 1041–1046, 2018.
- [183] C. Momblona, L. Gil-Escrig, E. Bandiello, E. M. Hutter, M. Sessolo, K. Lederer, J. Blochwitz-Nimoth, and H. J. Bolink, "Efficient vacuum deposited p-i-n and n-i-p perovskite solar cells employing doped charge transport layers," *Energy Environ. Sci.*, vol. 9, pp. 3456–3463, 2016.
- [184] W. A. Dunlap-Shohl, T. Li, and D. B. Mitzi, "Interfacial effects during rapid lamination within MAPbI<sub>3</sub> thin films and solar cells," *ACS Applied Energy Materials*, vol. 2, no. 7, pp. 5083–5093, 2019.
- [185] E. M. Hutter, J. Hofman, M. L. Petrus, M. Moes, R. D. Abellón, P. Docampo, and T. J. Savenije, "Charge transfer from methylammonium lead iodide perovskite to organic transport materials: Efficiencies, transfer rates, and interfacial recombination," *Advanced Energy Materials*, vol. 7, 7 2017.
- [186] N. Ishida, A. Wakamiya, and A. Saeki, "Quantifying hole transfer yield from perovskite to polymer layer: Statistical correlation of solar cell outputs with kinetic and energetic properties," *ACS Photonics*, vol. 3, no. 9, pp. 1678–1688, 2016.
- [187] C. S. Ponseca, E. M. Hutter, P. Piatkowski, B. Cohen, T. Pascher, A. Douhal, A. Yartsev, V. Sundström, and T. J. Savenije, "Mechanism of charge transfer and recombination dynamics in organo metal halide perovskites and organic electrodes, pcbm, and spiro-ometad: Role of dark carriers," *Journal of the American Chemical Society*, vol. 137, no. 51, pp. 16043–16048, 2015.
- [188] J. Peng, Y. Chen, K. Zheng, T. Pullerits, and Z. Liang, "Insights into charge carrier dynamics in organo-metal halide perovskites: from neat films to solar cells," *Chem. Soc. Rev.*, vol. 46, pp. 5714–5729, 2017.
- [189] M. Jung, S.-G. Ji, G. Kim, and S. I. Seok, "Perovskite precursor solution chemistry: from fundamentals to photovoltaic applications," *Chem. Soc. Rev.*, vol. 48, pp. 2011–2038, 2019.
- [190] J. Davies, J. Nicholls, and D. Verity, "Electron paramagnetic resonance of Ti<sup>2+</sup> in zinc-fired ZnSe," *Journal of Physics C: Solid State Physics*, vol. 13, no. 7, p. 1291, 1980.
- [191] J. Schneider and A. Räuber, "Electron spin resonance of Ti<sup>2+</sup> in ZnS," *Physics Letters*, vol. 21, no. 4, pp. 380–381, 1966.

- [192] R. Watts, "Electron spin resonance and optical absorption of  $\text{Ti}^{2+}$  in CdTe," *Physics Letters A*, vol. 27, no. 8, p. 469, 1968.
- [193] J. Xu, D. Wang, H. Yao, K. Bu, J. Pan, J. He, F. Xu, Z. Hong, X. Chen, and F. Huang, "Nano titanium monoxide crystals and unusual superconductivity at 11 K," *Advanced Materials*, vol. 30, no. 10, p. 1706240, 2018.
- [194] R. F. Howe and M. Gratzel, "EPR observation of trapped electrons in colloidal titanium dioxide," *J. Phys. Chem.*, vol. 89, no. 21, pp. 4495–4499, 1985.
- [195] M. Chiesa, M. C. Paganini, S. Livraghi, and E. Giamello, "Charge trapping in  $\text{TiO}_2$  polymorphs as seen by electron paramagnetic resonance spectroscopy," *Phys. Chem. Chem. Phys.*, vol. 15, pp. 9435–9447, 2013.
- [196] P. Szirmai, B. Náfrádi, A. Arakcheeva, E. Szilágyi, R. Gaál, N. M. Nemes, X. Berdat, M. Spina, L. Bernard, J. Jaćimović, A. Magrez, L. Forró, and E. Horváth, "Cyan titania nanowires: Spectroscopic study of the origin of the self-doping enhanced photocatalytic activity," *Catalysis Today*, vol. 284, pp. 52 – 58, 2017.
- [197] I. R. Macdonald, S. Rhydderch, E. Holt, N. Grant, J. M. Storey, and R. F. Howe, "EPR studies of electron and hole trapping in titania photocatalysts," *Catalysis Today*, vol. 182, no. 1, pp. 39 – 45, 2012.
- [198] I. R. Macdonald, R. F. Howe, X. Zhang, and W. Zhou, "In situ EPR studies of electron trapping in a nanocrystalline rutile," *Journal of Photochemistry and Photobiology A: Chemistry*, vol. 216, no. 2, pp. 238 – 243, 2010.
- [199] P. Löper, M. Stuckelberger, B. Niesen, J. Werner, M. Filipič, S.-J. Moon, J.-H. Yum, M. Topič, S. De Wolf, and C. Ballif, "Complex refractive index spectra of  $\text{CH}_3\text{NH}_3\text{PbI}_3$  perovskite thin films determined by spectroscopic ellipsometry and spectrophotometry," *The Journal of Physical Chemistry Letters*, vol. 6, no. 1, pp. 66–71, 2015.
- [200] J. R. DeVore, "Refractive indices of rutile and sphalerite," *J. Opt. Soc. Am.*, vol. 41, pp. 416–419, June 1951.
- [201] G. Ghosh, "Dispersion-equation coefficients for the refractive index and birefringence of calcite and quartz crystals," *Optics Communications*, vol. 163, no. 1, pp. 95 – 102, 1999.
- [202] I. Nakamura, N. Negishi, S. Kutsuna, T. Ihara, S. Sugihara, and K. Takeuchi, "Role of oxygen vacancy in the plasma-treated  $\text{TiO}_2$  photocatalyst with visible light activity for NO removal," *Journal of Molecular Catalysis A: Chemical*, vol. 161, no. 1, pp. 205 – 212, 2000.
- [203] E. Carter, A. F. Carley, and D. M. Murphy, "Evidence for  $\text{O}^{2-}$  radical stabilization at surface oxygen vacancies on polycrystalline  $\text{TiO}_2$ ," *The Journal of Physical Chemistry C*, vol. 111, no. 28, pp. 10630–10638, 2007.

## Bibliography

---

- [204] X. Pan and Y.-J. Xu, "Defect-mediated growth of noble-metal (ag, pt, and pd) nanoparticles on  $\text{TiO}_2$  with oxygen vacancies for photocatalytic redox reactions under visible light," *The Journal of Physical Chemistry C*, vol. 117, no. 35, pp. 17996–18005, 2013.
- [205] K. Mantulnikovs, P. Szirmai, M. Kollár, J. Stevens, P. Andričević, A. Glushkova, L. Rossi, P. Bugnon, E. Horváth, A. Sienkiewicz, L. Forró, and B. Nafradi, "Light-induced charge transfer at the  $\text{CH}_3\text{NH}_3\text{PbI}_3/\text{TiO}_2$  interface – a low-temperature Photo-EPR assay." under review.
- [206] Q. Tai, K.-C. Tang, and F. Yan, "Recent progress of inorganic perovskite solar cells," *Energy Environ. Sci.*, vol. 12, pp. 2375–2405, 2019.
- [207] L. K. Ono and Y. Qi, "Research progress on organic–inorganic halide perovskite materials and solar cells," *Journal of Physics D: Applied Physics*, vol. 51, p. 093001, feb 2018.
- [208] M. I. H. Ansari, A. Qurashi, and M. K. Nazeeruddin, "Frontiers, opportunities, and challenges in perovskite solar cells: A critical review," *Journal of Photochemistry and Photobiology C: Photochemistry Reviews*, vol. 35, pp. 1 – 24, 2018.

## Konstantins Mantulnikovs

EPFL SB IPHYS LPMC, PH D2 485, (Bâtiment PH)  
Station 3, CH-1015, Lausanne, Switzerland

+41 21 69 34438

[konstantins.mantulnikovs@epfl.ch](mailto:konstantins.mantulnikovs@epfl.ch)

[linkedin.com/in/konstantins-mantulnikovs](https://www.linkedin.com/in/konstantins-mantulnikovs)



### Education

**Ecole polytechnique fédérale de Lausanne (EPFL),**

Nov 2015 – Oct 2019

Doctor of Science in Physics

- Focus on Materials Science and Device Engineering

**University of Copenhagen (UCPH),**

Sept 2013 – Aug 2015

Master of Science in Nanotechnology

- Project in design and simulation of radiation shielding using Monte-Carlo method

**Moscow Institute of Physics and Technology, State University (MIPT),**

Sept 2009 – Aug 2013

Bachelor of Science in Applied Physics and Mathematics

- Focus on semiconductor physics

### Core Experience

**Laboratory of Physics of Complex Matter (LPMC), EPFL (Doctoral Thesis),**

Nov 2015 – Oct 2019

Study of the promising hybrid-organic perovskite materials  $\text{CH}_3\text{NH}_3\text{PbI}_3/\text{Br}_3$  using mainly electronic transport and photoluminescence. Design of three experimental setups using CAD and PyVISA in < 3 months each. Proof of principle gas-sensing device engineering leading to potential new implementations of hybrid-organic perovskites as well as deeper understanding of underlying processes to increase the solar cell efficiencies.

**University of Copenhagen (UCPH)/ESS/DTU Risø (Master Thesis),**

2014 – 2015

Creation of a concept, choice of materials and simulation of radiation shielding for BIFROST neutron scattering setup at ESS utilizing MCNPX nuclear code in conjunction with ray tracing software McStas in a timespan of 9 months.

**University of Copenhagen (UCPH) Department of Chemistry (Student research assistant),**

2014 – 2015

Work on spectroscopy of various materials. Proof-of-principle experiment of biological imaging using fluorescent spectroscopy performed in < 6 months.

**Center for Quantum Devices, University of Copenhagen (UCPH) (Student assistant),**

2013 – 2014

Design of a new 48 channel filter PCB for low-temperature, high-precision cryo-measurements in < 6 months.

**Institute of Microelectronics Technology and High Purity Materials, Chernogolovka, Russia (Research intern)**

2012 – 2013

Design of a new setup for tunneling spectroscopy in < 3 months and further investigation of semiconducting materials.

### Additional Experience

Supervising Practical Laboratory Exercises for 3<sup>rd</sup> year Bachelor students in Physics (TP3) EPFL

2015 – 2019

## Technical Skills

### Physical and Structural Characterization Techniques:

AC and DC electronic transport, Photocurrent measurements, Material spectroscopy (Absorption, Excitation, Emission via UV-VIS), X-Ray Diffraction (XRD), Neutron Scattering, Nuclear Magnetic Resonance (NMR), Electron Spin Resonance (ESR), Tunneling spectroscopy, Microscopy (Optical, SEM, TEM)

### Simulation:

Neutron Scattering Ray Tracing Software (McStas), Monte-Carlo N-Particle Transport Code (MCNPX)

### Mechanical design:

Setup design and testing, device engineering, CAD (SoliWorks, Inventor), PCB Design (Altium Designer), 3D printing

### IT:

MatLab, OriginLab, Modeling and Simulation in Simulink, Python (SciPy, PyVISA), C, C++, Scientific Software Development. Expert Command of MS Office (ECDL certificate No. LVS003328-10.06.2008) and LaTeX.

### Automotive design:

Powertrain sizing and analysis (Classical, Battery-Electrical and Hybrid Vehicles), Control theory, Sensor Fusion & Non-linear Filtering

## Languages

English	Fluent spoken (C1) and written (C2)
French	Intermediate level spoken and written (B2)
Danish	Intermediate level spoken and written (B1)
Latvian	Fluent spoken (C1) and written (C1)
Russian	Native language

## Extracurricular Activities

- European Jodo (FEJ) and Iaido (FEI) member (2 years)
- Volleyball team member (2 years)

## Personal Information

29, single, Latvian (EU), Swiss Permit B since 2015. No military obligations.  
Swiss driver's license (Type B) since 2008.

## Publications

- **Mantulnikovs K. et al.** “Light-induced charge transfer at the  $\text{CH}_3\text{NH}_3\text{PbI}_3/\text{TiO}_2$  interface – a low-temperature Photo-EPR assay” submitted to Journal of Physics: Photonics
- **Mantulnikovs K. et al.** “Differential response of the photoluminescence and photocurrent of polycrystalline  $\text{CH}_3\text{NH}_3\text{PbI}_3$  and  $\text{CH}_3\text{NH}_3\text{PbBr}_3$  to the exposure to Oxygen and Nitrogen” ACS Applied Electronic Materials (published on the 4<sup>th</sup> of September 2019, DOI: 10.1021/acsaelm.9b00329)
- Glushkova A. , **Mantulnikovs K.**, Girit G. , Semeniuk K. , Forró L. , Horváth E. and Arakcheeva A. “Effect of Thermal Cycling on the Structural Evolution of Methylammonium Lead Iodide Monitored around the Phase Transition Temperatures”. Solar RRL 2019, 3
- **Mantulnikovs K. et al.** “Morphology and Photoluminescence of  $\text{CH}_3\text{NH}_3\text{PbI}_3$  Deposits on Nonplanar, Strongly Curved Substrates” ACS Photonics 2018, 5, 4, 1476-1485
- **K. Mantulnikovs**, M. Bertelsen, C.P. Cooper-Jensen, K. Lefmann and E.B. Klinkby, “Neutron guide shielding for the BIFROST spectrometer at ESS” Journal of Physics: Conference Series, 2016, 746 (1)
- Z. Liao, M. Tropiano, **K. Mantulnikovs**, S. Faulkner, T. Vosch and T. J. Sørensen, “Spectrally resolved confocal microscopy using lanthanide centred near-IR emission” Chem. Commun., 2015, 51, 2372-2375

## Conference Contributions

- Poster entitled “Differential response of the photo-luminescence and photo-current of polycrystalline  $\text{CH}_3\text{NH}_3\text{PbI}_3$  and  $\text{CH}_3\text{NH}_3\text{PbBr}_3$  to the exposure to Oxygen and Nitrogen” presented at the IPEROP19 conference, Kyoto, Japan, 27 – 29 January 2019 (Authors: Konstantins Mantulnikovs, Anastasiia Glushkova, Péter Matus, Luka Ćirić, Márton Kollár, László Forró, Endre Horváth and Andrzej Sienkiewicz).
- Poster entitled “Transfer of photo-induced charge carriers on the interface between  $\text{CH}_3\text{NH}_3\text{PbI}_3$  and  $\text{TiO}_2$  detected by ESR” presented at MANEP 2018, Les Diablerets, Switzerland, 29 – 31 August 2018 (Authors: Konstantins Mantulnikovs, Péter Szirmai, Márton Kollár, Jeremy Stevens, Pavao Andricevic, Endre Horváth, László Forró, and Bálint Náfrádi).
- Oral presentation entitled “Morphology, photo-luminescence and photo-current of polycrystalline  $\text{CH}_3\text{NH}_3\text{PbI}_3$  and  $\text{CH}_3\text{NH}_3\text{PbBr}_3$  grown on strongly curved substrates” presented at conference From Solid State to BioPhysics IX (2018), Cavtat, Croatia, 16 – 23 June 2018 (Authors: Konstantins Mantulnikovs, Anastasiia Glushkova, Péter Matus, Luka Ćirić, Márton Kollár, László Forró, Endre Horváth and Andrzej Sienkiewicz).
- Poster entitled “Morphology and photoluminescence of  $\text{CH}_3\text{NH}_3\text{PbI}_3$  deposits on non-planar, strongly curved substrates” presented at HOPV18, Benidorm, Spain, 28 – 31 May 2018 (Authors: Konstantins Mantulnikovs, Anastasiia Glushkova, Péter Matus, Luka Ćirić, Márton Kollár, László Forró, Endre Horváth and Andrzej Sienkiewicz).
- Poster entitled “Morphology and photoluminescence of  $\text{CH}_3\text{NH}_3\text{PbI}_3$  deposits on non-planar, strongly curved substrates” presented at HOPV17, Lausanne, Switzerland, 21 – 24 May 2017 (Authors: Konstantins Mantulnikovs, Andrzej Sienkiewicz, Péter Matus, Luka Ćirić, Anastasiia Glushkova, Márton Kollár, Endre Horváth and László Forró).
- Poster entitled “Magnetoresistivity measurements on single crystal of  $\text{CH}_3\text{NH}_3\text{PbI}_3$  under weak illumination” presented at MANEP 2016, Les Diablerets, Switzerland, 6 – 8 July 2016 (Authors: Konstantins Mantulnikovs, Péter Szirmai, Andrea Pisoni, Bálint Náfrádi, Endre Horváth, and László Forró).

